BROADBAND PROPERTIES OF ACTIVE GALACTIC NUCLEI

Thesis by
Richard Edelson

In Partial Fulfillment of the Requirements
for the Degree of
Doctor of Philosophy

California Institute of Technology
Pasadena, California

1987
(Submitted 12 November 1986)

To my family and friends

ACKNOWLEDGEMENTS

Many people have contributed to my development as a scientist, and this thesis is a result of their efforts as well as mine. I hope that I can carry on this tradition by helping others advance science as I have been helped.

I thank my thesis advisors, Maarten Schmidt and Alan Moffet for their guidance. I am grateful for the freedom and independence they allowed me to pursue my ideas, and the direction and help they gave to me to turn them into reality.

Without my friend and collaborator Matthew Malkan, this thesis would look much different. From helping me develop these ideas to collaborating in the gathering and understanding of the data, he has left an indelible imprint. None but the sturdiest of souls could have worked so long and closely with me–he has witnessed a particularly concentrated form of my unique brand of insanity.

As my mentor during my undergraduate years, Sumner Davis inspired me to develop the discipline and knowledge a scientist needs. Tony Readhead and Nick Scoville were always willing to help me with any problem, scientific or otherwise, that I encountered. Although progress has generated dislocation and angst in today's society, these men remind me of the compassionate side of science.

Many others have contributed to this work. Walter Rice and Helen Hanson spent a great deal of time helping me understand the IRAS data which formed the backbone of the second, third, fifth, and seventh chapters of this thesis. Harry Hardeback, Richard Moore, and the rest of the Owens Valley Radio Observatory staff helped me gather the radio data used in the third and fourth chapters. George Rieke helped gather the near-infrared data used in Chapter 5 and collaborated in writing the paper. Tom Wahl reduced much of the IRAS variability data used in Chapter 6. John Huchra provided me with the list of CfA Seyfert galaxies long, long before publication. Roger Blandford, Sterl Phinney, and Jeremy Mould gave me much useful advice. David Cudaback, Carl Heiles, Ken Turner, and Harold

Weaver aided my development as an undergraduate. Marshall Cohen, Nick Scoville, Maarten Schmidt, Alan Moffet, Tony Readhead, Tom Phillips, and the institute itself provided financial support for my research. My long hours in the library were made more pleasant by the presence of Helen Knudson. I am also grateful to Kieth Shortridge, Mike Lesser, Peter Parniky, and Chris Lee for their tireless efforts to keep the computers running and helping me with programming questions, and to Lilo Hauck, Jill King, Ann Palfreymann, Marilyn Rice, Wendy Zhorne and the other Caltech and IPAC personnel for helping me through the maze of paperwork.

The company of my fellow graduate students and postdocs was very important to me. I really enjoyed the company of my office mates Erich Grossman, Dean Chou, Frank Evans, and Fernando Selman. Special thanks also goes to Shri Kulkarni, Jules Halpern, Alex Filippenko, Dave Tytler, Blaise Canzian, Chuck Steidel, Chris Impey, Jim Schombert, Lynn Deutsch, Gary Hinshaw, Charley Lawrence, Greg Bothun, Lucy Ziurys, Haimin Wang, Lee Mundy, Kwok-Wai Cheung, Kevin Lind, Alain Porter, and all you others who helped and watched me grow.

This moment of reflection also reminds me how lucky I am to have such great friends. When work became too much for me, their company preserved the remnants of my sanity. To all of my crazy friends in L.A., Berkeley, and the other parts of the world (especially the denizens of our house on Prospect Street), I love you. This goes especially for my parents, brother, and grandmother. Surely this is what gives life meaning.

Once again, to all of you who have shared this endeavor with me, thanks.

ABSTRACT

The broadband radio-infrared-optical-ultraviolet properties of active galactic nuclei are used to investigate the nature of the central engine and the surrounding environment. Optically selected quasars (which have $\overline{\alpha}_{IR} = -1.09$; $S_\nu \propto \nu^\alpha$) and Seyfert 1 galaxies ($\overline{\alpha}_{IR} = -1.15$) tend to have relatively flat infrared spectra and low reddenings, while most Seyfert 2 galaxies ($\overline{\alpha}_{IR} = -1.56$) and other dusty objects have steep infrared spectra and larger reddenings. The infrared spectra of most luminous radio-quiet active galaxies turn over near ~80 μm. It appears that the infrared spectra of most quasars and luminous Seyfert 1 galaxies are dominated by unreprocessed radiation from a synchrotron self-absorbed source of order a light day across, about the size of the hypothesized accretion disk. Seyfert 2 galaxies and other reddened objects have infrared spectra which appear to be dominated by thermal emission from warm (~50 K) dust, probably in the disk of the underlying galaxy. A broad emission feature, centered near 5 μm, is present in many luminous quasars and Seyfert 1 galaxies.

Highly polarized objects ("blazars") can be strongly variable at far-infrared wavelengths over time scales of months. There is no conclusive evidence for far-infrared variations in normal (low-polarization) quasars or Seyfert galaxies, although low-level flickering (at the ~30% peak-to-peak level) cannot be ruled out.

Seyfert galaxies tend to have steep radio spectra ($\alpha_{rad} \approx -0.7$). The radio spectra of Seyfert 1 galaxies often flatten out near 2 cm. There is no significant difference in the mean radio luminosities of Seyfert 1 and 2 galaxies. There are of order 10^5 Seyfert galaxies/Gpc^3, most of which have 6 cm luminosities between $10^{37.0}$ and $10^{39.4}$ ergs/s and 60 μm luminosities between $10^{42.2}$ and $10^{45.0}$ ergs/s. The Seyfert 2 galaxy radio luminosity function cuts off sharply below $10^{37.4}$ ergs/s.

TABLE OF CONTENTS

Chapter One

INTRODUCTION

Active galactic nuclei (AGNs) are the most powerful objects known to exist in the universe. They are believed to be powered by a supermassive ($\sim 10^8\ M_\odot$) black hole, accreting matter at the rate of ($\sim 1\ M_\odot$/year), and converting it into energy with a relatively high ($\sim$ 10%) efficiency and a very large bandwidth ($\gtrsim 10$ octaves). Their high energy output ($\sim 10^{46}$ ergs/sec) often exceeds that of all other processes in the galaxy combined. However, all of this energy is ultimately thought to be generated in a black-hole-accretion-disk system which is only of order a light day across. The precise method by which these enormous amounts of matter are converted in to energy is not yet known.

These objects produce nonthermal radiation over a very broad bandwidth. Therefore, only by measuring the continuum (its shape, variability, and polarization) is it possible to study the central regions directly. Other techniques (emission lines, mapping, etc.) are sensitive to radiation produced in much larger regions.

The primary purpose of this work is to determine the contribution of the nucleus and other more extended emission regions to the broad-band continuum. Studying the broad-band characteristics of these components and their relation to other spectral characteristics will yield information about the physical conditions and processes occurring in and around the nucleus.

Besides this introduction and a concluding chapter, this thesis consists of five separate but related papers, each confined to studies in a given wavelength range. Four have been submitted to *the Astrophysical Journal*, and the remaining one will be submitted shortly. There is one appendix, which gives the optical spectra of the Seyert galaxies used in Chapters 4 and 5.

The remainder of this chapter is devoted to a discussion of the motivation and justification for this work. This work can be convieniently broken into three sections. The importance of the infrared-optical-ultraviolet spectral properties of AGNs is discussed in the next section. The rationale behind the study of far-infrared variability is discussed in the next section, and radio spectra are dealt with in the final section. Each section consists of a discussion of previous work and the scientific justification for the research undertaken.

I. INFRARED-OPTICAL-ULTRAVIOLET SPECTRAL ENERGY DISTRIBUTIONS

A) Previous Work

Much has already been learned from previous studies of the ultraviolet-optical-infrared continuum properties of AGNs. In a pioneering study, Rieke (1978) found that the spectra of Seyfert galaxies rose from the optical into the near-infrared ($\alpha_{IR} \approx -1; S_\nu \propto \nu^\alpha$). Their spectra are much steeper than those of normal galaxies, which cut off sharply near 1.5 μm. This near-infrared excess was explained as thermal emission from hot dust ($T \gtrsim 1000$ K). That study also found that the ultraviolet-excess Markarian survey was biased against the inclusion of objects with strong infrared excesses.

Neugebauer *et al.* (1979) studied the optical-near-infrared spectra of quasars. They favored a nonthermal explanation for the infrared excess. They also found that the 2.2–3.5 μm spectral indices of many quasars were steeper than their 1.2–2.2 μm spectral indices, although this discovery was not followed up for many years.

Malkan and collaborators (Malkan and Sargent 1982, Malkan and Oke 1983, Malkan 1983) fit the ultraviolet through near-infrared continuua of AGNs with a multi-component physical model. They used a nonthermal power law to model the near-infrared excess. They also found that the ultraviolet excess could be explained as a combination of thermal emission from a hot accretion disk ($T \approx 26,000$ K) and Balmer continuum emission.

Thus, the nature of the infrared excess has not been definitively established. This can be seen in two models of the optical-near-infrared continuum of the best studied Seyfert 1 galaxy, NGC 4151. Rieke and Lebofsky (1981) modeled it as thermal emission from dust, while Malkan and Sargent (1982) used a nonthermal power law. Both papers obtain reasonable fits, and find that the other explanation is not acceptable.

B) Scientific Justification

The fundamental cause of the disagreement over the nature of the infrared emission lies in the fact that the ground-based data were always limited to wavelengths $\lambda \leq 10\ \mu m$, and often to $\lambda \leq 2 - 3\ \mu m$. This coverage is not sufficient to allow the infrared excess component to be unambiguously separated from other emission components (galactic starlight and the ultraviolet blackbody). A second problem is that those studies used arbitrarily chosen objects, instead of well-defined samples. For instance, only one Seyfert 2 galaxy (NGC 1068) was carefully studied. This greatly reduced the power of statistical arguments to discriminate between different processes in different types of objects.

This study addresses these issues directly. Chapter 2 contains detailed model fits to the 0.1-100 μm spectral energy distributions of a heterogeneous sample of bright AGNs. Extending the wavelength coverage to 100 μm allows clean separation of the optical-ultraviolet components from the infrared excess. It also allows the first systematic study of the near-infrared feature discovered by Neugebauer *et al.* (1979), as well as an analysis of the effects of reddening and a detailed study of the ultraviolet, optical, and near-infrared features studied previously.

Detailed statistical analysis of the infrared (1-100 μm) properties of the brightest PG/BQS quasars and the CfA Seyfert galaxies are presented in Chapters 3 and 5, respectively. These chapters focus on determining the nature of the infrared emission from the nucleus and the underlying galaxy. Use of these complete, optically selected samples makes powerful statistical tools available.

II. FAR-INFRARED VARIABILITY

A) Previous Research

Highly polarized AGNs (BL Lac objects and OVV quasars) are generally strongly variable at all wavelengths from X-rays to radio (see, e.g., Bregman *et al.* 1985). Seyfert 1 galaxies and normal (low-polarization) quasars are less violently variable, but variability from X-ray to near-infrared wavelengths have been well documented (e.g., Halpern 1982, Cutri *et al.* 1985, Neugebauer *et al.* 1986), while Seyfert 2 galaxies are generally not variable. Most normal AGNs cannot be detected from the ground at wavelengths longer than 10 μm, so only one object (NGC 4151) has been monitored longward of 3.5 μm (Rieke and Lebofsky 1981).

B) Scientific Justification

Detectable thermal emission from AGNs at wavelengths significantly longer than 10 μm must generally emanate from a region many light-decades across. Therefore, the detection of far-infrared variations would demonstrate that the continuum emission is nonthermal. In Chapter 6, pointed IRAS observations are used to monitor the far-infrared fluxes of blazars, normal quasars, and Seyfert 1 and 2 galaxies.

III. RADIO EMISSION

A) Previous Research

Although the first quasars were discovered because of their intense radio emission, only a small fraction of all AGNs are "radio-loud" objects. Radio surveys of optically selected AGNs have generally had poor detection rates (see, e.g., Condon *et al.* 1981), so the radio properties of the underlying population of AGNs are not known. The nature of the difference between radio-loud and radio-quiet AGNs has been an outstanding question since quasars were first discovered.

B) Scientific Justification

Two different approaches to this problem are pursued in this thesis. The first involves use of the IRAS data. The spectra of most radio-quiet AGNs rise from the optical into the infrared, but (unlike radio-loud objects) this component must cut off somewhere in the far-infrared-submillimeter region. Depending on the nature of the infrared emission, determination of this turnover frequency can be used to determine source parameters. The derivation and implications of the low-frequency cutoff is discussed in Chapters 2, 3, and 5.

Also, the radio properties of the CfA Seyfert galaxies are discussed directly in Chapter 4. This is the first study of optically selected (i.e., radio-quiet) AGNs for which 100% are detected at radio wavelengths, and three frequency radio spectra were determined for a majority of the objects. This allows the radio properties of optically selected Type 1 and 2 Seyfert galaxies to be properly studied with powerful statistical tools. These properties include radio spectra, variability, resolution effects, and luminosity function.

REFERENCES

Bregman, J. *et al.* 1986, *Ap. J.*, **301**, 708.

Condon, J. *et al.* 1981, *Ap. J.*, **246**, 624.

Cutri, R. *et al.* 1985, *Ap. J.*, **296**, 423.

Halpern, J. 1982, *Ph.D. Thesis, Harvard University.*

Malkan, M. A. 1983, *Ap. J.*, **268**, 582.

Malkan, M. A. and Sargent, W. L. W. 1982, *Ap. J.*, **254**, 22.

Malkan, M. A. and Oke, J. B. 1983, *Ap. J.*, **265**, 92.

Neugebauer, G. *et al.* 1979, *Ap. J.*, **230**, 79.

Neugebauer, G. *et al.* 1987, *Ap. J.*, in press.

Rieke, G. 1978, *Ap. J.*, **266**, 550.

Rieke, G. and Lebofsky, M. J. 1981, *Ap. J.*, **250**, 87.

Chapter Two

SPECTRAL ENERGY DISTRIBUTIONS OF ACTIVE GALACTIC NUCLEI BETWEEN 0.1 AND 100 MICRONS *

Reprinted from *The Astrophysical Journal* (1986, v. **308**, pp. 59-78)

---

* Written in collaboration with M. Malkan

THE ASTROPHYSICAL JOURNAL, 308:59–77, 1986 September 1

SPECTRAL ENERGY DISTRIBUTIONS OF ACTIVE GALACTIC NUCLEI BETWEEN 0.1 AND 100 MICRONS

R. A. EDELSON
Palomar Observatory, California Institute of Technology
AND
M. A. MALKAN
Department of Astronomy, University of California, Los Angeles
Received 1985 October 28; accepted 1986 February 20

ABSTRACT

We have combined new photometry from the *Infrared Astronomy Satellite* with ground-based optical and near-infrared spectrophotometry and ultraviolet spectrophotometry from the *International Ultraviolet Explorer* to study the spectral energy distributions from 0.1 to 100 μm for 29 active galactic nuclei. After correcting for the effects of starlight and foreground and internal reddening, we fitted the spectra with a simple model, varying the minimum number of parameters needed to describe the data accurately. The infrared continua of quasars and Seyfert 1 galaxies with low reddening were well fitted by a power law with a relatively flat slope ($\overline{\alpha}_{\rm pl} = -1.36 \pm 0.21$). Their fitted power law appears to be nonthermal in origin, and the power-law luminosity is well correlated with the 2 keV luminosity, with an average slope from optical to X-ray frequencies of $\overline{\alpha}_{\rm ox} = -1.15 \pm 0.02$. In 16 of the 29 AGNs the power law had a low-frequency turnover shortward of 100 μm, and many of the less luminous objects probably have turnovers which are undetected because of emission from cold dust from the underlying galaxy. For most of the Seyfert 1 galaxies and quasars in our sample, the turnover appears to be due to synchrotron self-absorption in a region similar in size to the hypothesized inner accretion disk.

The infrared continua of Seyfert 2 galaxies and other reddened objects tend to be steep ($\overline{\alpha}_{\rm pl} = -1.58 \pm 0.40$), and cannot be accurately described by a power law. In these dusty objects, the flux beyond 10 μm is dominated by thermal reradiation from dust in a volume similar to that of the narrow-line region, at a minimum temperature of 40–80 K, hotter than dust in normal galaxies.

An additional flux component was required to fit accurately the near-infrared continua of over half the Seyfert 1 galaxies and quasars. We described it as a parabola, and found it was always centered near 58 THz (5.2 μm), with a width of about 3.3 octaves. The strength of this feature, which contains up to 40% of the luminosity between 2.5 and 10 μm, is correlated with the luminosity and Hβ/[O III] ratio. The ultraviolet continua of all of the Seyfert 1 galaxies without large internal reddenings required the inclusion of a hot thermal component in the fits, which we described as a blackbody with fitted temperatures around 26,000 K. The mean Balmer continuum/Hα ratio is 2.1 ± 0.6 for Seyfert 1 galaxies, which is about 50% higher than the case B prediction.

Subject headings: galaxies: nuclei — galaxies: Seyfert — infrared: spectra — quasars — radiation mechanisms — spectrophotometry

I. INTRODUCTION

A major obstacle to understanding energy generation in active galactic nuclei (AGNs) has been the difficulty of measuring the complete continuous energy spectrum, which has a comparable luminosity per octave (in νF_ν) at infrared, ultraviolet, and hard X-ray wavelengths. The largest gap in previous spectral coverage has been between 10 μm and 1 cm, where low atmospheric transmission and poor instrumental sensitivity have prevented detection of all but the very brightest AGNs. The far-infrared region (30–1000 μm) is especially important because it can include the bulk of an AGN's integrated power, and the transition from infrared to radio wavelengths requires a dramatic spectral turnover in all but the strongest radio sources.

Until recently, only a handful of AGNs had been detected in the far-infrared. The brightest Seyfert galaxy, NGC 1068, was found to have a peak flux density around 80 μm (Hildebrand *et al.* 1977; Telesco and Harper 1980). The quasar 3C 273 has been detected at centimeter, millimeter, submillimeter, and far-infrared wavelengths (Robson *et al.* 1983), as has 3C 345 (Harvey, Wilking, and Joy 1982). Rickard and Harvey (1984) observed NGC 1068, NGC 3227, NGC 4051, and NGC 7469 from 40 to 160 μm.

The *Infrared Astronomy Satellite* (*IRAS*) recently surveyed 98% of the sky with unprecedented sensitivity in broad wavelength bands centered at 12, 25, 60, and 100 μm. It greatly increased the available data on the far-infrared continua of the brightest AGNs, making it possible to study a large sample with uniquely broad wavelength coverage. In this paper we combine new photometry from *IRAS* with ground-based optical and near-infrared spectrophotometry, and ultraviolet spectrophotometry from the *International Ultraviolet Explorer* (*IUE*), to study the broad-band properties of AGNs.

An outstanding question is the relative importance of thermal and nonthermal emission at infrared wavelengths. There is little doubt that thermal emission from warm dust grains dominates the 10–100 μm flux (and therefore the total energy output) of NGC 1068 and most, if not all, other

Seyfert 2 nuclei (Rieke and Lebofsky 1979*a*). Some Seyfert 2 nuclei, most notably NGC 1068, must also have a smaller quantity of hotter dust which can dominate the spectrum at wavelengths as short as 3 μm (e.g., Malkan and Oke 1983, hereafter MO). A related observation is that all closely studied Seyfert 2 nuclei have emission-line regions with at least a moderate amount of reddening not produced in the Milky Way, e.g., with internal continuum dust optical depths $\tau \geq 1$ below 3000 Å (see § IV*d* and Malkan 1986).

The mechanism producing the far-infrared emission of Seyfert 1 galaxies and quasars is more controversial (Rieke and Lebofsky 1979*b*). Some highly reddened objects such as Mrk 231 must have infrared spectra dominated by thermal emission. Like NGC 1068, Mrk 231 has a spectra dip around 10 μm which has been identified as silicate absorption (Rieke 1976). Only two Seyfert 1 galaxies, NGC 3227 and NGC 7469, have had detected emission in the 3.3 μm dust feature, but, in NGC 7469 at least, much of it comes from H II regions in the galaxy rather than from the nucleus (Cutri *et al.* 1984; Cutri 1986).

On the other hand, many Seyfert 1 nuclei have optical to near-infrared spectral energy distributions (SEDs) which extend smoothly to 10 μm with a relatively constant power-law slope $\alpha \sim -1.2$ ($F_\nu \propto \nu^\alpha$) (Malkan and Filippenko 1983, hereafter MF). Careful narrow-band photometry in the near-infrared has failed to detect silicate absorption, or any emission features (e.g., at 3.3 or 11.6 μm) which are known to come from dust grains (Rudy *et al.* 1982*b*; Roche *et al.* 1984). Moreover, the optical to ultraviolet colors of many Seyfert 1 nuclei, especially the luminous ones, are confined to a relatively narrow, blue range which rules out continuum reddenings exceeding $E_{B-V} = 0.05$–0.10 (Malkan 1984). This is consistent with upper limits derived from the absence of 2175 Å dust absorption (Malkan and Sargent 1982, hereafter MS), or the absence of soft X-ray absorption (Pounds and McHardy 1985). In § III we present further evidence that most of the Seyfert 1 and quasar SEDs in this study are not strongly affected by dust.

One of the major goals of this paper is to determine the relation between properties derived at different wavelengths. We used the Spearman rank test (see Siegel 1956), a nonparametric test, to search for correlations between derived parameters when no upper limits were present in the data, and the Cox proportional hazard method when some of the data for one variable contained upper limits. A good discussion of the Cox test is given in Isobe, Feigelson, and Nelson (1986).[1]

We describe the data and methods used to construct the broad-band SEDs in the next section, and the multicomponent fits to the SEDs in § III. We discuss the determination and implications of the far-infrared emission and low-frequency turnover in § IV. The strong, broad feature found to be centered at 5 μm in many SEDs is discussed in § V. The nature of the ultraviolet emission is discussed in § VI, and the relationship between properties determined from the 0.1–100 μm SEDs and those derived at other frequencies is discussed in § VII. The major results of this paper are summarized in § VIII. Throughout, we adopt a value of $H_0 = 75$ km s^{-1} Mpc^{-1} and $q_0 = 0$.

II. DATA

Our sample consists of 29 of the brightest AGNs which have good *IRAS* detections, complete ground-based optical and infrared spectrophotometry, and *IUE* data. These data together provide nearly continuous spectral coverage over 10 octaves of frequency.

This sample is a heterogeneous collection of AGNs. Some sources selected for our study were originally identified in ultraviolet-excess surveys, which tend to miss reddened objects. On the other hand, the limited sensitivity of *IRAS* will tend to single out AGNs with exceptionally strong far-infrared continua. These conflicting biases undoubtedly operated on the present sample. Only three of the brightest Seyfert 2 galaxies, NGC 1068, Mrk 3, and Mrk 348, had sufficiently complete spectral coverage to be included.

We required that all program objects have ultraviolet spectra, usually in both the long and short-wavelength cameras of the *IUE*. Fortunately, *IUE* has now observed most of the brighter Seyfert galaxies at least once. Data were taken from the literature (see references in Table 1) or the archives of the National Space Sciences Data Center, using standard reduction programs at the Regional Data Analysis Facility in Greenbelt. The ultraviolet data were binned in ~ 100 Å bands devoid of strong emission lines, to give typical signal-to-noise ratios of 10 or more. *IUE*'s 10″ × 20″ oval aperture agrees adequately with the ~ 10″ apertures used in the optical and near-infrared, especially because most of the ultraviolet flux is unresolved.

The ~ 10″ apertures used in the optical are a good compromise between the conflicting requirements of obtaining accurately calibrated absolute spectrophotometry of the unresolved nucleus while excluding as much of the starlight as possible. We do not use broad-band optical photometry (i.e., *UBV*), since it does not allow precise separation of emission lines and Balmer continuum emission from the principal object of our study, the underlying continuum. The sources of our intermediate-resolution optical spectrophotometry are listed in Table 1. Some optical spectrophotometry for objects in this study without previously published fluxes is presented in the Appendix. As with the ultraviolet data, we excluded optical wavelengths near strong emission lines.

Low resolution is acceptable in the infrared, which seems to be free of strong emission lines. Thus, for objects without narrow-band infrared spectra, we have used broad-band infrared fluxes, at *J* (1.2 μm), *H* (1.6 μm), *K* (2.2 μm), *L* (3.5 μm), *N* (10.6 μm), and *Q* (21 μm). We converted the magnitudes to absolute fluxes using the calibrations from Campins, Rieke, and Lebofsky (1985) and Rieke, Lebofsky, and Low (1985). New near-infrared photometry for some of the AGNs analyzed in this paper is presented in the Appendix. A number of objects in this study have published CVF spectra. For NGC 1068 we adopted the average of the 8–13 μm spectra from Roche *et al.* (1984) and Rudy *et al.* (1982*b*). Rudy *et al.* (1982*b*) adjusted the absolute flux levels of the near-infrared spectra to agree with broad-band *K* (2.2 μm) and *L* (3.5 μm) measurements. We readjusted them to agree with the *K* and *L* fluxes appropriate for the epoch and aperture size of our multiwavelength spectra.

The far-infrared *IRAS* photometry, at 12, 25, 60, and 100 μm, is discussed in the Appendix. The correction of the *IRAS* fluxes to 10″ apertures using ground-based 10.6 and 21 μm data is discussed in § III*b*. Observations at 100 and 160 μm from Rickard and Harvey (1984) were also included for the four galaxies in common with this study.

Although most of our ultraviolet/optical/near-infrared/far-infrared spectra were not simultaneously observed, they are well matched at 0.3 and 1.0 μm, and are probably quite similar to spectra which would result from truly simultaneous obser-

---

[1] The nonparametric Kolmogorov-Smirnov (K-S) test was used to test for differences in the distribution of univariate data (Siegel 1956).

TABLE 1

AGN Sample Data

Source Name	Coordinate Name	E_{B-V} Galactic[a]	E_{B-V} Internal[b]	Scale Factor[c]	Fraction Starlight[d]	References
Mrk 335	0003+19	0.00	0.02	0.75	0.13	1–4
Mrk 348	0046+31	0.05	0.15	0.80	0.56	2, 5, 6
I Zw 1	0050+12	0.04	0.06	0.75	0.19	1, 2, 6, 7
NGC 1068	0240−00	0.01	0.29	0.75	0.72	6, 8–10
3C 84	0316+41	0.03	0.02	1.00	0.38	4, 5, 10–13
3C 120	0430+05	0.03	0.06	0.85	0.18	4–6, 10, 13, 14
Akn 120	0513−00	0.09	0.02	0.65	0.13	1, 13, 15
Mrk 3	0609+71	0.15	0.10	0.55	0.90	8
Mrk 6	0645+74	0.09	0.22	0.95	0.78	8
Mrk 376	0710+45	0.09	0.10	0.45	0.33	2, 5
Mrk 9	0732+58	0.03	0.08	0.85	0.18	2, 3, 5, 16
Mrk 79	0738+49	0.06	0.18	0.65	0.37	2, 3, 5, 14, 17
PG	0906+48	0.00	0.03	1.00	0.30	9
NGC 3227	1020+20	0.02	0.33	0.65	0.59	2, 5, 18
NGC 3516	1103+72	0.02	0.10	0.70	0.68	2, 5, 17
NGC 4051	1200+48	0.00	0.08	0.55	0.52	2, 5, 18
NGC 4151	1208+39	0.00	0.13	0.85	0.23	2, 3, 5, 12, 17–19
3C 273	1226+02	0.04	0.05	0.90	0.04	1–3, 6, 10, 20
Mrk 231	1254+57	0.00	0.20	1.00	0.30	2, 10, 11
PG	1351+64	0.03	0.03	1.00	0.08	21, 22
Mrk 279	1351+69	0.00	0.13	0.65	0.40	2, 5
NGC 5548	1415+25	0.00	0.02	0.90	0.26	2, 3, 5, 12
Mrk 817	1434+59	0.00	0.06	0.80	0.19	1
Mrk 478	1440+35	0.00	0.01	0.85	0.21	2, 5
Mrk 841	1501+10	0.00	0.10	0.75	0.12	1, 23
3C 390.3	1845+79	0.03	0.22	1.00	0.25	16, 24
Mrk 509	2041−10	0.03	0.00	0.75	0.11	1–4, 6, 10, 25
II Zw 136	2130+09	0.04	0.06	1.10	0.10	1, 2, 5
NGC 7469	2300+28	0.03	0.07	0.70	0.34	2, 4, 10–12, 25

[a] Extinction, in visual magnitudes, due to line-of-sight dust in the Milky Way, estimated from 21 cm H I column density method of Burstein and Heiles 1982.

[b] Extinction, in visual magnitudes, attributed to Seyfert nucleus, in order to obtain good fit to ultraviolet continuum, assuming a standard Milky Way reddening law.

[c] Scale factor by which all *IRAS* far-infrared fluxes were multiplied to force them to agree with ground-based measurements which refer to the nuclear emission (within a small aperture).

[d] Fraction of total flux at 5450 Å which is produced by starlight from the underlying galaxy.

References.—(1) This paper. (2) De Bruyn and Sargent 1978. (3) Malkan and Sargent 1982. (4) Rudy *et al.* 1982*a*. (5) Rieke 1978. (6) Roche *et al.* 1984. (7) Snijders *et al.* 1982. (8) Malkan and Oke 1983. (9) Neugebauer *et al.* 1979. (10) Rudy *et al.* 1982*b*. (11) Aitken, Roche, and Phillips 1981. (12) McAlary *et al.* 1983. (13) Sargent, de Bruyn, and Readhead 1987. (14) Oke and Zimmerman 1979. (15) Glass 1981. (16) Oke and Goodrich 1981. (17) McAlary, McLaren, and Crabtree 1979. (18) Balzano and Weedman 1981. (19) Boksenberg *et al.* 1978. (20) Ulrich *et al.* 1982. (21) Neugebauer *et al.* 1980. (22) Maraschi, Tanzi, and Treves 1980. (23) Rudy, LeVan, and Rodriguez-Espinosa 1982. (24) Miley *et al.* 1984. (25) Malkan and Filippenko 1983.

vations. Fortunately, the near-infrared continua of most AGNs are known to have small amplitudes of variability (Cutri *et al.* 1985; Lebofsky and Rieke 1980). In the few cases where the published optical spectrophotometry of de Bruyn and Sargent (1978) did not agree well with the *IUE* spectra or the near-infrared data, as noted in Table 1, we replaced it with new optical spectra supplied by Sargent, de Bruyn, and Readhead (1986).

III. FITS TO THE SPECTRAL ENERGY DISTRIBUTIONS

a) Underlying Galaxies

Because of their steep luminosity functions, the brightest AGNs tend to be nearby and of low luminosity. Thus, many of our program spectra include significant starlight from the underlying galaxy, which must be accurately subtracted to study the nonstellar continuum. We use the estimates of starlight fluxes from Crenshaw and Peterson (1985), MF, MO, and Neugebauer *et al.* (1985).

For Seyfert galaxies not included in those studies, we made new estimates of starlight fluxes based on direct SIT pictures and slit spectroscopy at the Palomar 1.5 m telescope. The technique used to measure the starlight is essentially the same as in MF. Our new estimates, included in column (6) of Table 1, may not be quite as accurate as those of MF, owing to the lower resolution and signal-to-noise ratios of the spectra. The spectrum of the galaxy was assumed to be the average spectrum given in Lebofsky and Rieke (1985). It is very similar to the early-type "standard galaxy" spectrum in MO, and should be an adequate description of the nuclear regions of most of the program Seyfert galaxies.

In most cases starlight contributes less than 25% of the visual flux, and our starlight subtraction does not significantly increase the uncertainties of our fits. However, in a few of the Seyfert 1 galaxies (NGC 3227, NGC 3516, NGC 4051, and Mrk 6) and in all the Seyfert 2 galaxies (NGC 1068, Mrk 3, and Mrk 348) starlight is a major component, dominating the near-infrared spectra of these objects, which leads to larger uncertainties in the fits to the nonstellar flux in the red and near-infrared.

b) IRAS Scale Factors

All but three of the objects studied (Akn 120, Mrk 817, and Mrk 841) were detected by *IRAS* at 12 μm, and from the ground at 10.6 μm. Eight also have ground-based measurements at 21 μm which can be compared with the *IRAS* 25 μm fluxes. Since the ground-based photometry was obtained with small apertures ($\sim 10''$ in diameter), the measured fluxes can be lower than the *IRAS* fluxes (which usually include all of the infrared emission from the entire galaxy). This difference is still present after allowing for the shorter wavelengths of the ground-based observing windows.

Our aim was to estimate the far-infrared emission coming from the central region of the galaxy (within 5″ of the nucleus), since all our data at shorter wavelengths also refer to that region. We attempted to correct the large-aperture *IRAS* data by scaling them down to match the small-aperture ground-based fluxes.

For each object, all four *IRAS* fluxes were multiplied by a constant scale factor, listed in Table 1, which varied from unity (for sources with no extended flux) to 0.45 (for the objects with the most contamination from the underlying galaxy). The *IRAS* scale factor was determined by taking the ratio of the 10.6 and 12 μm fluxes, assuming a spectral slope $\alpha = -1$. When 21 μm measurements were also available, the 21–25 μm ratios were also determined, and the scale factor was taken to be the average of these two values (which generally agreed quite well). The scale factors of the three objects which lacked 10 μm data were determined by extrapolation from shorter wavelengths, and consequently have larger uncertainties.

The adopted scale factors could be in error by as much as 0.10. As expected, they are correlated with the redshifts of the AGNs, since the nearest sources (subtending the largest angles) are the best resolved. One object (II Zw 136) had a scale factor of 1.1, probably due to uncertainty in the 10.6 or the 12 μm measurement or to mild variability. In the worst cases (NGC 4051, Mrk 376, and the Seyfert 2 galaxies) we may have overestimated the far-infrared flux arising in the nucleus, since the sources are likely to be more compact at 10–12 μm than at longer wavelengths. The bulk of their observed 60 and 100 μm flux could actually arise outside the nucleus, in the galactic disk. NGC 6814 had such an extreme infrared scale factor (only 0.30), and so much starlight, that we were unable to include it in our sample.

The far-infrared flux from the galactic disk was independently estimated from published large-aperture *B*-magnitudes, using standard values of $\alpha^{B}_{80\,\mu\mathrm{m}}$ for Sab galaxies taken from de Jong *et al.* (1984). In most cases this was a negligible fraction of the flux at 60 and 100 μm. However, for three objects (NGC 3516, NGC 4151, and NGC 5548) this estimate is over 25% of the 60 and 100 μm flux. Our failure to detect the low-frequency turnovers (see § IV) for these and a few other low-luminosity AGNs (such as NGC 3227 and NGC 4051) may be due to contaminating extranuclear emission from cold dust in the disk of the surrounding galaxy. This is the simplest explanation of why such a high proportion (two-thirds) of the AGNs with small scale factors (≤ 0.70) had no detectable turnover frequency.

Rickard and Harvey (1984) observed four of the sources with extremely small scale factors in this sample (NGC 1068, NGC 3227, NGC 4051, and NGC 7469). They used a 40″ beam at 40, 50, 100, and 160 μm. We have included their 100 and 160 μm data, with no scale factor correction applied because their aperture was much smaller than that used by *IRAS*. Their small-aperture fluxes agree well with the scaled *IRAS* 100 μm data, providing independent evidence that our scale factors (derived at 12 and 25 μm) adequately correct for the contamination from the extended disk at 60 and 100 μm in most cases.

The uncertainty in these scale factors makes it virtually impossible to search for 10 μm variability by comparing *IRAS* data with previous ground-based measurements. There is no evidence for strong (e.g., $\Delta m \geq 0.5$ mag) variability at 10 μm, because no *IRAS* scale factor was found to be significantly larger than unity.

c) Reddening

The fits were all reddened assuming a standard extinction law (Seaton 1979), by amounts estimated from the 21 cm H I column densities in the Milky Way (Burstein and Heiles 1982). In 17 cases, additional internal nuclear reddening (at the AGN's redshift) of $E_{B-V} \geq 0.07$ had to be invoked. Our approach has been conservative—we never included any more than the minimum internal reddening necessary to (1) be consistent with observed 2175 Å absorption dips, such as those seen in 3C 84, 3C 120, Mrk 9, Mrk 79, Mrk 279, and NGC 7469, or (2) produce enough downward curvature at ultraviolet wavelengths to match the steep drop in fluxes seen in NGC 1068, NGC 3227, I Zw 1, and Mrk 376. If the strength of the 2175 Å feature varies as much as it does along lines of sight in the Milky Way, any individual reddening estimate based on that feature could be wrong by as much as a factor of 2. The internal reddening $E_{B-V} = 0.07$ is the smallest value which we believe can be detected unambiguously, given *IUE*'s poor sensitivity at 2100 Å, and the strong Fe II lines at wavelengths longer than 2200 Å. The true internal continuum reddenings are probably at least as large as the values listed in Table 2, and in some cases could be significantly larger.

To assess the reality of these internal continuum reddenings, we have compared our estimates with those obtained by other techniques. Simple emission-line–free narrow-band optical ultraviolet color ratios, either f_{4220}/f_{1770} or f_{4220}/f_{1450}, were suggested by Malkan (1984) to measure the redness of the continuum. In luminous objects these ratios are clustered around lower bounds of 1.5 and 1.7, respectively. Malkan (1984) interpreted these ratios as unreddened quasar colors, and suggested that they could be used to set strict upper limits on continuum reddening. (They do not require the presence of the 2175 Å absorption feature in the reddening law.) We estimated these two intrinsic optical/ultraviolet colors, and took their average, corrected for (1) Milky Way reddening, (2) our estimates of internal reddening, and (3) starlight flux at 4220 Å (assumed to be 0.38 times the starlight flux at 5450 Å), for each of the 21 objects with $E_{B-V} \leq 0.5$. The larger, more uncertain reddenings of the other eight AGNs introduce greater scatter in their ultraviolet colors. We then checked these ratios for our sample of AGNs for consistency with Malkan's results. The average optical/ultraviolet flux ratio is 1.5, with an individual scatter of ± 0.2. The small scatter of this ratio around the value previously found for more luminous objects indicates that most of our internal continuum reddening estimates in Table 1 are not in error by more than 0.1 in E_{B-V}, independent of the strength of the 2175 Å dust feature. The simplest hypothesis, that the internal reddening is described by a standard interstellar law, which includes a bump around 2175 Å, is consistent with all the spectra, except possibly those of NGC 1068 (see MO) and NGC 3227.

The continuum reddenings can also be compared with estimates of emission-line reddenings, from the Paα line (Lacy *et al.* 1982; McAlary *et al.* 1986) the He II recombination lines (Malkan 1986), and the forbidden lines of [O II] and [S II] (Malkan 1983*a*). In 14 of 18 cases, our continuum reddenings are within the ranges of reddening found by these emission-line techniques. The emission-line reddenings of Mrk 231, Mrk 348, and 3C 120 are somewhat larger than our estimated continuum reddening, while the weak Paα line in Mrk 376 would imply no reddening (compared with our estimate of $E_{B-V} = 0.18$). Our estimates of foreground plus internal reddening are well correlated with the observed Hα/Hβ and Lyα/Hβ line ratios. The correlation between our estimated continuum reddening and the observed Lyα/Hα ratio, significant at the 99.5% level, is shown in Figure 1. The fitted regression line is consistent with an average intrinsic Lyα/Hα ratio of 3.2, subjected to the same extinction as the continuum, for a normal reddening law. Thus it is evident that our estimated continuum reddenings are also applicable to the emission lines, for most AGNs.

Fortunately, the internal reddenings in two-thirds of our program Seyfert 1 nuclei do no exceed $E_{B-V} = 0.10$. Thus errors in dereddening the SEDs of these objects are expected to be small. The larger dereddening uncertainties expected in the remaining AGNs still principally affect our estimates of the ultraviolet blackbody parameters. Our measures of the other fitting parameters are insensitive to the reddening corrections adopted.

d) *Model-fitting Results*

We fitted all the SEDs with an empirical model, with 7 free parameters, the minimum number necessary to reproduce all the data accurately. The 4 components are (1) a power law, with the strength $F_{\rm pl}$ (the flux at 5450 Å), slope $\alpha_{\rm pl}$, and low-frequency exponential cutoff to be fitted; (2) optically thin Balmer continuum with a flux at 3646 Å ($F_{\rm bc}$) to be fitted;

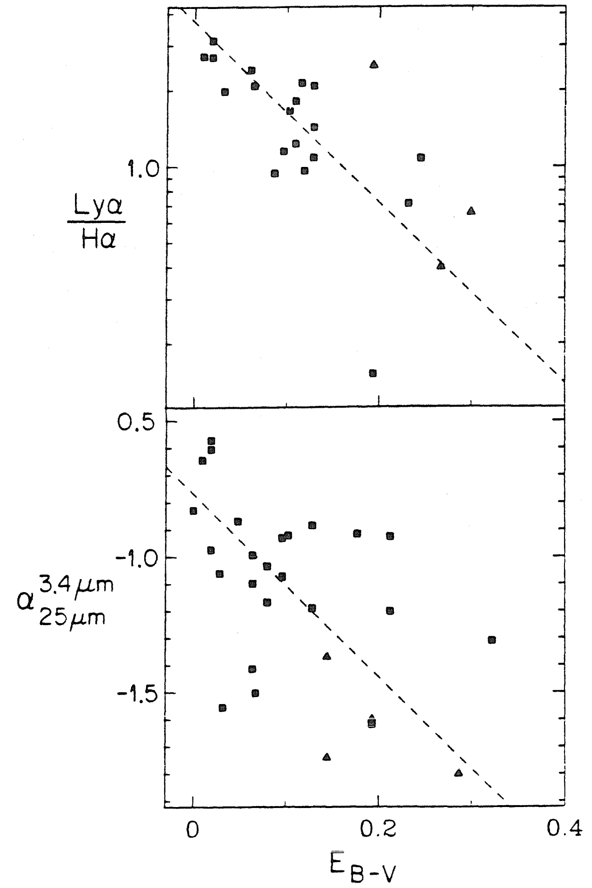

FIG. 1.—Correlations of continuum reddening with Lyα/Hα and spectral slope from 3 to 25 μm. In the upper correlation, total continuum reddening (internal plus foreground) is plotted; in the lower correlation, internal reddening is the dependent variable. The first correlation indicates that continuum and emission-line reddenings are the same on average. The second shows that reddened, dusty active galactic nuclei have far-infrared fluxes which are significantly contaminated by thermal reradiation.

(3) an ultraviolet blackbody with temperature T_{bb} and strength F_{bb} to be fitted; and (4) a 5 μm excess, fitted by a parabola centered at 5.2 μm, with a width of 3.3 octaves FWHM, and strength F_b, to be determined.

The contribution to the continuum from numerous blended Fe II lines was also included, with the overall line flux levels scaled to the observed Hα flux using the model of Grandi (1981). These emission-line strengths were set by other sources, and were not allowed to vary in the fits. Errors in the proper Fe II strengths would affect primarily our estimates of the Balmer continuum.

The three components other than the power law are quite localized, and only contribute significantly to the spectrum over limited frequency ranges of an octave or two. Thus, each component is accurately determined by the data, independent of the description of the other components (which dominate at other wavelengths). The correlation matrices calculated by our nonlinear least-squares fitting program confirm that each of the fitting parameters is relatively independent of the others.

The work of MF and others has already indicated that a component of approximately power-law shape dominates the total energy output of AGNs, at least from 0.6 to 10 μm. As expected, it is a major component in our fits to the Seyfert 1 SEDs. MS and others have already shown that the blending of higher Balmer series emission lines, merging into strong Balmer continuum emission, produces a small jump from 4000 to 3600 Å. They also found that a much larger component, with an approximately thermal shape, is required to explain the strong flux in the blue and ultraviolet, often referred to as the "ultraviolet bump." It has been adequately fitted by a single Planck function, with a typical temperature of ~26,000 K, and includes a sizable fraction of the total energy output of many AGNs. Thus we needed all three components to fit most of our SEDs.

The components described above were sufficient to give a fairly good fit to most of the SEDs, but the fits to many objects improved dramatically when we added a bump centered at ~5 μm. Also, the SEDs of many objects were found to cut off in the far-infrared. This is the first time that these features have been systematically studied for a large sample, and the results, discussed in §§ IV and V, constitute some of the major new findings of this investigation.

The results of the fits are stated in Table 2. The object's name is in column (1), the slope of the power law in column (2), the ratio of hot blackbody to power law at 5450 Å in column (3), the blackbody temperature in column (4), the ratio of the Balmer continuum to Hα in column (5), and the logarithm of the integrated luminosity between 0.1 and 100 μm in ergs s^{-1} in column (6).

Figure 2 shows the data plotted in log (νF_ν) versus log ν, corrected to zero redshift, and fits (represented by solid lines), reddened by the amounts listed in Table 1. Horizontal SEDs in these plots would have equal powers in each octave. Figure 3 is a plot of the data for three objects 3C 273, Mrk 335, and NGC 4151, along with fits, decomposed into the individual components.

IV. INFRARED EMISSION

a) *Determination of the Turnover Frequency*

The *IRAS* data show that the power-law slopes found in the optical and near-infrared ($\alpha \sim -1.2$; see MF) continue well into the far-infrared. However, the broad-band SEDs of most AGNs generally peak near 80 μm. We find that 16 of the 29 objects studied (55%) have detectable turnovers shortward of 100 μm. Most of the remaining objects have 1.4 mm limits which constrain the turnover frequency to occur shortward of ~300 μm.

We determined the turnover frequency (ν_t) by fitting a parabola to the 25, 60, and 100 μm points in (log F_ν, log ν)-space, and taking the point at which $\alpha = 0$ as the turnover. For objects in which $\alpha = 0$ lies outside this range, the turnover frequency is considered to be undetected. For the three objects with upper limits at 100 μm (Mrk 335, Mrk 841, and 3C 390.3), the 12, 25, and 60 μm points were used. The calculated values of ν_t are in column (2) of Table 3.

This method gave more consistent results than the exponential cutoff used in the fits to the SEDs. Because of the exponential cutoff term, that method tended to assign objects with steep infrared slopes higher turnover frequencies than flatter objects which had $\alpha = 0$ at the same frequency. The parabolic fits to the far-infrared data are also preferable because they are based solely on *IRAS* data, so any uncertainties in the *IRAS* scale factor will not affect the result.

During the fitting process (see § III) we tried to model the turnover with a second-order term in the power law ($F_\nu \propto \nu^{\alpha + \beta \log \nu}$). This gave unacceptable results for almost all objects. The fits tended to be too high in the near-infrared and too low in the optical-ultraviolet, when the turnover itself was well fitted. This is because the functional form used causes the slope of the power law to change too gradually. This is evidence that the power law has a constant slope from at least the optical through the mid-infrared, and it cuts off sharply in the far-infrared.

b) *Thermal or Nonthermal?*

In this paper we seek new ways to distinguish between thermal and nonthermal emission in the infrared. We find strong correlations between internal reddening, derived from the many independent estimates in § III*c*, and the slope of the infrared continuum. A steep infrared continuum is indicative of dust emission, while a flat spectrum indicates that nonthermal emission dominates (de Grijp *et al.* 1985; Neugebauer *et al.* 1985). A further confirmation of this trend is that our model, which has an infrared power-law component but no thermal dust emission component, generally fitted objects with flat infrared spectra and low reddening much better than objects with steep spectra and high reddening.

These correlations are quite strong. For example, the half of the sample with internal reddenings $E_{B-V} < 0.10$ has $\overline{\alpha_{\rm pl}} = -1.36 \pm 0.05$ (error in the mean), while the half with internal reddenings $E_{B-V} \geq 0.10$ has $\overline{\alpha_{\rm pl}} = -1.58 \pm 0.10$. The correlation can also be seen without power-law fitting. Figure 1 shows the correlation of internal reddening with $\alpha_{25\,\mu\rm m}^{3.4\,\mu\rm m}$. This correlation is significant at the 99% level. In general, we find that most objects with $\alpha_{25\,\mu\rm m}^{3.4\,\mu\rm m} > -1.2$ have infrared spectra dominated by nonthermal emission, while most with $\alpha_{25\,\mu\rm m}^{3.4\,\mu\rm m} < -1.2$ have strong dust contamination. The model-independent parameter $\alpha_{25\,\mu\rm m}^{3.4\,\mu\rm m}$ is a reliable indicator of dust content.

c) *Nonthermal Emission*

The good power-law fits to the SEDs of relatively dust-free Seyfert 1 galaxies with $\alpha_{25\,\mu\rm m}^{3.4\,\mu\rm m} > -1.2$, such as II Zw 136, NGC 3516, 3C 120, 3C 273, Mrk 9, Mrk 79, Mrk 335, and Mrk 509, suggest that their infrared emission is primarily synchrotron radiation (see Fig. 1 in Neugebauer, Soifer, and Miley 1985). Under this assumption, the low-frequency turnover can

TABLE 2

MODEL FITTING PARAMETERS

Source	$\alpha_{\rm pl}$[a]	$F_{\rm pl}$[b] (mJy)	$F_{\rm bb}/F_{\rm pl}$[c]	$T_{\rm bb}$[d] (K)	Bac/Hα[e]	log L[f] (ergs s^{-1})
Mrk 335	−1.34	5.5	0.60	25600	3.0	44.80
Mrk 348	−1.75	1.4	<0.14	...	...	43.69
I Zw 1	−1.53	4.6	0.37	19000	0.6	45.55
NGC 1068	−2.19	36	<0.05	...	1.3	44.86
3C 84	−1.53	9.9	0.12	20000	1.8	44.83
3C 120	−1.33	4.4	0.16	29000	1.9	44.83
Akn 120	−1.00	8.1	0.31	24000	2.1	44.89
Mrk 3	−2.58	0.2	<0.10	...	1.3	44.35
Mrk 6	−1.72	1.6	<0.10	...	1.7	44.26
Mrk 376	−1.16	3.2	0.13	19000	2.1	45.05
Mrk 9	−1.45	2.7	0.41	27300	1.8	44.91
Mrk 79	−1.36	2.8	1.6	31000	2.7	44.50
0906+48	−1.39	0.5	0.71	23600	...	45.24
NGC 3227	−1.49	7.0	<0.10	...	...	43.44
NGC 3516	−1.30	5.9	0.52	22800	2.0	43.97
NGC 4051	−1.39	5.8	<0.15	...	2.4	42.81
NGC 4151	−1.37	30	0.43	24500	2.0	43.67
3C 273	−1.20	9.5	1.0	28200	1.8	46.64
Mrk 231	−1.99	6.6	<0.10	...	0.5	45.99
1351+64	−1.70	1.3	2.8	16300	...	45.53
Mrk 279	−1.18	2.8	1.1	21400	2.2	44.64
NGC 5548	−1.23	7.1	0.17	27200	2.8	44.44
Mrk 817	−1.55	3.5	0.68	24800	...	44.93
Mrk 478	−1.13	2.5	0.24	29000	1.7	45.39
Mrk 841	−1.16	5.5	0.34	24300	...	44.79
3C 390.3	−1.40	2.7	0.12	32000	2.3	45.00
II Zw 136	−1.44	2.6	0.50	35500	1.7	45.29
Mrk 509	−1.09	9.6	0.23	26000	2.0	45.12
NGC 7469	−1.69	9.3	0.42	21400	3.0	44.92

[a] $\alpha_{\rm pl}$ is the spectral slope of the fitted power law ($S_\nu \propto \nu^\alpha$).

[b] $F_{\rm pl}$ is the fitted flux of the power law at 5450 Å, corrected for reddening.

[c] $F_{\rm bb}/F_{\rm pl}$ is the ratio of fitted blackbody to power law fluxes at 5450 Å.

[d] $T_{\rm bb}$ is the temperature of fitted ultraviolet blackbody continuum component.

[e] BaC/Hα is the ratio of Balmer continuum flux (integrated assuming an optically thin shape at 13,000 K) to the Hα flux, corrected for reddening.

[f] log L is the logarithm of total observed luminosity (including emission lines and starlight), integrated from 0.1 to 100 μm.

be interpreted as the frequency at which the source becomes self-absorbed. On the short-wavelength side, optically thin emission presumably produces the power-law slope.

We assume a brightness temperature $T_b = 10^{12}$ K, because it is believed that most self-absorbed synchrotron sources are near this limit (Kellermann and Pauliny-Toth 1981). Cyclotron emission, with a low-frequency self-absorbed cutoff in the far-infrared, can be ruled out. A cyclotron frequency, above which little energy is emitted, as large as $\sim 10^{13}$ Hz requires magnetic fields of 3×10^6 G. This is unacceptably high, indicating that the source must be radiating by the synchrotron process, which requires relativistic electrons with brightness temperatures above $T_b = 10^{11}$ K. Above the 10^{12} K limit, inverse Compton radiation would have cooled the source and caused it to emit far more X-rays than we observe.[2]

The following formula allows us to estimate the size of the emitting region:

$$r_s = D\lambda\left(\frac{F_t}{2k_B T_b}\right)^{1/2},$$

where r_s is the size of the emitting region, D is the distance to the source, F_t is the flux density of the turnover at wavelength λ, and k_B is Boltzmann's constant. This quantity is tabulated in column (6) of Table 3.

If we assume that the central engine is powered by a black hole, we can derive a lower limit to the Schwarzschild radius and mass by assuming that all the luminosity in the power-law and ultraviolet bump between 0.1 and 100 μm is ultimately powered by accretion at the Eddington limit. This is a reasonable assumption for the more powerful AGNs in our study, although the weaker ones are probably sub-Eddington. Thus,

---

[2] Independent equipartition calculations suggest that T_b is generally of order 10^{11}–10^{12} K for these objects.

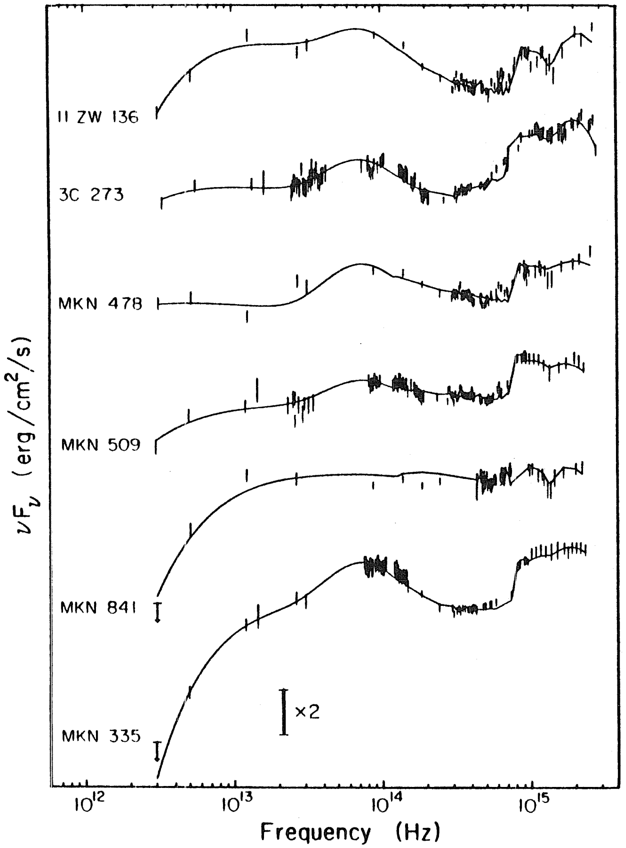

FIG. 2*a*

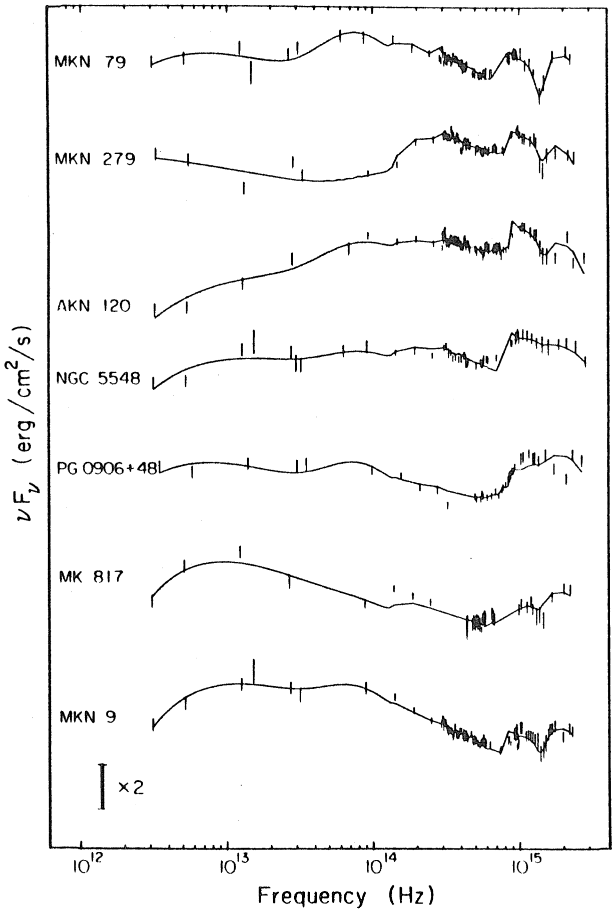

FIG. 2*b*

FIG. 2.—(*a*) **Fits to the infrared/optical/ultraviolet SEDs of six AGNs (II Zw 136, 3C 273, Mrk 478, Mrk 509, Mrk 841, and Mrk 335). Observed binned continuum fluxes are shown with vertical error bars. The lines show the best-fitting models with a power law, near-infrared bump, and ultraviolet blackbody (including corrections for reddening, starlight and recombination radiation). Vertical scale is the logarithm of νF_ν, so that a power law of slope −1 (with equal power per decade) would appear as a horizontal line. The large vertical bar shows a factor of 2 change in flux. (*b*) Same as (*a*), for the AGNs Mrk 79, Mrk 279, Akn 120, NGC 5548, PG 0906+48, Mrk 817, and Mrk 9.**

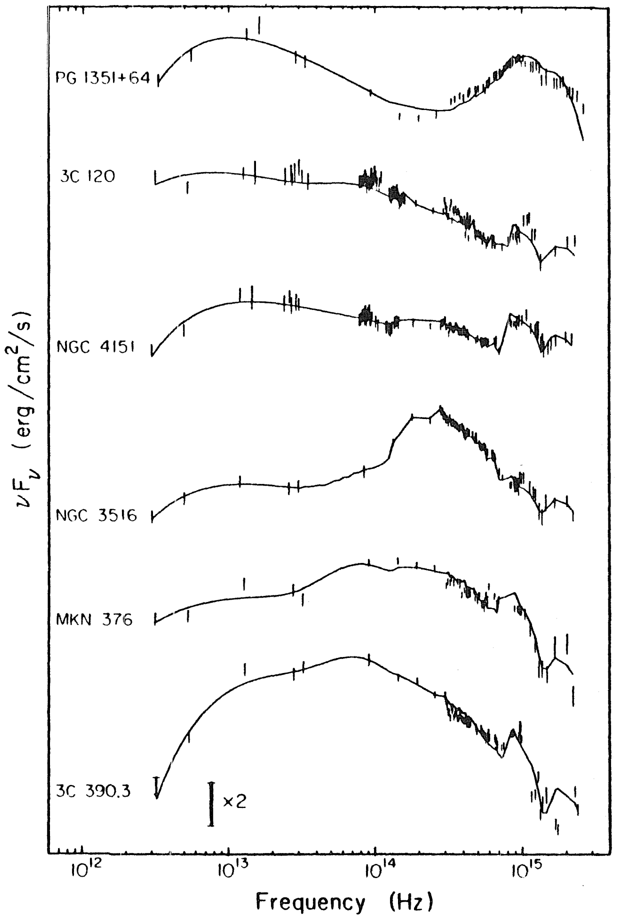

Fig. 2c

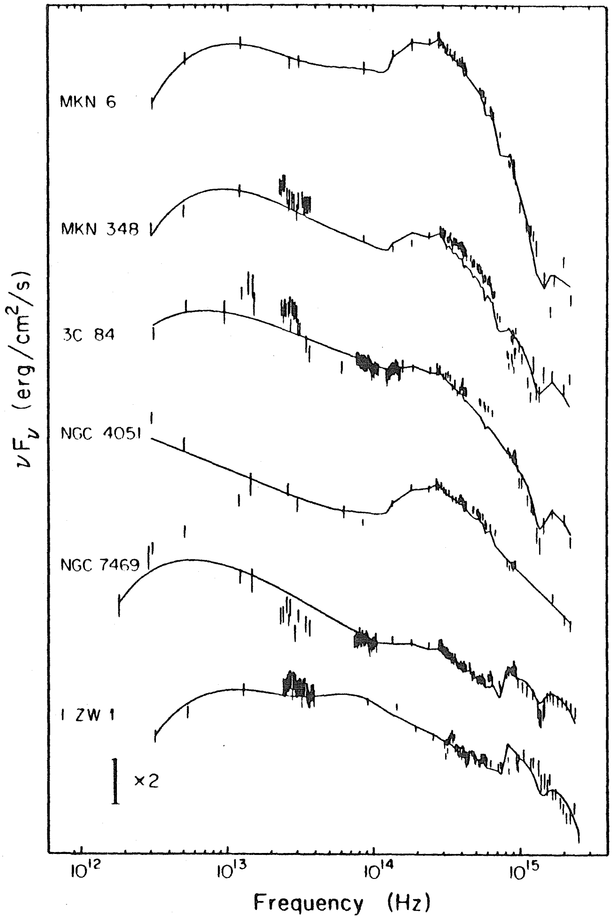

Fig. 2d

Fig. 2 (*cont.*).– (*c*) Same as (*a*), for the AGNs PG 1351 + 64, 3C 120, NGC 4151, NGC 3516, Mrk 376, and 3C 390.3. (*d*) Same as (*a*), for the AGNs Mrk 6, Mrk 348, 3C 84 (= NGC 1275), NGC 4051, NGC 7469, and I Zw 1.

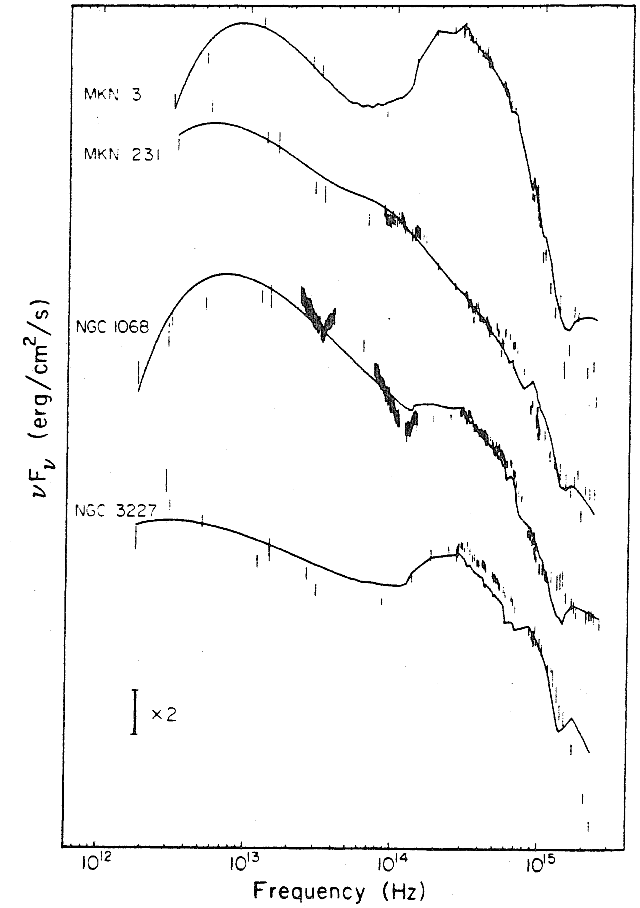

FIG. 2 (*cont.*).—(*e*) Same as (*a*), for the AGNs Mrk 3, Mrk 231, NGC 1068, and NGC 3227

this will yield a lower limit on the mass and radius of the central black hole. The mass, $m_{\rm bh}$, and the radius, $r_{\rm bh}$, are tabulated in columns (7) and (8), respectively, of Table 3. We use the following relations (Rybicki and Lightman 1979):

$$m_{\rm bh} = \frac{L_{\rm E}\,\sigma_{\rm T}}{4\pi G M_{\rm H} c} ,$$

where $L_{\rm E}$ is the luminosity in the power law and ultraviolet blackbody, $\sigma_{\rm T}$ is the Thomson cross section, and $M_{\rm H}$ is the mass of hydrogen, and

$$r_{\rm bh} = \frac{2Gm_{\rm bh}}{c^2} .$$

These calculations show that black hole masses of at least 2×10^6 to 400×10^6 $M_\odot$ are required for the central objects. The minimum radii range from 2×10^{12} to 4×10^{14} cm, corresponding to light-travel times of minutes to hours. The synchrotron sources have sizes ranging from 10^{14} to 3×10^{15} cm. The synchrotron radii are typically 10–100 times the minimum Schwarzschild radii, suggesting that the synchrotron emission is produced in a region comparable to the inner parts of the hypothesized accretion disk.

The possibility that the turnover could be due to free-free absorption from broad-line clouds can be rejected for most objects in this sample. *EXOSAT* measurements or upper limits of the hydrogen column density place the free-free absorption frequency of these objects in the millimeter region. Free-free absorption from either the narrow-line region or the hot intercloud medium hypothesized to confine the broad-line clouds is not important in the far-infrared; their low electron densities would put the cutoff frequency at radio wavelengths. The Razin effect is unlikely to explain the turnover, since it would require densities which are too low and magnetic fields which are too high.

d) *Thermal Dust Emission*

Our fits to the SEDs of the three Seyfert 2 galaxies (NGC 1068, Mrk 3, and Mrk 348) and other dusty objects (3C 84, Mrk 231, NGC 3227, and NGC 7469) confirm the findings of

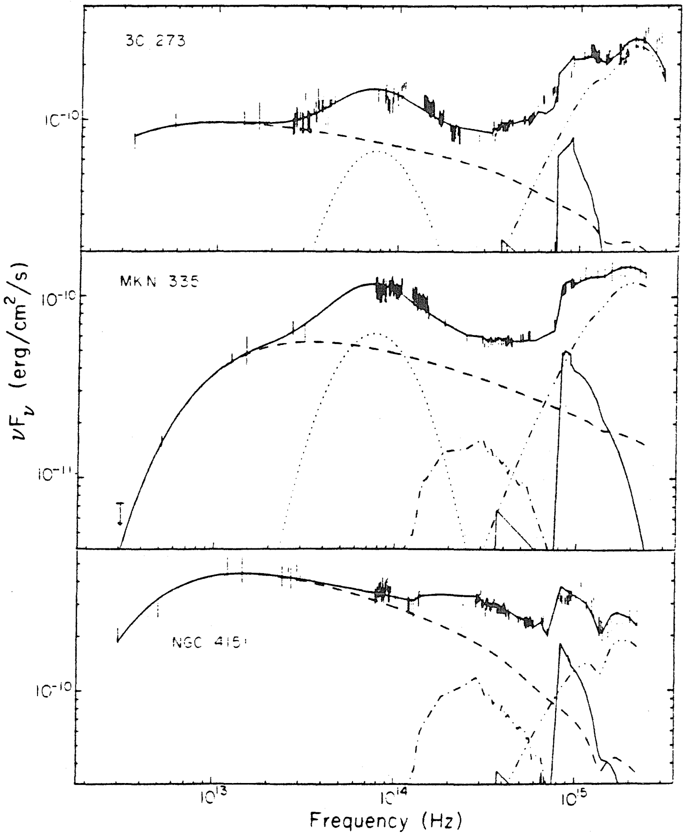

FIG. 3.—Detail of model fits to SEDs of 3C 273, Mrk 335, and NGC 4151. The individual components shown are the infrared power law (*dashed line*, which dominates the far-infrared), the near-infrared bump (*dotted line*; not detected in NGC 4151), the galactic starlight (*dot-dash line*; not detectable in 3C 273), the recombination continuum (*solid line*—only the Balmer continuum, and a little of the Paschen continuum are strong enough to show in the figures), and the ultraviolet blackbody (*dot-dot-dash line*). All components have been reddened by the galactic and internal reddening estimates given in Table 1. The sum of these components equals the fitted model, shown by the upper solid line.

MO: No power law of any slope, with or without an exponential low-frequency turnover, can reproduce their nonstellar spectra. Nor can they be fitted with the inclusion of a quadratic term to the power law. The observed SEDs show too much downward curvature to be accurately described by the power-law fits, a property of Seyfert 2 galaxies previously noted by Miley, Neugebauer, and Soifer (1985). Thus our fits tend to overpredict the 2–3.5 μm flux because the Seyfert 2 nonstellar light curves down very sharply from the mid- to the near-infrared. Also, the local slopes such as $\alpha_{25\,\mu m}^{12\,\mu m}$ tend to disagree significantly with the fitted power-law slope. Finally, the fits, which require very steep power-law slopes to fit the mid-infrared Seyfert 2 fluxes, underpredict the optical continuum, where the nonstellar flux evidently has a flatter slope.

These infrared spectra are easily understood as thermal infrared emission from dust at a range of temperatures. Although each temperature component produces a thermal spectrum with an exponentially steep high-frequency cutoff, the range of temperatures smears it into the observed steep mid-infrared spectrum. The thermal Wien cutoff causes the integrated spectrum to curve downward steeply to higher frequencies, quite unlike a power law. The shape of the weak nonstellar component, detectable only at wavelengths shortward of 10 μm, is poorly determined, but could be similar to the nuclear components of unreddened Seyfert 1 galaxies and quasars (see MO).

If we assume that the infrared emission is dominated by dust with an emissivity $\epsilon \propto 1/\lambda$, the mid-infrared radiation arises from grains with a wide range of temperatures. The turnover is then taken as the peak of a thermal spectrum, and the minimum temperature of the dust is derived. If we assume that all the luminosity between 10 and 100 μm is coming from this component, we can derive the minimum size and mass of the thermal emitting region. The minimum size is given by

$$r_d = \frac{1}{T_d^2} \sqrt{\frac{L_d}{4\pi\sigma}} ,$$

where r_d is the radius of the emitting region, L_d is the luminosity between 10 and 100 μm, T_d is the dust temperature, and

TABLE 3

Derived Turnover and Bump Parameters

Source	ν_t[a] (THz)	T_d[b] (K)	r_d[c] (10^{18} cm)	m_d[d] ($M_\odot$)	r_s[e] (10^{12} cm)	m_{bh}[f] (10^6 $M_\odot$)	r_{bh}[g] (10^{12} cm)	f_b[h] (%)	ΔL[i]
Mrk 335	8.6	105	47	26	117	6.3	1.9	44	0.131
Mrk 348	< 3.0	...	...	...	...	...	...	< 10	−0.061
I Zw 1	3.7	44	300	2400	1500	35	10	25	0.068
NGC 1068	3.0	37	690	26	1000	7.3	2.2	< 10	−0.102
3C 84	4.1	50	72	170	800	6.8	2.0	< 10	−0.098
3C 120	< 3.0	...	...	...	...	...	...	15	0.035
Akn 120	< 3.0	...	...	...	...	...	...	23	...
Mrk 3	6.3	76	41	26	230	2.3	0.7	< 10	−0.397
Mrk 6	5.7	70	34	49	230	1.8	0.5	12	−0.097
Mrk 376	< 3.0	...	...	...	...	...	...	32	0.096
Mrk 9	3.3	40	200	1300	760	8.1	2.4	23	0.085
Mrk 79	< 3.0	...	...	...	...	...	...	42	0.052
0906+48	< 3.0	...	...	...	...	...	...	28	0.066
NGC 3227	< 3.0	...	...	...	...	...	...	< 10	−0.173
NGC 3516	< 3.0	...	...	...	...	...	...	< 10	−0.142
NGC 4051	< 3.0	...	...	...	...	...	...	< 10	−0.157
NGC 4151	< 3.0	...	...	...	...	...	...	< 10	−0.014
3C 273	3.7	45	2100	16000	4200	430	130	36	0.112
Mrk 231	5.1	62	600	570	3200	99	30	22	0.089
1351+64	4.0	48	340	3700	1400	34	10	< 10	−0.063
Mrk 279	< 3.0	...	...	...	...	...	...	< 10	−0.080
NGC 5548	< 3.0	...	...	...	...	...	...	15	0.070
Mrk 817	5.0	61	96	260	600	8.4	2.5	< 10	...
Mrk 478	< 3.0	...	...	...	...	...	...	43	0.069
Mrk 841	7.3	88	67	90	210	6.1	1.8	< 10	...
3C 390.3	8.8	110	31	120	230	10	2.9	27	0.100
II Zw 136	5.8	71	180	540	550	20	5.7	25	0.113
Mrk 509	4.7	57	170	370	550	13	4.0	33	0.070
NGC 7469	4.0	48	98	180	1200	9.8	2.9	< 10	−0.057

[a] ν_t is the frequency of far-infrared continuum turnover, where a parabolic fit to the IRAS fluxes has $\alpha = 0$.

[b] T_d is the minimum temperature of dust grains (assuming graybody radiation) required to produce low-frequency turnover.

[c] r_d is the minimum radius of an optically thick sphere of dust at T_d required to produce far-infrared peak luminosity.

[d] m_d is the mass of dust required to produce far-infrared peak luminosity.

[e] r_s is the radius of synchrotron-emitting region required to produce turnover in far-infrared spectrum by self-absorption, assuming a brightness temperature of 10^{12} K.

[f] m_{bh} is the mass of a black hole required to produce total nuclear luminosity by accretion at the Eddington limit.

[g] r_{bh} is the Schwarzschild radius for black hole mass m_{bh}.

[h] f_b is the fitted fraction of 2.5 to 10 μm luminosity in the near-infrared bump component.

[i] ΔL is the near-infrared excess at 3.5 μm, measured logarithmically, over a linear interpolation between 2 and 10 μm.

σ is the Stefan-Boltzmann constant. These temperatures are tabulated in column (3) of Table 3. The minimum mass is given by

$$m_d = \frac{D^2 F_t}{\kappa B_\nu(T)},$$

where m_d is the mass of dust, D is the distance to the object, F_t is the observed flux density at the turnover, κ is the mass absorption coefficient, and $B_\nu(T)$ is the Planck function at the turnover. We use $\kappa = 250$ cm^2 g^{-1} (Draine and Lee 1984). These quantities are tabulated in columns (4) and (5) of Table 3, respectively.

These calculations yield typical dust temperatures of 40–80 K for those objects whose far-infrared emission is likely to be dominated by dust. This is warmer than dust in normal galaxies, whose SEDs rise steeply with color temperatures ~30 K (de Jong *et al.* 1984) between 60 and 100 μm. The high dust temperature suggests that much of the dust emission is probably not coming from beyond the narrow-line region.

The size of the emitting region was derived under the assumption that it was optically thick; an optically thin region would be larger. We found minimum sizes of order 100 pc. This is beyond the broad-line region (which is not observed in many of the dusty objects), but well within the narrow-line region.

We found typical dust masses of order 100 $M_\odot$, which imply gas masses of 10^4–10^5 $M_\odot$, for an assumed gas/dust ratio of $m_g/m_d = 200$ in this region. These figures are not unreasonable for the narrow-line region (Baldwin 1975).

V. FIVE MICRON EXCESS

The fits in § III revealed the presence of an excess at about 5 μm in about half of the objects studied. Apparently this feature has been previously observed, although not systematically studied. Previous investigators (Neugebauer *et al.* 1979; MF; Malkan 1983*b*), have called it the 3 μm bump, although we find that the central wavelength is closer to 5 μm.

The low contrast of the bump relative to the power law and the lack of uniform moderate-resolution infrared spectral coverage for most objects made it difficult to determine its precise shape. We modeled it with a parabola in log F_ν versus log ν, given by

$$\log_2 F_b(\nu) = \log_2 F_b(\nu_0) - \left[\frac{\log_2 (\nu/\nu_0)}{\log_2 (\sigma_b/2)}\right]^2 ,$$

where $F_b(\nu)$ is the flux due to the bump at frequency ν, ν_0 is the center frequency, and σ_b is the FWHM in octaves. The base 2 logarithm is referred to by $\log_2$. Besides the parabola, we tried to fit the bump with a Gaussian, which has a low-frequency tail relative to the parabola. As would be expected, the peak frequencies determined with the Gaussian were systematically a little higher than those determined with the parabola (by about 0.1 decade), but the widths were very similar. The fits were equally good in the two cases.

We also tried to fit the SEDs by replacing the single power law plus bump model with a broken power law which steepened above some fitted break frequency (typically around 90 THz). None of the SEDs with a prominent 5 μm bump could be fitted even crudely with this scheme. The broken power law, even with a spectral steepening of $\Delta\alpha > 1$, still failed to produce a sharp enough inflection. The fits to the SEDs with the strongest bumps required $\Delta\alpha \sim 1.7$, yet the data require a localized excess flux superposed on a power law with relatively constant slope from the visual to the far-infrared.

We used the parabolic representation in our final fits. Allowing the center frequency to vary while the width was held constant, we found a mean center frequency of 58 THz (5.2 μm), with an individual dispersion of 11 THz. Although the bump strength relative to the underlying power law (i.e., its contrast) is highest near the L (3.5 μm) filter, the peak bump flux actually occurs at a significantly longer wavelength. This is because the bump feature is added to a power law which increases sharply toward longer wavelengths.

Likewise, holding the center frequency fixed while allowing the width to vary in the fitting process, we found a mean width of 3.3 octaves, with a dispersion of 0.3 octaves for individual objects. The dispersions in the width and central frequency were small, little larger than their individual fitting uncertainties. These results are consistent with a single universal shape for the 5 μm bump, which varies only in overall strength. Therefore, we fixed the central frequency and width of the 5 μm feature at 58 THz and 3.3 octaves, respectively, and allowed only the strength of the bump to vary in the fits.

We define the bump strength (f_b) to be the ratio of the luminosity in the bump to the total integrated luminosity, defined between 2.5 and 10 μm. This parameter is tabulated in column (9) of Table 3. The bump contributes up to 40% of the total luminosity between 2.5 and 10 μm.

We could also parameterize the bump in a model-independent fashion, using only the observed H, K, L, and N fluxes. We define the near-infrared excess, ΔL, as the logarithmic excess at L over an interpolation between the average of the H and K points and the N point. This parameter is tabulated in column (10) of Table 3. It is apparent that the two parameterizations of the bump strength are very well correlated. For instance, every object except one with $\Delta L < 0$ lacks a detectable bump in the fits (i.e., $f_b < 10\%$), and no object with a detected bump has a negative value of ΔL. A pure power law will produce a value of $\Delta L = 0$, but the presence of starlight will produce an excess at H and K, so that an object with stars plus a power law, but no 5 μm bump, will actually have a deficit at L. To confirm this, we determined ΔL for seven starburst galaxies (M82, NGC 253, NGC 1614, NGC 2903, NGC 5253, NGC 6764, and NGC 6946). We found a mean $\Delta L = -0.273$, with a dispersion of 0.086 for individual objects. This suggests that, while most of the AGNs studied have a 5 μm bump, there is a bias which makes it appear weaker and possibly undetectable in objects in which starlight is important.

Using the rank correlation test described in § I, we found that f_b is strongly anticorrelated with [O III]/Hβ and is strongly correlated with luminosity. These correlations, shown in Figure 4, are significant at the 99.5% confidence level. The bump strength was not significantly correlated with any other parameters. The poor correlation observed between f_b and F_{bb} (ultraviolet blackbody strength) suggests that the 5 μm bump does not arise directly around the continuum source.

The well-known relationship between luminosity and [O III]/Hβ makes it difficult to decide which parameter is most directly linked with the 5 μm bump. The strong correlations among these parameters mean that the correlation of one of them with f_b could give rise to an incidental correlation between f_b and the other one.

For the objects with clearly detected 5 μm bumps and Balmer continua, the observed total luminosity in recombination radiation (Balmer, Paschen, and free-free continua plus Balmer, Paschen, and Fe II emission lines) was 0.5–1.3 times the luminosity in the bump. With a typical reddening correction to the recombination emission at shorter wavelengths, the bump is actually weaker than the emission from the broad-line region.

This approximate coincidence of powers suggests that there may be enough energy in the broad-line region to produce the 5 μm bump, if it is done with reasonable efficiency. Since the bump is, on average, less than half as strong as the observed blackbody flux (integrated down to 0.12 μm), and less than a quarter of the total inferred blackbody flux, it would represent a rather small perturbation on the total nuclear energy budget.

Puetter and Hubbard (1985) suggest that free-free emission from very dense broad-line clouds ($n_e \geq 10^{11}$ cm^{-2}) could produce an excess similar in strength, width and central frequency to that observed. Their model implies that the objects with strong bumps will have depressed Paα/Hβ ratios, since the very high densities will make even the Paα optical depths large. Yet we found no correlation between Paα/Hα and f_b for the 15 objects in our sample with published Paα/Hα ratios (see Fig. 4). The bump strength, f_b, was also uncorrelated with the Hα/Hβ and Paα/Hβ ratios.

VI. ULTRAVIOLET COMPONENTS

a) Ultraviolet Blackbody Component

We found no case where the ultraviolet blackbody component was convincingly detected at a temperature markedly different from the mean of 26,000 K. The 1 σ scatter of individ-

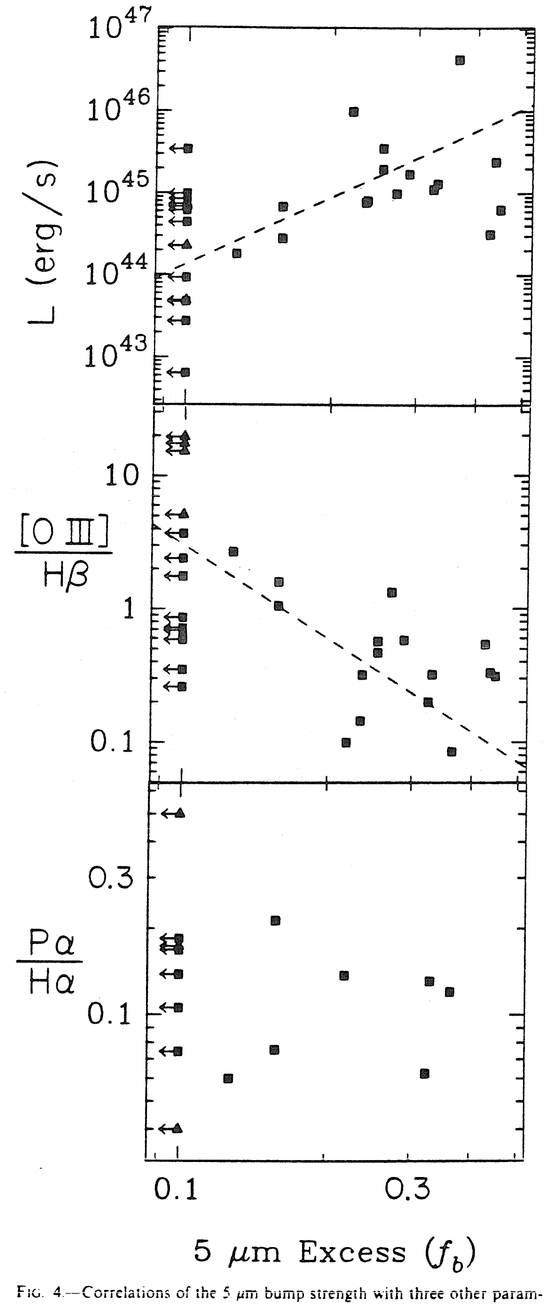

FIG. 4.—Correlations of the 5 μm bump strength with three other parameters. In the top box the abscissa is total bolometric luminosity, integrated from 0.1 to 100 μm. In the middle box it is the [O III]/Hβ emission-line ratio, and in the lower box it is the Paα/Hβ emission-line ratio. The lines are proper least-squares fits to the points. The top two correlations are highly significant (at the 99.5% level), while the lower one is not.

ual estimates is 4000 K, a little larger than the fitting uncertainties. A few objects (e.g., I Zw 1, PG 1351+64, and Mrk 376) may appear to have lower temperatures because their internal (nuclear) continuum reddenings were underestimated. However, as noted in MS and Malkan (1983*b*), this thermal component is probably broader than a single blackbody, and the fitted single temperature may not have a simple direct physical interpretation. The fitted blackbody temperature was not correlated with any other property of the AGNs, but its range is relatively narrow compared with the fitting uncertainties.

A useful measure of the blueness of the continuum, used in MS, is the ratio of fitted blackbody to power-law fluxes at 5450 Å (F_{bb}/F_{pl}), given in column (4) of Table 2. The ratios span the same range found in MS and Malkan (1983*b*). The object 3C 273 is at the high end, with a ratio of 1.0. This is not unique: some QSOs (e.g., PKS 1004+13, Malkan 1984; 4C 31.30, 4C 37.43, and 4C 34.47, Richstone and Schmidt 1980) have even stronger "blue bumps." The average blackbody/power law ratio at 5450 Å is 0.3 in those AGNs where the blackbody is detected. In eight AGNs, including all three Seyfert 2 galaxies, there is no detectable blackbody component, and a typical upper limit on its strength is $F_{bb}/F_{pl} \leq 0.1$. These eight objects also have some of the strongest contamination from starlight and show evidence of internal reddening and dust. These may have prevented us from detecting a weak blackbody component which might be present at the same strength as in some of the other Seyfert 1 galaxies.

Our fitting procedure unambiguously detects the blackbody components in NGC 4151 and NGC 5548, which are among the weakest blackbodies detected. They were missed by MS because their fits did not correct for the presence of starlight flux, which noticeably affects the observed spectrum, even in the blue. The data demonstrate that the blackbody/power law ratio is not tightly correlated with luminosity. MS had suggested such a correlation, but Malkan (1983*b*) found that it did not extend to high luminosities.

b) *Balmer Continuum*

Although the Balmer continuum flux around the Balmer jump (~3650 Å) is well determined, the shape of the high-frequency falloff is not. For comparison with previous estimates, we assumed that the Balmer continuum has an exponential falloff (i.e., it is not very optically thick) with a temperature of 13,000 K. The average Balmer continuum/Hα ratio in the 19 Seyfert 1 galaxies where it is well measured is 2.1 ± 0.6 (individual scatter), very similar to the values found in MS and for high-luminosity quasars by Malkan (1983*b*). The ratios are not determined with high precision, so it may not be surprising that they do not correlate with other AGN parameters. Comparisons of the Seyfert 1 galaxies with the strongest Balmer continuum/Hα ratios (Mrk 79, Mrk 335, NGC 5548, and NGC 7469) with those with the weakest ratios (I Zw 1, II Zw 136, 3C 273, Mrk 9, and Mrk 478) do not reveal any other significant distinctions between these two groups. Future models of emission from the broad-line region must account for the stability of the Balmer continuum strength under widely varying conditions.

Previous models (e.g., Kwan and Krolik 1981) predicted Balmer continuum/Hα ratios near 1.4, the value for case B recombination. They do not necessarily conflict with our observations, because they indicate that substantial Balmer continuum emission arises from regions with electron temperatures of only 8000 K. Thus our assumption of $T_e = 13{,}000$ K in deriving integrated Balmer continuum fluxes may be too high, because the derived Balmer continuum flux is proportional to T_e. On the other hand, the Balmer continuum may be optically thick, in which case it would extend to higher frequencies than in the optically thin case. The models of Puetter and Hubbard (1985) tend to overpredict Balmer continuum emission, except at low electron density or optical depth. The Balmer continuum/Hα ratios for NGC 1068 and Mrk 3 are significantly lower than those of the Seyfert 1 galaxies, and are consistent with case B recombination, which may adequately describe the hydrogen emission from the narrow-line region (MO).

VII. RELATION TO OTHER FREQUENCIES

a) X-Ray Luminosity

MS and Malkan (1984) found a tight linear correlation between the power-law flux measured in the red and infrared and the X-ray flux at 2 keV, with an infrared–to–X-ray slope $\overline{\alpha_{\rm IX}} = -1.18 \pm 0.02$. Thus, an extrapolation of the nonstellar flux measured at 3.5 μm with a power law of slope −1.18 predicts the X-ray flux to an accuracy of better than ±70%.

The present SEDs also show the same strong correlation. Figure 5 shows the correlation of fitted power-law luminosity at 5450 Å with 2 keV luminosity measured by the *Einstein* and *HEAO 1* satellites. The regression line in Figure 5 shows that the X-ray luminosity is linearly proportional to the power-law luminosity. The small scatter indicates that the X-ray luminosity can be predicted from the power-law fits to within a factor of 2. The true scatter may be even smaller, since the X-ray luminosities used in the correlation were measured years apart from the long-wavelength observations. The same direct proportionality is present when the power-law and X-ray fluxes, rather than luminosities, are correlated.

The regression line in Figure 5 implies a power-law slope from the visual to X-rays of −1.15 ± 0.02 (error in the mean). Since this slope is so similar to the typical power-law slope in the optical and near-infrared, the good correlation shown in Figure 3 is still present when the power-law luminosity is measured at other wavelengths. The power law–to–X-ray slope would also be close to −1.15. This slope is slightly flatter than the −1.18 slope between 3.5 μm and 2 keV because the 3.5 μm luminosity includes a contribution from the 5 μm bump in many AGNs. The small scatter in the correlation, its linearity over a wide range of luminosities, and the similarity of the infrared/optical and optical/X-ray slopes support the hypothesis that the power law and the X-rays have a common nonthermal origin in the dust-free Seyfert 1 galaxies and quasars.

The Seyfert 2 galaxies, indicated by triangles, are systematically deficient in X-rays by a factor of several, at a given optical power-law luminosity. One quasar, PG 1351+640, has unusually weak X-ray emission, 10 times too weak for its optical power-law luminosity.

b) Radio Emission

Five of the AGNs have a strong, compact, flat-spectrum radio source (3C 84, 3C 120, 3C 273, 3C 390.3, and Mrk 231). Such radio sources are frequently associated with extremely rapid (i.e., night-to-night) optical variability and high polarization (3%–20%). This is characteristic of the presence of a "blazar" continuum component which is believed to be nonthermal synchrotron emission and may be beamed along our line of sight (Malkan and Moore 1986). The quasar 3C 273 is known to vary by nearly a factor of 2 in the far-infrared (Robson *et al.* 1983). This highly variable red component has been identified as a "blazar" continuum (Impey and Malkan 1987), and could also be present in the other strong, flat-spectrum radio sources.

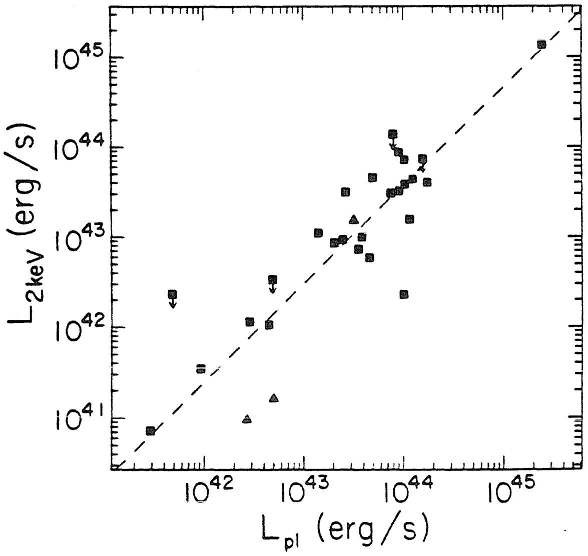

FIG. 5.—Correlation of 2 keV X-ray luminosity with fitted power-law luminosity at 5450 Å. The two open circles indicate the luminosities of the two Seyfert 2 galaxies, which were not used in the regression. The Seyfert 1 with unusually weak luminosity is PG 1351+640, discussed in the text.

The SEDs of radio-loud AGNs with a suspected "blazar" continuum do not stand out as being unusual. This is probably because the shape of the blazar continuum component is similar to that of the power law, which is also present in normal AGNs (see discussion in Malkan and Moore 1986). The objects 3C 84, 3C 120, and 3C 390.3 have relatively low blackbody power law ratios, which could be consistent with the idea that their infrared flux is enhanced by a (beamed?) blazar component. On the other hand, since they were selected for radio emission rather than ultraviolet excess, they could simply be more reddened than most other AGNs in our sample.

VIII. CONCLUSIONS

We combined data from *IRAS* and *IUE* with ground-based optical and infrared spectrophotometry to drive line-free spectral energy distributions for 29 AGNs between 0.1 and 100 μm. Although the contaminating effects of reddening and emission from stars and dust in the underlying galaxy are significant in some spectra, they can usually be adequately corrected. We find several good indicators of nuclear dust in active galaxies, all of which are well correlated: (1) steepness of infrared spectral index; (2) reddening derived from the shape of the ultraviolet continuum; (3) strength of the 2200 Å dust absorption feature; (4) line ratios, such as Hα/Hβ and Lyα/Hβ; and (5) line-free continuum colors, such as f_{4220}/f_{1770} and f_{4220}/f_{1450}. We used these indicators to determine the degree to which the SEDs of our program AGNs have been altered by absorption and thermal reradiation by dust grains.

We find that dust does not play a major role in most of the Seyfert 1 galaxies and quasars in this sample. The SEDs of these objects are generally well described by a simple model consisting of four spectral components, each of which dominates over a different wavelength region. The first, which usually contains most of the total luminosity between 0.1 and 100 μm, is a power law ($F_\nu \propto \nu^\alpha$), with $\overline{\alpha_{\rm pl}} = 1.36 \pm 0.21$ (rms scatter for individual objects). This power law usually has a sharp low-frequency cutoff before 100 μm, and the SEDs of most of the remaining objects are constrained to turn over by ~ 300 μm. The simplest explanation is that the infrared luminosity is dominated by synchrotron emission from a self-absorbed source which is about the size of the inner accretion disk. There is a strong correlation between the luminosity from this power law at 5450 Å and the 2 keV X-ray luminosity, which suggests that the power law may extend from X-ray to far-infrared wavelengths ($5\frac{1}{2}$ decades of frequency).

The second component, which was detected in over half the SEDs, was a broad near-infrared excess which was described by a parabola centered at 5.2 μm, with a FWHM of 3.3 frequency octaves. Although it contains less total energy than the Balmer continuum, it can account for up to 40% of the total luminosity between 2.5 and 10 μm. Its strength is well correlated with total luminosity and Hβ/[O III] ratio.

The far-ultraviolet is dominated by a component which we described as a blackbody at 26,000 $\pm$ 4000 K (individual scatter). The fitted Balmer continuum/Hα ratio for the Seyfert 1 galaxies is 2.1 $\pm$ 0.6, under the assumption that the emission is optically thin at $T_e = 13{,}000$ K. This ratio is significantly greater than the prediction of case B recombination, and shows no correlations with any other AGN properties. Seyfert 2 galaxies have a lower ratio than Seyfert 1's, consistent with the case B predictions.

Although the power-law model fitted the relatively dust-free objects well, it failed to reproduce the SEDs of Seyfert 2 and Seyfert 1 galaxies with strong dust indicators (i.e., NGC 3227, NGC 7469, and Mrk 231) because their fluxes beyond 10 μm are significantly contaminated by thermal emission from dust. Objects with dusty nuclei had minimum dust temperatures of 40–80 K, which is warmer than dust in normal spiral galaxies. The thermal emission appears to arise from 100 $M_\odot$ of dust in a volume similar to that of the narrow-line region. On the other hand, less luminous active galaxies with 100 μm fluxes dominated by dust emission from the underlying galactic disk showed large differences between small-aperture ground-based 10 μm and large-aperture *IRAS* 12 μm fluxes, and steep spectral indices between 60 and 100 μm.

The authors would like to thank A. Moffet, A. Readhead, R. Blandford, and S. Phinney for fruitful discussions, and C. Lawrence and S. Blatt for help with the manuscript. A. Readhead, W. Sargent, and G. de Bruyn generously provided spectrophotometry of three AGNs in advance of publication. W. Rice of the Infrared Processing and Analysis Center aided in the understanding of the *IRAS* data. R. Thompson and K. Feggins provided valuable assistance at *IUE*'s Regional Data Analysis Facility at NASA/Goddard Space Flight Center, where ultraviolet spectra from the National Space Sciences Data Center were analyzed. This research was partially supported by National Aeronautics and Space Administration grants NAG 5-427 and NAS 7-918.

APPENDIX

NEW OBSERVATIONS

We present new data gathered on the AGNs studied in this paper. These data consist of broad-band near-infrared photometry for seven of these AGNs, and optical spectrophotometry for two. Far-infrared photometry from *IRAS* is also tabulated.

Photometry from *IRAS* is presented in Table 4. For objects brighter than 0.5 Jy at 12 μm, the far-infrared fluxes were taken from the *IRAS Point Source* Catalog (Beichman *et al.* 1984). Fluxes for faint objects in the *IRAS Point Source Catalog* are biased because only observations in which a source was detected were used to measure the fluxes. This will tend to make objects with low signal-to-noise ratios appear brighter than they actually are. For this reason, fluxes of objects fainter than 0.5 Jy at 12 μm were determined from source extractions performed on co-added survey data. Data for one source (PG 0906+48) were taken from pointed AOs as discussed in Neugebauer *et al.* (1984). No spectral corrections to the *IRAS* data were necessary, because these objects had power-law slopes near -1. At 12, 25, and 60 μm, the thermal noise was about 25 mJy with a calibration error of about 10%, while at 100 μm, the errors were about 75 mJy and 15%.

TABLE 4

SATELLITE DATA

Source	$S_{12\ \mu m}$ (mJy)[a]	$S_{25\ \mu m}$ (mJy)[b]	$S_{60\ \mu m}$ (mJy)[b]	$S_{100\ \mu m}$ (mJy)[c]	Data[d]
Mrk 335	340	488	413	< 323	2
Mrk 348	274	743	1290	1620	2
I Zw 1	539	1260	2130	2430	1
NGC 1068	38300	86800	186000	239000	1
3C 84	1030	3630	7100	7760	1
3C 120	283	673	1300	2560	2
Akn 120	292	427	703	1130	2
Mrk 3	700	2860	3880	3350	1
Mrk 6	214	634	1190	994	2
Mrk 376	241	576	841	1330	2
Mrk 9	228	524	929	1110	2
Mrk 79	297	715	1450	2280	2
0906+48	40	89	190	340	3
NGC 3227	669	1750	7840	16900	1
NGC 3516	383	929	1730	2160	2
NGC 4051	779	1420	8160	20400	1
NGC 4151	2160	4810	6550	7950	1
3C 273	539	929	2180	2800	1
Mrk 231	1820	8560	33300	30100	1
1351+64	155	481	838	943	2
Mrk 279	198	289	1080	1970	2
NGC 5548	342	764	1110	1790	2
Mrk 817	356	1230	2340	2260	2
Mrk 478	139	175	561	857	2
Mrk 841	197	453	475	< 257	2
3C 390.3	130	306	260	< 231	2
II Zw 136	136	383	490	462	2
Mrk 509	366	701	1470	1490	2
NGC 7469	1300	5500	26700	34400	1

[a] Typical 12 μm statistical errors are 25 mJy with a 10% calibration uncertainty.

[b] Typical 25 and 60 μm statistical errors are 50 mJy with a 10% calibration uncertainty.

[c] Typical 100 μm statistical errors are 75 mJy with a 15% calibration uncertainty.

[d] Source of *IRAS* flux densities: 1) *IRAS Point Source Catalog*; 2) co-addition of raw survey data; 3) Neugebauer *et al.* 1984.

TABLE 5

NEW INFRARED MAGNITUDES

Source	J (1.2 μm)	H (1.6 μm)	K (2.2 μm)	L (3.5 μm)	Aperture	Date	Telescope[a]
Mrk 335	12.40	11.45	10.32	8.79	12″	1984 Aug 29	L61
I Zw 1[b]	12.19	11.20	10.10	8.36	27	1980 Aug 20	C60
Akn 120	11.71	10.89	9.95	...	8	1984 Feb 25	L61
	11.4	10.55	9.85	8.60	12	1984 Sep 14	L61
3C 273	11.63	10.84	9.70	8.36	11	1980 Jul 1	100
Mrk 817	11.70	10.98	10.24	...	5	1981	M60
II Zw 136	12.84	11.90	10.74	9.30	12	1984 Aug 30	L61
Mrk 509	11.72	10.77	9.80	8.64	12	1984 Aug 30	L61

[a] The following telescopes were used to collect the infrared data: L61 = Mount Lemmon 61 inch; M60 = Mount Wilson 60 inch; C60 = Cerro Tololo Inter-American Observatory 60 inch; 100 = Las Campanas DuPont 100 inch.

[b] Flux used in fits was corrected to 10″ aperture using multiaperture data.

TABLE 6

NEW OPTICAL MEASUREMENTS

A. Continuum Fluxes

	F_ν (mJy)	
λ_c (Å)	Mkn 817	Mkn 841
4200	...	6.4
4600	6.6	6.8
4800	7.3	6.9
5000	...	6.6
5200	7.2	6.8
5400	7.7	7.0
5600	7.2	6.8
5800	7.5	7.0
6000	8.2	7.4
6200	8.1	7.7
6400	8.4	7.6
6600	...	9.2
7000	8.0	8.4

B. Emission Line Fluxes

Emission	Flux (10^{-14} ergs cm^{-2} s^{-1})	
Line	Mkn 817	Mkn 841
Hδ	...	12
Fe II λ4570	15	14
Hγ	17	26
Hβ	46	56
[O III] λ5007	20	34
He I λ5876	6	16
Hα	190	257
[S II]	...	7

The co-added fluxes for 3C 390.3 disagree with some of the results of pointed AOs in Miley *et al.* (1984). Their data show an unusual *IRAS* spectrum, with a peak at 25 μm and another at 100 μm. Our data are consistent with theirs at 12, 25, and 60 μm, but we see no evidence for the unusually high 100 μm flux. We find a 3 σ upper limit of 230 mJy at 100 μm, compared with their value of 340 ± 60 mJy. Since their data were reduced very early in the mission, it is possible that confusion with infrared cirrus could have corrupted their measurements at 100 μm.

The near-infrared data were obtained at the Steward Observatory Mount Lemmon 61 inch (1.55 m), the Mount Wilson 60 inch (1.5 m), the Cerro Tololo 60 inch (1.5 m), and the Las Campanas Dupont 100 inch (2.54 m) telescopes (see references to Table 5). The usual *J* (1.2 μm), *H* (1.6 μm), *K* (2.2 μm), and *L* (3.5 μm) filters were used, with liquid nitrogen cooled InSb photometers. Standard stars from Elias *et al.* (1982) were measured throughout each night, yielding photometric scales good to 0.03–0.04 mag. The photometry, along with aperture diameters, observing dates, and telescopes, are listed in Table 5.

The optical spectrophotometry was done with the Palomar 60-inch (1.5 m) telescope. The SIT spectrograph was used, with a resolution of 20 Å and a 10″ slit. We combined spectra taken in the spring of 1984 to produce the averaged spectra, which were calibrated relative to BD +26°2606. We measured the emission-line fluxes, which are listed in Table 6B. We then removed these lines, and averaged the remaining points in 200 Å wide continuum bins. These continuum fluxes are tabulated in Table 6A. We estimate calibration uncertainties of 10% for the continuum fluxes and 15% for the line fluxes.

REFERENCES

Aitken, D. K., Roche, P. F., and Phillips, M. M. 1981, *M.N.R.A.S.*, **196**, 101P.

Baldwin, J. 1975, *Ap. J.*, **201**, 26.

Balzano, V. A., and Weedman, D. W. 1981, *Ap. J.*, **243**, 756.

Beichman, C., *et al.* 1984, *IRAS Point Source Catalog*.

Boksenberg, A., *et al.* 1978, *Nature*, **275**, 404.

Burstein, D., and Heiles, C. 1982, *A.J.*, **87**, 1165.

Campins, H. C., Rieke, G. H., and Lebofsky, M. J. 1985, *A.J.*, **90**, 896.

Crenshaw, D. M., and Peterson, B. M. 1985, *Ap. J.*, **291**, 677.

Cutri, R. M. 1986, private communication.

Cutri, R. M., Rudy, R. J., Rieke, G. H., Tokunaga, A. T., and Willner, S. P. 1984, *Ap. J.*, **280**, 521.

Cutri, R. M., Wisniewski, W. Z., Rieke, G. H., and Lebofsky, M. J. 1985, *Ap. J.*, **296**, 423.

de Bruyn, A. G., and Sargent, W. L. 1978, *A.J.*, **83**, 1257.

de Grijp, R. H. K., Miley, G. K., Lub, J., and de Jong, T. 1985, *Nature*, **314**, 240.

de Jong, T., Clegg, P. E., Soifer, B. T., Rowan-Robinson, M., Habing, H. J., Houck, J. R., Aumann, H. H., and Raimond, E. 1984, *Ap. J.* (*Letters*, **278**, L67.

Draine, B. T., and Lee, H. M. 1984, *Ap. J.*, **285**, 89.

Elias, J. H., Frogel, J. A., Matthews, K., and Neugebauer, G. 1982, *A.J.*, **87**, 1029.

Glass, I. S. 1981, *M.N.R.A.S.*, **197**, 1067.

Grandi, S. A. 1981, *Ap. J.*, **251**, 451.

Harvey, P. M., Wilking, B. A., and Joy, M. 1982, *Ap. J.* (*Letters*), **254**, L29.

Hildebrand, R. H., Whitcomb, S. E., Winston, R., Stiening, R. F., Harper, D. A., and Moseley, S. H. 1977, *Ap. J.*, **216**, 698.

Impey, C. D., and Malkan, M. A. 1987, in preparation.

Isobe, T., Feigelson, E. C., and Nelson, P. I. 1986, *Ap. J.*, **306**, 490.

Kellermann, K. I., and Pauliny-Toth, I. I. K. 1981, *Ann. Rev. Astr. Ap.*, **19**, 373.

Kwan, J., and Krolik, J. H. 1981, *Ap. J.*, **250**, 478.

Lacy, J. H., *et al.* 1982, *Ap. J.*, **256**, 75.

Lebofsky, M. J., and Rieke, G. H. 1980, *Nature*, **284**, 410.

———. 1985, private communication.

Malkan, M. A. 1983*a*, *Ap. J. (Letters)*, **264**, L1.

———. 1983*b*, *Ap. J.*, **268**, 582.

———. 1984, in *Proc. Garching Conf. on Ultraviolet and X-Ray Emission from Active Galactic Nuclei* (Garching: ESO), p. 121.

———. 1986, *Ap. J.*, in press.

Malkan, M. A., and Filippenko, A. V. 1983, *Ap. J.*, **275**, 477 (MF).

Malkan, M. A., and Moore, R. 1986, *Ap. J.*, **300**, 216.

Malkan, M. A., and Oke, J. B. 1983, *Ap. J.*, **265**, 92 (MO).

Malkan, M. A., and Sargent, W. L. W. 1982, *Ap. J.*, **254**, 22 (MS).

Maraschi, L., Tanzi, E. G., and Treves, A. 1980, in *Proc. Second IUE European Conf.* Tübingen (Garching: ESA), p. 299.

McAlary, C. W., McLaren, R. A., and Crabtree, D. R. 1979, *Ap. J.*, **234**, 471.

McAlary, C. W., McLaren, R. A., McGonegal, R. J., and Maza, J. 1983, *Ap. J. Suppl.*, **52**, 341.

McAlary, C. W., Rieke, G. H., Lebofsky, M. J., and Stocke, J. T. 1986, *Ap. J.*, **301**, 105.

Miley, G. K., Neugebauer, G., Clegg, P. E., Harris, S., Rowan-Robinson, M., Soifer, B. T., and Young, E. 1984, *Ap. J. (Letters)*, **278**, L79.

Miley, G. K., Neugebauer, G., and Soifer, B. T. 1985, *Ap. J. (Letters)*, **293**, L11.

Neugebauer, G., *et al.* 1980, *Ap. J.*, **238**, 502.

Neugebauer, G., Oke, J. B., Becklin, E. E., and Matthews, K. 1979, *Ap. J.*, **230**, 79.

Neugebauer, G., Soifer, B. T., and Miley, G. K. 1985, *Ap. J. (Letters)*, **295**, L27.

Neugebauer, G., *et al.* 1984, *Ap. J. (Letters)*, **278**, L83.

Neugebauer, G., Matthews, K., Soifer, B. T., and Elias, J. H. 1985, *Ap. J.*, **298**, 275.

Oke, J. B., and Goodrich, R. F. 1981, *Ap. J.*, **243**, 445.

Oke, J. B., and Zimmerman, B. 1979, *Ap. J. (Letters)*, **231**, L13.

Pounds, K., and McHardy, I. 1985, private communication.

Puetter, R. C., and Hubbard, E. N. 1985, *Ap. J.*, **295**, 394.

Richstone, D. O., and Schmidt, M. 1980, *Ap. J.*, **235**, 361.

Rickard, L. J., and Harvey, P. M. 1984, *A.J.*, **89**, 1520.

Rieke, G. H. 1976, *Ap. J. (Letters)*, **210**, L5.

———. 1978, *Ap. J.*, **266**, 550.

Rieke, G. H., and Lebofsky, M. J. 1979*a*, *Ap. J.*, **227**, 710.

———. 1979*b*, *Ann. Rev. Astr. Ap.*, **17**, 477.

Rieke, G. H., Lebofsky, M. J., and Low, F. J. 1985, *A.J.*, **90**, 900.

Robson, E. I., *et al.* 1983, *Nature*, **305**, 194.

Roche, P. F., Aitken, D. K., Phillips, M. M., and Whitmore, B. 1984, *M.N.R.A.S.*, **207**, 35.

Rudy, R. J., Jones, B., LeVan, P. D., Puetter, R. C., Smith, H. E., Willner, S. P., and Tokunaga, A. T. 1982*a*, *Ap. J.*, **257**, 570.

Rudy, R. J., LeVan, P. D., Puetter, R. C., Smith, H. E., and Willner, S. P. 1982*b*, *Ap. J.*, **253**, 53.

Rudy, R. J., LeVan, P. D., and Rodriguez-Espinosa, J. M. 1982, *A.J.*, **87**, 598.

Rybicki, G. B., and Lightman, A. P. 1979, *Radiative Processes in Astrophysics* (New York: Wiley), p. 47.

Sargent, W. L., de Bruyn, A. G., and Readhead, A. S. C. 1987, in preparation.

Seaton, M. J. 1979, *M.N.R.A.S.*, **187**, 73P.

Siegel, S. 1956, *Nonparametric Statistics for the Behavioral Sciences* (New York: McGraw-Hill).

Snijders, M. A., Boksenberg, A., Haskell, J. D., Fosbury, R. A., and Penston, M. V. 1982, in *Proc. Second IUE European Conference* (Tübingen) (Garching: ESA), p. 279.

Telesco, C. M., and Harper, D. A. 1980, *Ap. J.*, **235**, 392.

Ulrich, M. H., *et al.* 1982, *M.N.R.A.S.*, **192**, 561.

R. A. EDELSON: Palomar Observatory, 105-24, California Institute of Technology, Pasadena, CA 91125

M. A. MALKAN: Department of Astronomy, University of California, Los Angeles, CA 90024

Chapter Three

FAR-INFRARED PROPERTIES OF OPTICALLY SELECTED QUASARS

Reprinted from *The Astrophysical Journal,*
Letters to the Editor (1986, **v. 309**, pp. L69–L72)

The Astrophysical Journal, 309:L69–L72, 1986 October 15

FAR-INFRARED PROPERTIES OF OPTICALLY SELECTED QUASARS

R. A. Edelson
Owens Valley Radio Observatory, California Institute of Technology
Received 1986 May 19; accepted 1986 July 21

ABSTRACT

Pointed *IRAS* observations and ground-based near-infrared and radio measurements are used to study the far-infrared properties of 10 bright, optically selected quasars, nine of which were detected in at least three *IRAS* bands. Optically selected quasars tend to have very flat infrared spectra, with $\langle \alpha_{60\,\mu\mathrm{m}}^{12\,\mu\mathrm{m}} \rangle = -0.69 \pm 0.41$ (individual dispersion), and $\langle \alpha_{25\,\mu\mathrm{m}}^{2.2\,\mu\mathrm{m}} \rangle = -1.09 \pm 0.16$. The flat far-infrared power-law spectra, which extrapolate smoothly to near-infrared wavelengths, and the large observed 60–100 μm luminosities, provide strong evidence that the infrared continuum emission from most quasars is nonthermal in nature. Seven of the nine quasars with far-infrared detections had low-frequency turnovers determined. Optically selected quasars tend to have higher turnover frequencies than optically selected Seyfert galaxies. The infrared emission appears to be unreprocessed radiation from a synchrotron self-absorbed region a few light hours to a few light days across, about the size of the hypothesized accretion disk. Only three of the nine quasars in this complete, optically selected sample have $-1.25 \le \alpha_{60\,\mu\mathrm{m}}^{25\,\mu\mathrm{m}} \le -0.5$.

Subject headings: infrared: spectra — quasars

I. INTRODUCTION

The flight of the *Infrared Astronomical Satellite* (*IRAS*) has made it possible to study the far-infrared properties of a large number of active galactic nuclei (AGNs). The far-infrared properties of AGNs are important for two reasons: (1) It is critical to determine whether the infrared radiation is primarily nonthermal or thermal dust emission; and (2) the low radio flux densities observed from most AGNs (i.e., Condon *et al.* 1982; Edelson 1987; this *Letter*) generally require that the infrared continua, which rise from the optical through the infrared, cut off somewhere in the far-infrared-submillimeter region. Depending on the emission mechanism, this turnover can be used to determine source parameters which strongly constrain the physical conditions in AGNs.

Progress has been made in understanding the observed far-infrared properties of AGNs. Edelson and Malkan (1986, hereafter EM) determined the spectral energy distributions (SEDs) of a heterogeneous sample of 29 AGNs between 0.1 and 100 μm. Among their relevant results, they found (1) there is a strong correlation between infrared spectral index and reddening, in the sense that objects with large internal reddenings tend to have steep infrared SEDs; and (2) over half of the SEDs exhibited turnovers shortward of 100 μm. For objects with infrared SEDs which appear to be dominated by nonthermal emission (low-reddening Seyfert 1 galaxies and quasars), the best explanation is that the emission arises from a synchrotron self-absorbed source about the size of the hypothesized accretion disk. For Seyfert 2 galaxies and other dusty objects, the dust is warmer than that in normal galaxies ($T_d \approx 35$–70 K), and the infrared emission appears to originate in the narrow-line region.

The infrared-submillimeter properties of the complete, spectroscopically selected CfA sample of Seyfert galaxies were studied by Edelson, Malkan, and Rieke (1987, hereafter EMR). They found that Seyfert 1 galaxies tend to have significantly flatter infrared SEDs than Seyfert 2 galaxies, suggesting that the steepness of infrared SEDs provides a useful test for the presence of dust, and confirming the finding of EM that Seyfert 2 galaxies tend to have more dust than Seyfert 1 galaxies. Almost half of the CfA Seyfert galaxies detected at three or more *IRAS* frequencies were found to turn over shortward of 100 μm.

Miley, Neugebauer, and Soifer (1985) found that type 1 and 2 Seyfert galaxies tend to populate different regions of infrared color-color diagrams. Starburst and "normal" galaxies tend to have steep infrared SEDs, which are generally thought to be signatures of dust emission. Evidence that the SEDs of AGNs flatten out and turn over in the far-infrared can be seen in Figure 1 of Miley, Neugebauer, and Soifer (1985) and Figures 4 and 5 of Neugebauer *et al.* (1986*b*).

This *Letter* is organized as follows: The sample and data are discussed in the next section. The infrared spectral properties of this sample are analyzed in § III. The determination and implications of the far-infrared turnover are discussed in § IV. A concluding discussion and summary is given in § V. Throughout this *Letter*, values of $H_0 = 75$ km s^{-1} Mpc^{-1} and $q_0 = 0$ are assumed.

II. SAMPLE AND DATA

In order to study the far-infrared characteristics of a representative sample of quasars, a complete, optically selected sample has been formed, consisting of the 10 quasars in the PG/BQS sample with $B \le 15.00$ and $M_B \le -22.12$ (Schmidt and Green 1983). Far-infrared studies of complete, optically selected quasar samples have a number of advantages. Quasars are generally so distant that there is a negligible contribution from the underlying galaxy. Cold dust emission from the

TABLE 1

IRAS DATA FOR TON 1542

λ (μm)	S_ν (mJy)
12	121 ± 30
25	316 ± 88
60	160 ± 46
100	< 276

TABLE 2

RADIO DATA

Source	$S_{1.5\,\mathrm{cm}}$ (mJy)
0026+129	< 1.74
I Zw 1	< 1.35
Ton 951	< 1.23
3C 273	30500 ± 1530
Ton 1542	< 1.23
PB 1732	< 1.23
Mkn 478	< 1.50
1634+706	< 1.20
II Zw 136	2.51 ± 0.39
Mkn 304	< 1.26

galactic disk surrounding low-luminosity Seyfert nuclei can contaminate the low-resolution *IRAS* beam, causing infrared SEDs to appear to be steeper than that of the nucleus, and often masking the far-infrared turnover (EM).

Neugebauer *et al.* (1986*b*) present the results of pointed and survey observations of a heterogeneous collection of most known quasars detected with *IRAS*. However, the heterogeneous nature of their sample and the relatively low detection rate (less than 25% were detected in three *IRAS* bands, the minimum number needed for the spectral analysis undertaken in this *Letter*) mean that the sample of detected objects may contain unknown biases. One such bias is that unusually dusty objects (such as Mrk 231) are probably overrepresented in their sample.

The *IRAS* data for eight of the bright PG/BQS quasars are taken from and discussed extensively in Neugebauer *et al.* (1986*b*). In a few cases, these data disagree with those reported in EM, EMR, or the *IRAS Point Source Catalog* (Beichman *et al.* 1984). In these cases, the data of Neugebauer *et al.* (1986*b*) are generally used. The exception is the 100 μm flux density of II Zw 136, for which the value of 462 ± 75 mJy is taken from EM. One source (Ton 1542) was not discussed in Neugebauer *et al.* (1986*b*). The *IRAS* flux densities for this source, extracted from survey co-adds, are reported in Table 1. Nine of the bright PG/BQS quasars (90%) were detected in three or more *IRAS* bands. One object (0026 + 129) was not detected by *IRAS*, with a 3σ limit of 40 mJy at 60 μm, and it will not be discussed further. Near-infrared (1.1–3.5 μm) data were generally taken from Neugebauer *et al.* (1986*a*), except for I Zw 1, which was measured by Rieke (1978). The data for most of these sources are of high quality, but the far-infrared SEDs of 2 sources (Ton 1542 and Ton 951) are poorly determined, and Mrk 304 lacks near-infrared data.

The bright PG/BQS quasars were observed at 1.5 cm with the Owens Valley Radio Observatory 40 m telescope in 1985 June. The results of these measurements are presented in Table 2. A detailed description of the observing system can be found in Edelson (1987). Undetected objects have 3 σ upper limits quoted.

III. INFRARED SPECTRA

Table 3 contains spectral indices, redshifts, and luminosities derived for the bright PG/BQS quasars. Source names are given in the first column and redshifts (taken from Schmidt and Green 1983) are listed in the second column. The far-infrared spectral indices $\alpha^{12\,\mu\mathrm{m}}_{60\,\mu\mathrm{m}}$, $\alpha^{2.2\,\mu\mathrm{m}}_{25\,\mu\mathrm{m}}$, and $\alpha^{25\,\mu\mathrm{m}}_{60\,\mu\mathrm{m}}$ are given in the third through fifth columns ($F_\nu \propto \nu^\alpha$). The 60–100 μm luminosities (L_{ir}) are given in the sixth column, and the seventh column contains plotting offsets used in Figure 1. The quantity L_{ir} is given by

$$L_{ir} = 4\pi\left(\frac{cz}{H_0}\right)^2(\nu_1 F_{\nu_1} + \nu_2 F_{\nu_2}),$$

where ν_1 = 5 THz (60 μm) and ν_2 = 3 THz (100 μm).

The far-infrared SEDs of the nine bright PG/BQS quasars detected by *IRAS* are presented in Figure 1. The quantity νF_ν is plotted as a function of frequency, so a SED with $\alpha = -1$ (i.e., equal power per octave) will appear as a horizontal line. The general tendency for the objects with well-determined SEDs (i.e., the top six objects in Fig. 1) to have relatively flat, straight SEDs is apparent. A gentle flattening toward lower

TABLE 3

INFRARED SPECTRAL INDICES AND OTHER PARAMETERS

Source	z	$\alpha^{12\,\mu\mathrm{m}}_{60\,\mu\mathrm{m}}$	$\alpha^{2.2\,\mu\mathrm{m}}_{25\,\mu\mathrm{m}}$	$\alpha^{25\,\mu\mathrm{m}}_{60\,\mu\mathrm{m}}$	log L_{ir} (erg/s)	C
0026+129	0.142	…	> −0.66	…	…	…
I Zw 1	0.061	−0.89 ± 0.04	−1.18 ± 0.04	−0.84 ± 0.08	45.16	15.94
Ton 951	0.064	−0.16 ± 0.21	−1.16 ± 0.08	0.26 ± 0.36	44.12	13.09
3C 273	0.158	−0.91 ± 0.04	−0.92 ± 0.03	−0.75 ± 0.08	45.94	14.04
Ton 1542	0.064	−0.17 ± 0.24	−1.32 ± 0.09	0.78 ± 0.36	43.95	14.10
PB 1732	0.089	−0.21 ± 0.08	−0.89 ± 0.04	−0.01 ± 0.15	44.20	20.09
Mkn 478	0.077	−1.18 ± 0.08	−0.86 ± 0.04	−1.31 ± 0.10	44.86	15.49
1634+706	1.334	−1.03 ± 0.13	−1.23 ± 0.04	−0.88 ± 0.14	46.95	17.80
II Zw 136	0.061	−0.58 ± 0.04	−1.17 ± 0.04	−0.27 ± 0.08	44.43	18.62
Mkn 304	0.067	−1.06 ± 0.07	…	−1.45 ± 0.14	44.27	11.77

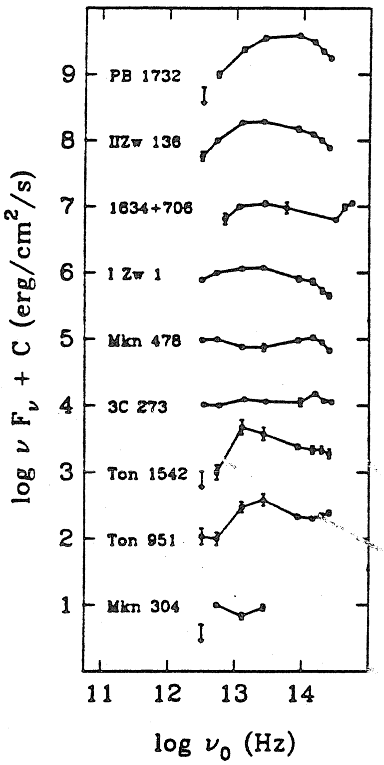

FIG. 1.—Far-infrared SEDs of the nine bright PG/BQS quasars detected by *IRAS*. The independent variable is log ν_0, where ν_0 is the frequency in the rest frame. The dependent variable log $\nu F_\nu + C$, where C is an arbitrary offset added for display purposes, tabulated in Table 3. Most of the data are of good quality, but the SEDs of the three quasars at the bottom (Ton 1542, Ton 951, and Mrk 304) are poorly determined.

frequencies is also seen in many SEDs. In particular, it should be noted that the far-infrared SEDs generally extrapolate smoothly to the near-infrared. The high-frequency excess in the high-redshift quasar 1614+706 is due to the "ultraviolet bump" seen in most AGNs (see EM).

The bright PG/BQS quasars generally have very flat infrared SEDs. The mean infrared spectral indices are $\langle \alpha_{60\,\mu\mathrm{m}}^{12\,\mu\mathrm{m}} \rangle = -0.69 \pm 0.44$ (dispersion for individual objects) and $\langle \alpha_{25\,\mu\mathrm{m}}^{2.2\,\mu\mathrm{m}} \rangle = -1.09 \pm 0.16$. This is flatter than the optically selected Seyfert 1 galaxies in the CfA Seyfert galaxy sample ($\langle \alpha_{60\,\mu\mathrm{m}}^{12\,\mu\mathrm{m}} \rangle = -1.08 \pm 0.44$ and $\langle \alpha_{25\,\mu\mathrm{m}}^{2.2\,\mu\mathrm{m}} \rangle = -1.15 \pm 0.29$, EMR), or the optically selected CfA Seyfert 2 galaxies ($\langle \alpha_{60\,\mu\mathrm{m}}^{12\,\mu\mathrm{m}} \rangle = -1.55 \pm 0.36$ and $\langle \alpha_{25\,\mu\mathrm{m}}^{2.2\,\mu\mathrm{m}} \rangle = -1.56 \pm 0.34$, EMR). These SEDs are also significantly flatter than those of normal galaxies.

De Grijp *et al.* (1985) report that a large fraction of *IRAS* sources with $-1.25 \le \alpha_{60\,\mu\mathrm{m}}^{25\,\mu\mathrm{m}} \le -0.5$ were found to be AGNs. However, only three of the nine bright PG/BQS quasars with $\alpha_{60\,\mu\mathrm{m}}^{25\,\mu\mathrm{m}}$ determined (33%) have $-1.25 \le \alpha_{60\,\mu\mathrm{m}}^{25\,\mu\mathrm{m}} \le -0.5$. Thus, their method finds only a fraction of all AGNs.

IV. LOW-FREQUENCY TURNOVER

All of the bright PG/BQS quasars except 3C 273 have low radio flux densities (see Table 2), which indicate that the SEDs which rise from the near-infrared through the far-infrared must cut off sharply in the far-infrared. This far-infrared cutoff has been studied before, for a heterogeneous sample of active galaxies in EM, and for the CfA Seyfert galaxies in EMR.

In EM, EMR, and the present study, the turnover frequency (ν_t) is determined by fitting a parabola in log ν–log F_ν space to the 25, 60, and 100 μm *IRAS* data (or, if the object is undetected at 100 μm or has a flux density minimum at 60 μm, to the 12, 25, and 60 μm data), and taking the point at which $\alpha = 0$ as the turnover, provided $\nu_t \ge 3$ THz (100 μm) in the observed frame. EM contains a detailed discussion of this method. The turnover frequencies of three objects (Ton 951, Ton 1542, and PB 1732) were measured with the higher frequency *IRAS* data. The turnover in Mrk 304 was measured by assuming that the 100 μm flux density was at the observed limit, so the value of ν_t reported for this object is actually a lower limit. The turnover frequencies (determined in the rest frame of the quasar) are tabulated in the second column of Table 4. Errors associated with the derived turnover frequencies can be as large as 50%.

Seven of the nine bright PG/BQS quasars detected in at least three *IRAS* bands (78%) had turnovers detected shortward of 100 μm. The turnover frequencies determined for the PG/BQS quasars also tend to be higher than those found in lower luminosity AGNs. Six of the nine bright PG/BQS quasars detected at three or more frequencies (67%) have been $\nu_t > 5$ THz. By comparison, only two of the 33 CfA Seyfert galaxies detected at 3 or more *IRAS* bands (6%) have $\nu_t > 5$ THz (EMR). The nonparametric logrank (Breslow) test of the distribution of a single parameter for data with limits (Feigelson and Nelson 1985) indicates that the PG/BQS quasars tend to have higher turnover frequencies than the CfA Seyfert galaxies at the 99.4% confidence level.

This turnover can be used to determine source parameters. If it is assumed that the infrared emission emanates from a synchrotron self-absorbed region with $T_b \approx 10^{12}$ K, source sizes can be derived (see EM for details). This parameter (r_{12}) is tabulated in the third column of Table 4. If it is assumed that the 2 keV X-ray emission arises from inverse-Compton-boosted infrared photons, one can estimate source sizes (r_c), brightness temperatures (T_c), and magnetic fields (B_c). A detailed discussion of this method can be found in EMR. These parameters are tabulated in the fourth through sixth columns of Table 4, respectively. Sources without reported

TABLE 4

INFRARED TURNOVER PARAMETERS

Source	ν_t (THz)	r_{12} (10^{15} cm)	r_c (10^{15} cm)	T_c (10^{10} K)	B_c (G)	r_s (10^{12} cm)	m_s (10^6 $M_\odot$)
I Zw 1	3.1	2.1	10	4.4	360	18	61
Ton 951	10.0	0.18	0.84	4.7	1100	2.3	7.9
Ton 1542	10.8	0.17	0.78	4.5	1200	2.5	8.5
PB 1732	7.8	0.32	1.4	5.2	670	4.3	14
1634+706	9.9	5.3	27	4.1	1300	870	3000
II Zw 136	5.6	0.53	2.5	4.7	560	3.8	13
Mkn 304	5.5	0.50	2.2	5.1	480	1.3	4.5

X-ray observations were assumed to have 2 keV flux densities of 3 μJy. This is not a very important assumption, because the source parameters depend very weakly on X-ray flux. Finally, lower limits to the Schwarzschild radius (r_s) and mass (m_s) of a hypothesized central black hole can be determined, by assuming that all of the 1–100 μm luminosity ultimately arises from accretion at the Eddington limit (EM). These parameters are tabulated in the seventh and eighth columns of Table 4, respectively.

The Compton method yields brightness temperatures of order $T_c \approx 5 \times 10^{10}$ K. This is typical for normal synchrotron self-absorbed radio sources. Typical magnetic fields of order 10^3 gauss are derived. The emitting regions have derived sizes which are typically of order a light-day across. These sizes correspond to upper limits of 100–1000 Schwarzschild radii, similar to the size of the hypothesized accretion disk.

V. DISCUSSION

Optically selected quasars have very flat infrared SEDs. These flat SEDs are strong evidence that the infrared emission is dominated by nonthermal radiation. Objects with infrared SEDs dominated by thermal dust emission (starburst galaxies, Seyfert 2 galaxies, normal galaxies, etc.) almost always have steep infrared SEDs, while objects known to be dominated by nonthermal emission (such as BL Lacertae objects and OVV quasars) usually have flat SEDs. EM found that AGNs believed to be dominated by nonthermal emission in the infrared generally had $\alpha_{25\,\mu\mathrm{m}}^{2.2\,\mu\mathrm{m}} > -1.25$, while those thought to be dominated by thermal dust emission usually had $\alpha_{25\,\mu\mathrm{m}}^{2.2\,\mu\mathrm{m}} < -1.25$. All but one of the bright PG/BQS quasars have $\alpha_{25\,\mu\mathrm{m}}^{2.2\,\mu\mathrm{m}} > -1.25$. Furthermore, EM found a strong correlation between reddening and infrared spectral slope, in the sense that objects with steep infrared SEDs tended to have high internal reddenings.

Further evidence of the nonthermal nature of the infrared emission from quasars is given by the large 60–100 μm luminosities. As Neugebauer *et al.* (1986*b*) point out, assuming that the far-infrared emission from luminous quasars is thermal emission from dust implies that the emitting regions must be a few kpc in size. The high turnover frequencies found would imply high dust temperatures, $T_d \geq 70$ K. The sizes and masses are too large for the narrow-line region, yet the high temperatures suggest that the dust could not lie outside the narrow-line region.

Finally, the fact that the bright PG/BQS quasars generally have straight or gently curving infrared SEDs, which extrapolate smoothly to near-infrared wavelengths, is also indicative of nonthermal emission. OVV quasars and BL Lacertae objects have infrared SEDs of this type. Dusty objects usually have curved infrared SEDs for which extrapolation to higher frequencies tends to underestimate the near-infrared flux density, because the dust cannot get hot enough to radiate at near-infrared wavelengths (EM). For the near-infrared and far-infrared emission to join up so well, yet be caused by two different mechanisms, requires an unlikely coincidence for a large number of objects.

In § IV, source sizes on the order of a light day are derived, under the assumption that the far-infrared SEDs are dominated by emission from a synchrotron self-absorbed source. As reported in EM and EMR, these sizes are of the same order as the hypothesized accretion disk.

Quasars have higher values of ν_t than type 1 (or type 2) Seyfert galaxies. There are two obvious possible explanations. The first is that both Seyfert 1 galaxies and quasars have relatively high turnover frequencies, but that emission from cold dust in the disk of the underlying galaxy masks it or shifts it to lower frequencies. This is supported by the fact that most of the nearest Seyfert galaxies in EMR and EM have undetected turnovers (i.e., $\nu_t < 3$ THz). The other is that there may be a physical limit to the size of the synchrotron self-absorbed source. Then, the more luminous and distant objects would become optically thick at a higher frequency. This is supported by the fact that the highest turnover frequency found for an object with a well-determined infrared SED is that of PG 1634+706, which is the most luminous and distant object in this study, EMR, or ER.

The author would like to thank A. Readhead, M. Malkan, M. Schmidt and N. Scoville for useful and interesting discussions. W. Rice provided invaluable help with the *IRAS* data. Analysis of *IRAS* data was supported by NASA grant NAG 5-427, and centimeter-wave astronomy at Owens Valley Radio Observatory is supported by NSF grant AST 85-09822.

REFERENCES

Beichman, C., *et al.* 1984, *IRAS Point Source Catalog*.
Condon, J. J., O'Dell, S. L., Puschell, J. J., and Stein, W. A. 1981, *Ap. J.*, **246**, 624.
de Grijp, R. H. K., Miley, G. K., Lub, J., and de Jong, T. 1985, *Nature*, **314**, 240.
Edelson, R. A. 1987, *Ap. J.*, in press.
Edelson, R. A., and Malkan, M. A. 1986, *Ap. J.*, **308**, 59 (EM).
Edelson, R. A., Malkan, M. A., and Rieke, G. 1987, *Ap. J.*, in press (EMR).
Feigelson, E. C., and Nelson, P. I. 1985, *Ap. J.*, **293**, 192.
Miley, G. K., Neugebauer, G., and Soifer, B. T. 1985, *Ap. J.* (*Letters*), **293**, L11.
Neugebauer, G., Green, R. F., Matthews, K., Schmidt, M., Soifer, B. T., and Bennett, J. 1986*a*, *Ap. J.*, in press.
Neugebauer, G., Miley, G. K., Soifer, B. T., and Clegg, P. E. 1986*b*, *Ap. J.*, **308**, 815.
Rieke, G. H. 1978, *Ap. J.*, **266**, 550.
Schmidt, M., and Green, R. F. 1983, *Ap. J.*, **269**, 352.

R. A. EDELSON: Palomar Observatory, 105-24, California Institute of Technology, Pasadena, CA 91125

Chapter Four

BROADBAND PROPERTIES OF THE CFA SEYFERT GALAXIES:
I. RADIO PROPERTIES

To appear in *The Astrophysical Journal* (1987, **v. 313**)

ABSTRACT

Quasi-simultaneous high-sensitivity observations of a complete, unbiased sample of 42 bright, spectroscopically selected Seyfert galaxies have been made at 1.5, 6, and 20 cm. All of the objects observed were detected above 0.3 mJy at 6 cm. Seyfert 2 galaxies tend to have steep, straight radio spectra with $\alpha \approx -0.7$. Although this is often true for Seyfert 1 galaxies as well, there is a higher tendency for Seyfert 1 galaxies to have flat spectra, and it appears that about 25% of the Seyfert 1 galaxies have highly curved spectra which flatten out toward higher frequencies. This may be because of emission from a compact core or from the low-frequency side of the infrared power law. There is evidence for extended emission, probably from the disk of the underlying galaxy, in about half of the objects studied. There is no significant difference in the mean 6 cm radio luminosities of types 1 and 2 Seyfert galaxies in this well-defined sample. The radio luminosity of Seyfert galaxies is well correlated with optical luminosity, but not with the presence of nearby companion galaxies. Fits to the relation $L_{rad} \propto L_{opt}^{s}$ yields a value of s significantly steeper than $s = 1$. While most Seyfert galaxies have $\alpha_{O-R} \approx 0$, the radio and optical-infrared continua apparently originate in different regions. Seyfert galaxies are generally not variable at 20 cm over time scales of $\sim$5 years. There are of order 10^5 Seyfert galaxies/Gpc^3 with radio luminosities between $10^{36.6}$ and $10^{39.4}$ erg/s. There is a sharp cutoff in the radio luminosity function of Seyfert 2 galaxies below $10^{37.2}$ ergs/s.

I. INTRODUCTION

The radio properties of "radio-quiet" active galactic nuclei (AGNs) are not well understood. The first quasars were discovered because of their radio emission, but only a small fraction of optically selected quasars (and Seyfert galaxies) are "radio-loud" objects (i.e., objects which have much higher flux densities at radio wavelengths than at optical wavelengths; see, e.g., Condon *et al.* 1981b). Some models of continuum emission (such as those involving beaming) posit that the intrinsic radio properties of radio-loud sources are the same as those of the underlying population of AGNs, although the observed radio properties are quite different. The radio properties of radio selected sources are well known (i.e., Kühr *et al.* 1981), but these objects tend to be at the extreme radio-loud end of the radio luminosity function, so their behavior is not representative of the underlying distribution of AGNs.

Relatively low detection rates in radio surveys of complete, homogeneous, optically selected samples of Seyfert galaxies and quasars have frustrated attempts to determine the radio properties of the underlying population of AGNs. Meurs and Wilson (1984), in work based partially on a survey by de Bruyn and Wilson (1976), detected 60% of a sample of Markarian Seyfert galaxies above ~4 mJy at 20 cm. These results were incorporated into a 6 cm study by Ulvestad and Wilson (1984a), which determined non-simultaneous spectral indices between 6 and 20 cm for 37% of the original sample of Markarian Seyfert galaxies. A survey of a heterogeneous collection of all active galaxies catalogued before mid-1982 and accessible to the VLA with $V_{rad} \leq 3100$ km/s, detected all of the objects at 6 cm (Ulvestad and Wilson 1984b). However, that sample consists mostly of nearby, low-luminosity objects and is not a complete, unbiased, optically selected sample.

Previous radio surveys of optically selected quasars have also had a low success rate. The similarities in the optical and X-ray properties of optically selected

Seyfert 1 galaxies and quasars suggest that their radio properties could also be similar. A 6 cm survey by Condon *et al.* (1981b) detected 40% of a heterogeneous sample of optically selected quasars above 0.5 mJy. A quick VLA survey of the PG/BQS quasars detected a similar fraction above 1 mJy at 6 cm (Schaffer *et al.* 1983). A larger fraction are detected in a deep survey (Kellerman 1985), the results of which have not yet been published. The most successful published multifrequency radio survey of optically selected quasars is Condon *et al.* (1981a), which determined the radio spectra of 10% of the sources observed.

This paper reports the results of three-frequency observations of the CfA Seyfert galaxies (Huchra and Berg 1987)–a well-defined sample of bright, optically selected Seyfert galaxies. All of the sources observed were detected at 6 cm, and for most, 1.5–20 cm spectra have been determined as well. This permits the radio properties of a well-defined sample of Seyfert galaxies to be probed.

This paper is organized as follows. In the next section, the sample is discussed, and the observations and data are discussed in § III. The radio spectral properties of optically selected Seyfert galaxies are derived and analyzed in § IV. The radio source sizes are discussed in § V, and the relation of radio luminosity to other properties such as optical luminosity and the presence of companion galaxies is investigated in § VI. The Seyfert galaxy radio luminosity function is derived and discussed in § VII, and § VIII contains a concluding discussion and summary of the major results of this paper. Throughout this paper, a value of $H_0 = 75$ km/s/Mpc is assumed. Since the largest redshift in this sample is $z = 0.06$, no corrections were made for cosmological effects in the luminosity distance or for evolution.

II. THE CfA SEYFERT GALAXIES

The objects observed were taken from the CfA sample of Seyfert galaxies, a collection of 25 Type 1 and 23 Type 2 Seyfert galaxies (Huchra and Berg 1987).

This sample was derived from the CfA redshift survey (Huchra *et al.* 1983) which obtained spectra of all galaxies with Zwicky magnitudes brighter than $m_{pg} = 14.5$ in a region of sky with $|b| \geq 30^o$, $\Omega = 2.66$ sr in extent. The presence of strong emission lines in these spectra was the sole selection criterion used to distinguish these objects from other galaxies in the survey.

For studies of the broad-band properties of Seyfert galaxies, the CfA Seyfert galaxies have a number of advantages over other samples. They are 1–2 magnitudes brighter (and therefore easier to detect at other frequencies) than both the PG/BQS quasars (Schmidt and Green 1983) and the Markarian Seyfert galaxies (Huchra and Sargent 1973). No ultraviolet-excess selection criterion was used in the CfA survey. Selection by ultraviolet-excess has been shown to bias samples against strong infrared emitters (Rieke 1978; Edelson, Malkan, and Rieke 1987), and the effect on radio properties is unknown. The Markarian survey is known to be incomplete at both the bright and faint ends (Huchra and Sargent 1973). The results of the V/V_m test performed by Huchra and Berg (1987) indicate that the CfA Seyfert galaxies are distributed uniformly in space, as one would expect from a complete, unbiased sample.

Forty-two of the 48 CfA Seyfert galaxies were observed. Three Seyfert 2 galaxies, NGC 3982, Mkn 461, and IC 4397, were not observed because they were added to the list after the radio measurements were made. Mkn 205 and Mkn 789, both Seyfert 1 galaxies, and NGC 4388, a Seyfert 2, were missed because good optical coordinates were not used. Omission of these six objects from the radio survey is not expected to significantly bias the results, and they will not be discussed further. Intermediate types (i.e., Seyfert 1.5 galaxies, etc.) are classified as Seyfert 1 galaxies.

III. OBSERVATIONAL RESULTS

a) Observations

Quasi-simultaneous high-sensitivity measurements of the CfA Seyfert galaxies were made at observing wavelengths $\lambda\lambda$ 1.5 cm, 6 cm, and 20 cm. The 1.5 cm measurements were made with the Owens Valley Radio Observatory 40-m telescope, on 1983 July 7-16. The observing system was a beam-switched radiometer using a reflected-wave maser of the NRAO-JPL design (Moore and Clauss 1979), with a cooled Dicke switch. The system temperature was 45 K, with an RF bandwidth of 400 MHz centered on 20.0 GHz (1.5 cm). The FWHM beamwidth was about $1\overset{\prime}{.}5$, and the beam separation was $7\overset{\prime}{.}1$. Contiguous 40-second scans of each object were combined to form observational records of up to 30 minutes in duration. Each source was observed a number of times during the nine-day run, and the data were combined to yield effective total integration times of a few hours per object. Typical 3σ upper limits of $\sim$2 mJy were obtained for undetected sources. Calibration was done relative to 3C 147, 3C 286, and 3C 295, assuming 1.5 cm flux densities of 1.75 Jy, 2.76 Jy, and 1.07 Jy, respectively (Baars *et al.* 1977).

The measurements at 6 cm and 20 cm were made at the VLA[1] on 1983 July 4. Fifty-megahertz bandwidths were used in the (compact) D-array, and the center frequencies were 4.89 GHz (6 cm) and 1.46 GHz (20 cm). Single snapshots were made of each object with integration times of about 10 minutes at 6 cm and of 2.5 minutes at 20 cm. Phase calibrators were observed once every hour. Flux calibration was done relative to 3C 286, which was assumed to have 6 cm and 20 cm flux densities of 14.5 Jy and 7.41 Jy respectively (Baars *et al.* 1977). Each source was mapped at 6 cm with an untapered synthesized beam of about $15''$

---

[1] The National Radio Astronomy Observatory is operated by Associated Universities, Inc., under contract with the National Science Foundation.

FWHM (referred to as 6 cm,h, hereafter) and with tapered beams of about $1\overset{'}{.}5$ (the size of the OVRO 40-m beam at 1.5 cm) at 6 cm (6 cm,l, hereafter) and at 20 cm. The maps were CLEANed with the standard AIPS software. An elliptical Gaussian with its size and orientation matched to those of the synthesized beam was fitted to each map. The position and the amplitude were allowed to vary in the high-resolution 6 cm,h map, allowing the right ascension, declination, and central peak flux density to be determined. This position was used and held fixed in fits to the low-resolution 6 cm,l and 20 cm maps. Only peak low-resolution flux densities were determined from these maps. The 1σ noise levels for faint and undetected point sources were about 0.1 mJy in the high-resolution 6 cm,h maps, 0.3 mJy in the low-resolution 6 cm,l maps, and 0.5 mJy at 20 cm.

With the exception of one object (0152+06, for which good optical astrometric positions are not available), the 6 cm,h sources were required to be within $15''$ of published optical astrometric positions. The data of Ledden *et al.* (1980) indicate that the brightest random source expected within $1'$ of 0152+06 and $15''$ of the 41 remaining optical positions should be weaker than 0.05 mJy. The faintest source detected at 6 cm was brighter than 0.3 mJy, so confusion was not a problem.

b) Data

The observational data are presented in Table 1. The first four columns, which give the name, type (Seyfert 1 or 2), redshift, and integrated optical flux density for each object, are taken from Huchra and Berg (1986). All quoted flux densities are in millijanskies. The optical flux densities are based on Zwicky magnitudes, which represent the sum of nuclear plus galactic light. Since all objects in the sample have $|b| \geq 30^o$, no correction is made for Galactic absorption. The positions in Columns 5 and 6 were determined with the VLA from the 6 cm,h maps and are generally good to $1''$. The last four columns contain the flux densities and uncertainties for the 20 cm data (S_{20cm}), the high-resolution 6 cm data ($S_{6cm,h}$), the low-resolution

6 cm data ($S_{6cm,l}$), and the 1.5 cm data ($S_{1.5cm}$). The quoted uncertainty is the quadratic sum of the statistical errors and an estimated 5% uncertainty in the calibration. Upper limits are at 3σ. Of the 42 sources observed, all were detected at 6 cm,h, 41 (98%) were detected at 6 cm,l, 38 (90%) were detected at 20 cm, and 24 (57%) were detected at 1.5 cm.

TABLE 1

Spectral indices are computed and presented in Table 2. The spectral index, α_{a-b}, is defined as

$$\alpha_{a-b} = \frac{\log S_a - \log S_b}{\log \nu_a - \log \nu_b}.$$

Columns 1-2 are the same as in Table 1. Columns 3-4 contain the spectral indices α_{6-20cm} (defined between 6 cm,l and 20 cm), and $\alpha_{1.5-6cm}$ (from 1.5 cm to 6 cm,l), respectively. Column 5 contains the quantity R, defined as

$$R = S_{6cm,h}/S_{6cm,l}.$$

Column 6 contains the radio-optical spectral index (α_{O-R}). This quantity is based on fluxes inferred from Zwicky's integrated galactic photographic magnitudes (with $m_{pg} = 14.5$ corresponding to F_ν=6.25 mJy at 4500 Å), and 6 cm,h radio measurements. Columns 7-8 contain the logarithm of the 6 cm,h monochromatic radio luminosity (L_{rad}) and monochromatic optical Zwicky galaxy luminosity (L_{opt}) in erg/s. They are given by

$$L_\nu = 4\pi\nu S_\nu \left(\frac{cz}{H_0}\right)^2,$$

where $\nu = 4.89$ GHz and 650 THz for L_{rad} and L_{opt}, respectively.

TABLE 2

c) Comparison with Previous Observations

De Bruyn and Wilson (1976), Meurs and Wilson (1981), and Wilson and Meurs (1982) observed 14 of the objects in this sample with WSRT with a similar beam size at 21 cm from 1975 through 1981. With the exception of one object (Mkn 573), their fluxes are in excellent agreement with those reported here. This indicates that Seyfert galaxies are not generally variable at 20 cm on time scales of $\sim$ 5 years. For Mkn 573, Wilson and Meurs (1981) find a 21 cm flux density of 21.1 ± 1.1 mJy, while Meurs and Wilson (1984) give a flux density of 11.4 mJy. This discrepancy is not explained. A 20 cm flux density of 16.1 ± 0.8 mJy for Mkn 573 is reported here.

Ulvestad and Wilson (1984a,b) made very high-resolution 6 cm observations, with the VLA in the A configuration, of 13 objects studied in this paper. In general, they found flux densities which were similar to, or slightly less than, the untapered 6 cm,h values reported here. This suggests that some objects are extended at the $\sim 0''.5$ level at 6 cm. The most extreme difference was for Mkn 231, which had a measured 6 cm flux density of 170 ± 10 mJy in Ulvestad and Wilson (1984a) and 278 ± 14 mJy reported here. Furthermore, Sramek and Tovmassian (1975) report a 6 cm flux density of 137 ± 20 mJy, which differs significantly from both of these results. As the 6 cm,h and 6 cm,l fluxes are in good agreement for this object, it is probably not extended, but the fact that it is one of the few CfA Seyfert galaxies with a flat spectrum radio source suggests that it may be variable.

IV. RADIO SPECTRA

FIGURE 1

a) Low-Frequency Spectra

Figure 1 contains spectra for the 24 objects which were detected at all three frequencies. Low-frequency spectral indices (α_{6-20cm}) were determined for the 38 sources (90%) detected at 6 and 20 cm. Figure 2 is a histogram of α_{6-20cm}. The top panel refers to Seyfert 1 galaxies, and the bottom refers to Seyfert 2 galaxies. For Seyfert 1 galaxies, the mean value of α_{6-20cm} was -0.66, with a dispersion of 0.28 for individual points. For Seyfert 2 galaxies, the mean value of α_{6-20cm} was -0.71 ± 0.23.

FIGURE 2

The Kolmogorov-Smirnov (K-S) test, a nonparametric rank test, was used to test for differences between two observed distributions of a parameter (Siegel 1956). The K-S test yields the parameter D, which can be used to determine if the hypothesis that two samples were derived from the same distribution can be rejected at a given confidence level.

Figure 2 suggests that Seyfert 1 galaxies may have a higher tendency to have flat low-frequency radio spectra than Seyfert 2 galaxies. Five Seyfert 1 galaxies (25%) have $\alpha_{6-20cm} > -0.5$, while only 2 Seyfert 2 galaxies are this flat. However, because of the small size of this sample, no statistically significant evidence was found with the K-S test for a difference in the distribution of α_{6-20cm} for types 1 and 2 Seyfert galaxies. A larger sample would be needed to determine the differences, if any, in the distributions of α_{6-20cm} for different types of Seyfert galaxies.

b) High-Frequency Spectra, Spectral Curvature

High-frequency spectral indices ($\alpha_{1.5-6cm}$) were determined for the 24 sources detected at all three wavelengths. Figure 3 is a plot of α_{6-20cm} vs. $\alpha_{1.5-6cm}$ for these 24 objects. This quantity appears to be distributed differently for types 1 and 2 Seyfert galaxies. Seyfert 1 galaxies have a mean high-frequency spectral index $\overline{\alpha}_{1.5-6cm} = -0.58 \pm 0.29$ (individual scatter), while for Seyfert 2 galaxies, $\overline{\alpha}_{1.5-6cm} = -0.83 \pm 0.15$. Not only is the mean value of $\alpha_{1.5-6cm}$ larger for Seyfert 1 galaxies than Seyfert 2 galaxies, but the width of the distribution for Seyfert 1 galaxies is also larger. The results of the K-S test indicates that $\alpha_{1.5-6cm}$ is distributed differently for types 1 and 2 Seyfert galaxies at the 95% confidence level. The median value of $\alpha_{1.5-6cm}$ is -0.62 for Seyfert 1 galaxies and -0.82 for Seyfert 2 galaxies. A difference would remain even if NGC 4235, a Seyfert 1 with $\alpha_{1.5-6cm} = +0.24$, were excluded from the sample.

FIGURE 3

Most Seyfert galaxies show little spectral curvature between 1.5 and 20 cm. The quantity $|\alpha_{6-20cm} - \alpha_{1.5-6cm}| < 0.25$ for 18 of the 24 objects with 3-point spectra. Three Seyfert 1 galaxies (NGC 4051, NGC 4235, and 2237+07), but no Seyfert 2 galaxies, have spectra with large upward curvature, $(\alpha_{6-20cm} - \alpha_{1.5-6cm}) > 0.40$. This suggests that the spectra of Seyfert 1 galaxies have a tendency to flatten out towards higher frequencies, although the sample is too small for the K-S test to find any statistically significant difference in the distribution of $(\alpha_{6-20cm} - \alpha_{1.5-6cm})$ for types 1 and 2 Seyfert galaxies. Possible explanations are discussed in § IVc. Three sources (Mkn 231, a Seyfert 1 galaxy, and NGC 5252 and 0152+06, both Seyfert 2 galaxies) show strong downward curvature, with $(\alpha_{6-20cm} - \alpha_{1.5-6cm}) < -0.35$. All of these sources have flat 6-20 cm spectra, so they are probably becoming optically thick near 6 cm.

c) *Discussion*

Seyfert 2 radio spectral properties are distributed in a similar fashion to those of "normal" optically-thin synchrotron sources. They have spectral indicies clustered around −0.7 to −0.8, with a small fraction ($\sim 10\%$) having flat radio spectra. They generally show little spectral curvature between 1.5 and 20 cm, and none of the Seyfert 2 galaxies in this sample show extreme spectral flattening toward higher frequencies.

The radio spectral properties of Seyfert 1 galaxies tend to be more broadly distributed than those of Seyfert 2 galaxies, and Seyfert 1 galaxies frequently have radio characteristics not often seen in optically selected sources. Seyfert 1 galaxies have flatter high-frequency spectra than Seyfert 2 galaxies (about 20% of the Seyfert 1 galaxies have flat spectra), and about 25% of the Seyfert 1 galaxies in this sample appear to show marked spectral flattening toward high frequencies.

This suggests that the radio emission from Seyfert 2 galaxies is dominated by synchrotron emission from an optically thin source. Most Seyfert 1 galaxies are also dominated by optically thin emission, but something else may be going on in the sources which flatten toward higher frequencies. Two possible explanations are: 1) Some Seyfert 1 galaxies contain a flat spectrum core not found in Seyfert 2 galaxies, which is becoming visible against the steep spectrum extended emission near 1.5 cm; or 2) In some Seyfert 1 galaxies, low-frequency emission from the nonthermal power law component, which dominates the optical-infrared continuum of Seyfert 1 galaxies and quasars (but appears to be absent or much weaker in Seyfert 2 galaxies) and which peaks near 100 μm (Edelson and Malkan 1986, Edelson, Malkan, and Rieke 1987), has a flux density which is similar to that of the extended radio emission near 1.5 cm. Millimeter-wave observations could help resolve this issue. The first scenario predicts a flat millimeter spectrum ($\alpha_{mm} \approx 0$), and the second, an inverted spectrum ($\alpha_{mm} \geq +1$).

V. RESOLUTION EFFECTS

Untapered 6 cm maps, with a beam width of about 15″, and tapered 6 cm maps, with a beam width of about 1ʹ.5, were made of the CfA Seyfert galaxies. This corresponds to about 4 and 25 kpc, respectively, for an object at a redshift $z = 0.02$ (the median redshift of the sample). Thus, the large beam typically samples the entire galaxy, including the disk, while the small beam contains only the central source. The quantity R, defined as the ratio of the flux in the central beam of the untapered map to that in the tapered map, is a good measure of the degree of resolution at 6 cm. Figure 4 contains a histogram of this quantity, which is tabulated in Column 5 of Table 2, for the 41 sources for which R was determined. Statistical fluctuations cause some sources to have values of R greater than unity. In no case is the value of R more than 1.5σ above unity.

FIGURE 4

Many of the Seyfert radio sources are extended at 6 cm. About half (20 of 41) of the sources have $R < 0.8$, and 3 sources (NGC 5033, NGC 5674, and NGC 5929) have $R < 0.5$. No difference was found in the distribution of R for types 1 and 2 Seyfert galaxies with the K-S test.

This effect is most easily explained as emission from the disk of the underlying galaxy. The 21 cm data of Hummel (1981), corrected to 6 cm with a spectral index of -0.7, yields a mean value of $S_{rad}/S_{opt} = 0.4$ for 6 cm disk emission from normal spiral galaxies. The mean value of S_{rad}/S_{opt} is 1.7 for Seyfert galaxies (see § VIc). This suggests that, on average, the disk will contribute about $0.4/1.7 = 24\%$ of the total 6 cm flux (i.e., $\overline{R} = 0.76$), although the ratio should be higher for Seyfert galaxies with low radio luminosities. The observed mean value is $\overline{R} = 0.81$ for the CfA Seyfert galaxies, in good agreement with this expectation.

VI. RELATION TO OTHER PROPERTIES

a) Radio Luminosity of Types 1 and 2 Seyfert galaxies

The relative luminosity of types 1 and 2 Seyfert radio sources is important for models which relate them in an evolutionary sequence, as well as models of the interaction between radio jets or plasmoids and broad-line-region gas (e.g., Osterbrock 1984). As all of the objects observed in this complete sample were detected at 6 cm, these data can be used for a rigorous investigation of the radio luminosities of Seyfert galaxies, as well as the relation between radio power and other properties.

Figure 5 is a plot of radio power (L_{rad}) as a function of optical power (L_{opt}). Solving for the mean of the logarithm of the luminosity is equivalent to taking its harmonic mean. For Seyfert 1 galaxies, this mean radio luminosity is $10^{37.98\pm0.90}$ erg/s (RMS scatter for individual objects), while for Seyfert 2 galaxies, it is $10^{38.16\pm0.67}$ erg/s. The median radio luminosity of Seyfert 1 galaxies is $10^{38.14}$ erg/s, while for Seyfert 2 galaxies, it is $10^{38.05}$ erg/s.

FIGURE 5

No difference was found in the distribution of L_{rad} for types 1 and 2 Seyfert galaxies with the K-S test. While the mean radio luminosities are clearly not significantly different, Seyfert 1 galaxies appear to have a broader distribution of radio luminosities than Seyfert 2 galaxies. However, this trend is not statistically significant in this small sample.

This result is different than that found by Meurs and Wilson (1984). Based on a higher radio detection rate for Seyfert 2 galaxies in a survey of a heterogeneous sample composed primarily of Seyfert galaxies taken from the Markarian survey, they concluded that Seyfert 2 galaxies are more powerful radio sources that Seyfert 1 galaxies. Selection effects are the most likely cause for this difference. Relative to Seyfert 1 galaxies, the ultraviolet-excess selected Markarian sample contains half as many Seyfert 2 galaxies as the CfA sample. It primarily missed red, low-luminosity Seyfert 2 galaxies, which were included in the spectroscopic CfA survey (Huchra, Wyatt, and Davis 1982). The strong correlation between optical and radio luminosity causes the Markarian sample to be biased against the inclusion of radio-weak Seyfert 2 galaxies. Furthermore, Seyfert 1 galaxies are more optically luminous (and therefore more distant in magnitude-limited surveys), and the distribution of α_{O-R} is broader for Seyfert 1 galaxies than for Seyfert 2 galaxies (see § VIc). These effects will all tend to depress the radio detection rate of Seyfert 1 galaxies relative to that of the Seyfert 2 galaxies in their sample.

Figure 5 shows that the intrinsic spread in L_{rad} for both types of Seyfert galaxies is much larger than any difference which there may be in the mean values of L_{rad}. (The same is true for L_{rad}/L_{opt}; see § VIc.) Differences in the radio powers of Seyfert galaxies of the same types are at least as great as global differences between different types. Theories which explain the radio luminosities of Seyfert galaxies in terms of confinement of the synchrotron source by broad-line region clouds must take this large spread in L_{rad} into account.

b) Radio and Optical Luminosity

All of the objects in this well-defined sample were detected at both radio and optical wavelengths, so it is valid to test for luminosity-luminosity correlations. Figure 5 suggests that there is a strong correlation between L_{rad} and L_{opt} for both types 1 and 2 Seyfert galaxies.

The Spearman rank correlation test (see Siegel 1956), a nonparametric rank test, was used to search for correlations between parameters. This test yields t, the student's t-statistic, which is used to determine if the hypothesis that that the two variables are uncorrelated can be rejected at a given confidence level. The results of this test indicates that L_{rad} and L_{opt} are correlated for both types of Seyfert galaxies above the 99.9% confidence level.

Proper least squares fits to the power law relation $L_{rad} \propto L_{opt}^{s}$ were made to the data. The final regression line is the mean of two regressions, each of which was done using a different variable as the independent variable. For Seyfert 1 galaxies, $s = 1.95 \pm 0.26$, for Seyfert 2 galaxies, $s = 1.66 \pm 0.30$, and for both types of Seyfert galaxy, $s = 1.81 \pm 0.21$. This steep slope is consistent with the results shown in Figure 7 of Meurs and Wilson (1984), although they found no correlation for Seyfert 1 galaxies, and only found a marginal correlation for Seyfert 2 galaxies, probably because of their relatively low detection rate. It is not immediately obvious why the slopes should be significantly steeper than $L_{rad} \propto L_{opt}$. It may be that the strength of the radio source is related to the nonthermal optical point source, and that contamination of the optical flux density with light from the underlying galaxy steepens the $L_{rad} - L_{opt}$ relation.

c) *Radio-Optical Spectral Index*

Figure 6 is a histogram of α_{O-R}, the radio-optical spectral index. This quantity, given in Column 6 of Table 2, is based on the high-resolution 6 cm data (6 cm,h) and the integrated Zwicky magnitudes.

FIGURE 6

Computing the mean radio-optical spectral index is equivalent to computing the harmonic mean of the radio-optical luminosity ratio. For Seyfert 1 galaxies, $\overline{\alpha}_{O-R} = 0.073$, with a 1σ scatter of 0.118 for individual objects, and for Seyfert 2 galaxies, $\overline{\alpha}_{O-R} = 0.017 \pm 0.109$.

The difference in $\overline{\alpha}_{O-R}$ for types 1 and 2 Seyfert galaxies is 0.056, which corresponds to Seyfert 2 galaxies being on average a factor of 1.9 brighter than

Seyfert 1 galaxies with the same optical brightness. The results of the K-S test indicates that the distribution of α_{O-R} for types 1 and 2 Seyfert galaxies is different at the 99% confidence level. This is a consequence of the fact that Seyfert 1 galaxies are optically more luminous than Seyfert 2 galaxies, while their radio luminosities are similar.

For all Seyfert galaxies, $\overline{\alpha}_{O-R} = 0.045$. which corresponds to $S_{rad}/S_{opt} = 1.7$. For most Seyfert galaxies, $\alpha_{6-20cm} \approx -0.7$. Edelson and Malkan (1986) and Edelson, Malkan, and Rieke (1987) find that the infrared spectral indicies of Seyfert 1 galaxies are clustered around $\alpha_{IR} \approx -1.2$, with most showing a sharp cutoff near 100 μm. Under the best assumption (synchrotron self-absorption), they found that the infrared emission was confined to a region of order a light day in size. Seyfert 2 galaxies and other dusty objects were found to have even steeper infrared spectra which also peaked in the far-infrared, presumably because of thermal dust emission.

Extrapolation of the far-infrared peak to 6 cm would require a spectral index $\alpha_{100\mu m-6cm} \geq +1$. No sources in this survey have such highly inverted radio spectra. Although this component may be becoming visible in some Seyfert 1 galaxies at 1.5 cm (see § IV), the 6–20 cm spectra of all sources are clearly dominated by more extended emission.

d) Companions

It has been suggested that activity such as radio emission from Seyfert galaxies could be triggered by interactions with other galaxies. Ulvestad and Wilson (1984a) found evidence for a correlation between radio emission from Seyfert galaxies and the presence of a companion galaxy, although Ulvestad and Wilson (1984b) did not confirm this result. This question is addressed quantitatively in this section.

Two different approaches are used. In the first approach, the CfA redshift survey data (Huchra *et al.* 1983) were used to determine the distance from each of the 14 Seyfert galaxies in this sample with $z \leq 0.015$ (8 Type 1 and 6 Type 2 Seyfert galaxies) to its closest companion. The nearest companion was defined to be the galaxy with the smallest angular separation on the sky, provided that galaxy's redshift was no more than 300 km/s different than that of the Seyfert galaxy and the companion had $m_{pg} \leq 14.5$. No correlation was found between projected distance and radio luminosity with the Spearman rank correlation test.

The second approach used a sample of 28 CfA Seyfert galaxies (15 Type 1 and 13 Type 2 Seyfert galaxies) for which 6 cm radio data and Dahari's (1985) "interaction parameter" are available. Again, the Spearman rank test was used to test for a correlation between interaction parameter and radio luminosity, but none was found. These results indicate that the radio luminosity of Seyfert galaxies is not a strong function of the presence of companion galaxies.

VII. RADIO LUMINOSITY FUNCTION

a) Introduction

The Seyfert galaxy radio luminosity function (RLF) is an important tool for understanding the nature of Seyfert galaxies and their relation to other objects. If possible, it would be best to determine the Seyfert galaxy RLF from a sample identified in a complete radio survey. Unfortunately, Seyfert galaxies are rather weak radio sources, and they are not found in large numbers in fully identified radio surveys, so this method cannot be used.

The next best method (which is used in this paper) is to make radio measurements of a complete, unbiased, optically selected sample. The RLF is derived from the optical luminosity function and the bivariate radio-optical luminosity distribution function. This method has the disadvantage that errors can be introduced by the spread in L_{rad}/L_{opt}. For instance, no extreme radio-loud objects such as 3C 120 are represented in the CfA Seyfert galaxy sample. Nonetheless, it is used because no other method for determining the Seyfert galaxy RLF is available.

Meurs and Wilson (1984) used this method to determine the RLF of Markarian Seyfert galaxies with 21 cm observations at Westerbork. As the V/V_m test shows that the Markarian survey is incomplete at both the bright and faint ends (Huchra and Sargent 1973), large corrections were applied to the data. However, nothing was done about the bias of the Markarian survey against low-luminosity Seyfert 2 galaxies (see § VI). Non-Markarian Seyfert galaxies were added to the sample and data were weighted according to the derived value of V/V_m in an attempt to offset the effect of incompleteness. Both the optical luminosity function and the bivariate radio-optical luminosity distribution function were binned. No discussion was made of errors introduced by the double binning process or by the spread in the L_{rad}/L_{opt}. Further assumptions about the distribution of L_{rad}/L_{opt} were required because only 60% of the sources observed were detected.

The CfA Seyfert galaxies form a complete, unbiased sample (Huchra and Berg 1987), so no large corrections for incompleteness are needed. The fact that the entire sample was detected at 6 cm means that few assumptions had to be made concerning the distribution of L_{rad}/L_{opt}.

b) Derivation

The derivation of the CfA Seyfert galaxy RLF is based on the V/V_m method described in Schmidt and Green (1983). The contribution of each object to the luminosity function is derived individually, and the final luminosity function is the sum of the individual contributions. This method has the advantage that the data are not binned until the last step, so information is not lost in intermediate steps.

The maximum accessible volume (V_m) is the volume of space within which an object could be detected above both survey limits. There are two possible values for V_m, one based on the optical survey limit ($V_{m_{opt}}$), and the other on the radio survey limit ($V_{m_{rad}}$). The accessible volume is the smaller of these two values, that is

$$V_m = \min(V_{m_{opt}}, V_{m_{rad}}).$$

This is equivalent to forming the contribution of each object to the RLF from its contribution to the optical luminosity function and the bivariate radio-optical luminosity distribution function.

Once these quantities have been calculated, the RLF is derived and binned. The differential RLF, $\Phi(L_{rad})$, is given by

$$\Phi(L_{rad}) = \frac{4\pi}{\Omega f \Delta L}\sum_{a=1}^{n}\frac{1}{V_{ma}}$$

summed over all n objects with L_{rad} in each bin of width ΔL (Huchra and Sargent 1973). In this equation, Ω is the amount of sky surveyed optically ($\Omega = 2.66$ sr), and f is the fraction of optically selected objects which were observed at radio frequencies ($f = 0.92$ for the Seyfert 1 galaxies, 0.83 for the Seyfert 2 galaxies, and 0.87 for the entire sample of Seyfert galaxies).

The data were binned using logarithmic bins of width $\Delta L = 10^{0.4}$ (corresponding to one "radio magnitude"). The RLF was determined for radio luminosities of $10^{37.0}$–$10^{39.4}$ erg/s. No CfA Seyfert galaxy had radio luminosities between $10^{36.6}$ and $10^{37.0}$ ergs/s, but an upper limit to the space density of Seyfert galaxies with L_{rad} within this range was derived by using a value of $V_m = 7.2\text{x}10^{-4}$ Gpc^3, which is appropriate for an object with $L_{rad} = 10^{36.8}$ erg/s at a survey limit of 0.35 mJy.

It is difficult to estimate the errors in a RLF derived from an optically selected sample. Besides those which arise from statistical fluctuations, errors can also be introduced by the spread in the distribution of L_{rad}/L_{opt} and by biases or incompleteness in the optical Seyfert galaxy selection process. The optical limit is usually the significant one in a survey with sufficient sensitivity to detect all of the sources at radio wavelengths (i.e., $V_{m_{opt}} < V_{m_{rad}}$ for most objects in this sample), so the spread in L_{rad}/L_{opt} gives rise to a spread in $V_m(L_{rad})$.

The differential RLF was derived for types 1 and 2 Seyfert galaxies separately, and for both types together. It is presented in Table 3 and Figure 7. Column 1 contains the binned values of L_{rad}. Columns 2-3, 4-5, and 6-7 give the space densities and number of objects in each bin for type 1's, type 2's, and both types together. The error bars in Figure 7 represent the 1σ statistical uncertainty, uncorrected for the effects discussed earlier. The crosses in Figure 7 represent the RLF of Meurs and Wilson (1984), scaled to the units used in this paper with a 6-20 cm spectral index $\alpha_{6-20cm} = -0.7$.

TABLE 3

FIGURE 7

c) *Discussion*

The RLF is determined between $10^{37.0}$ and $10^{39.4}$ erg/s. and limits are established for L_{rad} between $10^{36.6}$ and $10^{37.0}$ erg/s. The space density of Seyfert galaxies with radio luminosities between $10^{36.6}$ and $10^{39.4}$ ergs/s is of order 10^5 Gpc^{-3}. All but one of the Seyfert 2 galaxies studied fell within this luminosity range. Mkn 533 had $L_{rad} > 10^{39.4}$ erg/s. As is apparent in Figure 5, Seyfert 1 galaxies have a broader range of radio luminosities than Seyfert 2 galaxies (see § V). Two Seyfert 1 galaxies (NGC 4051 and NGC 5273) had $L_{rad} < 10^{36.6}$ erg/s and one (Mkn 231) had $L_{rad} > 10^{39.4}$ erg/s. For L_{rad} between $10^{36.6}$ and $10^{39.4}$ erg/s, Seyfert 2 galaxies are about 3 times more numerous than Seyfert 1 galaxies.

There is a dramatic turnover in the RLF of Seyfert 2 galaxies near $10^{37.2}$ erg/s. The space density near $10^{37.2}$ erg/s is more than one order of magnitude below that extrapolated from higher luminosities. The RLF of Seyfert 1 galaxies also appears to cut off near $10^{37.2}$ ergs/s, although it is not as strong as that of Seyfert 2 galaxies.

Only four points from the Meurs and Wilson (1984) Seyfert galaxy RLF were of sufficiently low luminosity to overlap the CfA Seyfert galaxy RLF. These points are plotted along with the CfA Seyfert RLF in Figure 7. The RLFs of the Seyfert 1 galaxies are in very good agreement. However, the type 2 Markarian Seyfert galaxy RLF is generally about a factor of two below that of the CfA Seyfert galaxies. This suggests that both the Markarian and CfA surveys found most of the Seyfert 1 galaxies, but the Markarian survey missed about half of the Seyfert 2 galaxies, probably because they are too red to satisfy the ultraviolet-excess selection criterion.

The Seyfert galaxy RLF can also be used to study the relative radio luminosities of Type 1 and 2 Seyfert galaxies. If the Seyfert 1 galaxy RLF is shifted by a factor of three (i.e., $\Delta log\Phi = 0.48$, to account for the fact that Seyfert 2 galaxies are more numerous),the two RLFs are almost identical. The similarity in the shape of the RLF of Seyfert 1 and 2 galaxies is further evidence that of the lack of significant difference in the distribution of radio luminosities for different types of Seyfert galaxies.

VIII. CONCLUSIONS

The results of 1.5, 6, and 20 cm observations of the CfA Seyfert galaxies are reported. The CfA Seyfert galaxies form a complete, spectroscopically selected sample which does not suffer from biases caused by use of the ultraviolet-excess selection technique. It appears that half of the low-luminosity Seyfert 2 galaxies in the CfA Seyfert galaxy sample are too red to be included in the ultraviolet-excess Markarian survey. All of the sources observed were detected at 6 cm. Two-frequency spectra were determined for 90% of these sources, and three-frequency spectra were determined for 57%. The high radio detection rate for this well-defined sample allows the "radio-quiet" end of the Seyfert galaxy radio luminosity function to be probed.

Seyfert 2 radio spectral properties are similar to those of "normal" optically-thin synchrotron sources. They have uncurved radio spectra with α_{6-20cm} clustered around -0.7, and about 10% have flat radio spectra. Most Seyfert 1 galaxies also have steep, uncurved radio spectra, but a larger fraction ($\sim$ 20%) have flat spectra, and about 25% appear to show strong spectral flattening toward higher frequencies. This could be caused by a second component (either a flat spectrum core or low-frequency emission from the nonthermal component which peaks near 100 μm) becoming visible at 1.5 cm.

Emission from the disk of the underlying galaxy is typically $\sim$20% of the total 6 cm flux density, and can be substantially higher for low-luminosity objects. The properties of radio emission from the disks of types 1 and 2 Seyfert galaxies are similar.

There is no significant difference in the radio luminosities of the types 1 and 2 Seyfert galaxies in this complete sample. The intrinsic spread in L_{rad} for either type of Seyfert galaxy is much larger than any differences in the mean radio luminosities. The luminosity of Seyfert galaxy radio sources is strongly correlated with the integrated optical galaxy luminosity. Fits to the power law relation $L_{rad} \propto L^{s}_{opt}$ yield $s = 1.95 \pm 0.26$ for Seyfert 1 galaxies, $s = 1.66 \pm 0.30$ for Seyfert 2 galaxies, and $s = 1.81 \pm 0.21$ for both types. It is not immediately clear why the slope is significantly steeper than $s = 1$.

In most cases, $\alpha_{IR} \approx -1.3$ and $\alpha_{6-20cm} \approx -0.7$, while $\alpha_{O-R} \approx 0$, suggesting that the radio and optical-infrared power law emission arises from different regions and/or physical mechanisms. There is no correlation between radio luminosity and the presence of a nearby companion galaxy. Seyfert galaxies are generally not variable on time scales of $\sim$5 years at 20 cm.

There are of order 10^5 Seyfert galaxies/Gpc^3 with radio luminosities between $10^{36.6}$ and $10^{39.4}$ erg/s. Seyfert 2 galaxies are about three times more numerous than Seyfert 1 galaxies in this luminosity range, but Seyfert 1 galaxies have a broader distribution of radio luminosities. There is a strong cutoff in the RLF of Seyfert 2 galaxies near $L_{rad} = 10^{37}$ erg/s, as the derived space density is more than one order of magnitude less than extrapolation from higher luminosities would predict.

The author would like to thank A. Moffet, A. Readhead, M. Schmidt, L. Dressel, and N. Scoville for useful and interesting discussions. The anonymous referee made an important contribution to the analysis of the RLF. The assistance of R. Moore and H. Hardebeck of OVRO and J. van Gorkom of the VLA in gathering and analyzing the data is also appreciated. J. Huchra kindly released the list of CfA Seyfert galaxies well ahead of publication. This work was partially supported by NSF grants AST 85-09822 and AST 83-14134.

TABLE 1

CfA SEYFERT GALAXY RADIO DATA

Source	Type	z	S_{opt} (mJy)	R. A.	Dec.	S_{20cm} (mJy)	$S_{6cm}(h)$ (mJy)	$S_{6cm}(l)$ (mJy)	$S_{1.6cm}$ (mJy)
Mkn 334	2	0.0220	6.9	0 0 35.65	21 40 55.0	26.9 ± 1.4	11.20 ± 0.57	11.4 ± 0.6	4.5 ± 0.7
Mkn 335	1	0.0259	10	0 3 45.26	19 55 29.0	4.1 ± 0.9	3.30 ± 0.18	2.9 ± 0.2	< 1.7
0048+29	1	0.0359	9.1	0 48 53.05	29 7 48.2	7.3 ± 0.5	2.03 ± 0.15	2.8 ± 0.3	< 1.8
I Zw 1	1	0.0604	7.6	0 50 57.84	12 25 19.7	8.4 ± 0.9	2.78 ± 0.17	3.1 ± 0.2	< 1.9
Mkn 993	2	0.0154	10	1 22 42.68	31 52 36.6	3.5 ± 0.5	2.16 ± 0.12	1.9 ± 0.2	< 2.2
Mkn 573	2	0.0173	10	1 41 22.90	2 5 56.5	16.1 ± 1.1	7.08 ± 0.39	7.4 ± 0.4	< 1.8
0152+06	2	0.0174	6.3	1 52 44.65	6 22 2.0	15.0 ± 2.1	9.43 ± 0.48	9.9 ± 0.6	3.7 ± 0.6
Mkn 590	1	0.0263	10	2 12 0.38	− 0 59 57.0	11.2 ± 1.4	5.23 ± 0.29	7.6 ± 0.4	3.6 ± 0.6
NGC 1068	2	0.0037	300	2 40 7.06	− 0 13 30.3	4610 ± 230	1330 ± 68	1800 ± 90	450 ± 34
NGC 1144	2	0.0288	21	2 52 38.84	− 0 23 7.0	146.0 ± 7.3	29.3 ± 1.7	49.4 ± 2.5	13.9 ± 1.3
Mkn 1243	1	0.0353	6.3	9 57 14.04	13 17 0.3	< 4.8	0.37 ± 0.07	< 0.6	< 2.6
NGC 3079	2	0.0037	130	9 58 34.91	55 55 16.0	591 ± 30	145.0 ± 8.4	259 ± 13	84.5 ± 6.5
NGC 3227	2	0.0038	52	10 20 46.73	20 7 6.9	101.0 ± 5.5	27.5 ± 1.4	35.0 ± 1.9	9.2 ± 1.2
NGC 3362	2	0.0227	14	10 42 15.25	6 51 34.7	11.6 ± 0.8	2.54 ± 0.20	4.5 ± 0.3	< 2.3
1058+45	2	0.0191	9.1	10 58 42.41	45 55 21.6	14.5 ± 1.8	3.67 ± 0.20	3.5 ± 0.4	< 2.6
NGC 3516	1	0.0085	48	11 3 23.20	72 50 22.8	15.5 ± 1.1	6.42 ± 0.46	10.6 ± 1.0	5.3 ± 1.0
Mkn 744	1	0.0091	16	11 37 4.78	32 11 12.8	17.5 ± 1.2	5.40 ± 0.30	7.0 ± 0.4	< 2.9
NGC 4051	1	0.0022	200	12 0 36.29	44 48 35.0	40.6 ± 2.4	7.37 ± 0.51	11.6 ± 0.7	7.4 ± 1.1
NGC 4151	1	0.0030	130	12 8 1.04	39 41 2.1	316 ± 16	125.0 ± 6.4	125.0 ± 6.3	39.9 ± 3.4
NGC 4235	1	0.0077	28	12 14 36.80	7 28 8.9	9.5 ± 0.8	4.68 ± 0.28	5.8 ± 0.3	8.1 ± 1.1
Mkn 766	1	0.0128	13	12 15 55.64	30 5 25.9	35.9 ± 1.9	15.80 ± 0.81	15.4 ± 0.8	5.3 ± 0.7
Mkn 231	1	0.0410	9.1	12 54 5.11	57 8 38.5	255 ± 13	270 ± 14	278 ± 13	123 ± 11
NGC 5033	1	0.0030	160	13 11 9.14	36 51 31.3	108.0 ± 5.6	12.90 ± 0.80	39.8 ± 2.0	15.6 ± 1.8
1335+39	2	0.0201	8.3	13 35 28.51	39 24 31.3	< 37.5	1.61 ± 0.11	1.3 ± 0.3	< 1.8
NGC 5252	2	0.0231	6.3	13 35 44.34	4 47 47.2	19.6 ± 1.1	16.20 ± 0.83	18.1 ± 0.9	8.4 ± 1.0
Mkn 266	2	0.0275	9.1	13 36 14.78	48 31 49.0	107.0 ± 6.2	33.4 ± 1.7	43.3 ± 2.2	14.9 ± 1.3
Mkn 270	2	0.0090	7.6	13 39 41.79	67 55 28.0	12.3 ± 0.8	4.92 ± 0.27	5.2 ± 0.4	< 3.7
NGC 5273	1	0.0036	33	13 39 55.31	35 54 20.0	< 2.8	1.59 ± 0.13	2.0 ± 0.3	< 2.4
Mkn 279	1	0.0304	6.3	13 51 53.63	69 33 12.8	22.4 ± 1.4	7.41 ± 0.39	7.3 ± 0.4	< 3.3
NGC 5548	1	0.0166	23	14 15 43.47	25 22 1.9	40.7 ± 2.2	10.50 ± 0.55	13.8 ± 0.9	3.8 ± 0.7
NGC 5674	2	0.0248	13	14 31 22.53	5 40 37.7	28.6 ± 1.7	3.69 ± 0.23	9.6 ± 0.6	2.9 ± 0.8
Mkn 817	1	0.0314	7.6	14 34 57.99	59 0 41.0	10.0 ± 0.9	6.01 ± 0.32	5.2 ± 0.4	< 2.5
Mkn 686	2	0.0122	11	14 35 19.53	36 47 3.2	5.6 ± 0.6	1.71 ± 0.10	2.9 ± 0.5	< 2.1
Mkn 841	1	0.0364	10	15 1 36.20	10 37 55.8	< 14.8	3.89 ± 0.93	6.5 ± 2.1	< 2.2
NGC 5929	2	0.0083	10	15 24 18.95	41 50 41.2	100.0 ± 5.2	20.8 ± 2.5	42.0 ± 2.1	14.3 ± 1.2
NGC 5940	1	0.0339	7.6	15 28 51.25	7 37 37.7	8.5 ± 1.2	2.35 ± 0.17	4.3 ± 0.3	< 1.9
1614+35	1	0.0280	9.1	16 14 40.08	35 49 48.6	9.3 ± 1.1	1.44 ± 0.09	2.8 ± 0.3	< 2.8
2237+07	1	0.0250	7.6	22 37 46.54	7 47 32.8	13.7 ± 1.1	4.63 ± 0.24	4.4 ± 0.4	2.1 ± 0.7
NGC 7469	1	0.0160	23	23 0 44.46	8 36 15.8	171.0 ± 8.9	66.1 ± 3.3	71.4 ± 3.6	22.2 ± 1.9
Mkn 530	1	0.0290	6.9	23 16 22.91	− 0 1 48.1	28.6 ± 1.6	11.50 ± 0.58	11.7 ± 0.6	4.2 ± 0.6
Mkn 533	2	0.0289	14	23 25 24.46	8 30 12.5	220 ± 11	66.5 ± 3.4	75.1 ± 3.8	16.7 ± 1.3
NGC 7682	2	0.0170	7.6	23 26 30.72	3 15 28.0	61.6 ± 3.1	24.6 ± 1.3	24.0 ± 1.2	5.7 ± 0.6

TABLE 2

CfA Seyfert Galaxy Radio Parameters

Source	Type	α^{20cm}_{6cm}	$\alpha^{6cm}_{1.5cm}$	R	α^{O}_{R}	log(L_{rad}) (erg/s)	log(L_{opt}) (erg/s)
Mkn 334	2	−0.71	−0.66	0.98	−0.036	38.70	43.62
Mkn 335	1	−0.29	...	1.13	0.077	38.32	43.92
0048+29	1	−0.78	...	0.72	0.105	38.39	44.17
I Zw 1	1	−0.82	...	0.89	0.070	38.98	44.54
Mkn 993	2	−0.51	...	1.14	0.107	37.69	43.47
Mkn 573	2	−0.64	...	0.96	0.023	38.30	43.57
0152+06	2	−0.34	−0.70	0.95	−0.030	38.43	43.38
Mkn 590	1	−0.32	−0.53	0.69	0.044	38.53	43.94
NGC 1068	2	−0.78	−0.98	0.74	−0.106	39.23	43.71
NGC 1144	2	−0.90	−0.90	0.59	−0.025	39.36	44.34
Mkn 1243	1	...	...	...	...	37.64	43.99
NGC 3079	2	−0.68	−0.80	0.56	−0.008	38.27	43.35
NGC 3227	2	−0.88	−0.95	0.79	0.044	37.57	42.98
NGC 3362	2	−0.78	...	0.56	0.122	38.09	43.97
1058+45	2	−1.17	...	1.05	0.063	38.10	43.62
NGC 3516	1	−0.31	−0.49	0.61	0.141	37.64	43.64
Mkn 744	1	−0.76	...	0.77	0.075	37.62	43.21
NGC 4051	1	−1.04	−0.32	0.64	0.183	36.52	42.78
NGC 4151	1	−0.77	−0.81	1.00	0.002	38.02	43.17
NGC 4235	1	−0.41	0.24	0.81	0.124	37.41	43.31
Mkn 766	1	−0.70	−0.76	1.03	−0.014	38.38	43.43
Mkn 231	1	0.07	−0.58	0.97	−0.241	40.63	44.28
NGC 5033	1	−0.83	−0.66	0.32	0.176	37.04	43.25
1335+39	2	...	...	1.20	0.115	37.78	43.62
NGC 5252	2	−0.07	−0.54	0.90	−0.068	38.91	43.62
Mkn 266	2	−0.75	−0.76	0.77	−0.093	39.37	43.94
Mkn 270	2	−0.71	...	0.95	0.029	37.57	42.88
NGC 5273	1	...	...	0.80	0.213	36.28	42.73
Mkn 279	1	−0.92	...	1.01	−0.013	38.81	43.86
NGC 5548	1	−0.89	−0.91	0.76	0.054	38.43	43.90
NGC 5674	2	−0.91	−0.85	0.39	0.089	38.33	44.01
Mkn 817	1	−0.53	...	1.15	0.015	38.74	43.97
Mkn 686	2	−0.55	...	0.60	0.130	37.38	43.31
Mkn 841	1	...	...	0.60	0.065	38.68	44.22
NGC 5929	2	−0.72	−0.76	0.50	−0.053	38.13	42.93
NGC 5940	1	−0.57	...	0.55	0.081	38.40	44.04
1614+35	1	−0.99	...	0.51	0.129	38.02	43.95
2237+07	1	−0.94	−0.54	1.05	0.033	38.43	43.77
NGC 7469	1	−0.72	−0.83	0.93	−0.076	39.20	43.86
Mkn 530	1	−0.74	−0.73	0.98	−0.037	38.96	43.86
Mkn 533	2	−0.89	−1.07	0.89	−0.110	39.72	44.18
NGC 7682	2	−0.78	−1.02	1.02	−0.085	38.82	43.44

TABLE 3

SEYFERT GALAXY RADIO LUMINOSITY FUNCTION

	Type 1		Type 2		Both Types	
$\log(L_{rad})$ erg/s	$\log(\Phi)$ $\mathrm{Gpc^{-3}mag^{-1}}$	N	$\log(\Phi)$ $\mathrm{Gpc^{-3}mag^{-1}}$	N	$\log(\Phi)$ $\mathrm{Gpc^{-3}mag^{-1}}$	N
36.6–37.0	< 3.87		< 3.90		< 3.89	
37.0–37.4	3.73	1	3.71	1	4.04	2
37.0–37.4	4.10	4	4.63	4	4.75	8
37.0–37.4	3.88	2	4.32	3	4.46	5
37.0–37.4	3.78	7	4.04	4	4.24	11
37.0–37.4	3.30	5	3.83	3	3.94	8
37.0–37.4	2.81	1	3.30	3	3.43	4

REFERENCES

Baars, J. W. H., Genzel, R., Pauliny-Toth, I. K. K., and Witzel, A. 1977, *Astr. Ap.*, **61**, 99.

de Bruyn, A. G., and Wilson, A. S. 1976, *Astr. Ap.*, **53**, 93.

de Bruyn, A. G., and Wilson, A. S. 1978, *Astr. Ap.*, **64**, 433.

Condon, J. J., Condon, M. A., Jauncey, D. L., Smith, M. G., Turtle, A. J., and Wright, A. E. 1981a, *Ap. J.*, **244**, 5.

Condon, J. J., O'Dell, S. L., Puschell, J. J., and Stein, W. A. 1981b, *Ap. J.*, **246**, 624.

Dahari, O. 1985, *A.J.*, **90**, 1772.

Edelson, R. A., and Malkan, M. A. *Ap. J.*, **308**, 59.

Edelson, R. A., Malkan, M. A. , and Rieke, G. *Ap. J.*, in press.

Geller, M., and Huchra, J. 1983, *Ap. J.Supp.*, **52**, 61.

Huchra, J, and Berg, R. 1986, *Ap. J.*, in press.

Huchra, J., Davis, M., Latham, D., and Tonry, J. 1983, *Ap. J. (Supp.)*, **52**, 89.

Huchra, J. P., Wyatt, W. F., and Davis, M. 1982, *Astron. J.*, **87**, 1628.

Huchra, J., and Sargent, W. L. W. 1973, *Ap. J.*, **186**, 433.

Hummel, E. 1981, *Astron. Ap.*, **93**, 93.

Kellerman, K. I. 1985, priv. comm.

Kühr, H., Witzel, A., Pauliny-Toth, I. I. K., and Nauber, U. 1981, *Astron. Ap.*, **45**, 367.

Ledden, J. E., Broderick, J. J., Condon, J. J., and Brown, R. L. 1980, *Astron. J.*, **85**, 780.

Moore, C. R. and Clauss, R. C. 1979, *IEEE Trans. MTT*, **27**, 249.

Meurs, E. J. A. and Wilson, A. S. 1981, *Astron. Ap. Supp.*, **45**, 99.

Meurs, E. J. A. and Wilson, A. S. 1984, *Astron. Ap.*, **136**, 204.

Osterbrock, D. E. 1984, *Q.J.R.A.S.*, **25**, 1.

Rieke, G. H. 1978, *Ap. J.*, **226**, 550.

Schaffer, D., Schmidt, M., and Green, R. F. 1983, IAU Symposium 97, Extragalactic Radio Sources, ed. D. S. Heeschen and C. M. Wade (Dordrecht:Reidel), p.367.

Schmidt, M., and Green, R. F. 1983, *Ap. J.*, **269**, 352.

Siegel, S. 1956, Nonparametric Statistics for the Behavioral Sciences (McGraw-Hill).

Sramek, R. and Tovmassian 1975, *Ap. J.*, **196**, 339.

Ulvestad, J. S., and Wilson, A. S. 1984a, *Ap. J.*, **278**, 544.

Ulvestad, J. S., and Wilson, A. S. 1984b, *Ap. J.*, **285**, 439.

Wilson, A. S. and Meurs, E. J. A. 1982, *Astron. Ap. Supp.*, **50**, 217.

FIGURE CAPTIONS

FIG 1.—Three-point radio spectra (S_ν vs. ν) of the 24 sources detected at all three radio frequencies. The Seyfert 1 galaxies are on the left and the Seyfert 2 galaxies are on the right. The two points at 6 cm are the high-resolution data (6 cm,h, open circles) and low-resolution data (6 cm,l, filled circles). The 6 cm,h points have been shifted slightly in frequency to prevent overlap with the 6 cm,l points.

FIG 2.—Histogram of α_{6-20cm} for the 38 sources detected at both 6 and 20 cm. The top panel contains the data for Seyfert 1 galaxies, and the bottom, for Seyfert 2 galaxies.

FIG 3.—Plot of α_{6-20cm} vs. $\alpha_{1.5-6cm}$ for the 24 sources detected at all three frequencies. The Seyfert 1 galaxies are denoted by triangles, and the Seyfert 2 galaxies, by circles. A source with $\alpha_{6-20cm} = \alpha_{1.5-6cm}$ would lie on the dashed line. Sources with $\alpha_{6-20cm} < \alpha_{1.5-6cm}$ (i.e., which flatten toward higher frequency) lie below this line. Errors associated with these spectral indices are generally about 0.07, which is slightly larger than the symbols.

FIG 4.—Histogram of R, a measure of the degree of resolution of the 6 cm radio source for the 41 sources detected with both 6 cm,h and 6 cm,l beams. The top panel contains the data for Seyfert 1 galaxies and the bottom, for Seyfert 2 galaxies.

FIG 5.—Plot of radio luminosity (L_{rad}) as a function of optical luminosity (L_{opt}). Seyfert 1 galaxies are denoted by triangles, and Seyfert 2 galaxies, by circles. The dashed line is a proper least squares power law fit for Seyfert 1 galaxies and the dotted line for Seyfert 2 galaxies.

FIG 6.—Histogram of α_{O-R} for all 42 sources observed. The top panel contains the data for Seyfert 1 galaxies and the bottom for Seyfert 2 galaxies. Mkn 231 is the Seyfert 1 with a low value of α_{O-R}.

FIG 7.—The RLF of Seyfert galaxies. Space density is plotted as a function of L_{rad}. Figure 7a is the RLF of Seyfert 1 galaxies, Figure 7b is that of Seyfert 2 galaxies, and Figure 7c is the RLF of all Seyfert galaxies. Error bars are 1σ statistical errors. Crosses represent the RLF of Meurs and Wilson (1984).

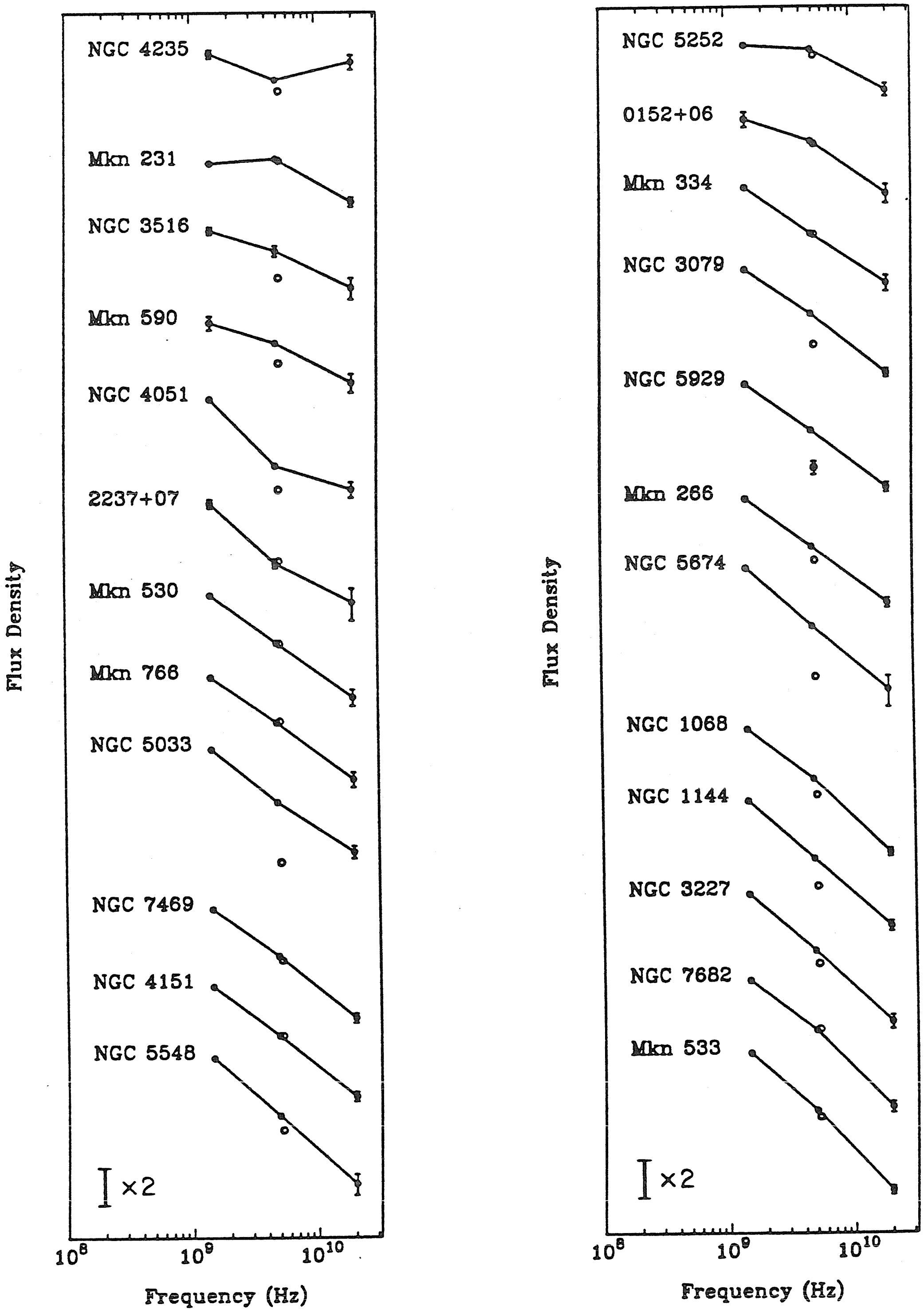
NGC 4235
Mkn 231
NGC 3516
Mkn 590
NGC 4051
2237+07
Mkn 530
Mkn 766
NGC 5033
NGC 7469
NGC 4151
NGC 5548
×2
Flux Density
10^8
10^9
10^{10}
Frequency (Hz)
NGC 5252
0152+06
Mkn 334
NGC 3079
NGC 5929
Mkn 266
NGC 5674
NGC 1068
NGC 1144
NGC 3227
NGC 7682
Mkn 533
×2
Flux Density
10^8
10^9
10^{10}
Frequency (Hz)

Figure 1

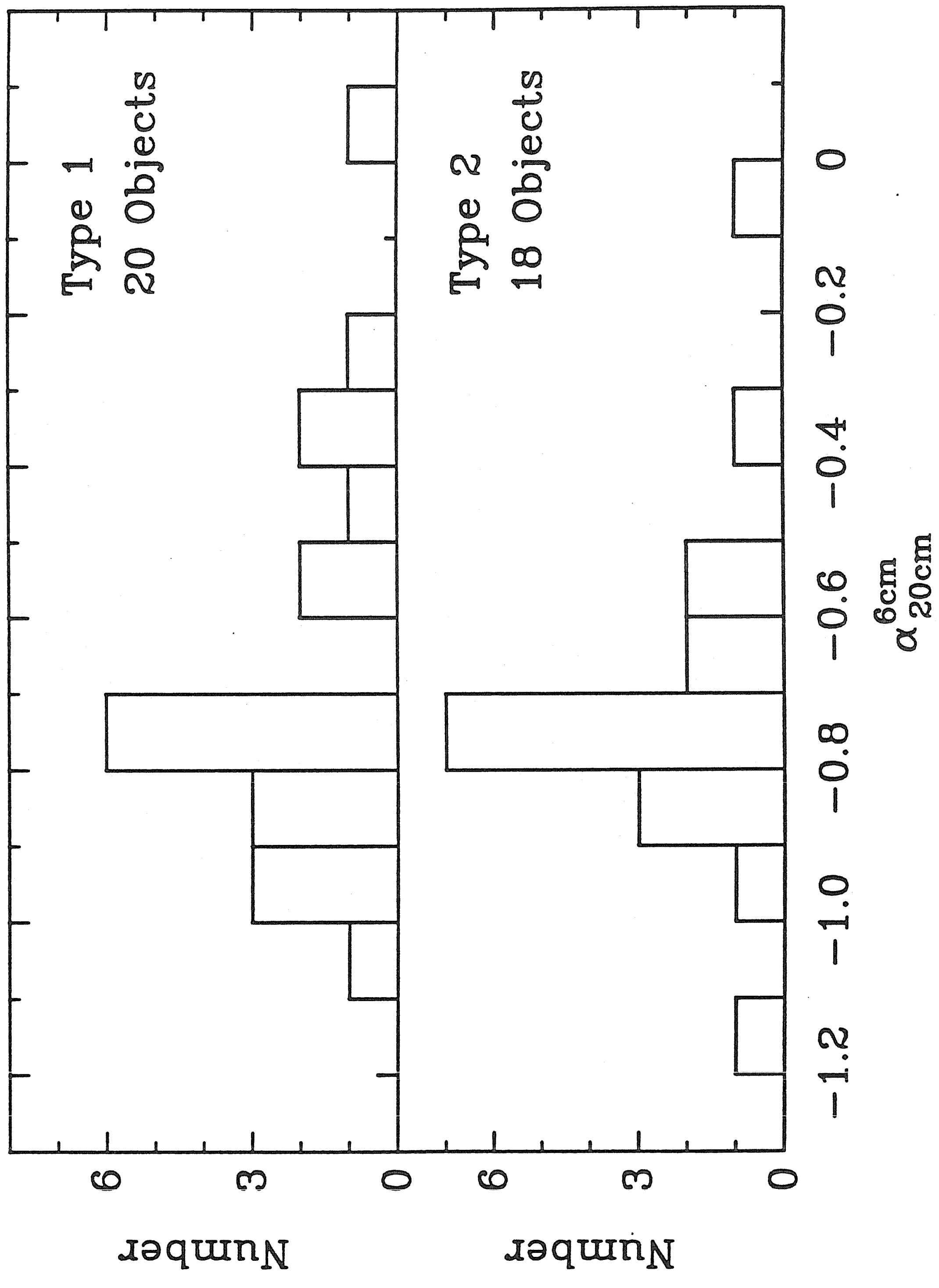
Type 1
20 Objects
Type 2
18 Objects
Number
Number
0
3
6
0
3
6
−1.2
−1.0
−0.8
−0.6
−0.4
−0.2
0
α^{6cm}_{20cm}

Figure 2

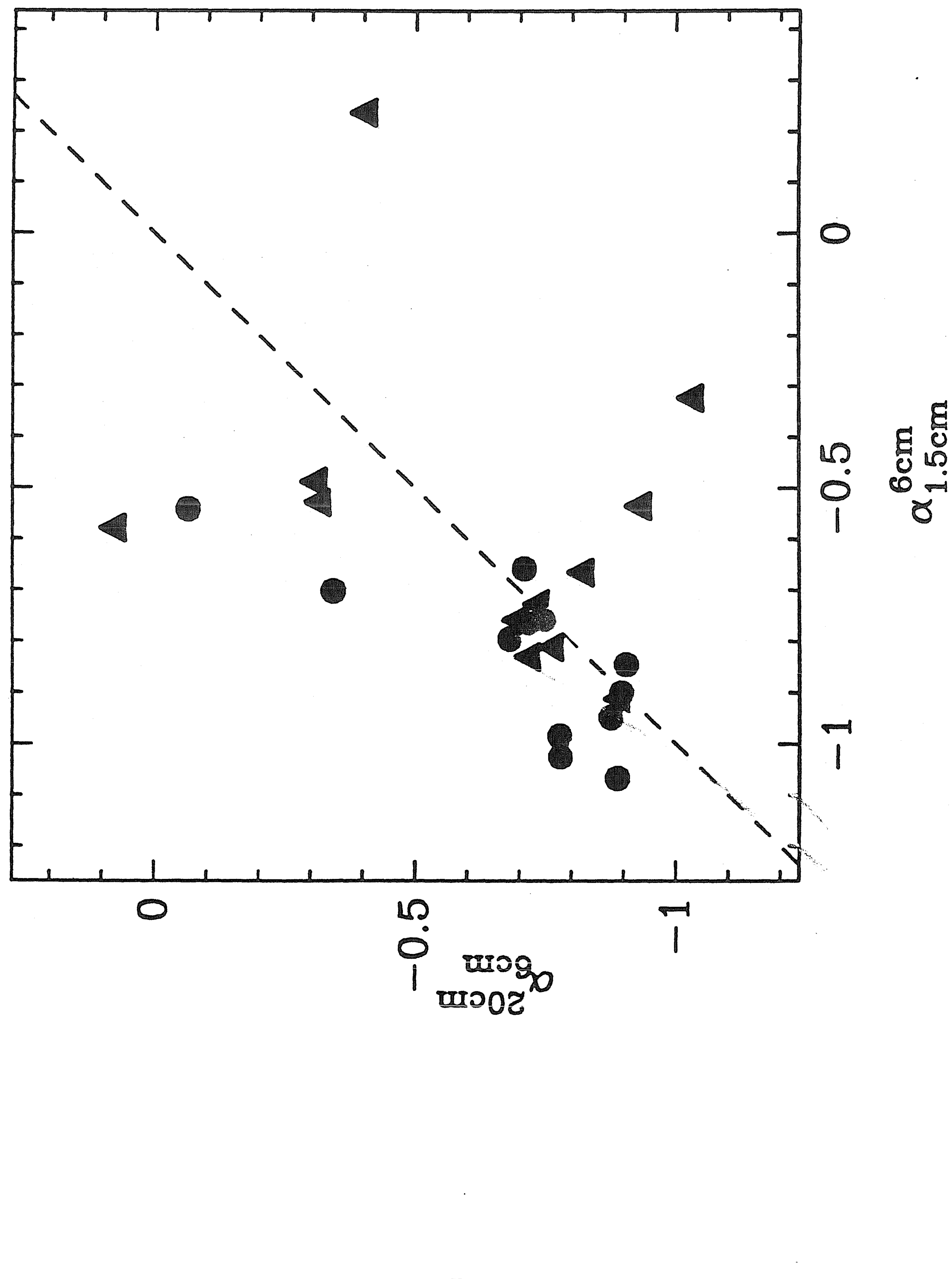

Figure 3

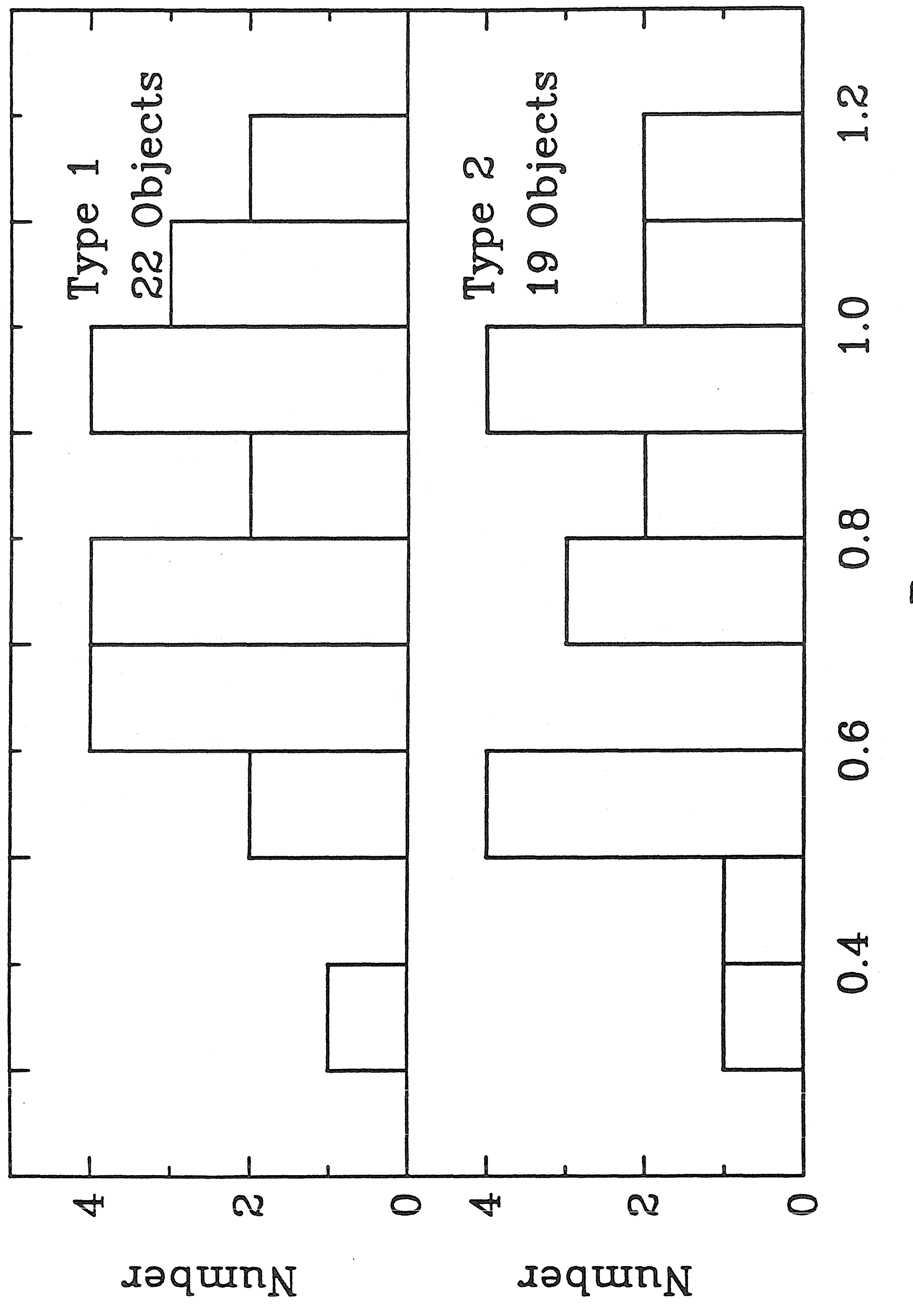
Type 1
22 Objects
Type 2
19 Objects
Number
Number
0
2
4
0
2
4
0.4
0.6
0.8
1.0
1.2
R

Figure 4

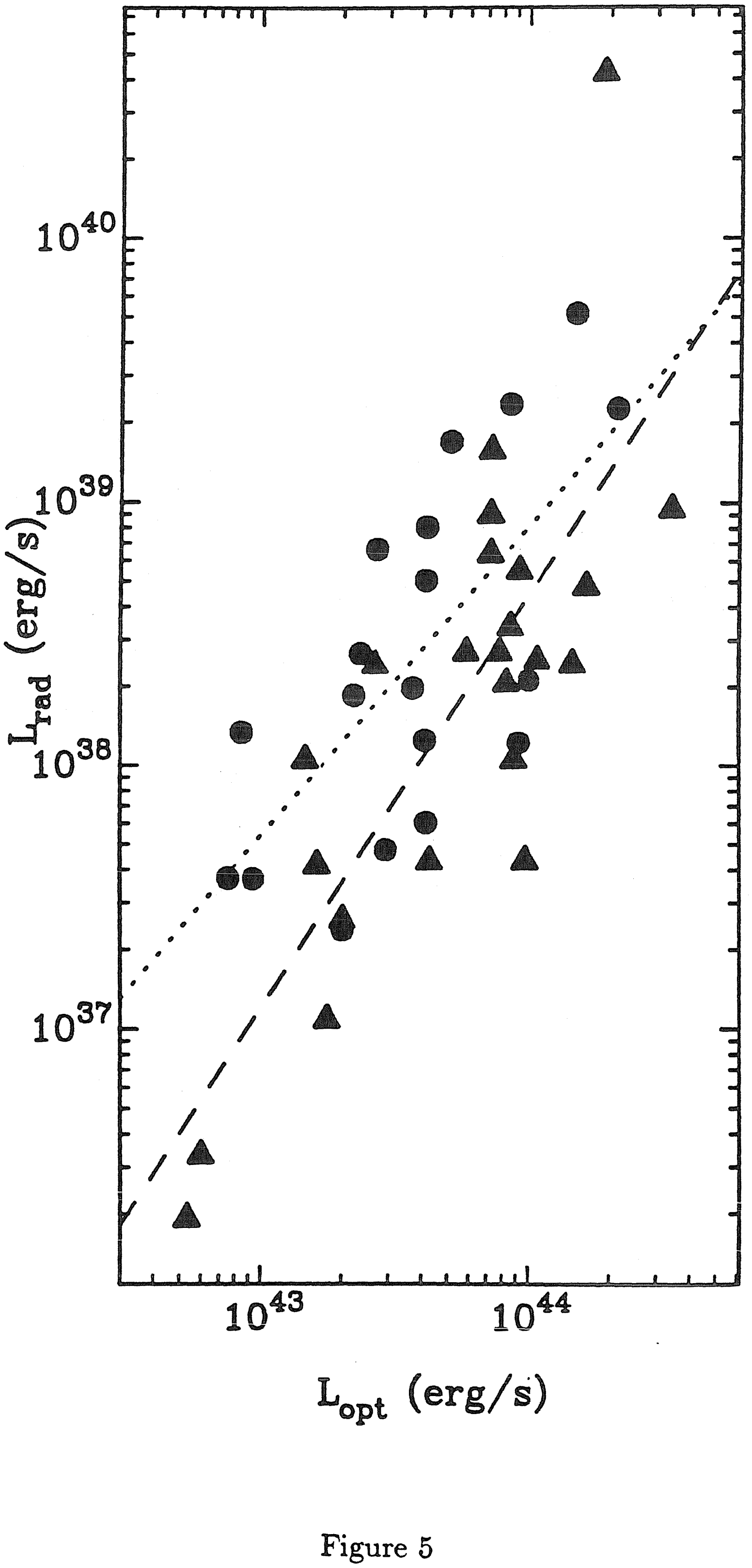

Figure 5

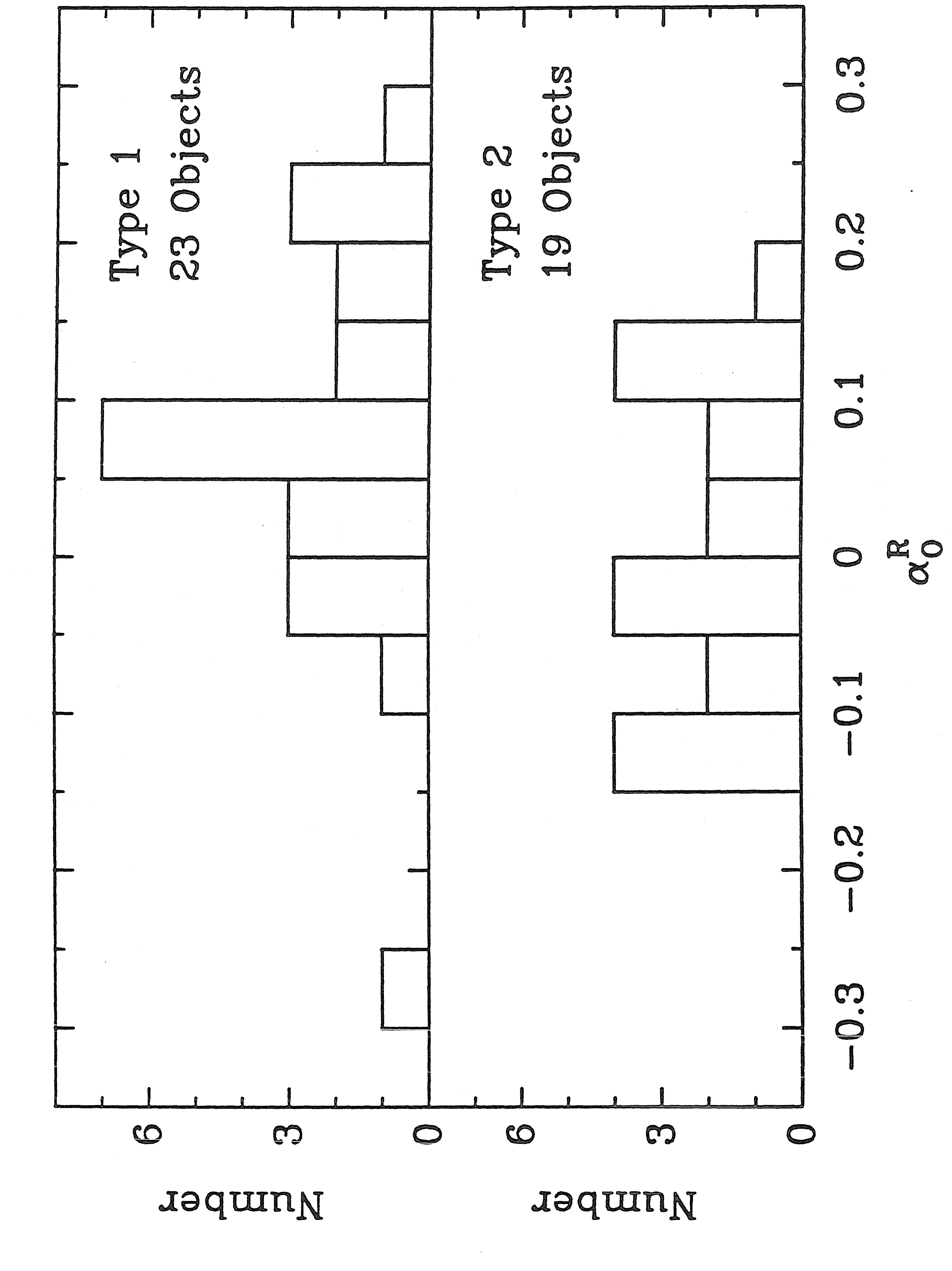
Type 1
23 Objects
Type 2
19 Objects
Number
Number
0
3
6
0
3
6
−0.3
−0.2
−0.1
0
0.1
0.2
0.3
α_0^R

Figure 6

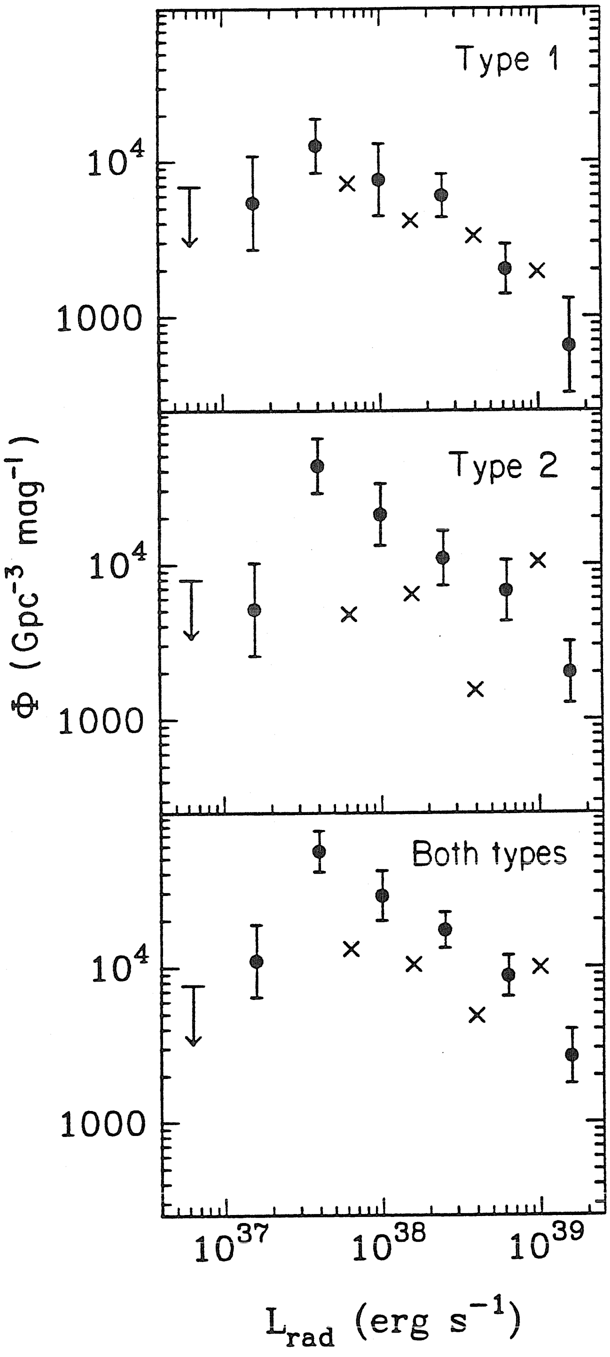
Type 1
Type 2
Both types
10^4
1000
Φ (Gpc^-3 mag^-1)
10^37
10^38
10^39
L_rad (erg s^-1)

Figure 7

Chapter Five

BROADBAND PROPERTIES OF THE CFA SEYFERT GALAXIES: II. INFRARED-MILLIMETER PROPERTIES *

Submitted to *The Astrophysical Journal*

---

* Written in collaboration with M. Malkan and G. Rieke

ABSTRACT

Observations between 1.2 μm and 1.3 mm are presented for an unbiased, spectroscopically selected sample of 48 Seyfert galaxies. Most objects have complete near and far-infrared detections, but none were detected at 1.3 mm. The infrared spectra of optically selected Seyfert 2 galaxies are steep ($\overline{\alpha}_{2.2-25\mu m} = -1.56$), in sharp contrast to optically selected quasars, which have flat infrared spectra ($\overline{\alpha}_{2.2-25\mu m} = -1.09$). This suggests that the infrared emission is predominantly thermal in Seyfert 2 galaxies and nonthermal in quasars. For optically selected Seyfert 1 galaxies, $\overline{\alpha}_{2.2-25\mu m} = -1.15$, and 70% have flat infrared spectra similar to the quasars and unlike the Seyfert 2 galaxies. Thus, the infrared emission from most Seyfert 1 galaxies appears to be dominated by nonthermal radiation, although thermal dust radiation is clearly important for some others.

Half of the objects detected at three or more IRAS wavelengths have far-infrared spectra which turn over shortward of 100 μm. In many of the others, emission from cold dust in the galactic disk appears to mask the turnover. For the Seyfert 2 galaxies and other dusty objects, this implies minimum dust temperatures of 35–65 K, significantly warmer than dust in normal galaxies. For the relatively dust-free Seyfert 1 galaxies, this implies that the infrared emission is dominated by unreprocessed radiation from a synchrotron self-absorbed source of order a light day in size, about the same size as the hypothesized accretion disks.

The radio and optical luminosities of Seyfert 1 and Seyfert 2 galaxies are strongly correlated with infrared luminosity. There are of order 10^5 Seyfert galaxies/Gpc^3 with L_{ir} between $10^{42.2}$ and $10^{45.0}$ ergs/s. The infrared luminosity functions of Seyfert 1 and 2 galaxies are similar. It appears that Seyfert nuclei tend to occur in relatively luminous host galaxies.

I. INTRODUCTION

Although Seyfert galaxies have been studied extensively at near-infrared wavelengths ($\lambda \leq 10\ \mu$m; c.f. Rieke 1978, hereafter referred to as R78), *the Infrared Astronomy Satellite* (IRAS) all-sky survey at 12, 25, 60, and 100 μm only recently provided the first far-infrared detections of a significant number of active galactic nuclei (AGNs). Edelson and Malkan (1986, hereafter referred to as EM) used IRAS, IUE and ground-based data to study the spectral energy distributions of a heterogeneous sample of 29 AGNs between 0.1 and 100 μm. Miley, Neugebauer, and Soifer (1985) reported the far-infrared colors of 120 active galaxies. Neugebauer *et al.* (1986) reported IRAS observations of 179 quasars (of which, 74 were detected in at least one IRAS wavelength), and Edelson (1986, hereafter referred to as E86) analyzed IRAS observations of the brightest PG/BQS quasars.

Virtually every known Seyfert galaxy emits a large fraction of its total energy at infrared wavelengths. In some cases, this is the result of the presence of dust in or around the nucleus. The dust can absorb and thermally re-radiate a significant portion of the emission from the central source (Rieke and Lebofsky 1979). The thermal emission produces a very steep infrared spectrum which curves downward at shorter wavelengths, due to the Wein cutoff below the peak wavelength of emission from the hottest surviving dust grains. Thermal far-infrared emission is also frequently associated with dust reddening of the nuclear emission lines and nonstellar continuum. EM found correlations between steepness of the infrared spectra and internal reddening and other dust indicators.

However, some active galactic nuclei produce their infrared continua by nonthermal processes. In the case of violently variable quasars and BL Lacertae objects, the rapid variability in the infrared and high polarization conclusively demonstrate this (Angel and Stockman 1980). In quasars and bright, unreddened Seyfert 1 nuclei, the case for nonthermal infrared (and optical) emission is less direct, since the continuum is neither highly polarized nor violently variable. The strongest indication is the relatively flat shape of the far-infrared-to-optical continuum, which is well-described by a power law with $\alpha \gtrsim -1.3$ ($F_\nu \propto \nu^\alpha$, EM). Optically selected quasars have very flat infrared spectra ($\overline{\alpha}_{2.2-25\mu m} = -1.09$), which E86 identified as predominately nonthermal emission. The strong correlation found between the 3.5 μm and 2 keV X-ray flux of quasars and Seyfert 1 galaxies (but not Seyfert 2 galaxies) suggests that the same process is responsible for emission at both wavelengths, implying that the lower frequency emission from these objects is nonthermal in origin (Malkan 1984).

In this paper, the infrared properties of a complete, unbiased sample of Seyfert galaxies are studied to determine the importance of different emission mechanisms. Previous AGN studies have been biased by the selection techniques used to construct their samples. For example, selection by ultraviolet-excess (such as that used by Markarian 1972 and Schmidt and Green 1982) has been shown to bias samples against strong infrared emitters (R78). This problem was avoided by examining the infrared-to-millimeter spectral energy distributions of the CfA Seyfert galaxies, a well-defined, unbiased, spectroscopically selected sample, to deduce the properties of the class as a whole. The CfA sample contains 26 Type 1 and 22 Type 2 Seyfert galaxies selected by optical spectroscopy (Huchra and Berg 1987). The selection of the sample is discussed in detail in Edelson (1987, hereafter referred to as Paper I) which also described their radio properties. (One object, NGC 3227, was incorrectly classified as a Seyfert 2 galaxy in Paper I.)

The near-infrared, IRAS, and millimeter-wave data are discussed in the next section. The infrared spectral energy distributions are discussed in § III, and the far-infrared turnover and the relation between far-infrared and millimeter emission are discussed in § IV. The relationship between infrared properties and those derived at other wavelengths are investigated in § V, and the 60 μm infrared luminosity function of Seyfert galaxies is derived and discussed in § VI. A summary of the major results of this paper is given in § VII.

Throughout this paper, a value of $H_0 = 75$ km/s/Mpc is assumed. As the largest redshift in this sample is $z = 0.06$, no corrections were made for cosmological effects in the luminosity distance or for evolution.

II. DATA

a) Near-Infrared Data

Near-infrared photometry was obtained with standard single-element InSb detectors on the Steward Observatory Catalina 61-inch reflector, and with an InSb array on the Steward Observatory Kitt Peak 90-inch reflector. The usual photometric bands, J [1.2 μm], H [1.6 μm], and K [2.2 μm] were used, with absolute flux calibrations from Campins, Rieke and Lebofsky (1985). Complete near-infrared (1.2–2.2 μm) photometry was obtained for 44 of the Seyfert galaxies (95%). Measurements were also made at L [3.5 μm] or L$'$ [3.6 μm] of objects which were sufficiently bright. The near-infrared database was supplemented with published measurements from the literature (R78, Rudy, LeVan and Rodriguez-Espinoza 1982, Cruz-Gonzales and Huchra 1984). Ground-based measurements of 20 objects at N [10.6 μm] were taken from the literature (R78; Deveraux, Becklin, and Scoville 1986), except for those listed at the end of Table 1. A total of 28 (58%) galaxies have 3.5 μm measurements while 24 (50%) have 10.6 μm measurements.

TABLE 1

Table 1 gives the new near-infrared data for the CfA Seyfert galaxies. Source names are presented in Column 1. Flux densities and uncertainties for the J, H, and K measurements are presented in Columns 2–4, respectively. The L and N measurements are included as footnotes to Table 1. Column 5 contains the date of observations. The magnitudes listed in Table 1 refer to 9″ apertures for the 61-inch measurements, and 10″ apertures for the 90-inch images. Thus the fluxes refer primarily to the nucleus. In the less luminous Seyfert galaxies, these fluxes also include a substantial contribution from starlight, and there was often significant galactic light outside the aperture. Several repeated observations agreed to within about 10%.

b) IRAS Data

Forty-six of the 48 CfA Seyfert galaxies were observed at least once by IRAS. Two objects (NGC 3362 and Mkn 744) lay in the ~2% of the sky which IRAS did not observe. One of the 46 objects observed (NGC 7682) lay within 4′ of a 10 Jy source, and could not be detected due to strong confusion. All of the remaining 45 objects were detected with IRAS, and 32 of the 46 objects observed (70%) were detected in all four IRAS wavelengths.

Far-infrared fluxes from IRAS are presented in Table 2. The source names are given in the first column. The flux densities and errors at 12, 25, 60, and 100 μm, or 3σ upper limits, are tabulated in Columns 2–5. For objects brighter than 0.5 Jy at 12 μm, photometry was taken from the IRAS point source catalogue (Beichman *et al.* 1984). Since the IRAS point source catalog fluxes ignored all observations in which a source was not detected, objects with low signal-to-noise ratios tend to appear brighter than they actually are. For this reason, all IRAS fluxes for objects fainter than 0.5 Jy at 12 μm were determined from source extractions performed on coadded survey data. No spectral corrections to the IRAS data were necessary, because these objects had power law slopes near $\alpha = -1$. The overall calibration uncertainty is estimated to be 10% at 12, 25, and 60 μm and 15% at 100 μm.

TABLE 2

The infrared fluxes of three objects are confused. Mkn 279 appears extended in the IRAS beam because it is only 41″ from a nearby spiral companion. Mkn 266 is actually a close binary galaxy (separation 9″). One of the galaxies has a Seyfert 2 nucleus, while the companion has a low ionization emission line spectrum (Fricke and Kollatschny 1984). NGC 5929 is only 90″ from NGC 5930, which appears to emit most of the IRAS flux observed from this interacting system. These objects are excluded from further analysis.

c) *Millimeter Data*

The CfA Seyfert galaxies were observed at 1.3 mm with the NRAO-Kitt Peak 12-m telescope on 9-16 June 1984. The QMC-Oregon 0.3 K millimeter bolometer was used with a typical system temperature of ~325 K on the sky (double sideband). The aperture efficiency was about 15%, giving an effective noise equivalent flux density of ~5 Jy $\sec^{\frac{1}{2}}$. The telescope had a 30″ beamwidth and the pointing was accurate to ~10″. Most sources were observed for integration times of about 15 minutes, yielding typical 1σ errors of ~200 mJy. The actual errors were a strong function of the integration time, the time of day an object was observed, and the amount of precipitable water vapor along the line of sight. No sources were detected at 1.3 mm. The 3σ upper limits are listed in Column 6 of Table 2.

III. INFRARED SPECTRA

a) *Introduction*

Figure 1 contains νF_ν plots for the CfA Seyfert galaxies. A wide variety of spectral shapes and features are seen in Figure 1. The overall spectral energy distributions range from very steep ($\alpha \lesssim -2$, as in Mkn 533 and NGC 1068), to flat ($\alpha \gtrsim -0.7$, as in Mkn 335 and Mkn 590). The spectra of many of the less luminous AGNs have a bump in the near-infrared due to starlight which peaks near

~1.5 μm. A far-infrared low-frequency turnover is detectable in about half of the infrared spectra.

FIGURE 1

FIGURE 1

To quantify the following discussion of spectral shapes, spectral indices have been calculated and tabulated in Table 3. Column 1 contains the source name, and the spectral indices $\alpha_{2.2-25\mu m}$, $\alpha_{12-60\mu m}$, $\alpha_{25-60\mu m}$, $\alpha_{60-100\mu m}$, and $\alpha_{100-1300\mu m}$ are presented in Columns 2–6, respectively.

TABLE 3

Table 4 contains parameters derived for these objects. Column 1 contains the source name, and Column 2, the Seyfert galaxy type, taken from Huchra (1987). Intermediate types (i.e., Seyfert 1.5 galaxies) are classified as Type 1. Using slit spectroscopy of the inner 10″ (Edelson and Wahl 1987), sources with strong ultraviolet excesses are denoted with a "B" in Column 3, while those with weak excesses have an "R". The compactness parameter, R, a measure of the degree of resolution at ~11 μm, is presented in Column 4 (see §IIIc). Sources with R more than 3σ below unity are labeled with a "E" in Column 5, while those with R greater than this value are labeled with a "C". On the basis of the spectral indices $\alpha_{2.2-25\mu m}$ and $\alpha_{12-60\mu m}$, the infrared spectra are classified with a "Q" (quasar-like or flat) or "D" (dusty or steep) in Column 6 (see §IIIc). Estimates of the 2.2 μm flux due to nuclear nonstellar emission are presented in Column 7 (see §IIIb). On the basis of Dahari's (1985) observations, interacting objects have an "I" in Column 8, while those with no companions have an "N" (see § Vb).

TABLE 4

As discussed in EM, the major features of the observed 1.2 μm–1.3 mm spectral energy distributions of Seyfert galaxies can be explained as a mixture of four components: 1) Starlight, which is only important shortward of 3.5 μm; 2) Far-infrared emission from cold dust in the disk of the underlying galaxy; 3) Emission from warm dust; and 4) A relatively flat nonthermal power law component with a sharp long-wavelength cutoff near 80 μm. A fifth component, a broad bump centered near 5 μm, is clearly detectable in some spectra, as discussed by EM. However, the lack of uniform coverage between 3.5 and 10 μm prevents a systematic study of this feature with these data.

b) Starlight

Starlight makes a substantial contribution to the near-infrared spectra of many objects. Continuum emission from galactic stellar populations peak near 1.5 μm and has a roughly Rayleigh-Jeans fall-off to longer wavelengths. Detailed multi-aperture measurements can be used to seperate the extended stellar and compact nuclear source components, but such data are available for only a few objects in this sample (Malkan and Filippenko 1984, McAlary and Rieke 1986). Therefore, alternate methods had to be used to estimate the contribution of starlight to the spectra in these objects. These data give little meaningful information about the stellar population itself. Instead, the goal is to remove its contribution so far as possible to obtain a better estimate of the spectrum of the nuclear source.

The starlight-corrected nuclear flux was estimated at 2.2 μm because there is virtually complete JHK data on the sample and the ratio of nuclear to stellar flux is expected to be largest at K for these data. These estimates are listed in Table 4. For the galaxies where JHKL data were available, a least squares fit was performed using an unreddened stellar spectrum with normal colors (i.e., J–H=0.7, H–K=0.2, and K–L=0.2) and a power law with a spectral index that was allowed to vary to optimize the fit. These estimates are indicated by an "a" in Table 4. Comparison with the uncorrected K fluxes in Table 1 shows that starlight corrections can be important in many of these objects. Where only JHK data were available and the spectrum rose from H to K, it was assumed that all the detected flux might arise from the nuclear source and assigned an upper limit equal to the flux at K. These estimates are indicated by a "b" in Table 4. Where the spectrum peaks at H or is level between H and K, a least squares fit was performed with the stellar spectrum and a power law with spectral index $\alpha = -1$. If the derived nuclear flux was less than 20% of the total at K, an upper limit of 20% of the K flux was assigned. These estimates are indicated by a "c". Although our methods are not expected to be very accurate, the results are generally in rough agreement with those found by Malkan and Filippenko (1984) and McAlary and Rieke (1986).

The importance of starlight can also be seen in the correlation between nuclear (12 μm) luminosity and $\alpha_{1.1-2.2\mu m}$. The non-parametric Spearman rank correlation test (Siegel 1956) shows that there is a negative correlation between $L_{12\mu m}$ and $\alpha_{1.1-2.2\mu m}$ at the 98% confidence level. As expected, an increasinigly dominant nucleus raises the 12 μm luminosity and makes the J–K color redder.

c) Extended Infrared Emission

Thermal emission from cool dust in the galactic disk is present to some degree in the infrared spectra of all normal spiral galaxies and can confuse the determination of the infrared spectrum of the active nucleus. This thermal emission from dust heated by starlight can, in principle, be separated from nuclear emission by its much greater spatial extent. For example, seven of the 38 sources in the IRAS point source catalog (18%) showed resolved structure on angular scales of $\gtrsim 20''$ at 12 μm.

In more distant galaxies, the galactic emission may be unresolved by IRAS, but can be identified by comparing the IRAS 12 μm measurements with ground-based 10.6 μm measurements made with small beams (typically $6''$ in diameter). This comparison is simplified by the fact that Seyfert galaxies usually have little spectral structure at 10.6 μm (Aitken and Roche 1984). We define the ratio of ground-based to IRAS flux as R, the "compactness parameter"; it is listed in Table 4 for the 18 galaxies in the sample which have the requisite measurements and do not appear to suffer confusion with nearby objects. The uncertainty in R has been estimated by combining the errors in the ground-based and IRAS photometry.

Two corrections must be applied to the measurements in computing R. First, the color corrections in the ground-based and IRAS photometry must be reconciled. The ground-based calibration gives equivalent monochromatic fluxes for stellar (Rayleigh-Jeans — ν^2) spectra at the effective wavelength of 10.6 μm (Rieke, Lebofsky, and Low 1984). No color corrections have been applied to the published Seyfert galaxy measurements nor to the new ones reported here. The IRAS system assumes color corrections appropriate to a ν^{-1} power law spectrum. To correct the ground-based 10.6 μm measurements to the same source spectrum, they must be multiplied by 1.22. This correction is a weak function of the spectral index near $\alpha = -1$. The second correction allows for the differing effective wavelengths of the IRAS and ground-based photometric bands. This correction was determined by fitting a power law to the IRAS 12 and 25 μm measurements and using it to extrapolate the 12 μm measurements to 10.6 μm.

Sources with R less than unity by at least 3σ are considered to be extended, and the remaining objects are defined as compact. These designations are indicated in Table 4 with an "E" and a "C", respectively. Not surprisingly, all the sources that are seen to be extended in the IRAS scans are also found to be extended with this test. Four sources had classifications at low signal-to-noise: Mkn 841 and 2237+07 were classified as compact, and NGC 7469 and Mkn 530 were classified as extended.

The classifications of these objects are not as reliable as the others.

The compactness parameter is a useful indicator of the presence of extended thermal emission from dust warmed by starlight in the galactic disk. Seyfert 1 galaxies with relatively luminous nuclei appear more compact in the infrared. Figure 2 shows the correlation of 12 μm luminosity with R. The Spearman rank correlation test shows that the extended sources are less luminous, at the 97% level of significance. Less compact sources also have significantly bluer H–K colors, at the 95% confidence level. Both results are easily understood as the increasing importance of galactic (extended) infrared emission in Seyfert galaxies with less luminous nuclei. Not surprisingly, the extended infrared emission is most common in those galaxies with the lowest redshifts in this magnitude-limited sample. Since these Seyfert galaxies have been more extensively observed at 10.6 μm, the frequency of strong extended infrared emission for a complete, unbiased sample of objects cannot be determined.

FIGURE 2

A grey dust grain will reach a temperature of 300 K and hence emit strongly at 10 μm at a distance of roughly 2 pc from a 4x10^{44} erg/s (10^{11} $L_\odot$) energy source. At the distance of the galaxies in this sample, 2 pc typically corresponds to $0\overset{''}{.}01$. Grains with realistic wavelength-dependant emissivity will reach 300 K significantly further from the energy source, but an unusual wavelength dependence would be required to account for the emission in the "E" galaxies farther than $3''$ (i.e., $\gtrsim$600 pc) from the nucleus. This suggests that the "E" galaxies have an extended source of luminosity in addition to the active Seyfert nucleus.

The correlation of $\alpha_{12-60\mu m}$ with compactness parameter, significant at the 99% confidence level, is shown in Figure 2. The far-infrared slopes observed in normal galaxies with high rates of current star formation tend to be steeper than those of active galactic nuclei (Miley, Neugebauer, and Soifer 1985). Much of this energy is generated in the disk of the galaxy (Persson and Helou 1986), so it would account easily for the correlation of extended emission with infrared spectral index. It is suspected that many of the "D" galaxies without direct measurements of extent also generate a significant portion of their infrared emission through star formation in the disks. Conversely, it is expected that far-infrared measurements with better spatial resolution would show that many of the CfA Seyfert galaxies with "D" spectra actually have flatter nuclear spectra that more closely resemble quasars.

c) *Nuclear Infrared Emission*

While both of the remaining components, thermal dust emission and nonthermal emission from the nucleus, are generally unresolved even with the small beams used in the near-infrared, they have very different spectral shapes. Nonthermal emission tends to produce flat, smooth spectra. The signature of warm dust is a steep, curved spectrum which can peak near 80 μm. EM found that objects with large internal reddenings and other dust indicators usually had steep infrared spectra ($\alpha \approx -2$), which are not well-fitted by a simple power law. As can be seen in Figure 1, Seyfert 1 galaxies tend to have flat, power law spectra, while Seyfert 2 galaxies usually have steeper, curved spectra. Only one Seyfert 2 galaxy (Mkn 461, which has a 3.1σ detection at 25 μm) appears to have a flat infrared spectrum.

This difference can also be seen in a color-color diagram. Figure 3 is a plot of $\alpha_{2.2-25\mu m}$ vs $\alpha_{12-60\mu m}$. Seyfert 1 galaxies are denoted by triangles, Seyfert 2 galaxies by circles, and bright PG quasars (taken from E86) by stars. An object which lies on the dotted line has $\alpha_{2.2-25\mu m} = \alpha_{12-60\mu m}$. For bright, optically selected quasars, E86 found that $\overline{\alpha}_{2.2-25\mu m} = -1.09 \pm 0.16$ (individual scatter), and $\overline{\alpha}_{12-60\mu m} = -0.69 \pm 0.44$. For Seyfert 1 galaxies, $\overline{\alpha}_{2.2-25\mu m} = -1.15 \pm 0.29$ (individual scatter), and $\overline{\alpha}_{12-60\mu m} = -1.08 \pm 0.44$. For the Seyfert 2 galaxies, $\overline{\alpha}_{2.2-25\mu m} = -1.56 \pm 0.34$, and $\overline{\alpha}_{12-60\mu m} = -1.55 \pm 0.36$. The non-parametric

Kolmagorov-Smirnov (K-S) test for differences in the distribution of a single parameter in different types of objects (Siegel 1956) shows that $\alpha_{2.2-25\mu m}$ and $\alpha_{12-60\mu m}$ are distributed differently for Type 1 and 2 Seyfert galaxies at the 99% and 97% level, respectively. Seyfert 2 galaxies tend to have stronger stellar components at 2.2 μm than Seyfert 1 galaxies; after removal of this component, the differences in the distribution of $\alpha_{2.2-25\mu m}$ becomes even stronger.

FIGURE 3

The dashed line in Figure 3 delineates a region with $\alpha_{2.2-25\mu m} \geq -1.37$ and $\alpha_{12-60\mu m} \geq -1.25$, which completely segregates Seyfert 2 galaxies from quasars. All of the optically selected quasars have $\alpha_{2.2-25\mu m} \geq -1.37$ and $\alpha_{12-60\mu m} \geq -1.25$, unlike any of the Seyfert 2 galaxies. Any infrared spectrum with $\alpha_{2.2-25\mu m} \geq -1.37$ and $\alpha_{12-60\mu m} \geq -1.25$ is designated as "quasar-like", and is denoted by a "Q"' in Table 4 and Figure 3. Any spectrum with either index steeper than these boundary values is designated as "dusty," and is denoted by a "D". The four objects which lie in the "quasar-like" region of Figure 3, but have $\alpha_{25-60\mu m} < -1.7$ or $\alpha_{60-100\mu m} < -2.0$ are denoted with a "Q(D)", because the flat quasar-like spectrum is apparently modified by cold dust emission near ~80 μm.

The steep infrared spectra of Seyfert 2 galaxies are produced by the superposition of thermal emission from dust grains at a range of temperatures (EM). The high-frequency Wien cut off causes the spectrum to curve downward steeply from the mid to near-infrared.

Seventy per cent of the Seyfert 1 galaxies lie in the upper right "quasar-like" region of Figure 3, indicative of flat power law emission. This clear spectral division from the Seyfert 2 galaxies is good evidence that thermal dust emission dominates the spectra of Seyfert 2 galaxies, while nonthermal radiation is the dominant mechanism for most Seyfert 1 galaxies. Several Seyfert 1 galaxies (e.g. Mkn 231, NGC 7469, etc.) occupy the "dusty" regions, suggesting that the infrared spectra of these objects are dominated by thermal emission.

It is interesting to compare this classification with the observed extent of the Seyfert galaxies at 10.6 μm. Of the 7 "Q" galaxies for which compactness parameters have been measured, none are extended. Of the 10 "D" galaxies with measured compactness parameters, only one (Mkn 231) is extended. Only one "Q(D)" galaxy (Mkn 530) has a measured compactness parameter. It is extended, but at low a signal noise ratio. This strong correlation between detectable source extension and a "D" spectrum suggests that many of the other Seyfert galaxies with "D" spectra are extende infrared sources. Unfortunately, only three remaining objects (Mkn 334, Mkn 766 and NGC 1144) have 12 μm measurements at better than 5:1 signal-to-noise ratios, so direct confirmation of this conclusion will be difficult.

Seyfert galaxies tend to have strong near-infrared excesses compared with normal field galaxies. The average H–K for Seyfert 1 galaxies is 0.68±0.29 (individual scatter), while for Seyfert 2 galaxies, it is 0.52±0.22. By contrast, the average H–K = 0.2±0.1 for field galaxies.

IV. LOW-FREQUENCY TURNOVER

The CfA Seyfert galaxies are generally strong far-infrared sources ($S_{60\mu m} \gtrsim 1$ Jy), with spectral energy distributions which rise from 1 to ~80 μm. However, none were detected above ~500 mJy at 1.3 mm. This means that a dramatic spectral turnover must occur in the far-infrared-submillimeter spectra of these objects. EM studied this turnover in a heterogeneous sample of AGNs, as did E86 for a sample of optically selected quasars. Over half of the objects in those studies were seen to turn over before 100 μm.

In EM, E86, and the present study, the turnover frequency (ν_t) is determined by fitting a parabola in log ν–log F_ν space to the 25, 60, and 100 μm IRAS data, and taking the point at which $\alpha = 0$ as the turnover, provided $\nu_t \geq 3$ THz (100 μm) in the observed frame. EM contains a detailed discussion of this method. The turnover frequency is actually a function of just $\alpha_{25-60\mu m}$ and $\alpha_{60-100\mu m}$. At zero redshift, it is given by the formula

$$\log\nu_t = 12.67 + \frac{1}{2.63 - 1.71(\alpha_{25-60\mu m}/\alpha_{60-100\mu m})}$$

(provided the spectrum is concave downward and $\log\nu_t \geq 12.48$). The turnover frequencies of two objects which were not detected at 100 μm (Mkn 335 and Mkn 841) were measured with higher frequency IRAS data. Table 5 contains the turnover frequencies and other parameters for the 15 unconfused objects with detected turnovers. Source names are given in Column 1, and turnover frequencies (in THz), in Column 2.

TABLE 5

Of the 34 unconfused objects detected at three or more IRAS wavelengths, 15 (44%) had turnovers detected shortward of 100 μm. The other 19 unconfused sources had turnovers which could not be determined because they occurred longward of 100 μm. However, the 1.3 mm limits require that the spectra of these objects cut off in the far-infrared-submillimeter region.

FIGURE 4

Figure 4 is a plot of $\alpha_{25-60\mu m}$ versus $\alpha_{60-100\mu m}$. A source on the dotted line would have $\alpha_{25-60\mu m}=\alpha_{60-100\mu m}$. The turnover frequency is a function of the spectral indices $\alpha_{25-60\mu m}$ and $\alpha_{60-100\mu m}$. Sources with detected turnovers lie in the region above and to the right of the dashed line in Figure 4. Sources which lie significantly below the dotted line have strong excesses near 80 μm, probably due to cold dust emission from the underlying galaxy. For these objects, the far-infrared spectrum of the nucleus may turn over, but it cannot be seen because of emission from the underlying galaxy.

Objects with extended far-infrared emission (i.e., those with an "E" in Column 5 of Table 4) are more likely to have undetected turnovers than compact sources. More luminous active nuclei are more likely to show detectable turnovers, and at higher frequencies: E86 found that 6 of 9 quasars (67%) had $\nu_t \geq 5$ THz, while only 2 of 34 of the CfA Seyfert galaxies (6%) did. This indicates that, especially in low-luminosity AGNs, the turnover can be masked by steep-spectrum emission from cold dust in the underlying galaxy.

There were no trends for turnover frequency to be correlated with Seyfert galaxy type or the shape of the infrared spectrum. Forty-five percent of the Seyfert 1 galaxies had turnovers detected shortward of 100 μm, as did 42% of the Seyfert 2 galaxies. Thirty-eight percent of the objects with "Q" spectra had detected turnovers, as did 50% 18 objects with "D" spectra. There may be a weak correlation between turnover frequency and ultraviolet color. Twelve of the 22 objects with blue ultraviolet colors (55%) had low-frequency turnovers detected, as did 3 of 12 red objects (25%). However, the effect was not significant with the K-S test.

The turnover frequency may be used to determine source parameters, when the mechanism responsible for the infrared continuum is known. If it is nonthermal emission from a synchrotron self-absorbed source (as appears to be the case in most Seyfert 1 galaxies), then it occurs at the frequency at which the source becomes optically thick. EM showed that other explanations of the turnover in low-reddening Seyfert 1s (such as free-free absorption in the broad-line region) are unlikely to be correct.

One more assumption is required to derive source parameters. If the X-ray flux is compton scattered radiation, brightness temperatures (T_B), magnetic fields (B), and source sizes (r_s) can be calculated (E86). These parameters are tabulated in Column 4–6 of Table 5, respectively. The typical inferred brightness temperature $T_B \approx 3\text{x}10^{10}$ K, implies a source size $r_s \approx 3\text{x}10^{15}$ cm, and magnetic fields $B \approx$ 300 Gauss. The Schwarzschild radius can be estimated by assuming that the source is accreting at the Eddington limit. These calculations yield infrared source sizes $r_s \approx 100$ Schwarzschild radii, that is, about the size of the hypothesized accretion disk. The derived brightness temperatures and magnetic fields are also reasonable for the accretion disk region. It is interesting to note that brightness temperatures $T_B \approx 3\text{x}10^{10}$ K are also found in the most compact regions of radio selected sources, using different assumptions (Readhead 1986).

If the infrared continuum is dominated by thermal emission from nuclear dust (as appears to be the case for Seyfert 2 galaxies), the turnover frequency can be used to determine the minimum characteristic dust temperature (T_d), size (r_d), and mass (m_d). These quantities are presented in Columns 6–8 of Table 5, respectively. A dust emissivity $\epsilon \propto 1/\lambda$ is assumed, with mass absorption coefficient of $\kappa =$ 60 cm^2/gm at 100 μm (Draine and Lee 1984). The derived size of the thermally-emitting region (discussed further in EM) is a lower limit. It could be much larger if the source is optically thin. For most Seyfert 2 galaxies, typical minimum dust sizes and temperatures of $r_d \approx 100$ pc and $T_d \approx 50$ K are found. This is warmer than dust in normal galaxies (de Jong *et al.* 1984), but similar to the temperature of dust in super-luminous infrared galaxies such as Arp 220 (Sanders *et al.* 1986). The sizes $r_d \gtrsim 100$ pc suggest that the warm dust resides in the narrow-line region or the galactic disk.

Table 3 contains limits to $\alpha_{100-1300\mu m}$, based on the 1.3 mm upper limits. The source NGC 1068 has $\alpha_{100-1300\mu m} \gtrsim +2.53$, which indicates that dust, and not synchrotron self-absorption is responsible for its cutoff. However, the strongest limits which can be set for any other sources are $\alpha_{100-1300\mu m} \gtrsim +1.5$. While the millimeter data is not yet sufficiently sensitive to discriminate between different causes for the turnover in these objects, they constrain the low-frequency side of the cutoff to be quite sharp.

V. RELATION TO OTHER PROPERTIES

a) Radio and Optical Luminosity

Six centimeter observations of 39 of the 45 CfA Seyfert galaxies detected at 60 μm with IRAS were discussed in Paper I. All were detected at 6 cm. The high detection rates (100% at 6 cm and 4500 Å, 97% at 60 μm) make it possible to search for luminosity correlations.

Figure 5 is a plot of nonthermal radio luminosity as a function of infrared luminosity. Seyfert 1 galaxies are denoted by triangles, and Seyfert 2 galaxies, by circles. The dashed line is a proper least-squares fit to the relation $L_{ir} \propto L^s_{rad}$ for Seyfert 1 galaxies, and the dotted line, for Seyfert 2 galaxies.

FIGURE 5

L_{ir} and L_{rad} are correlated for both types of Seyfert galaxy, although the correlation appears stronger for Seyfert 1 galaxies. The Spearman rank correlation test indicates that the two fluxes ($S_{60\mu m}$ and S_{6cm}) are correlated at the 99.9% confidence level, for both types of Seyfert galaxies. Assuming the power law relation $L_{ir} \propto L^s_{rad}$, $s = 0.90 \pm 0.10$ for Seyfert 1 galaxies, while for Seyfert 2 galaxies, $s = 1.06 \pm 0.14$.

Figure 6 is a plot of infrared luminosity as a function of integrated optical luminosity. Seyfert 1 galaxies are denoted by triangles, and Seyfert 2 galaxies, by circles. The dashed line is a proper least-squares fit to the relation $L_{ir} \propto L^s_{opt}$ for

Seyfert 1 galaxies, and the dotted line, for Seyfert 2 galaxies.

FIGURE 6

A clear correlation is also seen between L_{ir} and L_{opt}, but the fitted regression line is steeper than that for L_{ir} versus L_{rad}. The correlation in the optical and infrared fluxes is also somewhat weaker. For Seyfert 1 galaxies, $s = 1.73 \pm 0.13$ (significant at the 99.5% confidence level) and for Seyfert 2 galaxies, $s = 1.71 \pm 0.15$ (significant at the 99% confidence level). The steep slope seen in this relation, and in the $L_{rad} - L_{opt}$ relation (Paper 1), is consistent with the hypothesis that the nonthermal radio, infrared, and optical emission are all correlated, but that the optical luminosity of low-luminosity Seyfert galaxies are dominated by starlight from the underlying galaxy, which is not correlated with nonthermal luminosity.

b) Companions

It has been suggested that interactions can trigger star formation, leading to large extended infrared luminosities. Dahari (1985) has classified many of the CfA Seyfert galaxies for the presence of close companion galaxies at nearly the same redshift. As indicated in Table 4, 16 of the galaxies in the sample have close (physically associated) neighboring galaxies, which are denote by "I". The 15 Seyfert galaxies near which Dahari found no companions are denoted by "N". Histograms of $\alpha_{12-60\mu m}$ for interacting and non-interacting galaxies are presented in Figure 7. The K-S test indicates that the interacting Seyfert galaxies have significantly steeper far-infrared slopes than the isolated Seyfert galaxies at the 95% confidence level. The 60 μm luminosity (L_{ir}) is also larger for the interacting Seyfert galaxies, at the 95% confidence level. Evidently the galaxy interaction is associated with stronger emission from cool dust, which may be powered by new star formation in the body of the galaxy.

FIGURE 7

VI. INFRARED LUMINOSITY FUNCTION

Ideally, the Seyfert galaxy infrared luminosity function (IRLF) ought to be determined from a sample identified in a complete infrared survey such as the IRAS point source catalog. However, it is very difficult to identify a complete sample of Seyfert galaxies with the IRAS data. Completely identified portions of the IRAS survey tend to have a rather small percentage of Seyfert galaxies (Rieke and Lebofsky 1986). De Grijp *et al.* (1985) obtained a very high detection rate identifying Seyfert galaxies by selecting objects with $-0.5 \geq \alpha_{25-60\mu m} \geq -1.25$. However, Table 3 shows that 33 of the 40 CfA Seyfert galaxies (83%) with measured values or significant limits for $\alpha_{25-60\mu m}$ lie outside this range. This method of selecting Seyfert galaxies produces a sample which is too deficient in high-luminosity blue Seyfert 1 nuclei and in dusty Seyfert 2 galaxies to allow the construction of a reliable IRLF.

R78 found good evidence that the ultraviolet-excess selection criteria used in the Markarian Seyfert galaxies and PG quasars biased these samples against the inclusion of red objects. The CfA Seyfert galaxy sample, which used no ultraviolet-excess selection criterion, has a broad range of ultraviolet colors (Huchra, Wyatt, and Davis 1982; Edelson and Wahl 1987), making it ideal for studies of the relationship between ultraviolet excess and infrared spectra. Stronger ultraviolet excesses tend to be found in Seyfert 1 galaxies and AGNs with relatively little contamination from starlight.

Figure 8 is a histogram of $\alpha_{12-60\mu m}$ for objects with strong and weak ultraviolet excesses. Objects with strong ultraviolet excesses tend to have flatter infrared spectra than those with weak excesses. For the blue objects, $\alpha_{12-60\mu m} = -1.39 \pm 0.42$ (individual dispersion), while for the red objects, $\alpha_{12-60\mu m} = -1.51 \pm 0.45$.

The K-S test shows that $\alpha_{12-60\mu m}$ is distributed differently for the red and blue objects at the 97% confidence level.

FIGURE 8

The best alternative, which is used in this paper, is to make infrared measurements of a complete, unbiased, optically selected sample. The derivation of the CfA Seyfert galaxy IRLF is based on the modified V/V_m method suggested by Schmidt and Green (1982). Since this method is discussed in detail in Paper I, only a brief summary is given here.

The maximum accessible volume (V_m) is the volume of space within which an object could have been detected above both survey limits. The differential IRLF, $\Phi(L_{ir})$, is given by

$$\Phi(L_{ir}) = \frac{4\pi}{\Omega f \Delta L} \sum_{a=1}^{n} \frac{1}{V_{ma}}$$

summed over all n objects with L_{ir} in each bin of width ΔL (Huchra and Sargent 1973). In this equation, Ω is the amount of sky surveyed optically ($\Omega = 2.66$ sr), and f is the fraction of optically selected objects observed in the infrared ($f = 0.94$). The quantity L_{ir} is the monochromatic luminosity ($4\pi r^2 \nu F_\nu$) at 60 μm. The data were summed using logarithmic bins of width $\Delta L = 10^{0.4}$, corresponding to one magnitude.

The differential IRLF derived for Seyfert 1 and 2 galaxies separately, and for both types together is presented in Table 6 and Figure 9. Column 1 contains the binned values of L_{ir}. Columns 2-3, 4-5, and 6-7 give the space densities and number of objects in each bin for Type 1s, Type 2s, and both types together.

TABLE 6

FIGURE 9

The fact that a bivariate optical-infrared distribution function was used makes the IRLF subject to incompleteness for objects with infrared spectral indices steeper than that defined by the optical and infrared survey limits. Thus, this IRLF can be systematically deficient in objects with $\alpha_{O-IR} \leq -1.3$. As most Seyfert 2 galaxies, and many Seyfert 1 galaxies have infrared spectra this steep or steeper, this effect can be quite severe, and the derived IRLF should be considered a lower limit to the IRLF of all Seyfert galaxies.

The IRLF of Type 2 Seyfert galaxies was determined for luminosities of $10^{42.6}$ to $10^{45.0}$ ergs/s. The IRLF of Seyfert 1 galaxies and both types together were determined for luminosities of $10^{42.2}$ to $10^{45.0}$ ergs/s. Two Seyfert 1 galaxies (Mkn 231, $L_{ir} = 10^{45.73}$ erg/s, and NGC 5273, $L_{ir} = 10^{42.09}$ erg/s), and one Seyfert 2 galaxy (Mkn 270, $L_{ir} = 10^{41.96}$ erg/s) have infrared luminosities outside of this range. Nothing can be concluded from the present data about the IRLF of Seyfert galaxies with L_{ir} outside of $10^{42.2}$ to $10^{45.0}$ ergs/s. Since a significant fraction of the total luminosity of Seyfert galaxies is emitted in the far-infrared, the IRLFs derived above are in effect luminosity functions for the entire active galaxies.

The luminosities of Seyfert galaxies with "D" spectra are compared with that of field galaxies (Rieke and Lebofsky 1986) in Figure 10. Based on the arguments given earlier, it is expected that the bulk of their far-infrared luminosity is generated in the disk of the underlying galaxy for these objects. The Seyfert galaxy luminosities are plotted as a histogram above the horizontal line. Upper limits in the "Q" objects are plotted as a histogram below the line. These limits were set equal to the total infrared luminosity longward of 12 μm. The luminosities of the three rejected galaxies are identified with an R. The plot of the IRLF of field galaxies is normalized such that the total number of galaxies with infrared luminosity greater than 6×10^{41} erg/s (1.5×10^{8} $L_{\odot}$) is equal to the total number of Seyfert galaxies in the sample (including those rejected and those with upper limits for the cold excess). The luminosities of the Seyfert galaxies tend to be significantly higher than would be expected from an unbiased sample of field galaxies.

FIGURE 10

The conclusion rests primarily on eight galaxies (NGC 1068, NGC 1144, NGC 4388, Mkn 789, IC 4397, NGC 5674, NGC 7469, and Mkn 533) for which the infrared luminosities are greater than 4×10^{43} erg/s. All four of these galaxies with measured compactness parameters have $R < 0.6$, giving direct evidence that a significant amount of luminosity arises from outside the nucleus. They are also all well removed from the "quasar-like" region of Figure 3, providing further evidence that thermal dust emission is much more important than nonthermal emission in these objects. At least 7 additional objects with "D" or "Q(D)" spectra (Mkn 334, 0048+29, Mkn 231, 1335+39, NGC 5940, 1614+35, and Mkn 530) have luminosities greater than 4×10^{43} erg/s, although for various reasons the luminosity of the underlying galaxy is less certain for these objects.

If it is assumed that the bulk of their infrared luminosity is produced in their galactic disks (rather than in their Seyfert nuclei), the normalized luminosity function predicts that only 1.4 galaxies in this sample should have far-infrared luminosities larger than 4×10^{44} erg/s, rather than eight. This is evidence that Seyfert nuclei are more likely to be found in more luminous galaxies.

VII. CONCLUSIONS

For the first time, we can determine the infrared-millimeter properties of a complete, unbiased sample of Seyfert galaxies. This sample consists of the 48 Seyfert galaxies in the CfA redshift survey. For these galaxies, the following data have been obtained: IRAS measurements of 46 objects, JHK photometry of 45, L and N photometry of about half of the sample, and 1.4 mm upper limits for all. These observations allow the nuclear continuua between 1.1 μm and 1.3 mm to be studied. Seyfert galaxies have the following characteristics:

There is a highly significant trend for the slope of the infrared spectrum to steepen from quasars to Seyfert 1 galaxies to Seyfert 2 galaxies. This is caused by an increasingly large ratio of thermal to nonthermal infrared emission along this sequence. No Seyfert 2 galaxy has an infrared slope as flat as any of the optically selected quasars studied by E86, all of which have $\alpha_{2.2-25\mu m} > -1.25$ and $\alpha_{12-60\mu m} > -1.37$. Half of the Seyfert galaxy spectral energy distributions have sharp low-frequency turnovers around 80 μm.

About two-thirds of the Seyfert 1 galaxies have flat, quasar-like infrared spectra, indicating that nonthermal radiation is responsible for the observed infrared emission from these objects. The turnovers in the power law spectra of unreddened Seyfert 1 nuclei are attributed to synchrotron self-absorption, and imply source sizes of $\sim$100 Schwarzschild radii.

The thermal emission which characterizes all of the Seyfert 2 spectra and one-third of the Seyfert 1 spectra appears to come from dust in the nucleus (in a volume comparable to that of the narrow-line region where it absorbs much of the nuclear ultraviolet continuum), and in the disk of the galaxy (where it is warmed by starlight). In those objects with predominantly thermal far-infrared continua, the turnover frequency gives minimum dust temperatures of $\sim$50 K, warmer than those of normal spiral galaxies, but similar to those of "super-luminous" infrared galaxies like Arp 220. Although Seyfert 2 galaxies emit relatively more thermal flux than Seyfert 1 galaxies, their luminosity functions are not distinguishable up to 10^{45} erg/s. There is still no explanation of why Seyfert 2 nuclei, unlike Seyfert 1 nuclei, are never found to be essentially dust-free. Seyfert nuclei appear to reside in galaxies with higher than average far-infrared disk luminosities.

The authors would like to thank W. Rice for invaluable help with the IRAS data, and M. J. Lebofsky and W. F. Kailey for assistance. in obtaining some of the measurements reported. J. Huchra kindly released the list of CfA Seyfert galaxies in advance of publication. Analysis of IRAS data was supported by NASA grant NAS 7-918. Millimeter-wave astronomy at Caltech is supported by NSF grant AST 84-12473. Infrared astronomy at Steward Observatory is partially supported by the National Science Foundation. This work was partially supported by NSF grant AST 83-14134.

TABLE 1

CfA Seyfert Galaxy Near Infrared Data

Source	$S_{1.2\mu m}$ (mJy)	$S_{1.6\mu m}$ (mJy)	$S_{2.2\mu m}$ (mJy)	Date
Mkn 334	14.3 ± 0.7	20.8 ± 1.0	27.5 ± 1.4	15 Mar 84
0048+29	11.1 ± 1.1	14.5 ± 1.4	15.6 ± 1.5	13 Sep 84
Mkn 993	12.8 ± 0.6	14.2 ± 0.7	15.1 ± 0.8	
Mkn 573	22.0 ± 2.0	29.5 ± 3.0	26.3 ± 2.4	26 Sep 85
0152+06	6.0 ± 0.4	8.0 ± 0.5	7.4 ± 0.5	16 Sep 84
NGC 1144	12.2 ± 2.4	29.4 ± 3.0	31.5 ± 3.6	04 Mar 85
Mkn 1243	5.8 ± 0.6	7.4 ± 0.7	7.9 ± 0.8	Mar 86
NGC 3079[a]	31.0 ± 2.2	71.3 ± 4.0	91.9 ± 5.0	14 Apr 84
NGC 3362	5.8 ± 0.5	6.8 ± 0.6	5.2 ± 0.5	Mar 86
1058+45				
Mkn 744[a]	19.8 ± 2.0	25.9 ± 2.0	27.8 ± 2.4	15 Apr 84
NGC 3982[a]	9.2 ± 0.9		12.4 ± 1.2	14 Apr 84
NGC 4235[a]	21.1 ± 2.0	35.4 ± 3.0	29.9 ± 2.4	16 Apr 84
Mkn 766	23.1 ± 2.0	42.6 ± 3.0	50.1 ± 4.0	Mar 86
NGC 4388[a]	30.8 ± 2.0	48.5 ± 2.5	46.9 ± 2.5	04 Mar 85
NGC 5033[a]	44.1 ± 3.5	61.6 ± 5.0	47.8 ± 3.0	04 Mar 85
Mkn 789	5.6 ± 0.5	7.8 ± 0.6	7.3 ± 0.5	04 Mar 85
1335+39	7.7 ± 0.5	8.1 ± 0.6	7.9 ± 0.6	Mar 86
NGC 5252	11.6 ± 1.0	12.0 ± 1.0	16.1 ± 0.9	04 Mar 85
Mkn 266[a]	4.0 ± 0.5	8.8 ± 1.0	8.7 ± 0.8	04 Mar 85
NGC 5273[a]	14.6 ± 1.0	25.0 ± 1.5	23.1 ± 1.5	04 Mar 85
Mkn 461[a]	12.9 ± 0.8	17.4 ± 1.0	13.4 ± 0.9	04 Mar 85
IC 4397	6.9 ± 0.6	7.4 ± 0.5	6.3 ± 0.5	Mar 86
NGC 5674[a]	15.7 ± 1.3	19.5 ± 1.4	16.1 ± 1.0	Mar 86
Mkn 686	11.1 ± 0.8	15.7 ± 1.0	15.8 ± 1.0	15 Apr 84
NGC 5929[a]				
NGC 5940	4.4 ± 0.3	6.8 ± 0.5	8.7 ± 0.6	Mar 86
1614+35	3.6 ± 0.2	6.8 ± 0.7	6.9 ± 0.7	15 Mar 84
2237+07[a]	11.3 ± 0.6	17.8 ± 0.9	19.4 ± 1.0	13 Sep 84
Mkn 533[a]	10.1 ± 0.5	15.6 ± 0.8	24.2 ± 2.4	
NGC 7682	11.0 ± 1.1	14.9 ± 1.4	9.5 ± 0.9	15 Mar 84

[a] The following objects have been observed at 3.5 or 10 μm: NGC 3079 ($S_{3.5} = 73 \pm 6$ mJy, $S_{10.6} = 210 \pm 20$ mJy), Mkn 744 ($S_{3.5} = 31 \pm 3$ mJy), NGC 3982 ($S_{10.6} < 44$ mJy), NGC 4235 ($S_{3.5} = 22 \pm 2$ mJy), NGC 4388 ($S_{3.5} = 74 \pm 6$ mJy), NGC 5033 ($S_{3.5} = 43 \pm 3$ mJy, $S_{10.6} < 144$ mJy), Mkn 266 ($S_{3.5} = 7 \pm 1$ mJy), NGC 5273 ($S_{3.5} = 16 \pm 2$ mJy) Mkn 461 ($S_{3.5} < 15$ mJy), NGC 5674 ($S_{3.5} < 15$ mJy), NGC 5929 ($S_{10.6} < 53$ mJy), 2237+07 ($S_{3.5} = 16.4 \pm 1.7$ mJy, $S_{10.6} = 82 \pm 12$ mJy), Mkn 533 ($S_{3.5} = 46.4 \pm 4.6$ mJy, $S_{10.6} = 325 \pm 25$ mJy).

TABLE 2

CfA Seyfert Galaxy Far Infrared And Millimeter Data

Source	$S_{12\mu m}$ (mJy)	$S_{25\mu m}$ (mJy)	$S_{60\mu m}$ (mJy)	$S_{100\mu m}$ (mJy)	$S_{1.3mm}$ (mJy)
Mkn 334	212 ± 34	1070 ± 76	4310 ± 232	4660 ± 494	< 699
Mkn 335	341 ± 42	420 ± 99	414 ± 49	< 323	< 852
0048+29	186 ± 38	138 ± 41	931 ± 80	1990 ± 250	< 834
I Zw 1	540 ± 34	1260 ± 126	2130 ± 298	2430 ± 243	< 672
Mkn 993	< 93	< 102	260 ± 49	1210 ± 168	< 465
Mkn 573	198 ± 46	806 ± 73	1200 ± 93	1270 ± 173	< 915
0152+06	< 104	< 144	467 ± 53	1240 ± 174	< 591
Mkn 590	169 ± 44	247 ± 44	435 ± 61	1420 ± 183	< 309
NGC 1068	38300 ± 2300	88600 ± 5210	186000 ± 18600	239000 ± 23900	< 306
NGC 1144	307 ± 25	680 ± 52	5400 ± 288	11300 ± 1150	< 495
Mkn 1243	< 103	< 160	328 ± 46	1020 ± 162	< 615
NGC 3079	1250 ± 75	2040 ± 122	42400 ± 5950	87600 ± 8760	< 564
NGC 3227	562 ± 40	1750 ± 175	8030 ± 784	16900 ± 2370	< 738
NGC 3362					< 615
1058+45	130 ± 32	198 ± 34	631 ± 60	1530 ± 195	< 900
NGC 3516	384 ± 35	922 ± 57	1840 ± 107	2160 ± 239	< 744
Mkn 744					< 537
NGC 3982	457 ± 29	755 ± 84	6730 ± 683	15200 ± 1550	< 1230
NGC 4051	780 ± 78	1420 ± 142	8160 ± 816	20400 ± 2860	< 456
NGC 4151	2080 ± 104	4600 ± 230	6720 ± 336	8600 ± 430	< 318
NGC 4235	< 121	< 174	374 ± 60	736 ± 136	< 468
Mkn 766	431 ± 44	1430 ± 89	4010 ± 242	5060 ± 532	< 1431
Mkn 205	< 70	80 ± 22	290 ± 38	1310 ± 164	< 933
NGC 4388	1000 ± 60	3370 ± 214	10700 ± 1070	17300 ± 2440	< 1281
Mkn 231	1820 ± 109	8560 ± 514	33300 ± 3330	30100 ± 3010	< 342
NGC 5033	828 ± 47	995 ± 106	13600 ± 1310	42400 ± 4360	< 462
Mkn 789	< 146	610 ± 62	3720 ± 221	5330 ± 571	< 1350
1335+39	132 ± 34	168 ± 38	1070 ± 80	2630 ± 300	< 930
NGC 5252	< 119	< 167	425 ± 55	750 ± 130	< 816
Mkn 266	306 ± 38	976 ± 70	7320 ± 396	10400 ± 1090	< 1041
Mkn 270	< 85	< 78	117 ± 39	< 350	< 1131
NGC 5273	134 ± 37	242 ± 38	991 ± 87	2030 ± 248	< 1185
Mkn 461	< 109		443 ± 56	456 ± 106	< 1296
Mkn 279	199 ± 32	289 ± 27	1200 ± 79	1970 ± 225	< 1548
IC 4397	164 ± 37	151 ± 37	1680 ± 110	3130 ± 345	< 735
NGC 5548	343 ± 40	765 ± 60	1110 ± 87	1800 ± 211	< 1473
NGC 5674	128 ± 31	273 ± 44	1630 ± 104	3560 ± 382	< 765
Mkn 817	357 ± 32	1240 ± 70	2340 ± 134	2260 ± 242	< 1269
Mkn 686	< 82	< 80	605 ± 50	1800 ± 208	< 1098
Mkn 841	198 ± 30	453 ± 45	476 ± 50	< 257	< 762
NGC 5929	360 ± 33	1570 ± 89	9450 ± 491	12000 ± 1220	< 801
NGC 5940	124 ± 30	112 ± 32	794 ± 63	1820 ± 214	< 822
1614+35	< 80	< 72	481 ± 50	1790 ± 205	< 1050
2237+07	140 ± 42	392 ± 52	900 ± 76	1270 ± 186	< 303
NGC 7469	1300 ± 130	5500 ± 550	26700 ± 3740	34400 ± 6190	< 768
Mkn 530	180 ± 42	191 ± 56	856 ± 79	2140 ± 254	< 585
Mkn 533	720 ± 101	1930 ± 231	5470 ± 766	8190 ± 1450	< 903
NGC 7682					< 507

TABLE 3

CfA Seyfert Galaxy Spectral Indicies

Source	$\alpha_{2.2-25\mu m}$	$\alpha_{12-60\mu m}$	$\alpha_{25-60\mu m}$	$\alpha^{60\mu m}_{100\mu m}$	$\alpha^{1.4mm}_{100\mu m}$
Mkn 334	−1.51 ± 0.04	−1.87 ± 0.09	−1.59 ± 0.10	−0.15 ± 0.22	> 0.70
Mkn 335	−0.72 ± 0.10	−0.12 ± 0.11	0.02 ± 0.29	> 0.31	
0048+29	−0.90 ± 0.12	−1.00 ± 0.13	−2.18 ± 0.31	−1.49 ± 0.29	> 0.30
I Zw 1	−1.24 ± 0.06	−0.85 ± 0.09	−0.60 ± 0.19	−0.26 ± 0.33	> 0.46
Mkn 993	> −0.80	< −0.55	< −0.91	−3.01 ± 0.46	> 0.33
Mkn 573	−1.41 ± 0.05	−1.12 ± 0.14	−0.45 ± 0.14	−0.11 ± 0.30	> 0.09
0152+06	> −1.25	< −0.88	< −1.25	−1.91 ± 0.35	> 0.24
Mkn 590	−0.76 ± 0.07	−0.59 ± 0.18	−0.65 ± 0.26	−2.32 ± 0.37	> 0.55
NGC 1068	−2.11 ± 0.05	−0.98 ± 0.07	−0.85 ± 0.13	−0.49 ± 0.28	> 2.53
NGC 1144	−1.27 ± 0.06	−1.78 ± 0.06	−2.37 ± 0.10	−1.45 ± 0.21	> 1.17
Mkn 1243	> −1.27	< −0.65	< −0.70	−2.22 ± 0.42	> 0.15
NGC 3079	−1.28 ± 0.03	−2.19 ± 0.09	−3.47 ± 0.16	−1.42 ± 0.33	> 1.91
NGC 3227	−1.29 ± 0.06	−1.65 ± 0.07	−1.74 ± 0.16	−1.46 ± 0.33	> 1.16
NGC 3362					
1058+45		−0.98 ± 0.15	−1.32 ± 0.22	−1.73 ± 0.31	> 0.17
NGC 3516	−0.89 ± 0.05	−0.97 ± 0.07	−0.79 ± 0.10	−0.31 ± 0.23	> 0.38
Mkn 744					
NGC 3982	−1.70 ± 0.06	−1.67 ± 0.07	−2.50 ± 0.17	−1.59 ± 0.28	> 0.94
NGC 4051	−1.27 ± 0.06	−1.46 ± 0.09	−2.00 ± 0.16	−1.79 ± 0.33	> 1.42
NGC 4151	−1.31 ± 0.04	−0.73 ± 0.04	−0.43 ± 0.08	−0.48 ± 0.14	> 1.25
NGC 4235	> −0.75	< −0.63	< −0.74	−1.33 ± 0.48	> 0.12
Mkn 766	−1.38 ± 0.04	−1.39 ± 0.07	−1.18 ± 0.10	−0.46 ± 0.23	> 0.45
Mkn 205	−0.75 ± 0.11	< −0.82	−1.47 ± 0.33	−2.95 ± 0.36	> 0.09
NGC 4388	−1.77 ± 0.03	−1.47 ± 0.07	−1.32 ± 0.13	−0.94 ± 0.33	> 0.96
Mkn 231	−1.61 ± 0.05	−1.81 ± 0.07	−1.55 ± 0.13	0.20 ± 0.28	> 1.69
NGC 5033	−1.25 ± 0.05	−1.74 ± 0.07	−2.99 ± 0.16	−2.23 ± 0.28	> 1.70
Mkn 789	−1.83 ± 0.05	< −1.99	−2.07 ± 0.13	−0.70 ± 0.23	> 0.50
1335+39	−1.26 ± 0.09	−1.30 ± 0.15	−2.11 ± 0.24	−1.76 ± 0.26	> 0.37
NGC 5252	> −0.98	< −0.73	< −0.96	−1.11 ± 0.42	> −0.08
Mkn 266	−1.95 ± 0.05	−1.97 ± 0.08	−2.30 ± 0.10	−0.69 ± 0.22	> 0.85
Mkn 270	> −0.66	< −0.03	< −0.16	> −2.67	
NGC 5273	−0.97 ± 0.07	−1.24 ± 0.16	−1.61 ± 0.20	−1.40 ± 0.29	> 0.17
Mkn 461	−0.90 ± 0.11	< −0.81	−1.50 ± 0.35	−0.06 ± 0.50	> −0.47
Mkn 279	−1.05 ± 0.06	−1.12 ± 0.10	−1.63 ± 0.13	−0.97 ± 0.25	> 0.06
IC 4397	−1.31 ± 0.10	−1.45 ± 0.13	−2.75 ± 0.25	−1.22 ± 0.24	> 0.52
NGC 5548	−1.11 ± 0.05	−0.73 ± 0.09	−0.43 ± 0.13	−0.95 ± 0.27	> 0.04
NGC 5674	−1.17 ± 0.07	−1.58 ± 0.14	−2.04 ± 0.18	−1.53 ± 0.24	> 0.56
Mkn 817	−1.32 ± 0.03	−1.17 ± 0.06	−0.73 ± 0.09	0.07 ± 0.23	> 0.19
Mkn 686	> −0.69	< −1.20	< −2.24	−2.13 ± 0.27	> 0.16
Mkn 841	−1.13 ± 0.05	−0.55 ± 0.11	−0.06 ± 0.17	> 1.06	
NGC 5929		−2.03 ± 0.06	−2.05 ± 0.09	−0.47 ± 0.21	> 1.01
NGC 5940	−1.06 ± 0.10	−1.15 ± 0.14	−2.24 ± 0.30	−1.62 ± 0.27	> 0.27
1614+35	> −1.00	< −1.07	< −2.08	−2.57 ± 0.30	> 0.17
2237+07	−1.24 ± 0.05	−1.16 ± 0.17	−0.95 ± 0.18	−0.67 ± 0.32	> 0.51
NGC 7469	−1.57 ± 0.06	−1.88 ± 0.11	−1.80 ± 0.19	−0.50 ± 0.44	> 1.41
Mkn 530	−0.84 ± 0.12	−0.97 ± 0.14	−1.71 ± 0.31	−1.79 ± 0.29	> 0.46
Mkn 533	−2.23 ± 0.09	−1.26 ± 0.12	−1.19 ± 0.21	−0.79 ± 0.44	> 0.79
NGC 7682					

TABLE 4

CfA SEYFERT GALAXY SPECTRAL PARAMETERS

Source	Type	UVX	*R*	Ext.	SED	Nuclear Flux (mJy)	Int.
Mkn 334	2	B			D	$\leq 28^{b}$	
Mkn 335	1	B	0.78 ± 0.18	C	Q	71^{a}	N
0048+29	1	B			Q(D)	$\leq 16^{b}$	
I Zw 1	1	B	0.81 ± 0.10	C	Q	61^{a}	
Mkn 993	2	R				$\leq 15^{b}$	N
Mkn 573	2	R			D	9^{c}	N
0152+06	2	R				3^{c}	
Mkn 590	1	R			Q(D)	16^{a}	I
NGC 1068	2	B	0.66 ± 0.05	E	D	302^{a}	
NGC 1144	2	R			D	$\leq 31^{b}$	I
Mkn 1243	1	B				$\leq 8^{b}$	
NGC 3079	2	B	0.22 ± 0.03	E	D	52^{a}	I
NGC 3227	2	R	0.70 ± 0.06	E	D	41^{a}	I
NGC 3362	2	R				$\leq 1^{c}$	N
1058+45	2	R					N
NGC 3516	1	R	0.84 ± 0.13	C	Q	43^{a}	I
Mkn 744	1	R				18^{a}	I
NGC 3982	2	R	≤ 0.11	E	D	$\leq 12^{b}$	N
NGC 4051	1	B	0.55 ± 0.06	E	D	57^{a}	N
NGC 4151	1	B	0.94 ± 0.06	C	Q	155^{a}	N
NGC 4235	1	R				7^{a}	N
Mkn 766	1	B			D	$\leq 50^{b}$	N
Mkn 205	1	B				8^{a}	
NGC 4388	2	R	0.61 ± 0.05	E	D	17^{a}	I
Mkn 231	1	R	1.23 ± 0.15	C	D	175^{a}	
NGC 5033	1	R	0.07 ± 0.03	E	D	6^{a}	N
Mkn 789	1	B			D	3^{c}	
1335+39	2	B			D	2^{c}	N
NGC 5252	2	R				$\leq 16^{b}$	N
Mkn 266	2	R				4^{a}	I
Mkn 270	2	R				$\leq 3^{a}$	N
NGC 5273	1	R			Q	7^{a}	N
Mkn 461	2	B				$\leq 3^{a}$	
Mkn 279	1	B				8^{a}	
IC 4397	2	B			D	$\leq 1^{c}$	
NGC 5548	1	B	1.10 ± 0.15	C	Q	48^{a}	N
NGC 5674	2	R			D	3^{a}	N
Mkn 817	1	B			Q	43^{a}	
Mkn 686	2	R				$\leq 16^{b}$	N
Mkn 841	1	B	1.03 ± 0.23	C	Q	27^{a}	
NGC 5929	2	R	≤ 0.23	E			I
NGC 5940	1	B			Q(D)	$\leq 9^{b}$	
1614+35	1	R				5^{c}	
2237+07	1	B	0.85 ± 0.28	C	Q	$\leq 19^{b}$	N
NGC 7469	1	B	0.72 ± 0.09	E	D(D)	118^{a}	I
Mkn 530	1	B	0.53 ± 0.16	E	Q	12^{a}	N
Mkn 533	2	B	0.65 ± 0.11	E	D	$\leq 9^{b}$	I
NGC 7682	2	R					N

TABLE 5

Derived Turnover Parameters

Source	ν_t (THz)	r_s (10^{12}cm)	T_b (10^{10} K)	B (G)	T_d (K)	r_d (10^{18}cm)	m_d ($M_\odot$)
Mkn 334	4.5	3900	3.3	930	55	160	730
Mkn 335	7.9	720	4.2	1000	97	25	130
I Zw 1	3.7	8300	4.2	490	44	430	9400
Mkn 573	4.1	1500	4.5	470	50	79	520
NGC 1068	3.0	8800	1.8	2000	36	340	100
NGC 3079	3.5	3100	2.3	1500	43	120	54
NGC 3516	3.6	1100	4.3	440	44	58	190
Mkn 766	3.6	2600	3.7	620	44	130	470
Mkn 231	5.1	22000	2.1	2700	62	700	2100
Mkn 789	3.9	5700	3.7	670	47	270	2300
Mkn 461	4.6	720	5.2	390	56	37	270
IC 4397	3.5	1800	4.5	400	42	100	630
Mkn 817	5.0	3500	3.6	880	61	150	1000
Mkn 841	7.3	1200	4.3	910	88	44	360
NGC 7469	4.0	9400	2.4	1600	48	360	680

TABLE 6

SEYFERT GALAXY FAR INFRARED LUMINOSITY FUNCTION

	Type 1		Type 2		Both Types	
$\log(L_{ir})$ erg/s	$\log(\Phi)$ $\mathrm{Gpc^{-3}mag^{-1}}$	N	$\log(\Phi)$ $\mathrm{Gpc^{-3}mag^{-1}}$	N	$\log(\Phi)$ $\mathrm{Gpc^{-3}mag^{-1}}$	N
42.2–42.6	4.47	2	...	0	4.47	2
42.6–43.0	3.81	1	4.43	3	4.52	4
43.0–43.4	3.79	2	4.35	5	4.46	7
43.4–43.8	3.51	7	4.39	5	4.44	12
43.8–44.2	3.64	6	3.17	2	3.77	8
44.2–44.6	2.98	2	3.37	2	3.52	4
44.6–45.0	2.81	2	2.89	3	3.15	5

REFERENCES

Aitken, D. K. and Roche, P. F. 1985, *M. N. R. A. S.*, **213**, 777.

Angel, J. R. P. and Stockman, H. S. 1980, *Ann. Rev. Astr. Ap.*, **18**, 321.

Beichman, C. *et al.* 1984, *IRAS Point Source Catalog.*

Campins, H., Rieke, G. H., Lebofsky, M. J. 1985, *A. J.*, **90**, 541.

Cruz-Gonzalez, I. and Huchra, J. 1984 , *A. J.* , **89**, 441.

Cutri, R. M., Rieke, G. H., Lebofsky, M. J. 1985, *Ap. J.*, **287**, 566.

Cutri, R. M., Rudy, R. J., Rieke, G. H., Tokunaga, A. T. and Willner, S. P. 1984, *Ap. J.*, **280**, 521.

Dahari, O. 1985, *A. J.*, **90**, 1772.

de Grijp, R. H. K., Miley, G. K., Lub, J., de Jong, T. 1985, *Nature*, **314**, 240.

de Jong, T. *et al.* 1984, *Ap. J. Lett.*, **278**, L67.

Devereux, N. A., Becklin, E. E., and Scoville, N. Z., *Ap. J.*, in press.

Edelson, R. A. 1986, *Ap. J.*, **309**, in press (E86).

Edelson, R. A. 1987, *Ap. J.*, **313**, in press (Paper 1).

Edelson, R. A., and Malkan, M. A. 1986, *Ap. J.*, **308**, 59 (EM).

Edelson, R. A. and Wahl, T. 1987, *Ap. J Supp.*. in preparation.

Kollatschny, W. and Fricke, K. J. 1984, *Astr. Ap.*, **135**, 171.

Huchra, J, and Berg, R. 1987, *Ap. J.*, in press.

Huchra, J. P., Wyatt, W. F., and Davis, M. 1982, *Astron. J.*, **87**, 1628.

Huchra, J., and Sargent, W. L. W. 1973, *Ap. J.*, **186**, 433.

Malkan, M. A. and Filippenko, A. V. 1983, *Ap. J.*, **275**, 477.

Markarian, B. Y. 1972, *Astrofizika*, **8**, 165.

McAlary, C. W. and Rieke, G. H., 1986, *Ap. J.*, in press.

Neugebauer, G., Soifer, B. T., and Miley, G. K., *Ap. J. Lett.*, **295**, L27.

Neugebauer, G., Miley, G. K., and Soifer, B. T., and Clegg, P. E. 1986, *Ap. J.*, **308**, in press.

Readhead, A. S. C. 1986, private communication.

Rieke, G. H. 1978, *Ap. J.*, **266**, 550 (R78).

Rieke, G. H., and Lebofsky, M. J. 1979, *Ann. Rev. Astr. Ap.*, **17**, 477.

Rieke, G. H., and Lebofsky, M. J. 1986, *Ap. J.*, **304**, 376.

Sanders, D. *et al.* 1986, preprint.

Schmidt, M., and Green, R. F. 1983, *Ap. J.*, **269**, 352.

Siegel, S. 1956, Nonparametric Statistics for the Behavioral Sciences (McGraw-Hill).

Wynn-Williams, C. G., Becklin, E. E., Scoville, N. Z., *Ap. J.*, **297**, 607.

FIGURE CAPTIONS

FIG 1.—a) 1–100 μm νF_ν plots for the CfA Seyfert 1 galaxies. The objects are presented in approximate order of the ultraviolet excess, with the bluest objects at the top. Data is plotted in log νF_ν versus ν, so a horizontal line would have $\alpha = -1$ (i.e., equal power per octave of frequency). For the purpose of display only, the IRAS data is grey-shifted by the "compactness parameter", R, discussed in § IIIc, to account for the effects of emission from the underlying galaxy. One-sigma error bars are shown, and a factor of two is shown on the lower left for scale. An arbitrary scaling constant is added to the data for display purposes.

FIG 1.—b) Same as Figure 1a, except for the Seyfert 2 galaxies.

FIG 2.—Correlation of compactness parameter (R) with 12 μm luminosity and $\alpha_{12-60\mu m}$ are presented in panels a and b. These parameters are correlated at the 97% and 99% confidence level, respectively.

FIG 3.—Color-color diagram of $\alpha_{2.2-25\mu m}$ versus $\alpha_{12-60\mu m}$. Seyfert 1 galaxies are denoted by triangles, Seyfert 2 galaxies by circles, and bright quasars by filled stars. An object which lies on the dotted line has $\alpha_{2.2-25\mu m} = \alpha_{12-60\mu m}$. The dashed line delineates a region with $\alpha_{2.2-25\mu m} \geq -1.37$ and $\alpha_{12-60\mu m} \geq -1.25$. All quasars and 70% of the Seyfert 1 galaxies lie within this region, and all Seyfert 2 galaxies lie outside.

FIG 4.—Color-color diagram of $\alpha_{25-60\mu m}$ versus $\alpha_{60-100\mu m}$. Seyfert 1 galaxies are denoted by triangles, Seyfert 2 galaxies by circles, and bright quasars by filled stars. An object which lies on the dotted line has $\alpha_{25-60\mu m} = \alpha_{60-100\mu m}$. Sources with detected turnovers lie in the region above and to the right of the dashed line.

FIG 5.—Plot of L_{rad} versus L_{ir} for the 39 objects observed at 60 μm and 6 cm. Seyfert 1 galaxies are denoted with a triangle, while Seyfert 2 galaxies are denoted by circles. The dashed line is a proper least-squares fit to the relation $L_{ir} \propto L_{rad}^s$

for Seyfert 1 galaxies, and the dotted line, for Seyfert 2 galaxies.

FIG 6.—Plot of L_{opt} versus L_{ir} for the 45 objects detected at 60 μm. Seyfert 1 galaxies are denoted with a triangle, while Seyfert 2 galaxies are denoted by circles. The dashed line is a proper least-squares fit to the relation $L_{ir} \propto L_{opt}^{s}$ for Seyfert 1 galaxies, and the dotted line, for Seyfert 2 galaxies.

FIG 7.—Histograms of $\alpha_{12-60\mu m}$ for Seyfert galaxies classified by Dahari (1985) as interacting (I) or non-interacting (N). The two distributions are different at the 95% significance level.

FIG 8.—Histogram of $\alpha_{12-60\mu m}$ based on ultraviolet excess. The top panel contains the data for "blue" objects (i.e., those with strong ultraviolet excesses), and the bottom panel, for "red" objects. The two distributions are different at the 95% confidence level.

FIG 9.—Infrared luminosity function of Seyfert galaxies. The top panel contains the IRLF of Seyfert 1 galaxies, the middle panel, that of Seyfert 2 galaxies, and the bottom panel shows the IRLF of both types together. Error bars are 1σ errors. The error bars are 1σ Poisson statistical errors.

FIG 10.—Normalized IRLF of "D" Seyfert galaxies. Integrated infrared luminosities, L, are given in units of 10^{10} $L_{\odot}$. The curved line shows the field galaxy luminosity function (Rieke and Lebofsky 1986) normalized to the number of galaxies in the CfA Seyfert galaxy sample. The histogram above the horizontal line at N = 0 shows the luminosity distribution of the "D" Seyfert galaxies. The histogram below the line shows the distribution of upper limits (indicated with a "<") for the "quasar-like" objects and also the luminosities (indicated with an "R") of the three rejected galaxies discussed in the text.

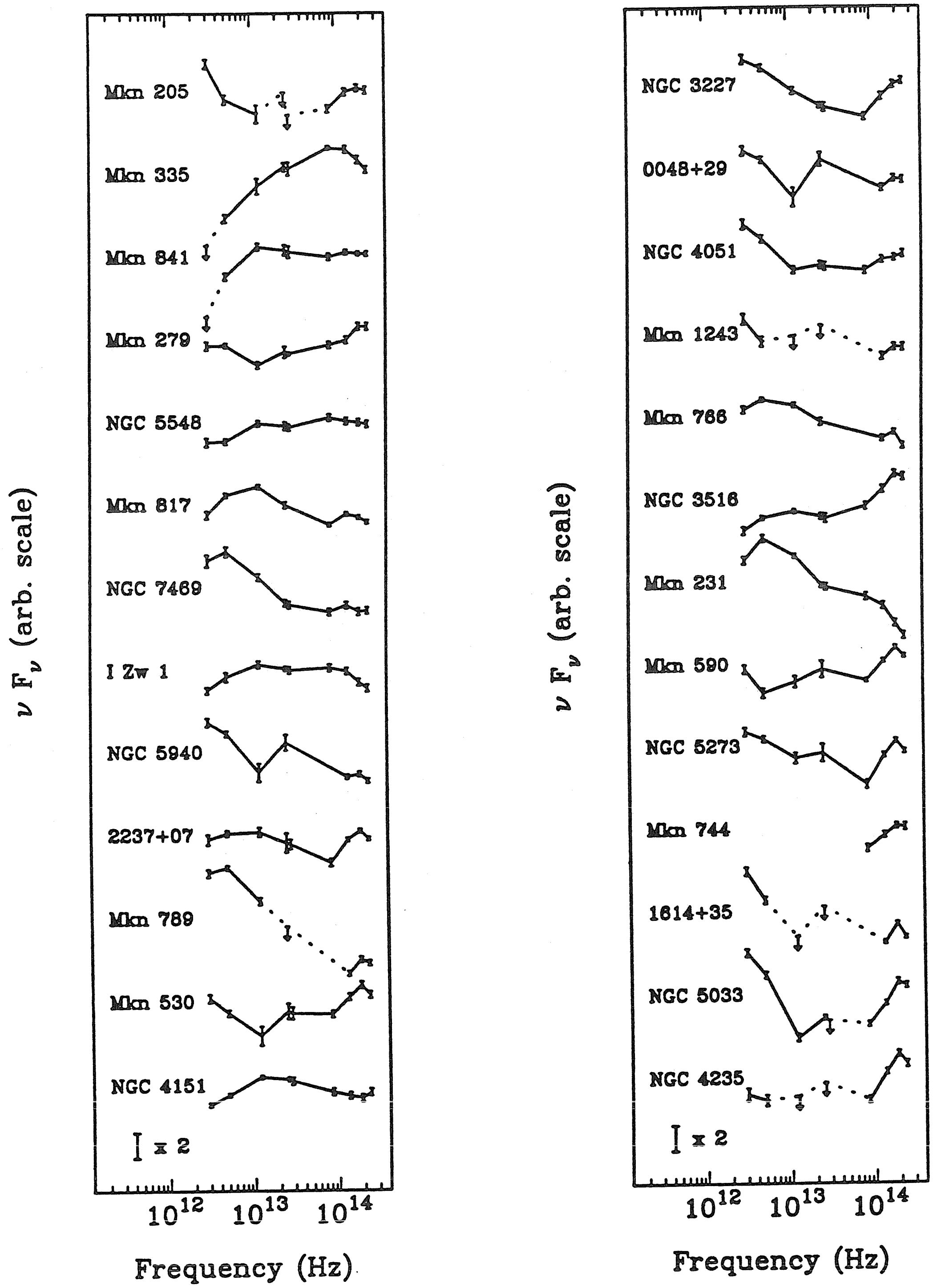
ν F_ν (arb. scale)
Mkn 205
Mkn 335
Mkn 841
Mkn 279
NGC 5548
Mkn 817
NGC 7469
I Zw 1
NGC 5940
2237+07
Mkn 789
Mkn 530
NGC 4151
x 2
10^12
10^13
10^14
Frequency (Hz)
ν F_ν (arb. scale)
NGC 3227
0048+29
NGC 4051
Mkn 1243
Mkn 766
NGC 3516
Mkn 231
Mkn 590
NGC 5273
Mkn 744
1614+35
NGC 5033
NGC 4235
x 2
10^12
10^13
10^14
Frequency (Hz)

Figure 1a

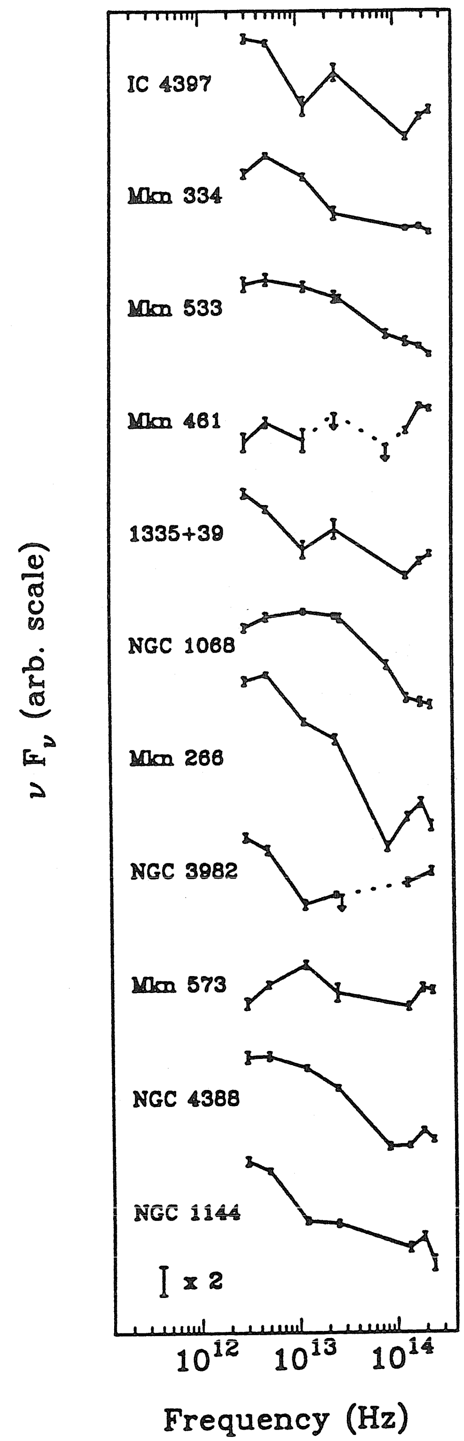
IC 4397
Mkn 334
Mkn 533
Mkn 461
1335+39
NGC 1068
Mkn 266
NGC 3982
Mkn 573
NGC 4388
NGC 1144
x 2
10^{12}
10^{13}
10^{14}
Frequency (Hz)
$\nu\ F_\nu$ (arb. scale)

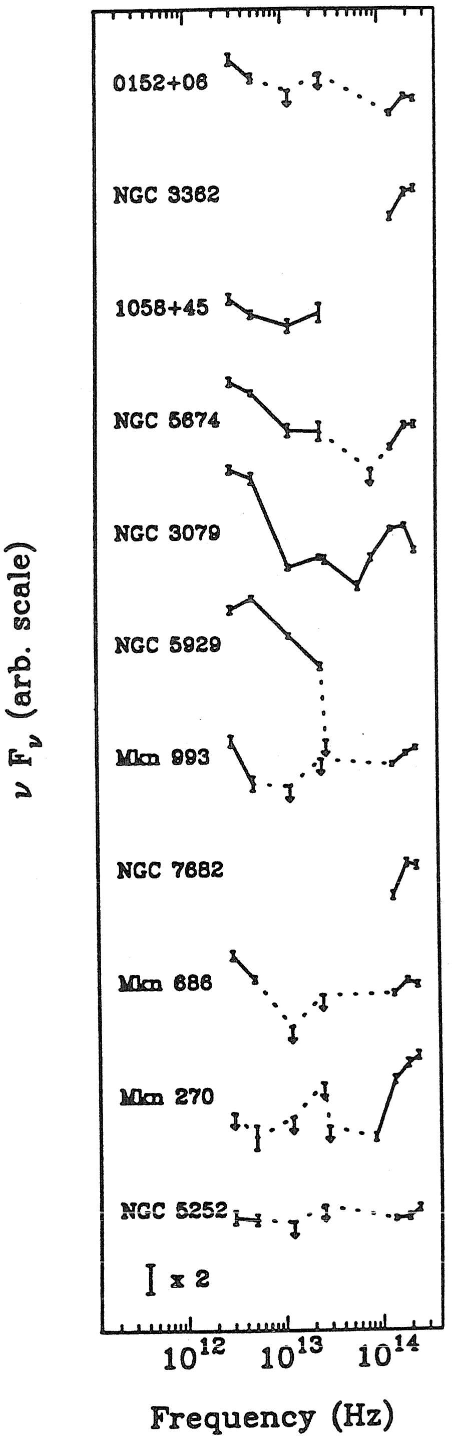
0152+06
NGC 3362
1058+45
NGC 5674
NGC 3079
NGC 5929
Mkn 993
NGC 7682
Mkn 686
Mkn 270
NGC 5252
x 2
10^{12}
10^{13}
10^{14}
Frequency (Hz)
$\nu\ F_\nu$ (arb. scale)

Figure 1b

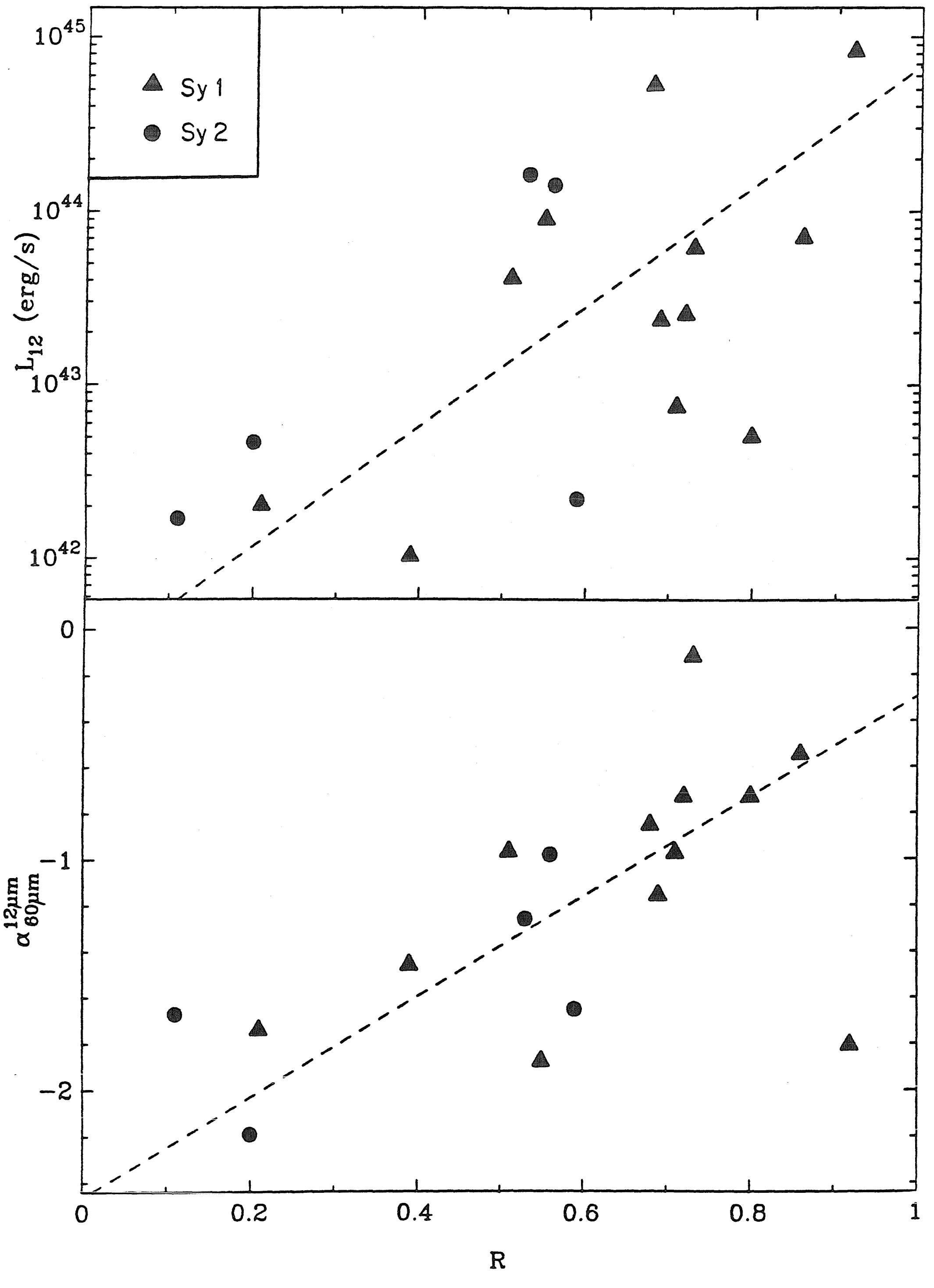
▲ Sy 1
● Sy 2
10^{45}
10^{44}
10^{43}
10^{42}
L_{12} (erg/s)
0
−1
−2
$\alpha^{12\mu m}_{60\mu m}$
0
0.2
0.4
0.6
0.8
1
R

Figure 2

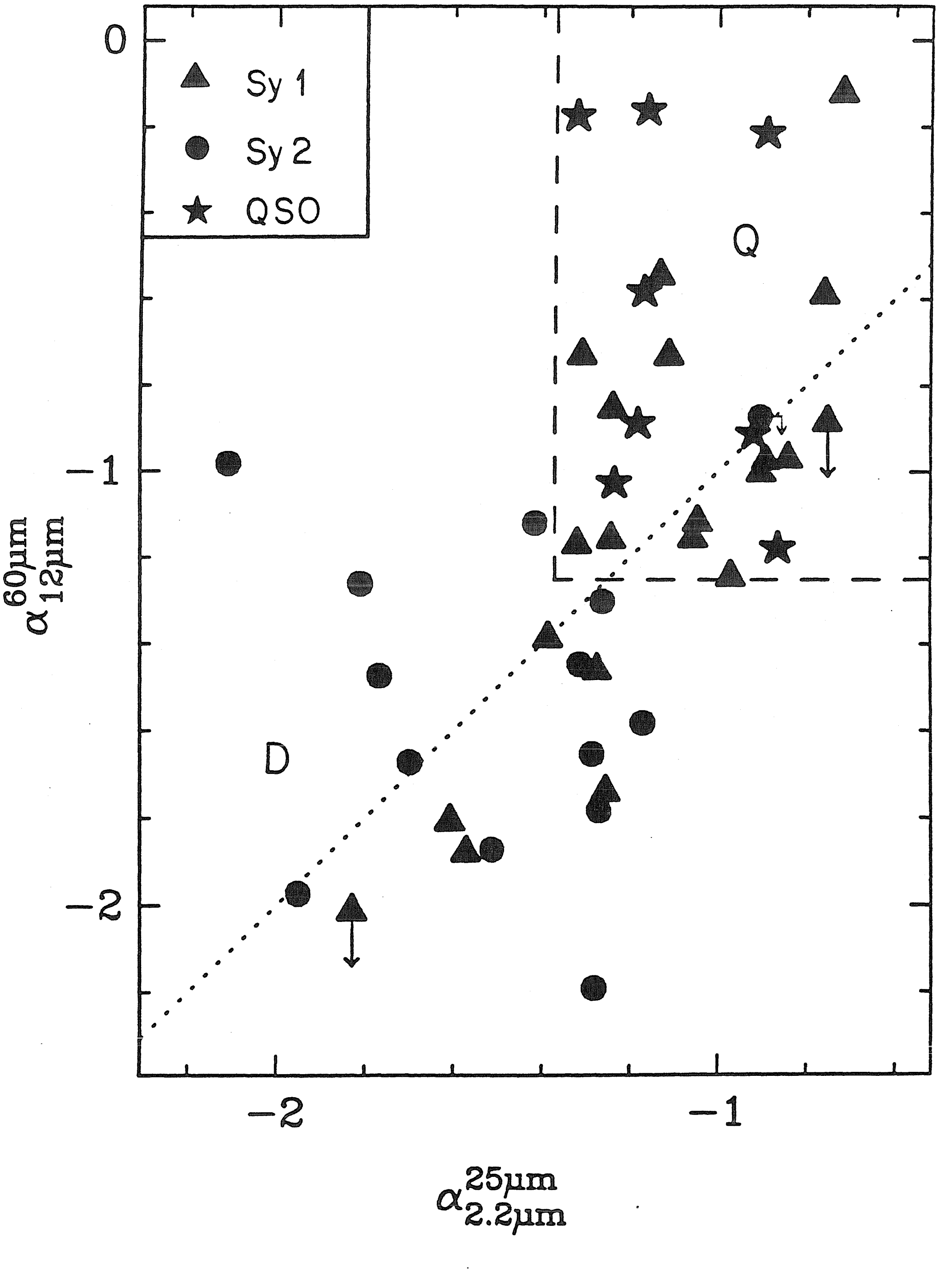

Figure 3

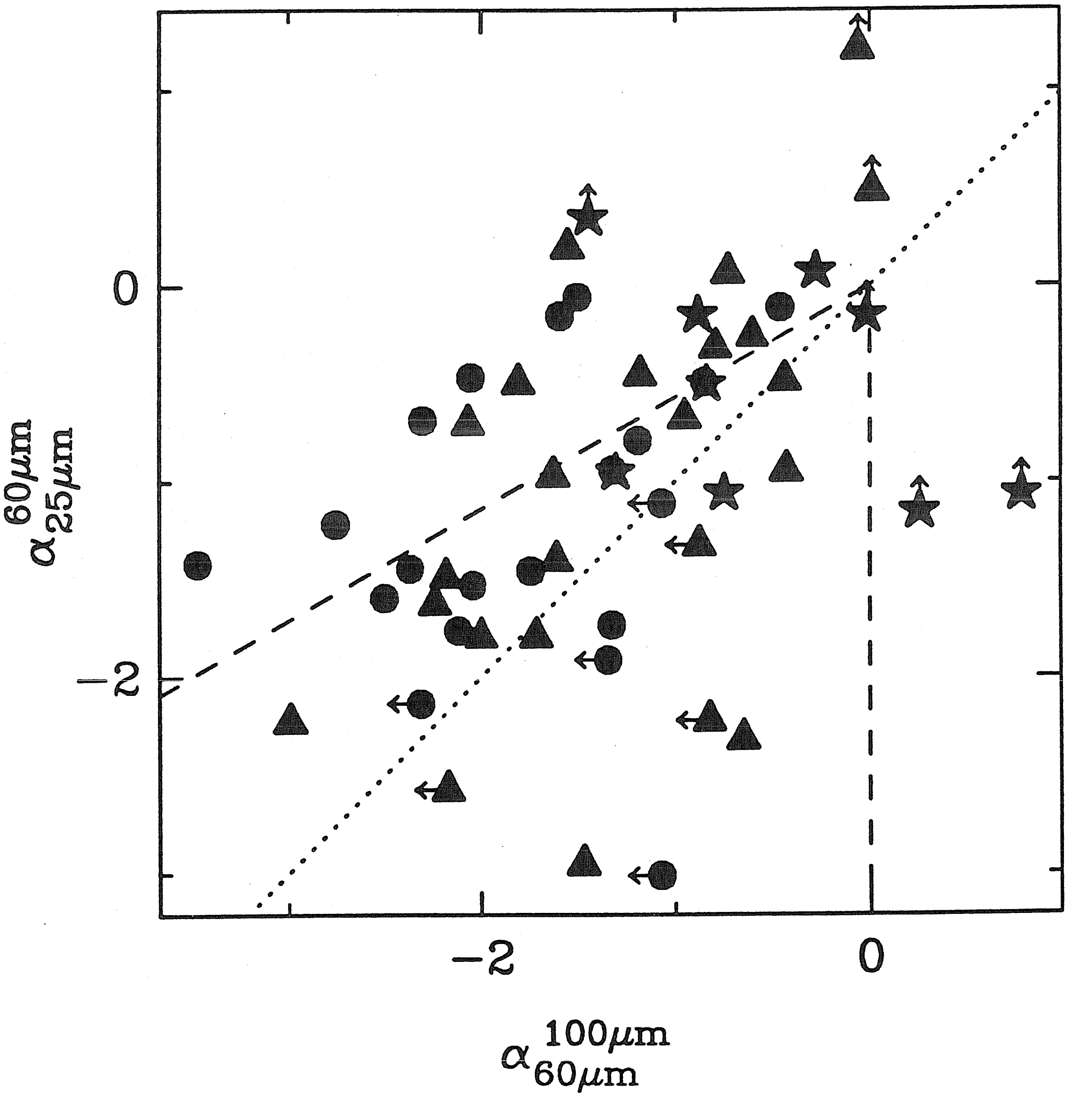

Figure 4

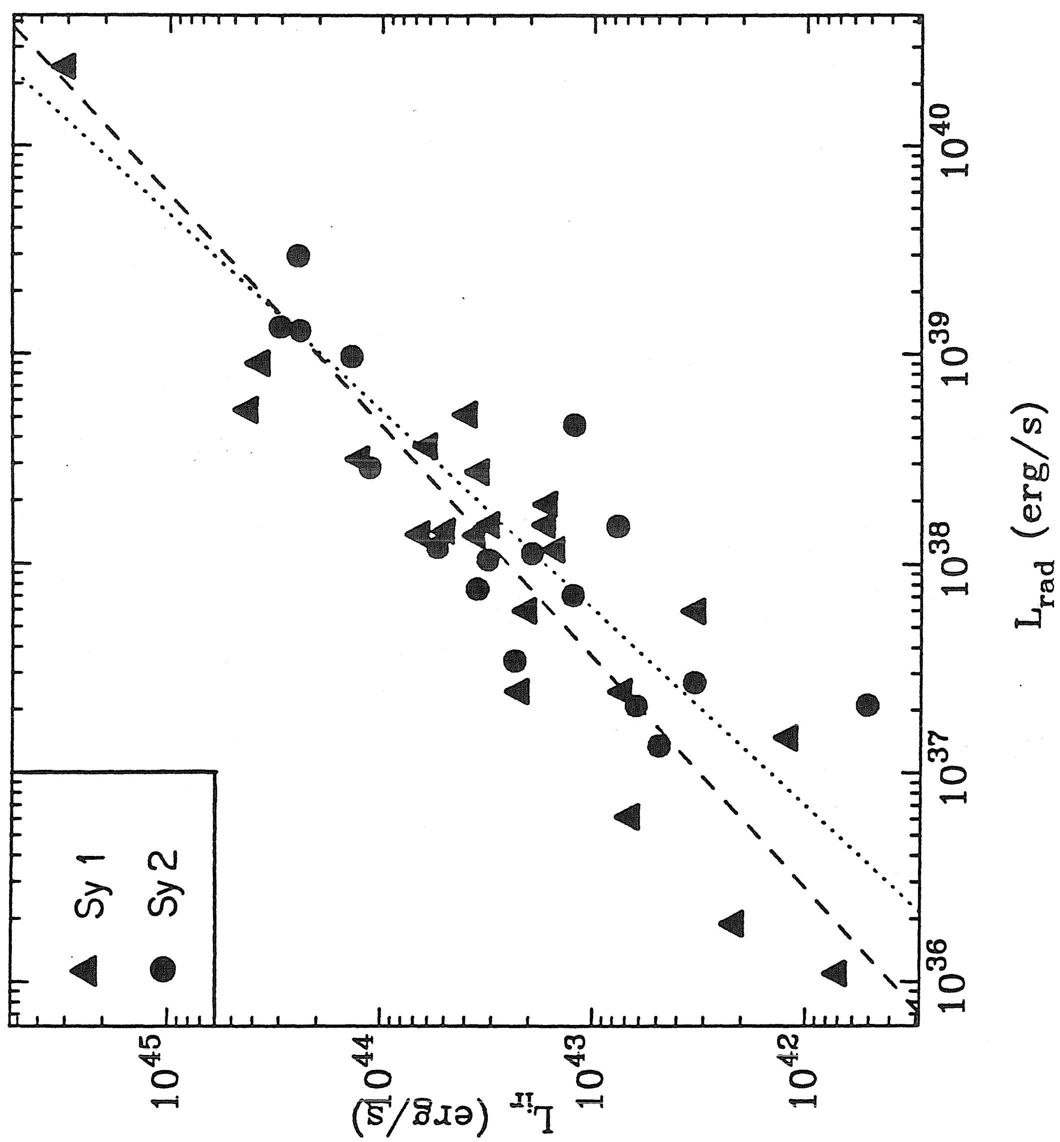
Sy 1
Sy 2
10^{36}
10^{37}
10^{38}
10^{39}
10^{40}
L_{rad} (erg/s)
10^{42}
10^{43}
10^{44}
10^{45}
L_{ir} (erg/s)

Figure 5

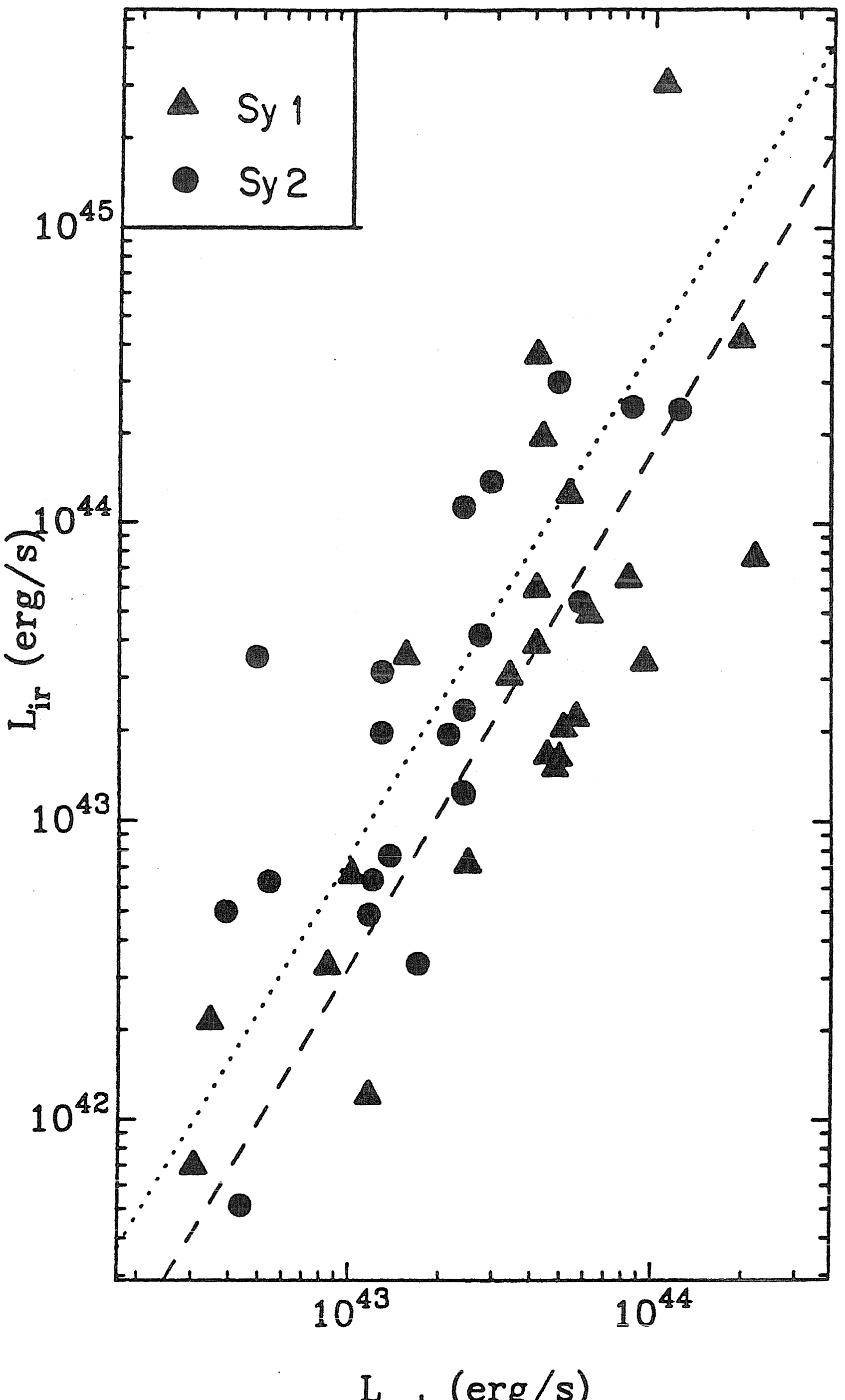

Figure 6

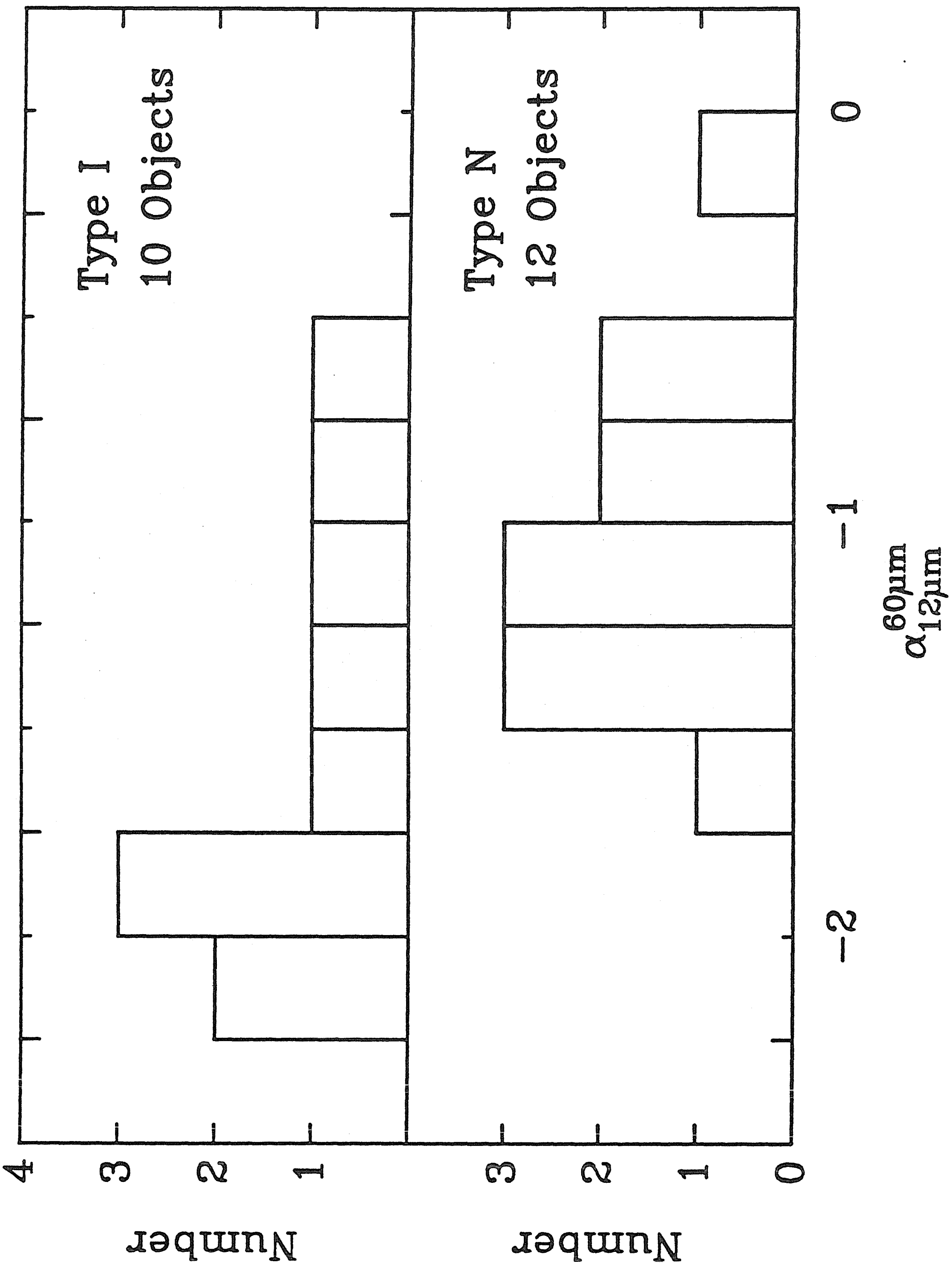
Type I
10 Objects
Type N
12 Objects
Number
Number
4
3
2
1
3
2
1
0
−2
−1
0
$\alpha_{12\mu m}^{60\mu m}$

Figure 7

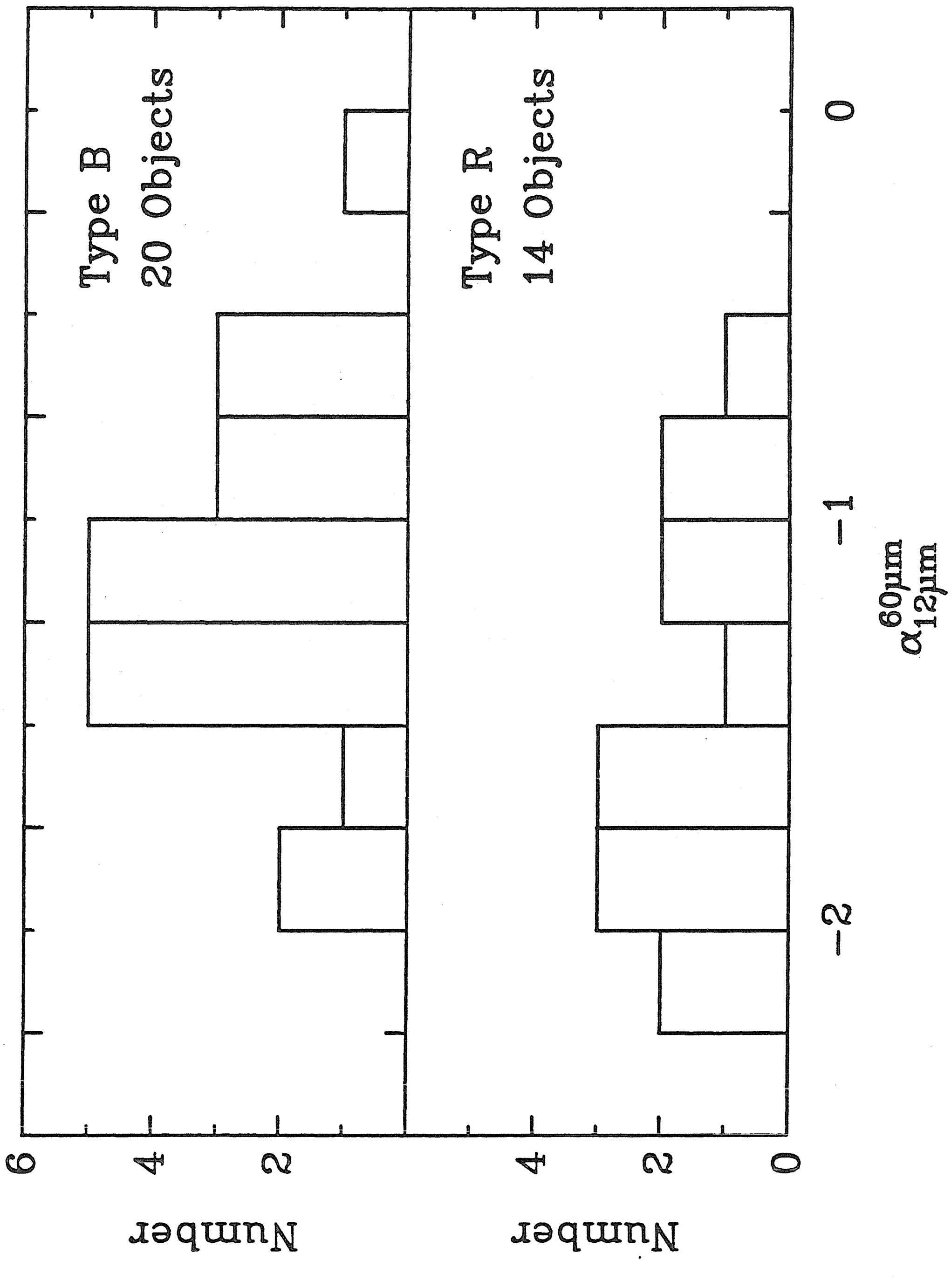
Type B
20 Objects
Type R
14 Objects
Number
Number
6
4
2
4
2
0
−2
−1
0
$\alpha^{60\mu m}_{12\mu m}$

Figure 8

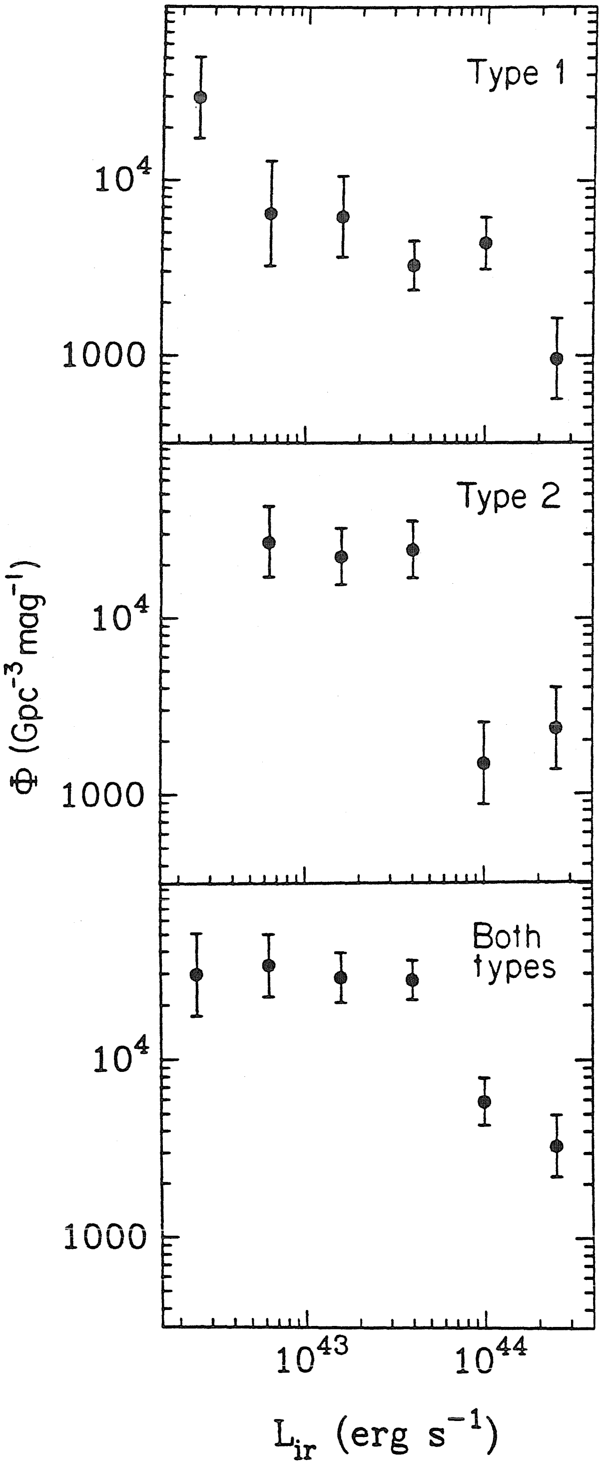
Type 1
Type 2
Both types
10^4
1000
Φ (Gpc^{-3} mag^{-1})
10^{43}
10^{44}
L$_{ir}$ (erg s^{-1})

Figure 9

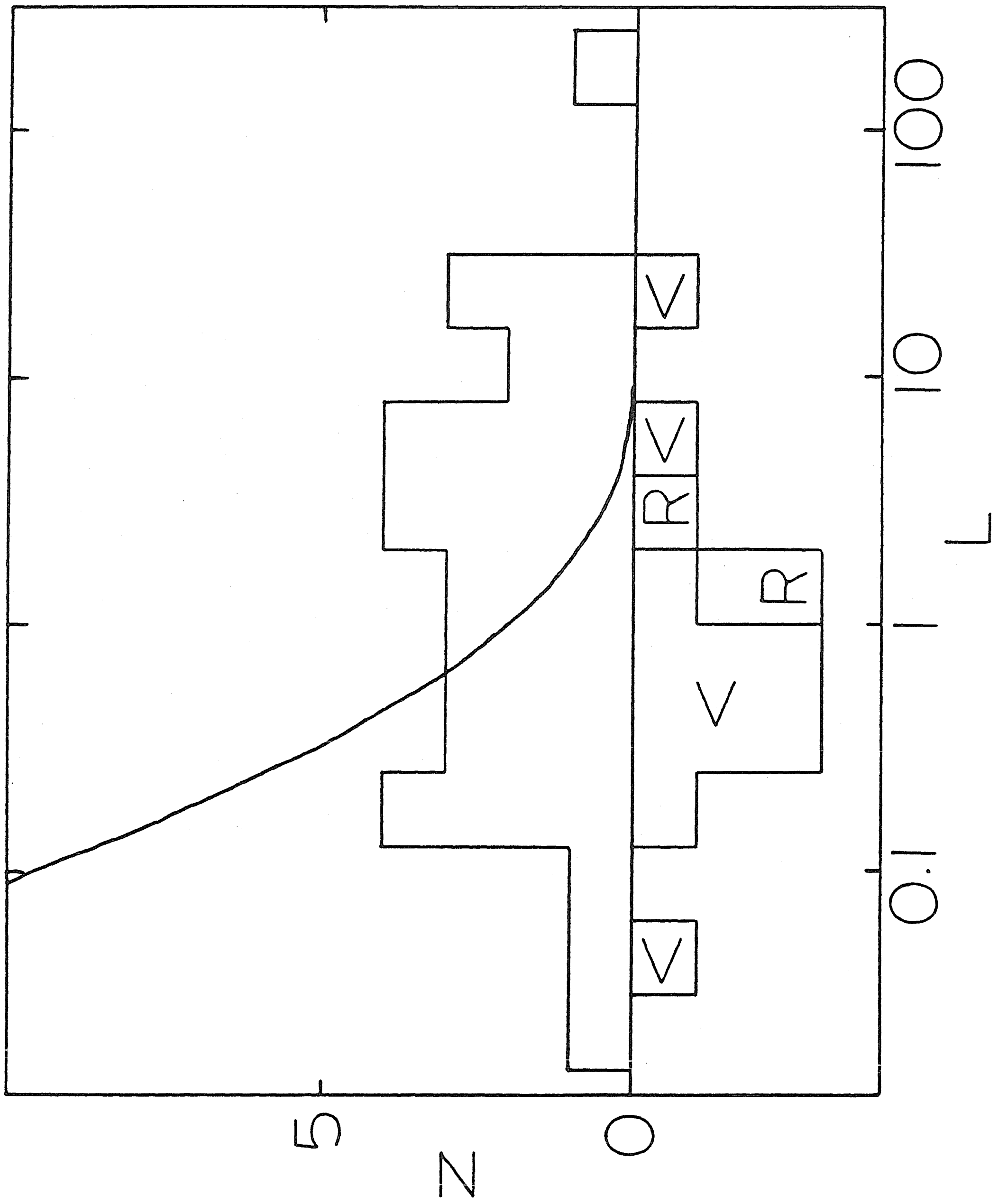

Figure 10

Chapter Six

FAR-INFRARED VARIABILITY IN ACTIVE GALACTIC NUCLEI *

---

* Written in collaboration with M. Malkan

ABSTRACT

Pointed IRAS observations were used to search for far-infrared variability in 22 active galaxies. Significant variability was seen in a number of objects, down to the levels of repeatability with which IRAS can measure fluxes. The far-infrared fluxes of three highly polarized objects ("blazars") varied by about a factor of two on time scales of a few months. In contrast, no convincing cases of variability greater than ~30% were found in any of the normal quasars or Seyfert galaxies studied. Thus, it appears that blazars may be strongly variable at all wavelengths, but normal active galaxies are systematically less variable in the far-infrared than at higher frequencies.

I. INTRODUCTION

The infrared emission from active galactic nuclei (AGNs) with high optical polarization (so-called "blazars", that is, BL Lac objects and highly polarized quasars) is generally believed to be nonthermal, possibly beamed, radiation from a compact source. Blazars are known to vary rapidly at all wavelengths at which they have been observed from X-rays to radio (see, e.g., Bregman *et al.* 1986). In particular, Ennis *et al.* (1982) and O'Dea *et al.* (1985) found that they have typical variability time scales of months at millimeter wavelengths. Robson *et al.* (1986) find that the infrared-millimeter spectrum of 3C 273 varies coherently over time scales of months to a year. This is strong evidence that these objects are dominated by nonthermal emission, because a thermally emitting region could not vary this rapidly. The nonthermal nature of the infrared continuum is confirmed by the high degree of linear polarization it frequently shows (Angel and Stockman 1980). Furthermore, Impey and Neugebauer (1987) found that radio selected AGNs (mostly blazars) tend to have flat far-infrared spectra ($\overline{\alpha}_{2.2-25\mu m} \approx -1; F_\nu \propto \nu^\alpha$), characteristic of nonthermal synchrotron radiation.

The far-infrared spectra of optically selected quasars (with $\overline{\alpha}_{2.2-25\mu m} = -1.09$, Edelson 1986, hereafter referred to as E86) and luminous Seyfert 1 galaxies ($\overline{\alpha}_{2.2-25\mu m} = -1.15$; Edelson, Malkan, and Rieke 1987, EMR hereafter) also tend to be flat, suggesting a similar nonthermal origin. However, normal quasars and Seyfert 1 galaxies are less violently variable than blazars. Nonetheless, X-ray, ultraviolet, optical, and near-infrared variablity have been well documented (e.g., Halpern 1982, de Bruyn, Readhead, and Sargent 1987, Cutri *et al.* 1985, Neugebauer *et al.* 1986). In particular, Cutri *et al.* (1985) found evidence that the variability in normal quasars becomes weaker from the optical to the near-infrared, though Neugebauer *et al.* (1986) found that the spectral index stayed relatively constant during outbursts. Unfortunately, normal quasars and Seyfert 1 galaxies are not strong far-infrared and millimeter sources, and only one of these objects (NGC 4151) has been monitored at wavelengths longer than 3.5 μm (Rieke and Lebofsky 1982). Although this variability is suggestive of nonthermal emission, some of it could also be attributed to variable thermal emission from an accretion disk or hot dust grains. In spite of the spectral evidence that their infrared continua are predominantly nonthermal, the normal quasars and Seyfert 1 galaxies are known to have low (but significant) continuum polarization (Stockman, Moore, and Angel 1983, Martin *et al.* 1983).

In sharp contrast, the continua of Seyfert 2 galaxies are not known to vary at any wavelength. Furthermore, Seyfert 2 galaxies tend to have very steep far-infrared spectra ($\overline{\alpha}_{2.2-25\mu m} = -1.56$), characteristic of thermal dust emission (EMR). Edelson and Malkan (1986, EM hereafter) and EMR found that low-luminosity Seyfert 1 galaxies can also have steep spectra, indicative of thermal emission. Thus, the observed spectral shapes suggest (but do not prove) that the far-infrared spectra of blazars, normal quasars, and luminous Seyfert 1 galaxies tend to be dominated by nonthermal emission, while the far-infrared spectra of Seyfert 2 galaxies and low-luminosity Seyfert 1 galaxies are dominated by thermal emission from dust.

EM and EMR showed that infrared thermally emitting regions in AGNs must be more than tens of light-years across, and thus cannot vary detectably on typical observing time scales (i.e., shorter than a decade). However, in AGNs with far-infrared emission which is predominantly nonthermal, it probably arises in a very small volume. EM, E86, and EMR found evidence that the far-infrared emission from quasars and luminous Seyfert 1 galaxies is dominated by radiation from a synchrotron self-absorbed source with a brightness temperature of $T \approx 3\text{x}10^{10}$ K, implying source sizes of order a light-day. Since the shortest allowed variability time scale for nonthermal emission in the infrared is thousands of times shorter than that for thermal emission in AGNs, variability is a potentially decisive probe of the nature of the far-infrared continuum. Detected variability is proof of a nonthermal continuum, but unfortunately the converse is not true: a constant source is not necessarily thermal.

In this paper, pointed observations made with *the Infrared Astronomical Satellite* (IRAS) are analyzed to determine the degree of variability of a heterogeneous sample of AGNs at far-infrared wavelengths. The sample and their IRAS measurements are discussed in the next section. The detection and analysis of variability is addressed in § III. The implications of variations are discussed in § IV. A concluding discussion and summary of the major results of this paper is given in § V. Throughout this paper, values of $H_0 = 75$ km/s/Mpc and $q_0 = 0$ are assumed.

II. SAMPLE AND DATA

The data for this study are ~400 pointed IRAS observations of 22 bright AGNs, which include most of the known AGNs detected with signal to noise ratio greater than 3 in at least four pointed IRAS observations, with at least one week between the first and last observation. Table 1 contains source information for the sample. The source name is given in Column 1, and the IRAS positional name, in Column 2. The resulting heterogeneous sample used in this survey consists of 6 blazars (denoted with a B in Column 3 of Table 1), 5 normal quasars (denoted with a Q) 9 Seyfert 1 galaxies (labeled with a 1), and 2 Seyfert 2 galaxies and other low-luminosity AGNs (denoted by a 2).

TABLE 1

Raw data from IRAS pointed observations were combined and mapped and source extractions performed in the standard fashion (Young *et al.* 1986). Positions of target AGNs and field stars (used for calibration) were taken from these maps. Data for individual pointed observations were also mapped seperatly, and source extractions were performed on these maps. The database of individual extractions were searched for sources with positions within 120″ of those determined in the summed maps. The source extractions produced a correlation coefficient, which measures how pointlike the source appears to be. All measurements with correlation coefficients less than 0.85 (less than 10% of the data) were rejected. A few bad points (less than 0.1% of the data) were also edited out, based on positional errors or the source being at the edge of the detector array.

Standard calibration constants were applied to convert the IRAS flux units to Janskys. The overall calibration uncertainty is estimated to be 10% at 12 μm, 15% at 25 μm and 60 μm, and 20% at 100 μm. Only one type of observing macro (DPS) was used, so the overall calibration of all fluxes is the same. Fortunately, the relative flux densities used in variability studies are much more accurately determined for most sources, as discussed below.

Table 2 is a summary of the IRAS pointed observations of these objects. The source name is listed in Column 1, and the observation wavelength (in microns) in Column 2. Column 3 contains the time interval (in days) between the first and last pointed IRAS observations, and Column 4 gives the number of pointed observations used. Column 5 gives the fraction of observations rejected due to low correlation coefficient. The mean flux density (in Janskys), and scatter in its observed value (in percent) are given in Columns 6 and 7, respectively.

TABLE 2

Light curves, dermined by combining the individual observations of each object, are presented in Figure 1. The fluxes and 1σ uncertainty bars are plotted as a function of time (UT day 1983). The data are normalized to a mean of unity, and the mean flux density is listed for each of the four wavelengths.

FIGURE 1

As an independent test of the stability of the fluxes extracted from the IRAS observations, 70 bright field sources were subjected to an identical analysis. Nearly half of the field sources were detected only at 12 μm and 25 μm, and are presumed to be stars. Most of the remaining field sources (detected mostly at 60 μm and 100 μm) are presumed to be galaxies. The results of this analysis is given are Table 3. Column 1 contains the IRAS positional name. All of the other columns are identical to those in Table 1.

TABLE 3

III. ANALYSIS

The light curves were tested for variability by fitting a model assuming a constant flux density throughout the IRAS observations. For the target sources, the mean flux densities (in Janskys) determined from this model are given in Column 6 of Table 2, and the goodness-of-fit parameter χ^2 is listed in Column 8. The probability (p) that a value of χ^2 this large could arise from chance is given in Column 9.

The 70 field sources (which are presumed to have non-variable fluxes) were tested in the same fashion. These data are presented in Table 3. The field sources were used to test the reliability of the fluxes. Light curves determined at 100 μm proved to be very unreliable, with 7 of 19 objects having derived values of χ^2 significant at the $p \leq 0.001$ level. This probably arises from the fact that the 100 μm detectors are not very reliable, or because the sources are confused due to interstellar cirrus or extended emission from the field galaxy. As the angle at which the satellite scanned the source changes as a function of time, an extended source will appear to have different flux densities in the highly elongated IRAS beam, producing spurious variations. Thus, the quantitative analysis was restricted to 12, 25, and 60 μm, with 100 μm light curves used only to confirm variations seen at other frequencies.

As many of the field sources were strongly detected at more than one wavelength, there were a total of 106 independent light curves measured. Four had χ^2 significant at the $p \leq 0.001$ level. However, none of these light curves showed any long term trends. Three of these were of galaxies at 60 μm. All of these objects showed evidence that extended emission from the galaxy or infrared cirrus may have confused the observation. The other occurs at 12 μm, and the large χ^2 is due to a single point being very low, probably due to a problem with the detector.

Several criteria were used to judge variability. First, a source was required to have a value of χ^2 such that the probibility of random occurence is $p \leq 0.001$. Second, the data must show a clear long-term trend, not just uncorrelated scatter at that wavelength. The same trend must also be present (but not necessarily at a statistically significant level) in at least one other IRAS wavelength. Finally, extended galaxies or fields with confusion due to infrared cirrus are rejected.

In spite of the possible sources of spurious variability discussed above, eighteen of the AGNs in the sample, III Zw 2, Fair 9, 3C 84, Mkn 3, Mkn 6, Mkn 79, PG 0838+77, NGC 4151, Ton 1542, Mkn 231, Mkn 279, Mkn 668, Mkn 841, 3C 351, 3C 371, 3C 390.3, Cyg A, and NGC 7469 showed no trace of significant variability at any of the four wavelengths observed. This list of non-variable AGNs includes objects with a wide range of fluxes, luminosities, and spectral shapes, which were observed on many different time scales. The observed scatter in their fluxes, which is fully consistent with their statistical uncertainties, is generally less than ~30% peak to peak. In fact, several of the brightest sources, Mkn 3, Mkn 79 and Mkn 231, and NGC 7469, have constant fluxes to better than the

10% level peak to peak. This excellent level of repeatability represents the highest precision obtainable from IRAS observations of bright AGNs free from any of the complications discussed above.

On the other hand, three AGNs (OJ 287, 3C 345, and BL Lac), but no field sources, fulfilled all the variability criteria. In addition, one other source (1E0241+62) had significant values of χ^2, but were rejected because they failed other tests. These four sources are discussed below.

a) 1E0241+62

This X-ray selected Seyfert 1 galaxy has a value of $\chi^2 = 3.18$ at 12 μm, corresponding to a probablity of $p = 0.0008$. However, this is due to uncorrelated scatter in data with no long term trends, and no strong variability is seen in the other IRAS bands, so this object does not exhibit confirmed far-infrared variability.

b) OJ 287

This BL Lac object is strongly variable at 12 μm, 60 μm, and 100 μm. It will be discussed in the next section.

c) 3C 345

This highly-polarized quasar is strongly variable at 12 and 100 μm. It is discussed in detail in the next section.

d) BL Lac

BL Lac is strongly variable at 25 μm. The light curve shows a definite long-term trend, which is also seen at 60 μm, although the variations are not as significant at 25 μm. It will be discussed in the next section.

The upper limits to infrared variability must be qualified by noting that the relevant range of time scales has not been sampled very completely. As IRAS rarely observed these objects more than once per day, objects with fast, low level variability would escape detection, being confused with observations which were rejected as having "uncorrelated scatter". These observations are not sensitive to variability, especially at low levels, with time scales shorter than a week. Over half of our observations are not sensitive to variations over one month, which would be somewhat shorter than the variability time scales typically found in monitoring of the optical and near-infrared continuum (Rieke and Lebofsky 1982; de Bruyn, Readhead, and Sargent 1987).

IV. DISCUSSION

Three of the six blazars observed (OJ 287, 3C 345, and BL Lac) were found to vary at far-infrared wavelengths. The temporal sampling of the IRAS observations is not well-suited to determining the shortest variability time scales in these objects. It is estimated that these blazars have far-infrared variability with a typical doubling time scale of about three months. The implied light-crossing size of three light months yields minimum brightness temperatures in the far-infrared of $T_b \gtrsim 10^6$ K. Since these temperatures are at least three orders of magnitude above the hottest possible thermally-emitting dust grains, the far-infrared variability is further confirmation that the continuum in these objects is predominantly nonthermal.

The size of the emitting region can be estimated if (as appears to be the case) the infrared emission from these blazars is synchrotron radiation which becomes self-absorbed at the break frequency of $\sim 10^{12}$ Hz (see EM, E86, and EMR for details). These calculations yield source sizes of order one light-day. There is also strong evidence that the emission from these objects is beamed (see Cohen and Unwin 1986), with typical $\Gamma \approx 5$. Thus, variability over time scales of a few hours, considerably more rapid than those observed, would not be ruled out by light-travel time arguments. These objects can vary this rapidly at optical and X-ray wavelengths (see Moore *et al.* 1982, Halpern 1982). Although these data are not ideally suited for studying fast variability, strong (factor of 2) variations would have been detected. There is no evidence for strong variations in any of these objects over time scales shorter than a few days. In this sense, blazars do not appear to vary as rapidly in the infrared as they possibly could.

EM and EMR argued that the steep far-infrared spectra of several of the AGNs which were found to be non-variable are predominantly thermal. The constancy of the far-infrared emission in Mkn 3, Mkn 6, Mkn 79, Mkn 231, NGC 7469, Cyg A, 3C 84 and 3C 390.3 could be simply explained if it is produced in a region which is too large to show significant variability on time scales as short as one year. This would certainly be the case for thermal emission from dust grains. In several of these objects, EMR found that some of their far-infrared flux shows a significant spatial extent (on scales of 100 pc or more) and thus does not arise in the active nucleus. It is still possible that these active nuclei emit some nonthermal far-infrared energy which is intrinsically variable by more than ~30%, but was undetectable in the large IRAS beams.

Unlike some of the blazars, the normal AGNs in this study showed no evidence of far-infrared variability on time scales of up to a few months. Our most interesting upper limits to variability are for those high-luminosity objects whose relatively flat infrared spectra give little indication of the presence of significant thermal contamination, such as Fairall 9, NGC 4151, Mkn 841, Ton 1542 and PG 0838+77. The lack of variability in these normal quasars and luminous Seyfert 1 galaxies does not rule out a possible thermal origin for much of the far-infrared continuum, but unfortunately it also does not rule out a nonthermal origin, either.

It is significant that the upper limits to far-infrared variability set in this paper are smaller than the variability many of the same AGNs show at ultraviolet and X-ray, and in some cases, optical wavelengths. This suggests that continuum variability is an increasing function of observing frequency. However, our sensitivity in the far-infrared is still too poor compared to that attained at shorter wavelengths to study this wavelength-dependence in detail. The most sensitive monitoring programs at red and near-infrared wavelengths (Rieke and Lebofsky 1982 , Cutri *et al.* 1985, Neugebauer *et al.* 1986) usually detect variability of only ~30%. Unfortunately, the IRAS observations are not sufficiently precise to exclude the possibility that the far-infrared continuum is variable, at the same levels as these previous studies detected at shorter wavelengths.

V. CONCLUSIONS

This study used pointed IRAS observations to study the variability of 22 AGNs. Three blazars were found to vary by about a factor of two over time scales of a few months. This variability is not as rapid as may be possible from these objects. No normal quasars or Seyfert galaxies were found to vary, although these data are not sufficiently sensitive to detect slow, small scale flickering at the same levels often seen at optical and near-infrared wavelengths.

Unfortunately, the poor temporal sampling of the IRAS pointed data makes it difficult to use these results to strongly constrain the emission mechanism in normal quasars and Seyfert 1 galaxies. The radio emission from these blazars appears to be beamed with typical $\Gamma \approx 5$ (Cohen and Unwin 1986). If this is also the case with the infrared emission, then the true variability time scale is of the order of one year. The IRAS data are never sensitive to variations over time scales longer than 6–8 months (and for most objects, they are only sensitive to variations with much shorter time scales). Thus, it is quite possible that normal quasars and Seyfert 1 galaxies are variable in the far-infrared, but on time scales longer than the lifetime of IRAS.

EM, E86, and EMR presented evidence that the infrared continuua of normal quasars and Seyfert 1 galaxies are dominated by synchrotron radiation from a self-absorbed source of order a light day across. The electron lifetimes are also expected to be very small. The failure to detect strong variability in normal quasars and Seyfert galaxies, and the fact that the variability time scales observed in blazars also appear to be much longer than the light-crossing times, suggests the possibility there may be some physical process which regulates this nonthermal luminosity so that it does not vary detectably on time scales less than a year.

The authors would like to thank H. Hanson of the Infrared Processing and Analysis Center for tirelessly performing the IRAS source extractions, and W. Rice of IPAC for helping us understand the IRAS data. This research was supported by NASA grant NAS 7-918.

TABLE 1

VARIABILITY STUDY SOURCE LIST

Source	Position	Type
III Zw 2	0007+1041	Q
Fair 9	0121−5903	Q
1E	0241+6215	1
3C 84	0316+4119	B
Mkn 3	0609+7102	2
Mkn 6	0645+7429	1
Mkn 79	0738+4955	1
PG	0838+7704	Q
OJ 287	0851+2017	B
NGC 4151	1207+3941	1
Ton 1542	1229+2026	1
Mkn 231	1254+5708	Q
Mkn 279	1351+6933	1
Mkn 668	1404+2841	Q
Mkn 841	1501+1037	1
3C 345	1641+3954	B
3C 351	1704+6048	B
3C 371	1807+6949	B
3C 3903	1845+7943	1
Cyg A	1957+4035	2
BL Lac	2200+4202	B
NGC 7469	2300+0836	1

TABLE 2

Sample Variability Study Data

Source	λ (μm)	N	Days	Rej.	Flux (Jy)	Scatter (%)	χ^2	p
III Zw 2	12	12	10	0.00	0.11	71	0.78	0.6589
III Zw 2	25	10	9	0.00	0.17	51	0.56	0.8290
III Zw 2	60	14	10	0.07	0.21	64	2.24	0.0064
Fair 9	12	4	14	0.00	0.38	15	1.66	0.1740
Fair 9	25	4	14	0.00	0.55	8	0.46	0.7104
Fair 9	60	4	14	0.00	0.59	13	0.75	0.5242
Fair 9	100	4	14	0.00	0.83	9	0.12	0.9454
0241+62	12	7	37	0.30	0.48	27	3.42	0.0022
0241+62	25	8	37	0.20	0.74	20	1.96	0.0564
0241+62	60	3	4	0.70	0.65	19	1.93	0.1447
3C 84	12	13	178	0.00	1.00	15	0.79	0.6653
3C 84	25	13	178	0.00	3.24	21	1.25	0.2444
3C 84	60	13	178	0.00	7.52	23	1.40	0.1575
3C 84	100	12	178	0.08	9.96	19	2.26	0.0095
Mkn 3	12	3	12	0.00	0.65	1	0.03	0.9733
Mkn 3	25	4	12	0.00	2.69	3	0.21	0.8906
Mkn 3	60	4	12	0.00	3.82	9	0.53	0.6639
Mkn 6	12	40	33	0.00	0.20	70	1.44	0.0376
Mkn 6	25	62	33	0.00	0.67	25	0.66	0.9801
Mkn 6	60	65	33	0.00	1.29	19	0.45	0.9999
Mkn 6	100	45	33	0.00	1.40	66	1.17	0.2084
Mkn 79	12	4	163	0.00	0.29	16	0.92	0.4298
Mkn 79	25	4	163	0.00	0.70	13	0.78	0.5064
Mkn 79	60	4	163	0.00	1.52	6	0.19	0.9017
Mkn 79	100	4	163	0.00	2.80	6	0.36	0.7844
0838+77	25	5	3	0.00	0.11	34	0.61	0.6558
0838+77	60	14	22	0.00	0.18	74	1.14	0.3152
OJ 287	12	11	215	0.00	0.22	122	6.45	0.0000
OJ 287	25	11	215	0.00	0.43	33	0.76	0.6716
OJ 287	60	11	215	0.00	0.93	65	10.27	0.0000
OJ 287	100	11	215	0.00	1.58	54	7.88	0.0000
NGC 4151	12	5	26	0.00	1.84	8	0.42	0.7941
NGC 4151	25	6	26	0.00	4.72	11	0.38	0.8629
NGC 4151	60	6	26	0.00	6.94	23	1.54	0.1750
NGC 4151	100	6	26	0.00	10.17	16	0.82	0.5322
Ton 1542	12	7	8	0.13	0.10	45	0.79	0.5787
Ton 1542	25	9	8	0.00	0.18	66	1.10	0.3622
Ton 1542	60	5	3	0.29	0.18	31	0.71	0.5865

TABLE 2

SAMPLE VARIABILITY STUDY DATA (cont.)

Source	λ (μm)	N	Days	Rej.	Flux (Jy)	Scatter (%)	χ^2	p
Mkn 231	12	4	20	0.00	1.75	6	0.36	0.7833
Mkn 231	25	4	20	0.00	8.45	7	0.54	0.6516
Mkn 231	60	4	20	0.00	33.34	7	0.24	0.8705
Mkn 231	100	4	20	0.00	38.94	8	0.74	0.5266
Mkn 279	12	6	138	0.00	0.14	30	1.21	0.3011
Mkn 279	25	6	138	0.00	0.28	32	3.49	0.0037
Mkn 279	60	6	138	0.00	1.27	6	0.14	0.9833
Mkn 279	100	6	138	0.00	2.74	15	0.95	0.4491
Mkn 668	12	4	29	0.00	0.60	14	1.47	0.2192
Mkn 668	25	4	29	0.00	0.40	33	3.97	0.0077
Mkn 668	60	4	29	0.00	0.79	12	0.82	0.4841
Mkn 668	100	4	29	0.00	1.20	27	2.51	0.0566
Mkn 841	12	9	31	0.00	0.20	32	0.94	0.4844
Mkn 841	25	10	31	0.00	0.50	23	0.86	0.5644
Mkn 841	60	10	31	0.00	0.56	37	1.23	0.2725
3C 345	12	31	100	0.03	0.12	98	2.44	0.0000
3C 345	25	32	100	0.00	0.28	35	1.23	0.1741
3C 345	60	32	100	0.00	0.68	40	1.43	0.0562
3C 345	100	24	90	0.04	1.30	68	3.17	0.0000
3C 351	12	3	1	0.25	0.06	18	0.21	0.8078
3C 351	25	18	86	0.00	0.13	67	1.11	0.3315
3C 351	60	5	81	0.71	0.20	26	0.49	0.7409
3C 371	12	25	68	0.14	0.10	55	0.64	0.9061
3C 371	25	61	72	0.02	0.16	114	1.28	0.0692
3C 371	60	65	72	0.02	0.25	128	1.12	0.2355
3C 371	100	2	6	0.82	0.81	33	0.67	0.4118
3C 390.3	12	59	177	0.00	0.13	115	1.15	0.2005
3C 390.3	25	83	178	0.00	0.32	41	1.14	0.1878
3C 390.3	60	82	194	0.01	0.22	156	1.28	0.0475
Cyg A	12	18	197	0.00	0.14	31	0.54	0.9327
Cyg A	25	18	197	0.00	0.81	12	0.60	0.8980
Cyg A	60	14	192	0.22	2.74	19	1.01	0.4389
BL Lac	12	17	47	0.00	0.12	78	0.94	0.5204
BL Lac	25	18	47	0.00	0.23	56	2.80	0.0001
BL Lac	60	18	47	0.00	0.45	51	1.42	0.1179
NGC 7469	12	4	22	0.00	1.10	12	1.18	0.3143
NGC 7469	25	4	22	0.00	4.93	10	0.86	0.4625
NGC 7469	60	4	22	0.00	26.53	6	0.31	0.8192
NGC 7469	100	3	13	0.25	43.75	3	0.06	0.9408

TABLE 3

Field Source Variability Study Data

Source	λ (μm)	N	Days	Rej.	Flux (Jy)	Scatter (%)	χ^2	p
0008+1022	12	15	10	0.00	0.32	42	2.04	0.0122
0007+1051	12	15	10	0.00	0.19	46	0.72	0.7565
0009+1035	60	14	9	0.07	0.23	78	1.90	0.0249
0009+1002	60	7	8	0.30	0.29	49	1.32	0.2454
0007+1041	60	14	10	0.07	0.21	64	2.24	0.0064
0241+6155	12	8	35	0.11	0.08	59	0.80	0.5868
0241+6155	25	8	37	0.20	0.14	34	1.07	0.3798
0239+6214	12	7	35	0.00	0.09	92	2.65	0.0143
0239+6214	25	4	5	0.43	0.10	59	0.75	0.5204
0240+6259	12	6	5	0.00	0.80	22	2.43	0.0330
0240+6259	25	6	5	0.00	0.22	21	0.82	0.5346
0239+6222	12	10	37	0.00	0.41	21	1.21	0.2841
0239+6222	25	10	37	0.00	0.13	137	2.36	0.0116
0244+6158	12	10	37	0.00	0.23	35	1.02	0.4187
0244+6158	25	5	5	0.00	0.08	39	0.78	0.5378
0317+4054	12	10	178	0.00	0.33	38	1.09	0.3626
0316+4047	12	10	178	0.00	0.18	42	0.74	0.6763
0315+4100	12	6	2	0.33	0.12	83	1.10	0.3557
0317+4038	12	6	178	0.25	0.10	128	2.41	0.0339
0314+4154	12	5	174	0.17	0.09	84	1.37	0.2418
0318+4041	60	10	178	0.00	0.47	82	1.49	0.1456
0316+4127	60	13	178	0.00	0.33	187	8.83	0.0000
0611+7137	12	4	12	0.00	0.27	29	2.23	0.0823
0648+7445	12	63	33	0.00	0.47	36	0.79	0.8790
0648+7445	25	45	33	0.00	0.21	115	1.60	0.0070
0643+7419	12	54	33	0.00	3.01	27	0.83	0.8000
0643+7419	25	58	33	0.00	0.94	43	1.40	0.0252
0646+7411	12	64	33	0.00	0.34	75	1.39	0.0226
0646+7411	25	16	31	0.24	0.11	78	0.67	0.8192
0645+7429	60	65	33	0.00	1.29	19	0.45	0.9999
0645+7429	12	4	163	0.00	0.29	16	0.92	0.4298
0645+7429	25	4	163	0.00	0.70	13	0.78	0.5064
0645+7429	60	4	163	0.00	1.52	6	0.19	0.9017
0737+5039	25	5	3	0.00	0.11	34	0.61	0.6558
0737+5039	60	14	22	0.00	0.18	74	1.14	0.3152

TABLE 3

FIELD SOURCE VARIABILITY STUDY DATA (cont.)

Source	λ (μm)	N	Days	Rej.	Flux (Jy)	Scatter (%)	χ^2	p
0851+2009	12	11	215	0.00	0.45	78	1.68	0.0792
0851+1946	12	9	207	0.10	0.51	27	1.41	0.1882
0852+2027	60	11	215	0.00	0.25	71	1.28	0.2365
0851+2024	60	10	215	0.00	0.16	66	0.93	0.5016
0851+2040	60	4	45	0.20	0.18	126	4.15	0.0060
1207+3942	12	4	18	0.00	0.89	12	0.61	0.6056
1207+3942	25	6	26	0.00	0.23	31	0.59	0.7109
1206+3911	60	6	26	0.00	0.40	40	1.19	0.3099
1229+2111	12	10	12	0.00	0.27	36	1.86	0.0532
1228+2029	12	10	12	0.00	0.19	70	1.95	0.0403
1230+2101	60	10	12	0.00	0.26	22	0.64	0.7650
1229+2009	60	7	8	0.22	0.11	27	0.25	0.9580
1229+2020	60	9	12	0.00	0.14	67	1.61	0.1167
1251+5705	12	4	20	0.00	1.25	6	0.37	0.7761
1251+5705	25	4	20	0.00	0.32	35	3.00	0.0293
1349+6923	12	5	138	0.17	0.43	19	2.86	0.0220
1349+6923	25	5	138	0.00	0.10	55	0.82	0.5101
1404+2840	12	4	29	0.00	0.60	14	1.47	0.2192
1404+2840	25	4	29	0.00	0.40	33	3.97	0.0077
1404+2900	60	4	29	0.00	0.14	77	2.87	0.0351
1501+1028	12	10	31	0.00	0.38	19	0.99	0.4448
1501+1028	25	7	15	0.13	0.13	101	1.97	0.0657
1501+1055	12	10	31	0.00	0.81	16	0.86	0.5621
1501+1055	25	10	31	0.00	0.21	72	0.80	0.6137
1641+4021	12	20	43	0.09	0.11	77	1.62	0.0450
1640+3944	12	31	100	0.00	0.12	223	2.97	0.0000
1640+3944	25	32	100	0.00	0.16	54	1.07	0.3677
1640+3944	60	32	100	0.00	1.56	29	1.59	0.0195
1641+3954	12	5	92	0.17	0.09	99	1.90	0.1071
1641+3954	60	10	90	0.09	0.35	29	1.11	0.3518
1640+3932	60	17	43	0.19	0.19	130	1.70	0.0394
1640+4022	60	16	64	0.06	0.16	89	0.81	0.6666
1702+6023	25	5	7	0.17	0.08	38	0.40	0.8117
1702+6023	60	8	14	0.00	1.11	154	6.13	0.0000
1702+6037	60	12	16	0.08	0.16	95	1.69	0.0687
1703+6047	60	11	82	0.39	0.21	80	1.14	0.3259

TABLE 3

Field Source Variability Study Data (cont.)

Source	λ (μm)	N	Days	Rej.	Flux (Jy)	Scatter (%)	χ^2	p
1804+6950	12	8	66	0.20	0.09	55	0.34	0.9369
1804+6950	25	12	45	0.00	0.09	73	0.46	0.9287
1804+6950	60	69	72	0.00	0.74	82	1.37	0.0229
1807+6936	12	5	56	0.17	0.10	45	0.24	0.9129
1807+6936	25	5	27	0.00	0.10	44	0.32	0.8618
1807+6936	60	56	68	0.03	0.24	134	1.35	0.0448
1802+6932	60	37	28	0.08	0.34	178	1.82	0.0019
1808+7009	25	6	32	0.14	0.09	53	0.26	0.9357
1808+7009	60	58	54	0.03	0.31	102	1.78	0.0003
1842+7926	25	29	79	0.06	0.15	102	1.34	0.1077
1842+7926	60	41	79	0.00	0.74	46	1.08	0.3411
1854+8017	60	25	49	0.04	0.20	89	1.17	0.2586
1850+7922	12	27	194	0.00	0.28	72	1.22	0.2000
1850+7922	25	8	47	0.27	0.10	60	1.04	0.4002
1846+8019	60	4	16	0.00	0.11	74	1.17	0.3182
1957+4116	12	8	21	0.11	4.10	9	0.43	0.8843
1957+4116	25	8	21	0.00	2.43	9	0.55	0.7939
1957+4116	60	8	21	0.00	1.30	46	3.03	0.0035
1957+4104	12	16	197	0.11	0.60	24	1.70	0.0432
1957+4104	25	18	197	0.00	0.18	61	2.16	0.0037
1958+4032	12	18	197	0.00	1.78	16	0.70	0.8070
1958+4032	25	18	197	0.00	1.25	29	1.91	0.0129
1958+4025	12	15	197	0.06	0.09	101	1.30	0.1953
1958+4025	25	7	197	0.13	0.07	174	1.31	0.2474
1957+4025	12	18	197	0.00	0.24	34	1.14	0.3046
1957+4025	25	18	197	0.00	0.13	34	0.58	0.9096
2204+4131	25	6	4	0.00	0.17	30	1.12	0.3454
2204+4131	60	7	5	0.00	1.85	12	0.51	0.7983
2202+4122	12	4	16	0.33	0.09	46	0.51	0.6722
2202+4122	25	9	17	0.25	0.12	91	0.95	0.4734
2202+4122	60	11	17	0.00	1.20	22	1.18	0.2960
2201+4214	12	4	40	0.00	0.08	138	2.55	0.0538
2201+4214	25	14	44	0.07	0.11	114	1.96	0.0196
2201+4214	60	18	47	0.00	0.98	11	0.30	0.9976
2200+4208	12	18	47	0.00	2.31	29	0.89	0.5914
2200+4208	25	18	47	0.00	0.76	26	1.16	0.2889
2200+4208	60	18	47	0.00	0.22	47	0.90	0.5729
2301+0901	60	4	22	0.00	0.84	8	0.35	0.7921
2300+0822	12	4	22	0.00	0.29	11	0.26	0.8568

REFERENCES

Angel, J. R. and Stockman, H. S. 1980, *Ann. Rev. Astr. Ap.*, **18**, 321.

Bregman, J. *et al.* 1986, *Ap. J.*, **301**, 708.

Clegg, P. G. *et al.* 1983, *Nature*, **305**, 194.

Cohen, M. H. and Unwin, S. C. 1986, *IAU Symposium*, # **110**, 95.

Cutri, R. M. *et al.* 1985, *Ap. J.*, **296**, 423.

de Bruyn, A. G., Readhead, A. S. C., and Sargent, W. L. W. 1987, in preparation.

Edelson, R. A. 1986, *Ap. J. (Letters)*, **309**, L69 (E86).

Edelson, R. A. and Malkan, M. A. 1986, *Ap. J.*, **308**, 59 (EM).

Edelson, R. A., Malkan, M. A., Rieke, G. H. 1986, *Ap. J.*, in press (EMR).

Ennis, D. J. *et al.* 1982, *Ap. J.*, **262**, 451.

Halpern, J. P. 1982 *Ph.D. Thesis, Harvard University.*

Impey, C. D. and Neugebauer, G. 1987, *Ap. J.*, in preparation.

Martin, P. G., Thompson, I. B., Maza, J., Angel, J. R. 1983, *Ap. J.*, **266**, 470.

Moore, R. L. *et al.* 1982, *Ap. J.*, **260**, 415.

Neugebauer, G. *et al.* 1986, *Ap. J.*, in press.

O'Dea, C. P. *et al.* 1985, *Proceedings of Garching Conference on Ultraviolet and X-Ray Emission from Active Galactic Nuclei*, p. 63.

Rieke, G. H. 1978, *Ap. J.*, **226**, 550.

Rieke, G. H. and Lebofsky, M. J. 1982, *Ap. J.*, **250**, 87.

Robson, I. *et al.* 1986, preprint.

Stockman, H. S., Moore, R., Angel, J. R. 1984, *Ap. J.*, **279**, 485.

Young, E. T. *et al.* 1985, *User's Guide to the IRAS Pointed Data Products.*

FIGURE CAPTIONS

FIG 1.—Far-infrared light curves for 22 AGNs. Normalized flux density is plotted as a function of time, with 1σ error bars. The caption to each panel gives the source name, observing wavelength, and mean flux density, in Janskys.

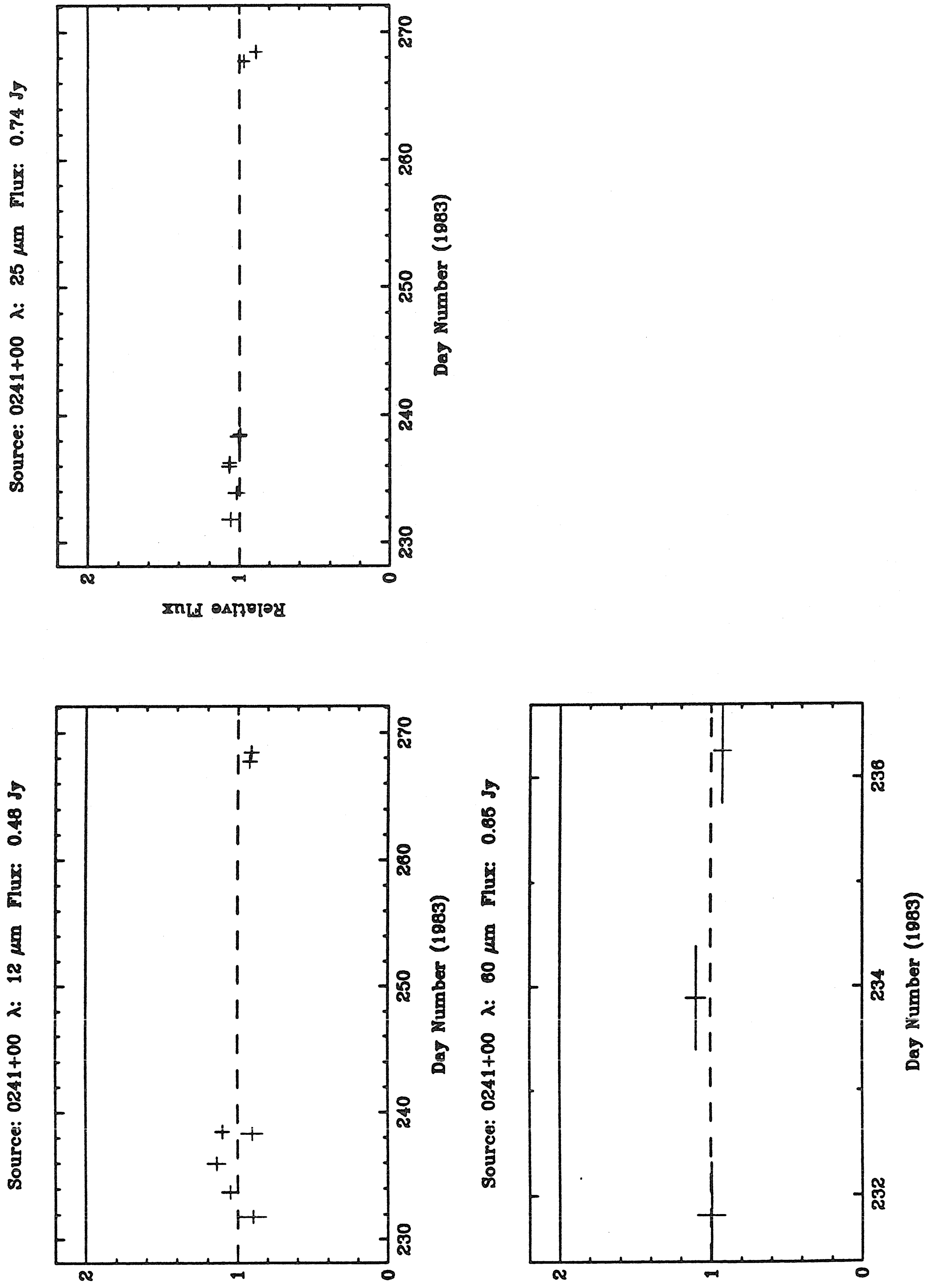
Source: 0241+00 λ: 25 μm Flux: 0.74 Jy
Relative Flux
0
1
2
Day Number (1983)
230
240
250
260
270
Source: 0241+00 λ: 12 μm Flux: 0.48 Jy
Relative Flux
0
1
2
Day Number (1983)
230
240
250
260
270
Source: 0241+00 λ: 60 μm Flux: 0.65 Jy
Relative Flux
0
1
2
Day Number (1983)
232
234
236

Figure 1 (a)

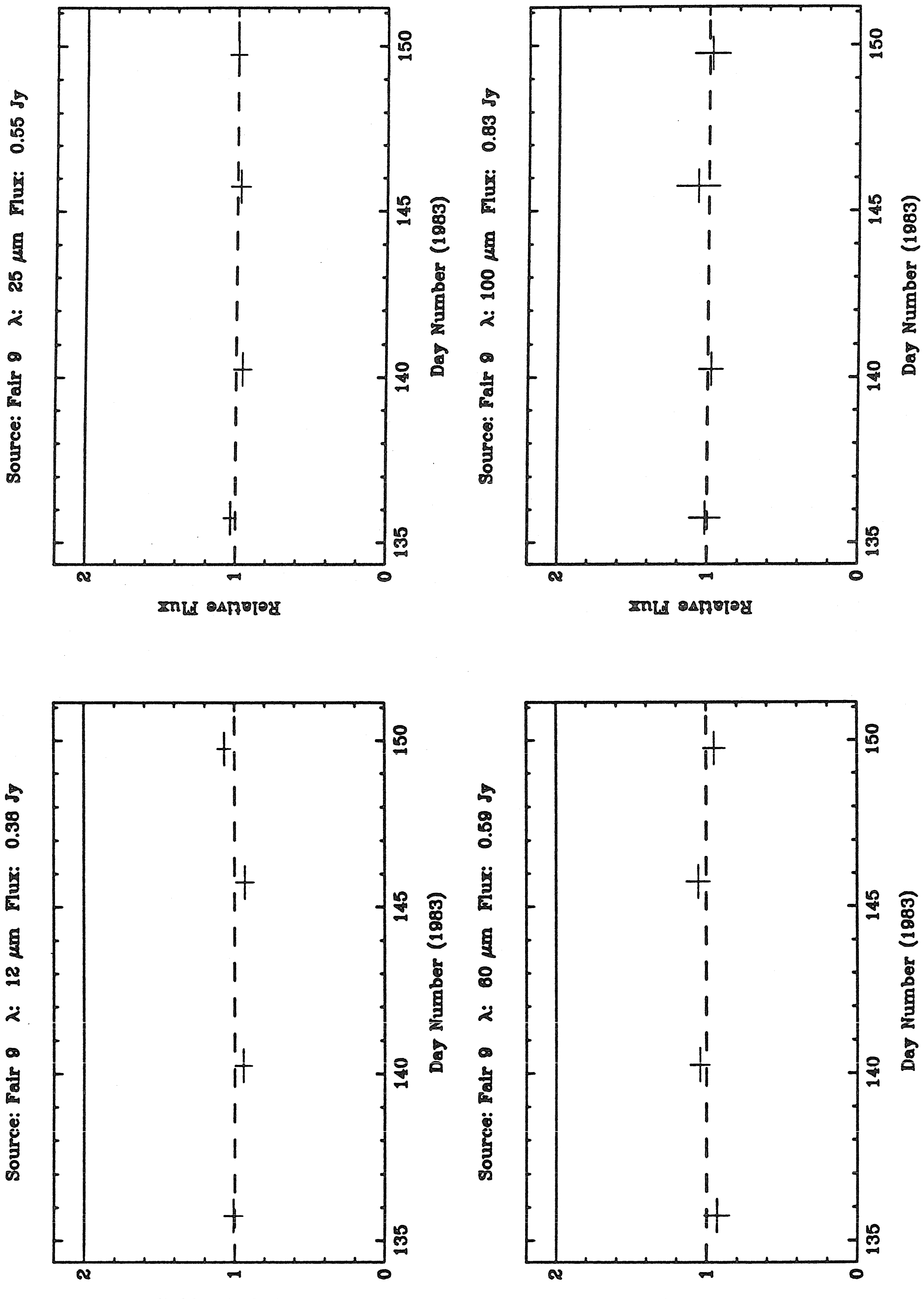
Source: Fair 9 λ: 12 μm Flux: 0.38 Jy
Source: Fair 9 λ: 25 μm Flux: 0.55 Jy
Source: Fair 9 λ: 60 μm Flux: 0.59 Jy
Source: Fair 9 λ: 100 μm Flux: 0.83 Jy
Relative Flux
0
1
2
Day Number (1983)
135
140
145
150

Figure 1 (b)

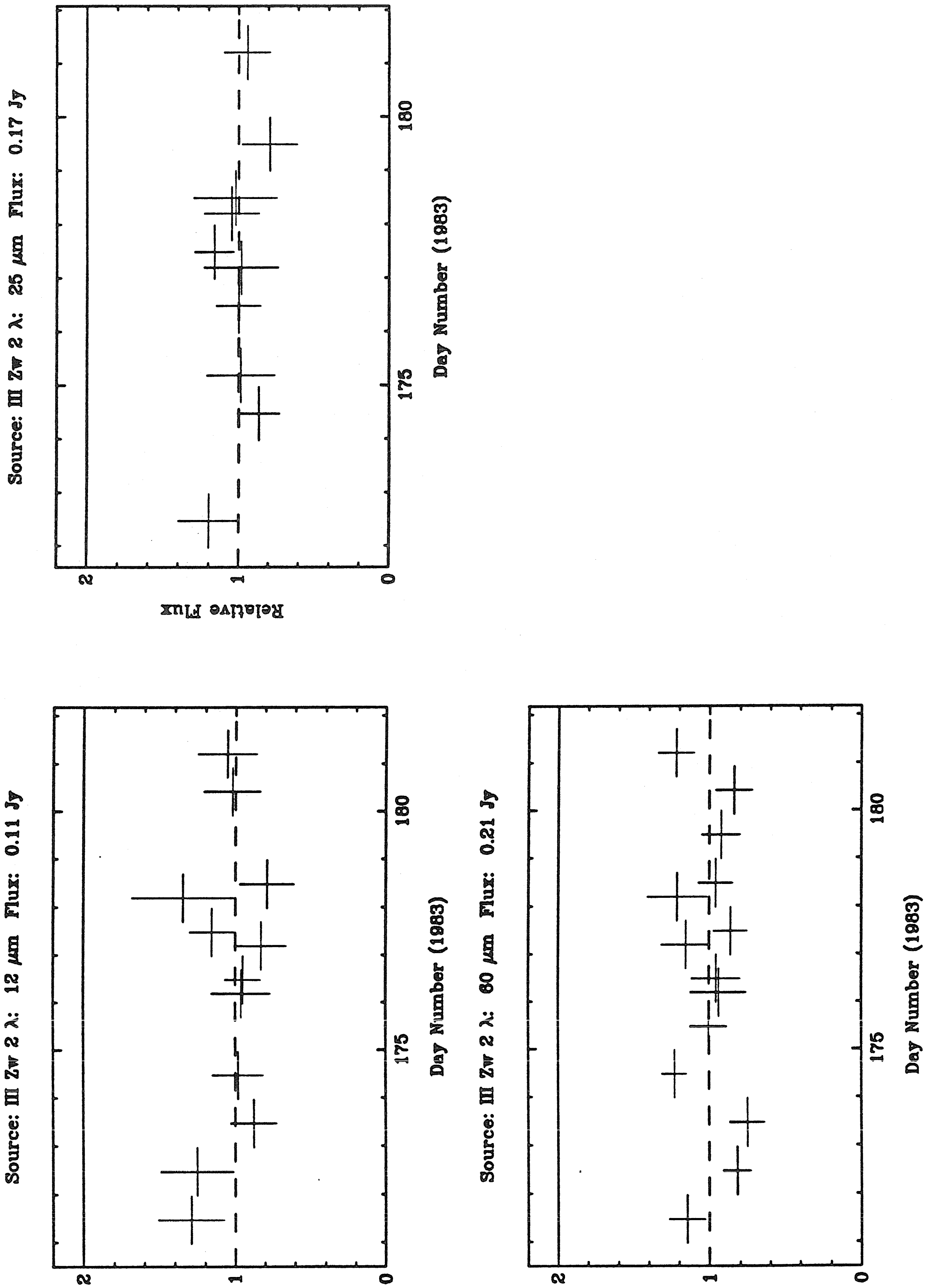
Source: III Zw 2 λ: 25 μm Flux: 0.17 Jy
Relative Flux
0
1
2
175
180
Day Number (1983)
Source: III Zw 2 λ: 12 μm Flux: 0.11 Jy
Relative Flux
0
1
2
175
180
Day Number (1983)
Source: III Zw 2 λ: 60 μm Flux: 0.21 Jy
Relative Flux
0
1
2
175
180
Day Number (1983)

Figure 1 (c)

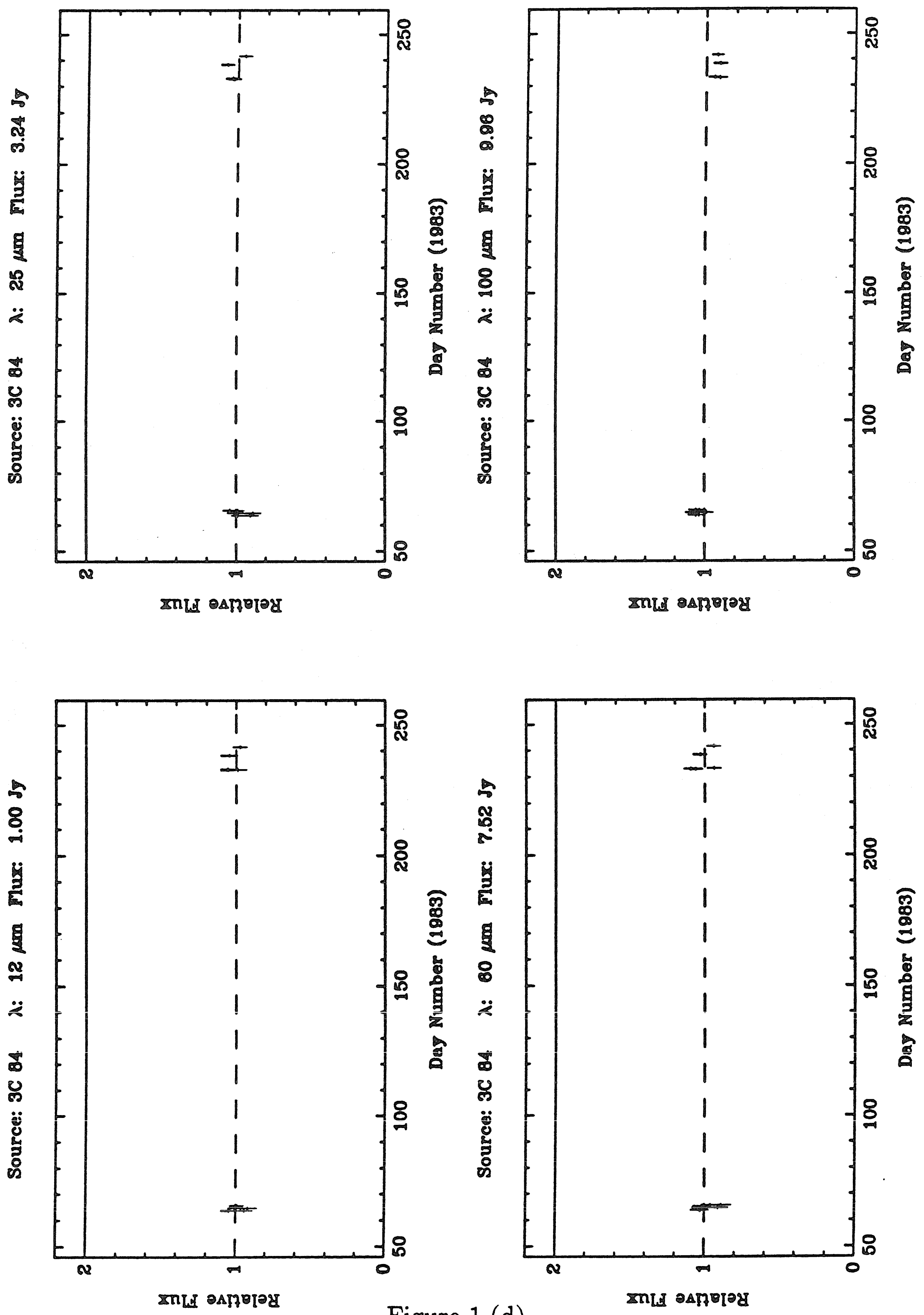
Source: 3C 84 λ: 25 μm Flux: 3.24 Jy
Source: 3C 84 λ: 100 μm Flux: 9.96 Jy
Source: 3C 84 λ: 12 μm Flux: 1.00 Jy
Source: 3C 84 λ: 60 μm Flux: 7.52 Jy
Day Number (1983)
Relative Flux
0
1
2
50
100
150
200
250

Figure 1 (d)

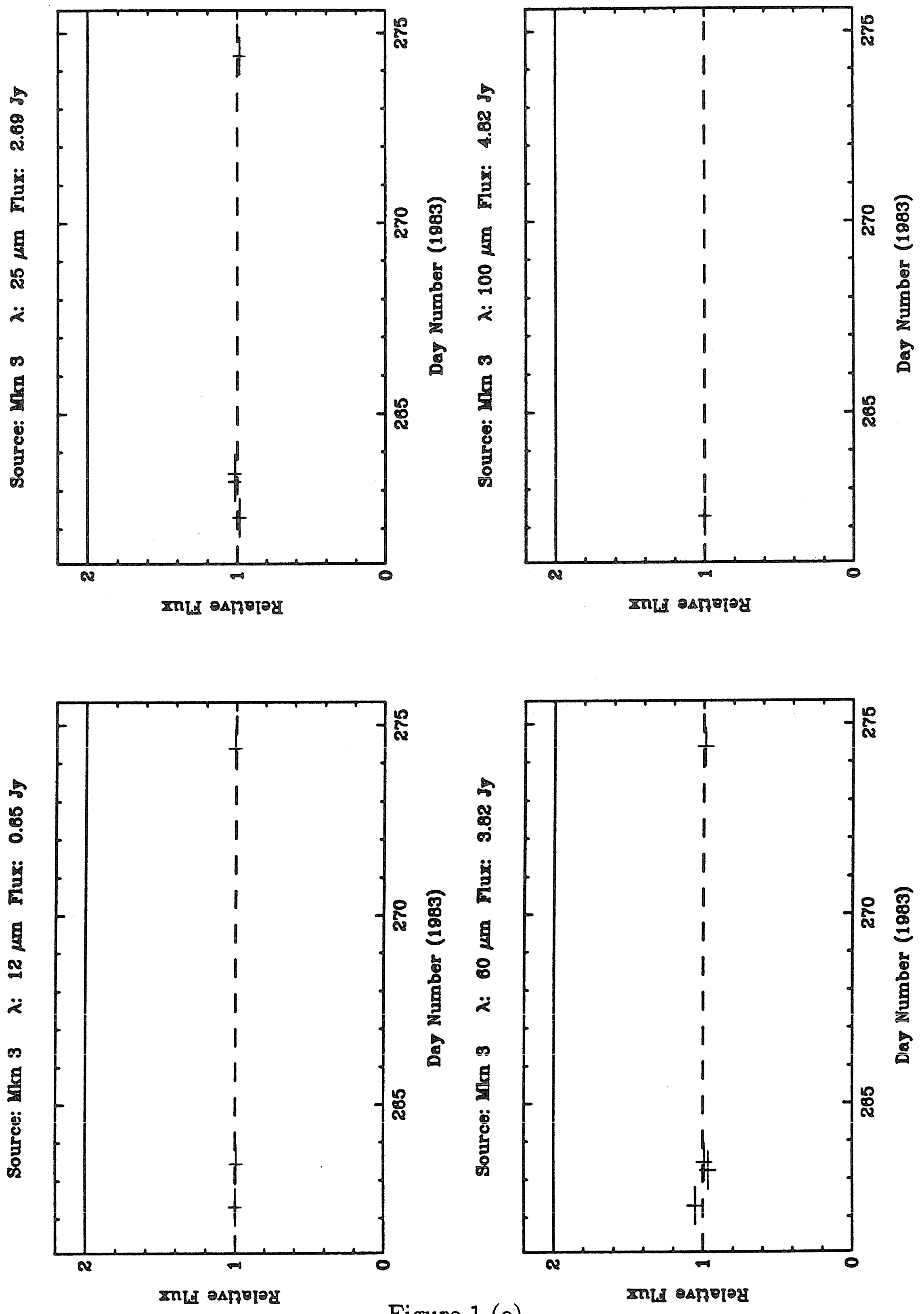
Source: Mkn 3 λ: 12 μm Flux: 0.65 Jy
Source: Mkn 3 λ: 25 μm Flux: 2.69 Jy
Source: Mkn 3 λ: 60 μm Flux: 3.82 Jy
Source: Mkn 3 λ: 100 μm Flux: 4.82 Jy
Relative Flux
0
1
2
Day Number (1983)
265
270
275

Figure 1 (e)

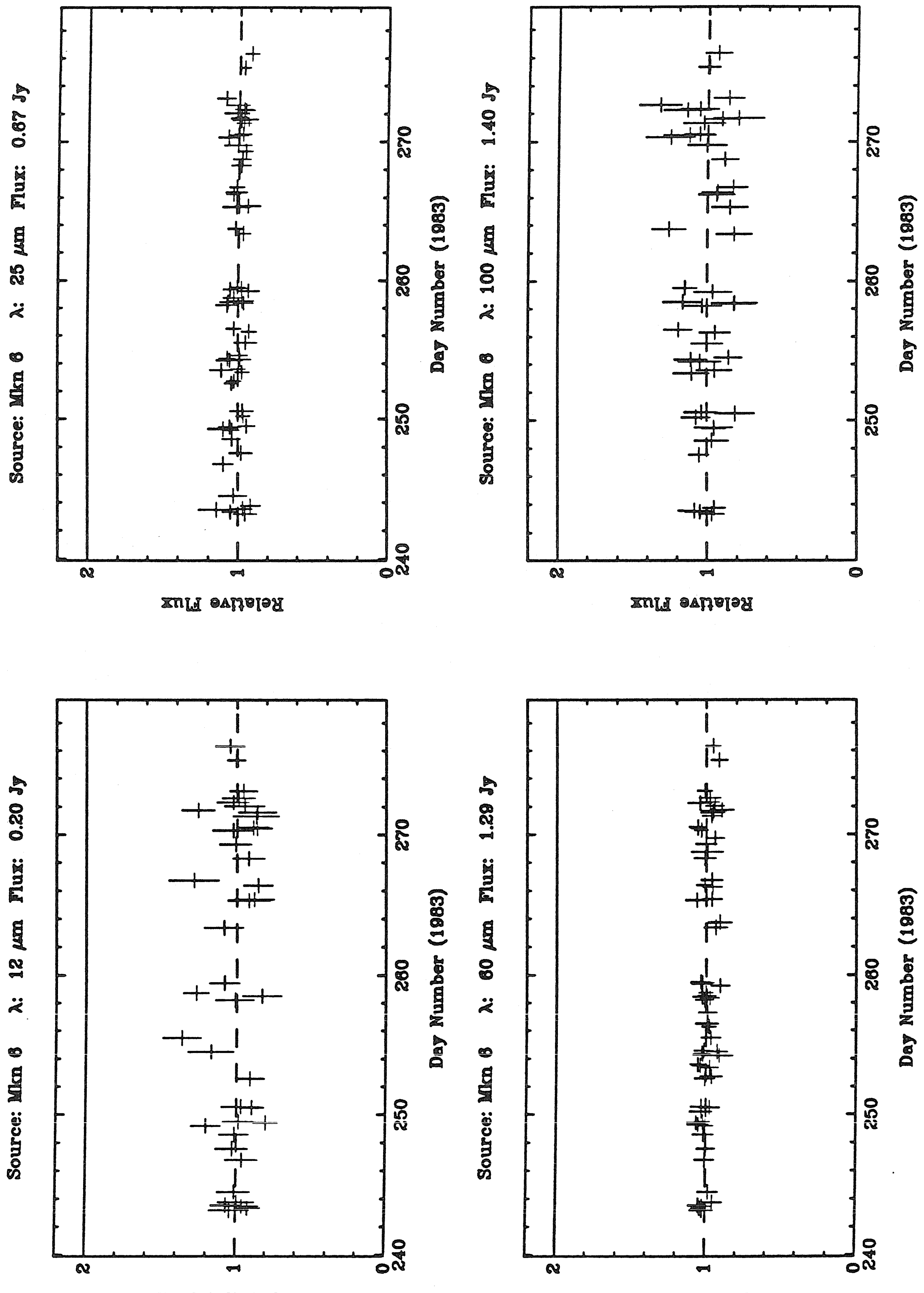
Source: Mkn 6 λ: 25 μm Flux: 0.67 Jy
Source: Mkn 6 λ: 100 μm Flux: 1.40 Jy
Source: Mkn 6 λ: 12 μm Flux: 0.20 Jy
Source: Mkn 6 λ: 60 μm Flux: 1.29 Jy
Relative Flux
0
1
2
240
250
260
270
Day Number (1983)

Figure 1 (f)

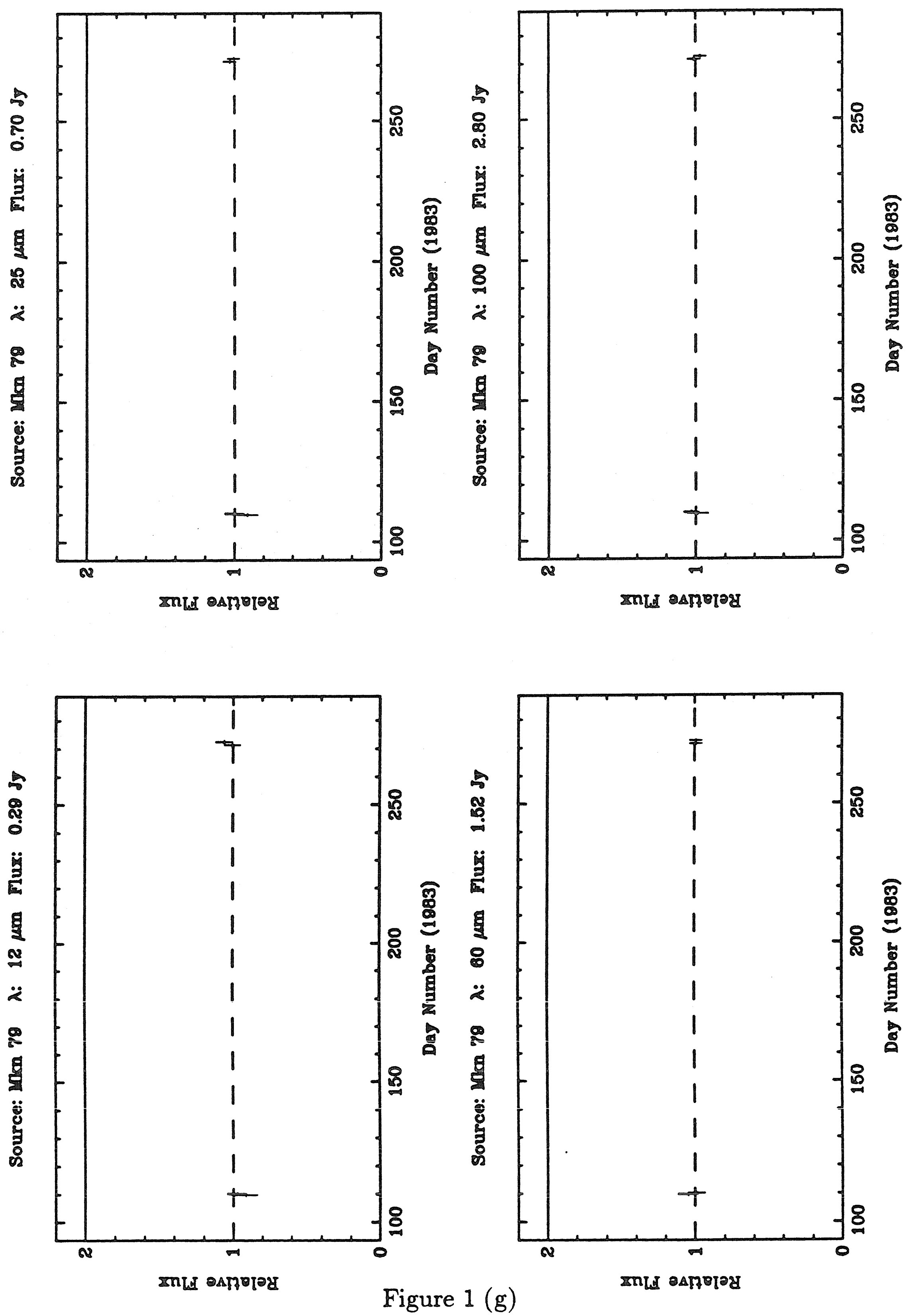
Source: Mkn 79 λ: 12 μm Flux: 0.29 Jy
Source: Mkn 79 λ: 25 μm Flux: 0.70 Jy
Source: Mkn 79 λ: 60 μm Flux: 1.52 Jy
Source: Mkn 79 λ: 100 μm Flux: 2.80 Jy
Relative Flux
0
1
2
Day Number (1983)
100
150
200
250

Figure 1 (g)

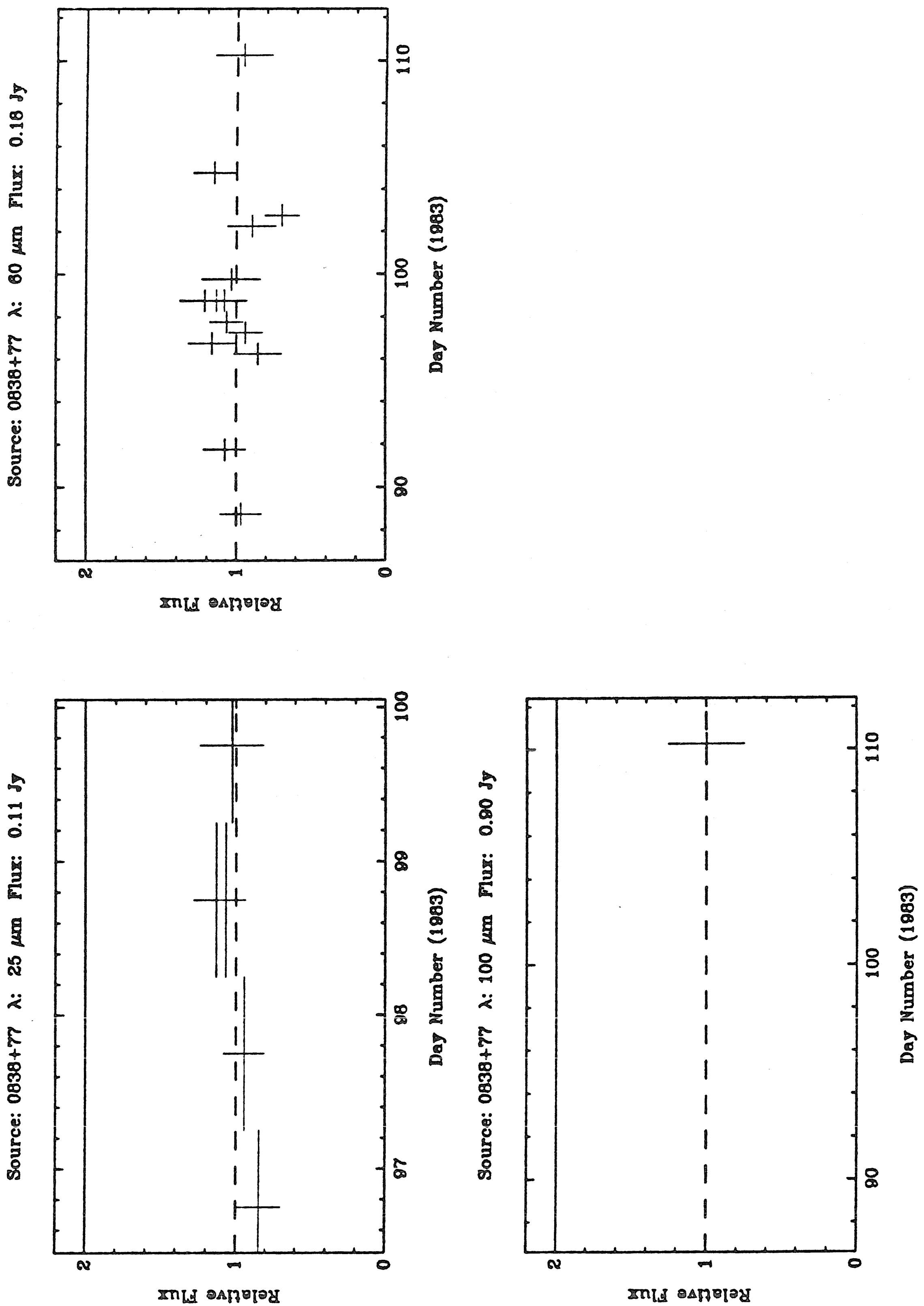
Source: 0838+77 λ: 60 µm Flux: 0.18 Jy
Relative Flux
0
1
2
Day Number (1983)
90
100
110
Source: 0838+77 λ: 25 µm Flux: 0.11 Jy
Relative Flux
0
1
2
Day Number (1983)
97
98
99
100
Source: 0838+77 λ: 100 µm Flux: 0.90 Jy
Relative Flux
0
1
2
Day Number (1983)
90
100
110

Figure 1 (h)

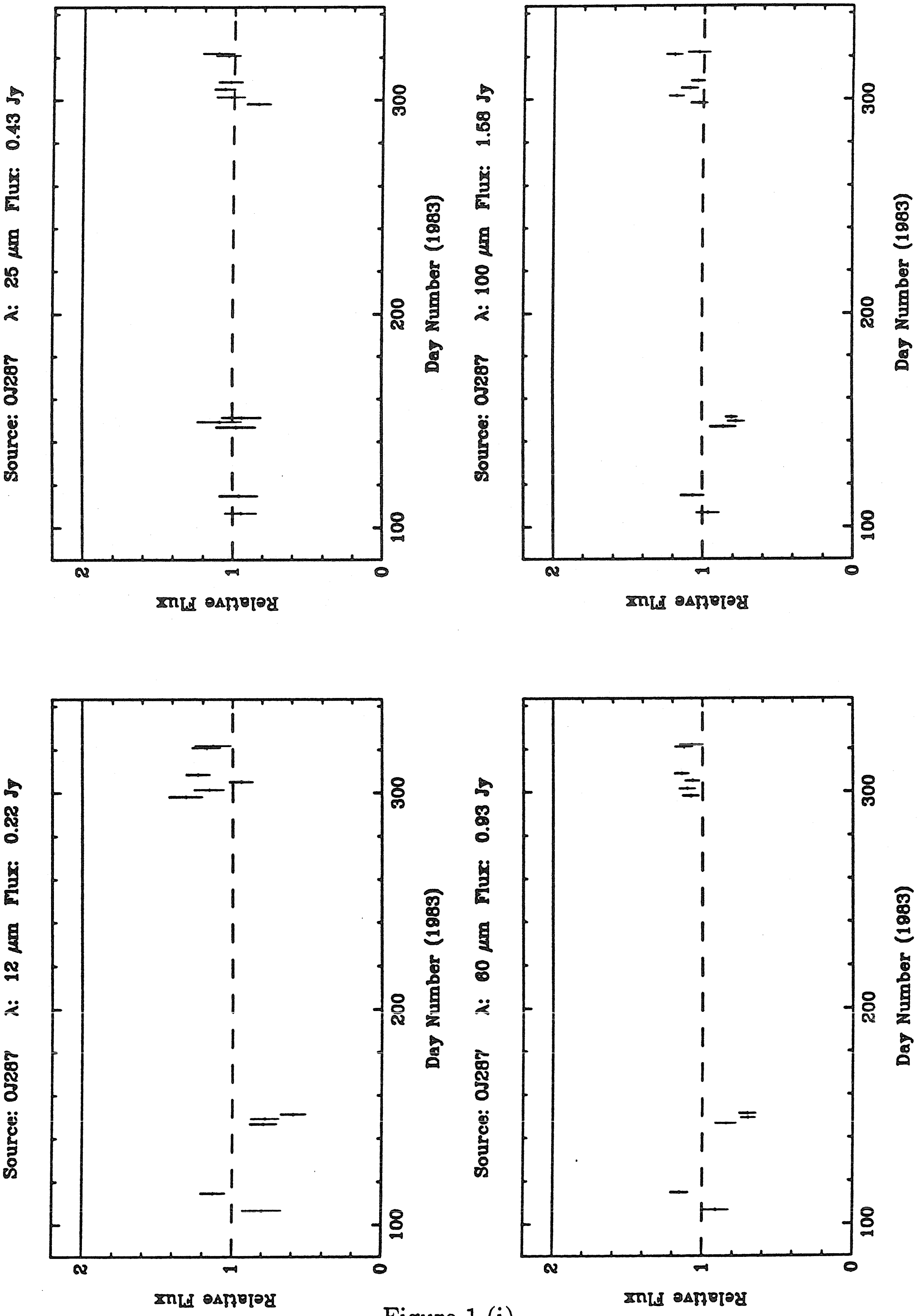
Source: OJ287 λ: 25 μm Flux: 0.43 Jy
Source: OJ287 λ: 100 μm Flux: 1.58 Jy
Source: OJ287 λ: 12 μm Flux: 0.22 Jy
Source: OJ287 λ: 60 μm Flux: 0.93 Jy
Relative Flux
Day Number (1983)
0
1
2
100
200
300

Figure 1 (i)

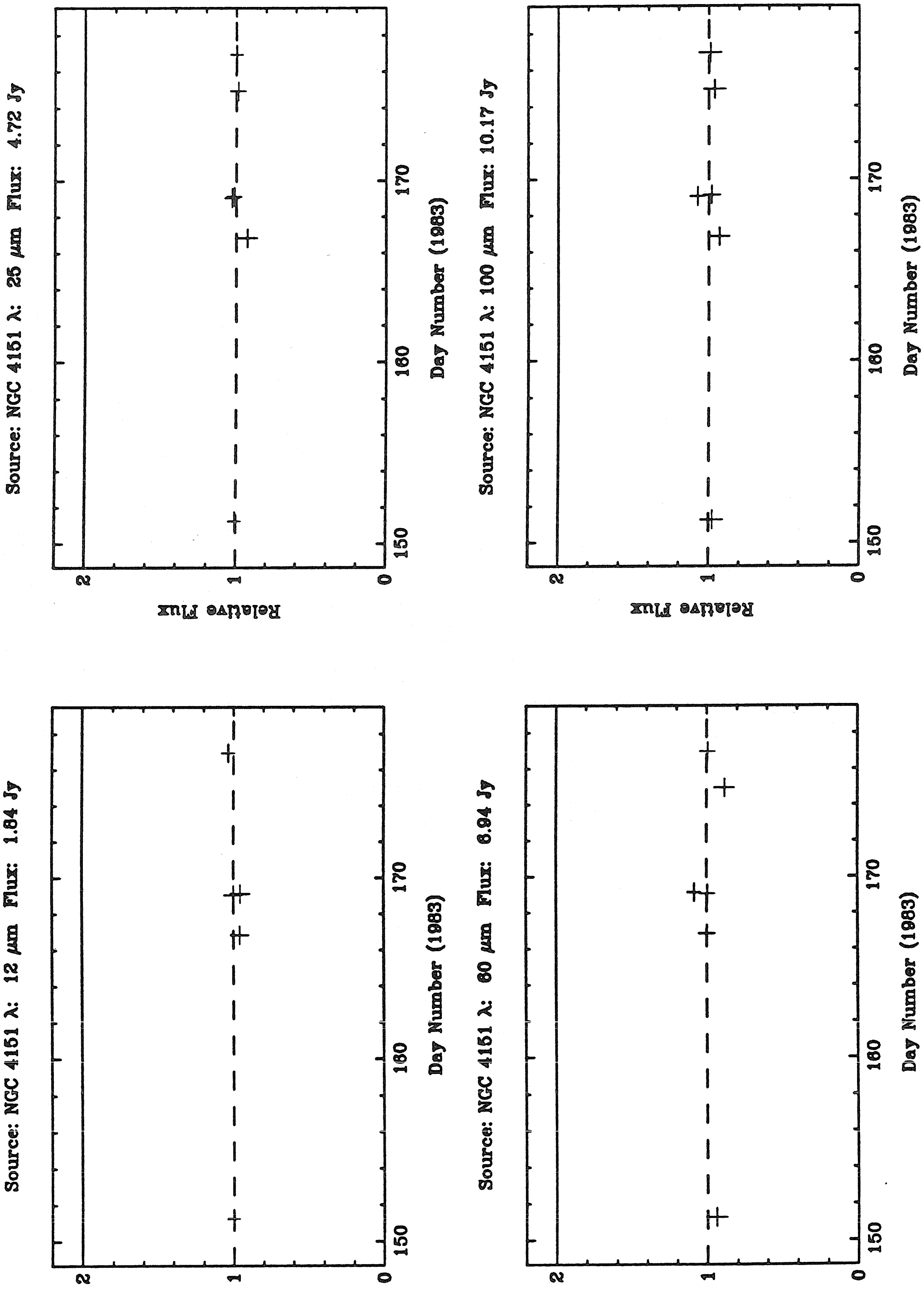

Source: NGC 4151 λ: 25 μm Flux: 4.72 Jy

Source: NGC 4151 λ: 100 μm Flux: 10.17 Jy

Source: NGC 4151 λ: 12 μm Flux: 1.84 Jy

Source: NGC 4151 λ: 60 μm Flux: 6.94 Jy

Figure 1 (j)

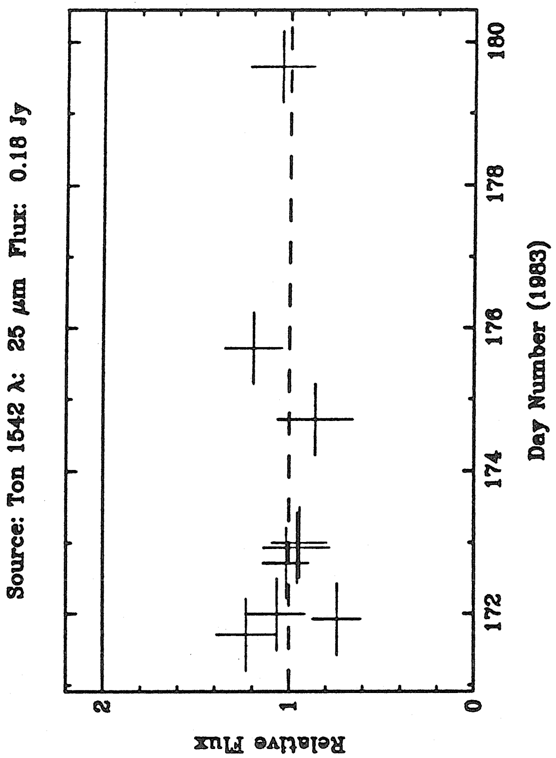
Source: Ton 1542 λ: 25 μm Flux: 0.18 Jy
Relative Flux
2
1
0
Day Number (1983)
172
174
176
178
180

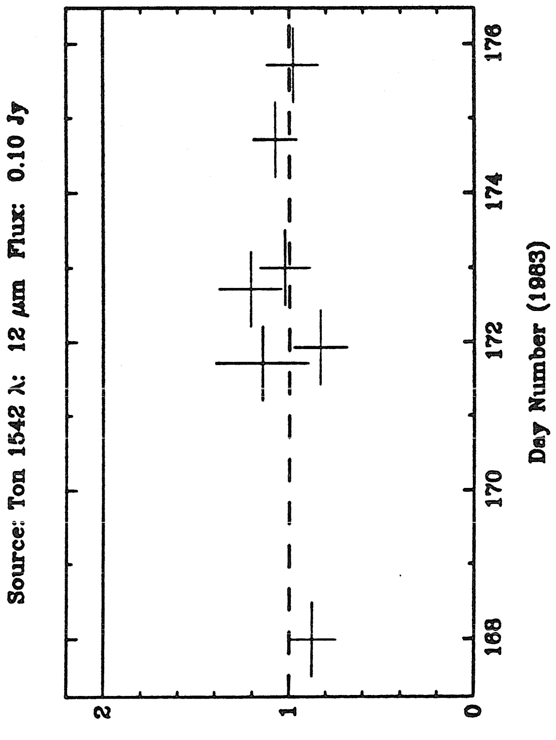
Source: Ton 1542 λ: 12 μm Flux: 0.10 Jy
Relative Flux
2
1
0
Day Number (1983)
168
170
172
174
176

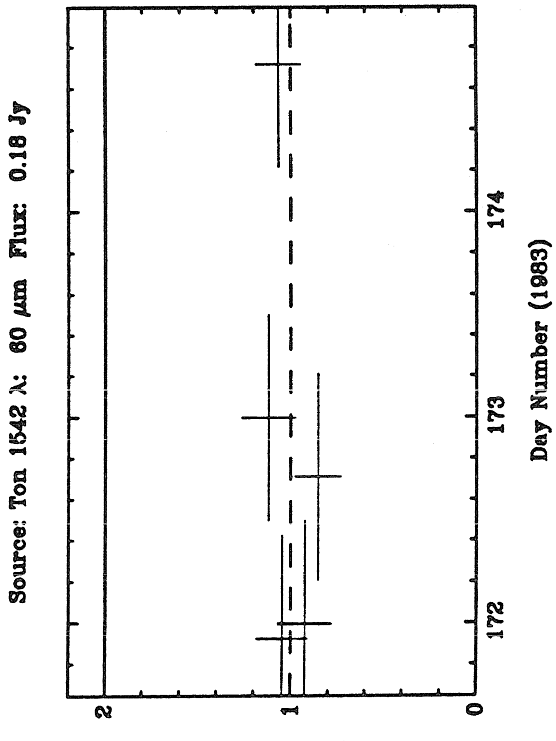
Source: Ton 1542 λ: 60 μm Flux: 0.18 Jy
Relative Flux
2
1
0
Day Number (1983)
172
173
174

Figure 1 (k)

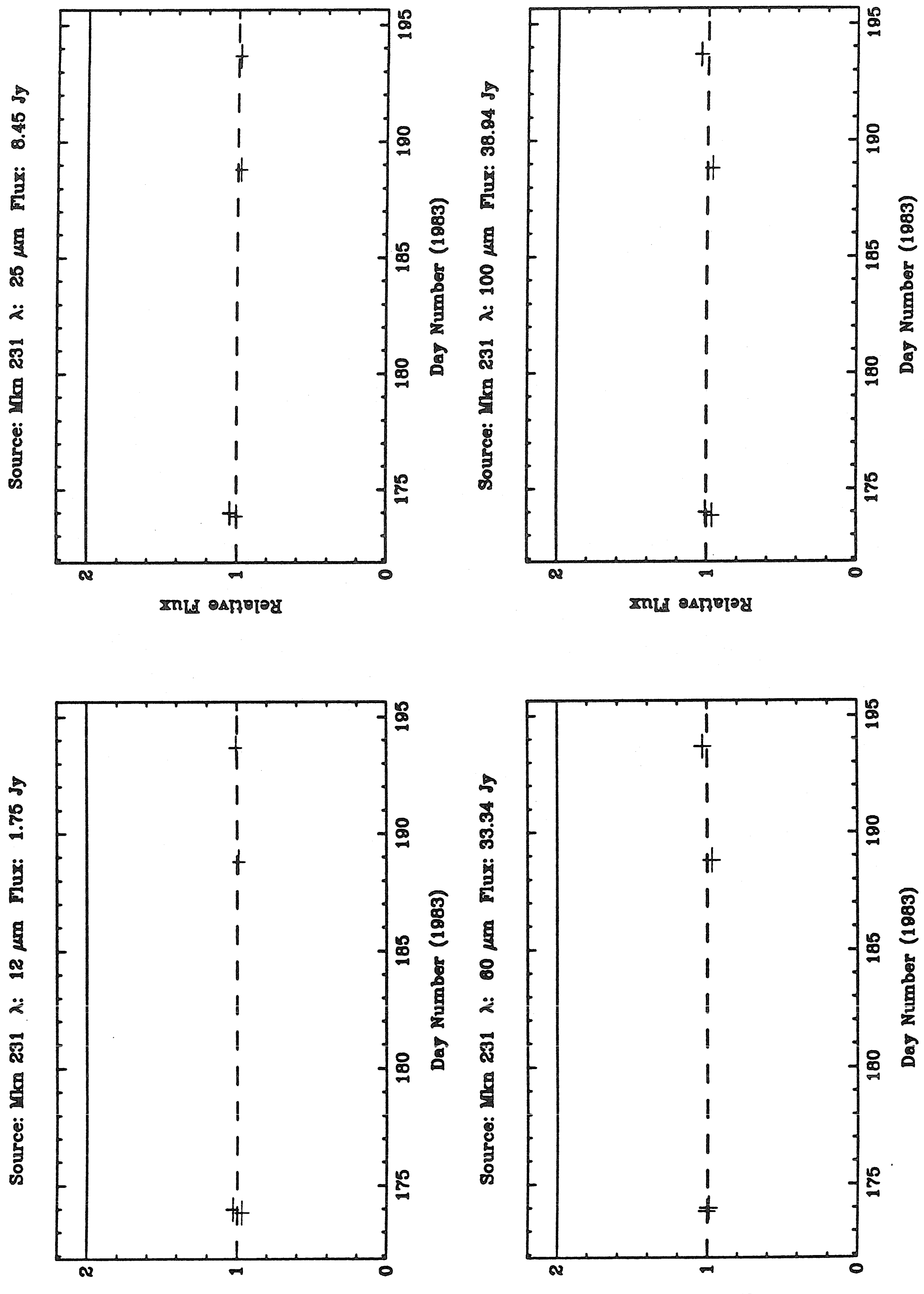
Source: Mkn 231 λ: 25 μm Flux: 8.45 Jy
Source: Mkn 231 λ: 100 μm Flux: 38.94 Jy
Source: Mkn 231 λ: 12 μm Flux: 1.75 Jy
Source: Mkn 231 λ: 60 μm Flux: 33.34 Jy
Relative Flux
0
1
2
Day Number (1983)
175
180
185
190
195

Figure 1 (l)

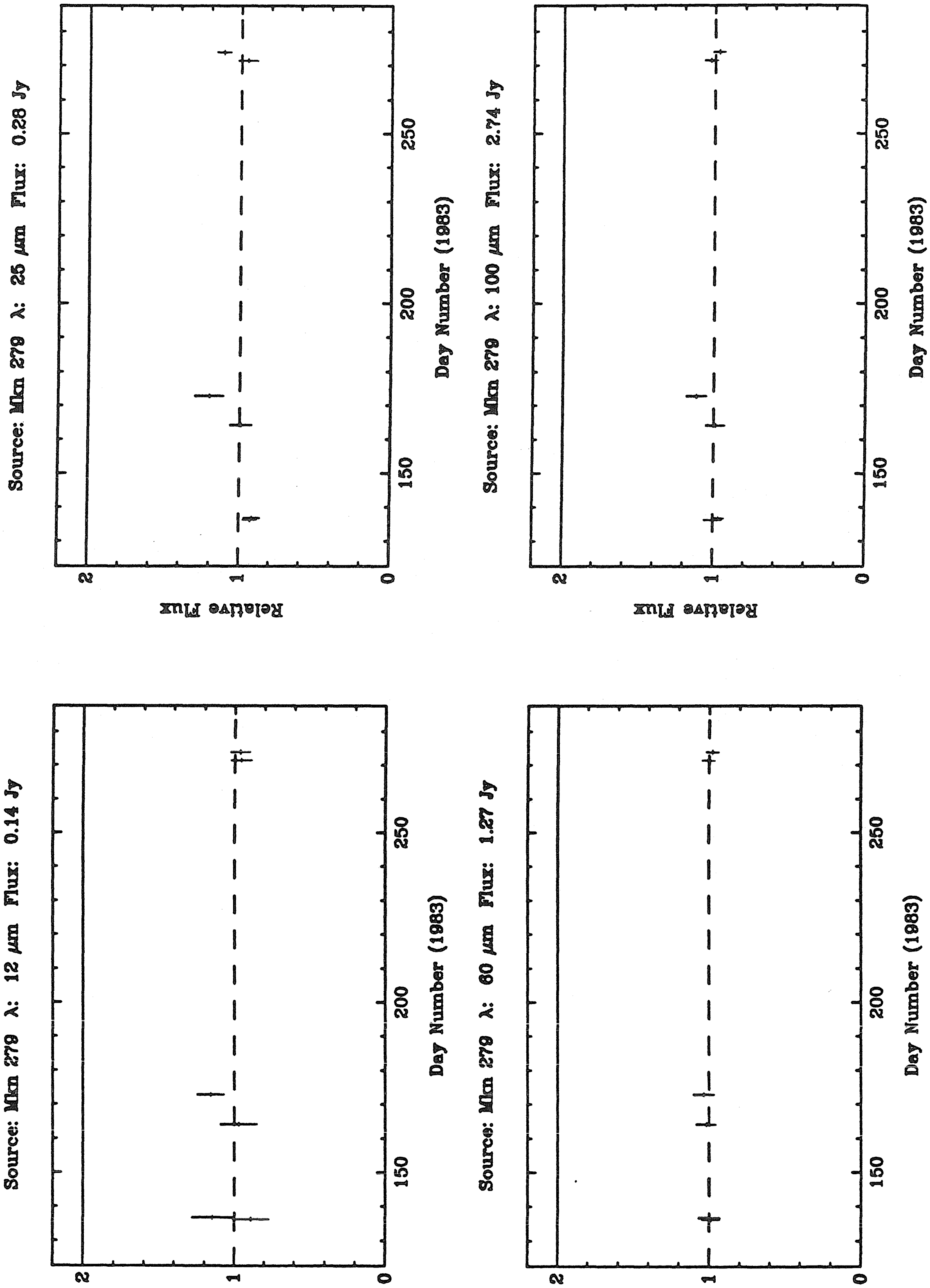
Source: Mkn 279 λ: 12 μm Flux: 0.14 Jy
Source: Mkn 279 λ: 25 μm Flux: 0.28 Jy
Source: Mkn 279 λ: 60 μm Flux: 1.27 Jy
Source: Mkn 279 λ: 100 μm Flux: 2.74 Jy
Relative Flux
0
1
2
Day Number (1983)
150
200
250

Figure 1 (m)

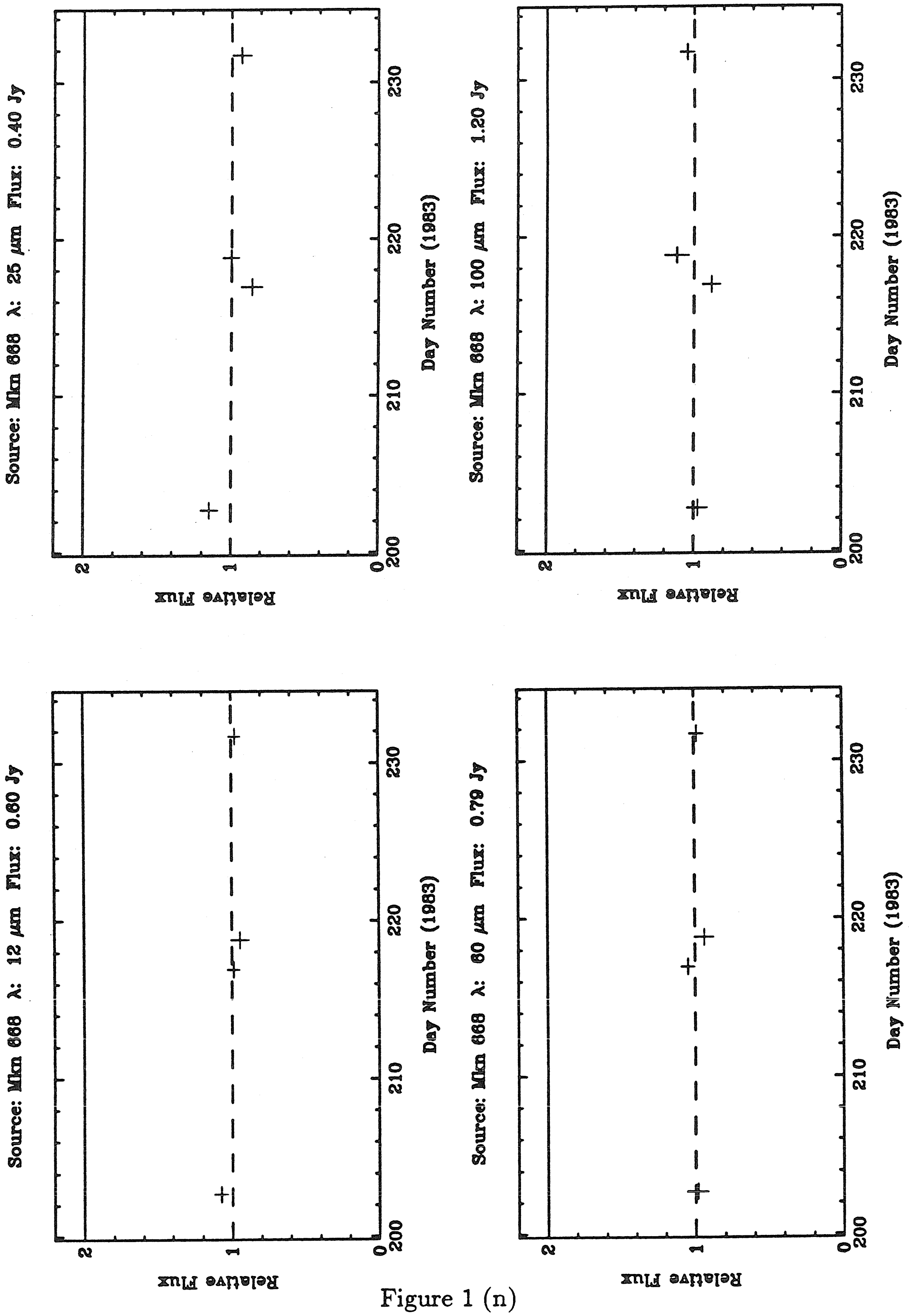
Source: Mkn 668 λ: 12 μm Flux: 0.60 Jy
Source: Mkn 668 λ: 25 μm Flux: 0.40 Jy
Source: Mkn 668 λ: 60 μm Flux: 0.79 Jy
Source: Mkn 668 λ: 100 μm Flux: 1.20 Jy
Relative Flux
0
1
2
Day Number (1983)
200
210
220
230

Figure 1 (n)

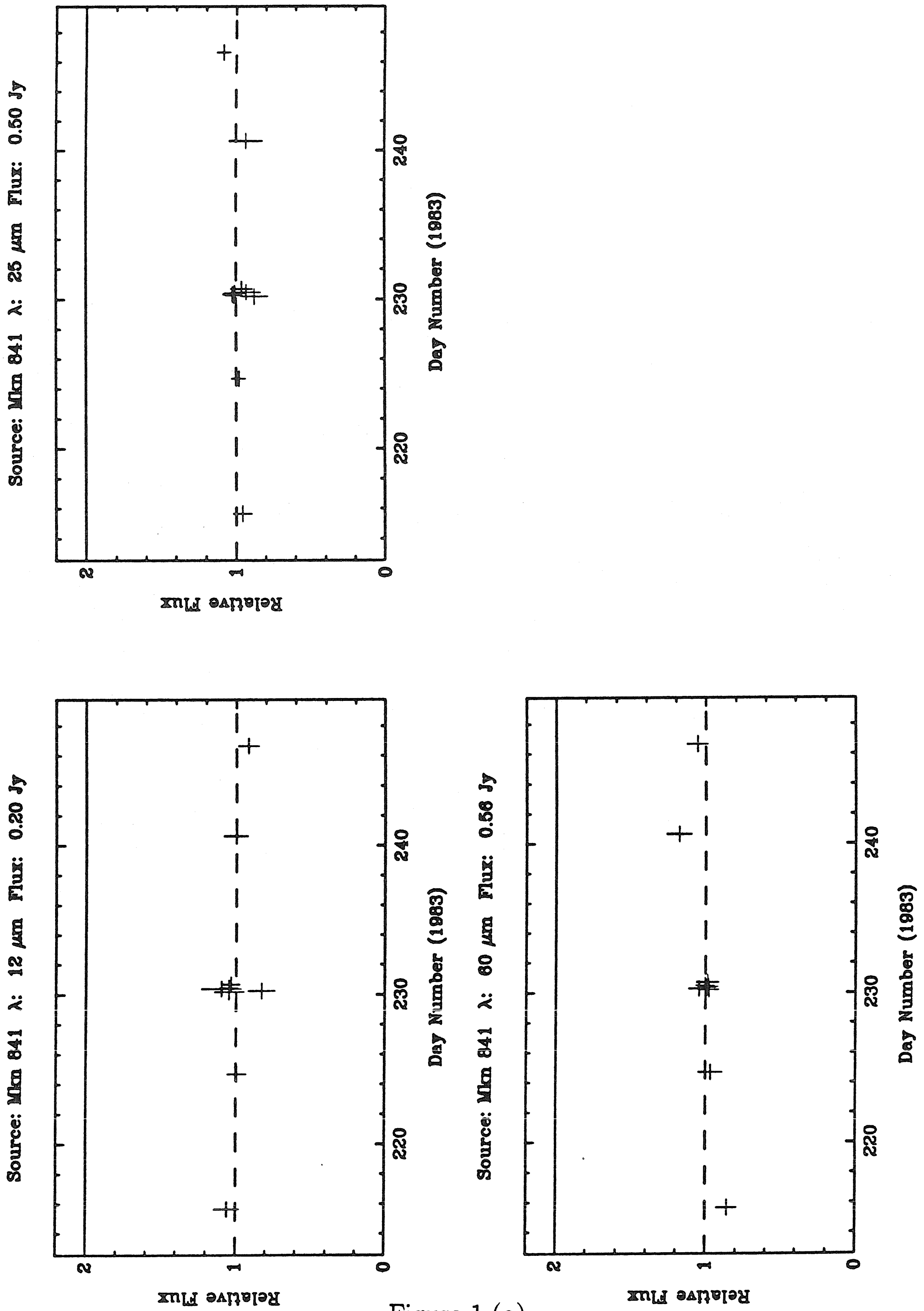
Source: Mkn 841 λ: 25 μm Flux: 0.50 Jy
Relative Flux
2
1
0
220
230
240
Day Number (1983)
Source: Mkn 841 λ: 12 μm Flux: 0.20 Jy
Relative Flux
2
1
0
220
230
240
Day Number (1983)
Source: Mkn 841 λ: 60 μm Flux: 0.56 Jy
Relative Flux
2
1
0
220
230
240
Day Number (1983)

Figure 1 (o)

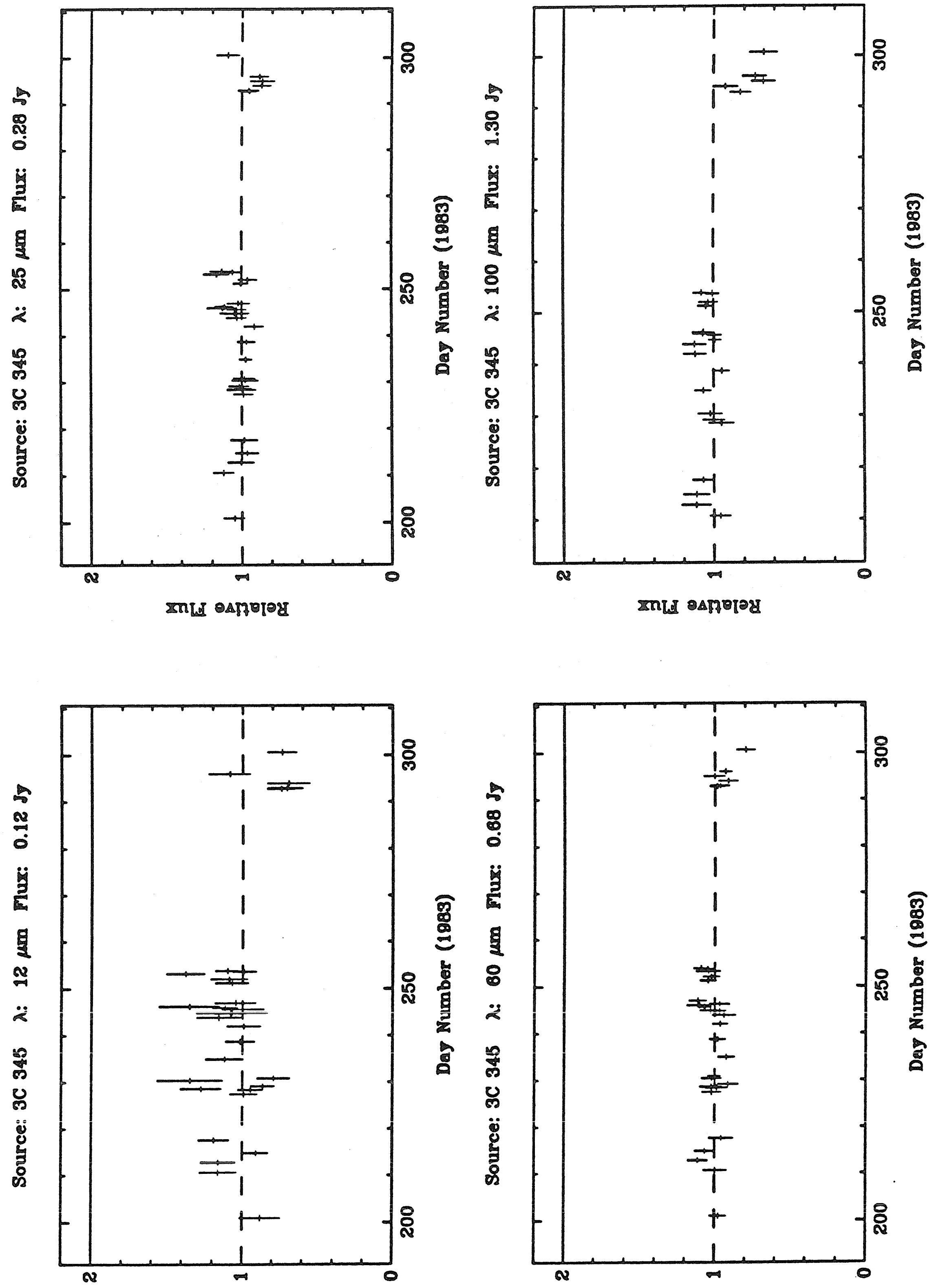
Source: 3C 345 λ: 12 µm Flux: 0.12 Jy
Source: 3C 345 λ: 25 µm Flux: 0.28 Jy
Source: 3C 345 λ: 60 µm Flux: 0.68 Jy
Source: 3C 345 λ: 100 µm Flux: 1.30 Jy
Relative Flux
Day Number (1983)
0
1
2
200
250
300

Figure 1 (p)

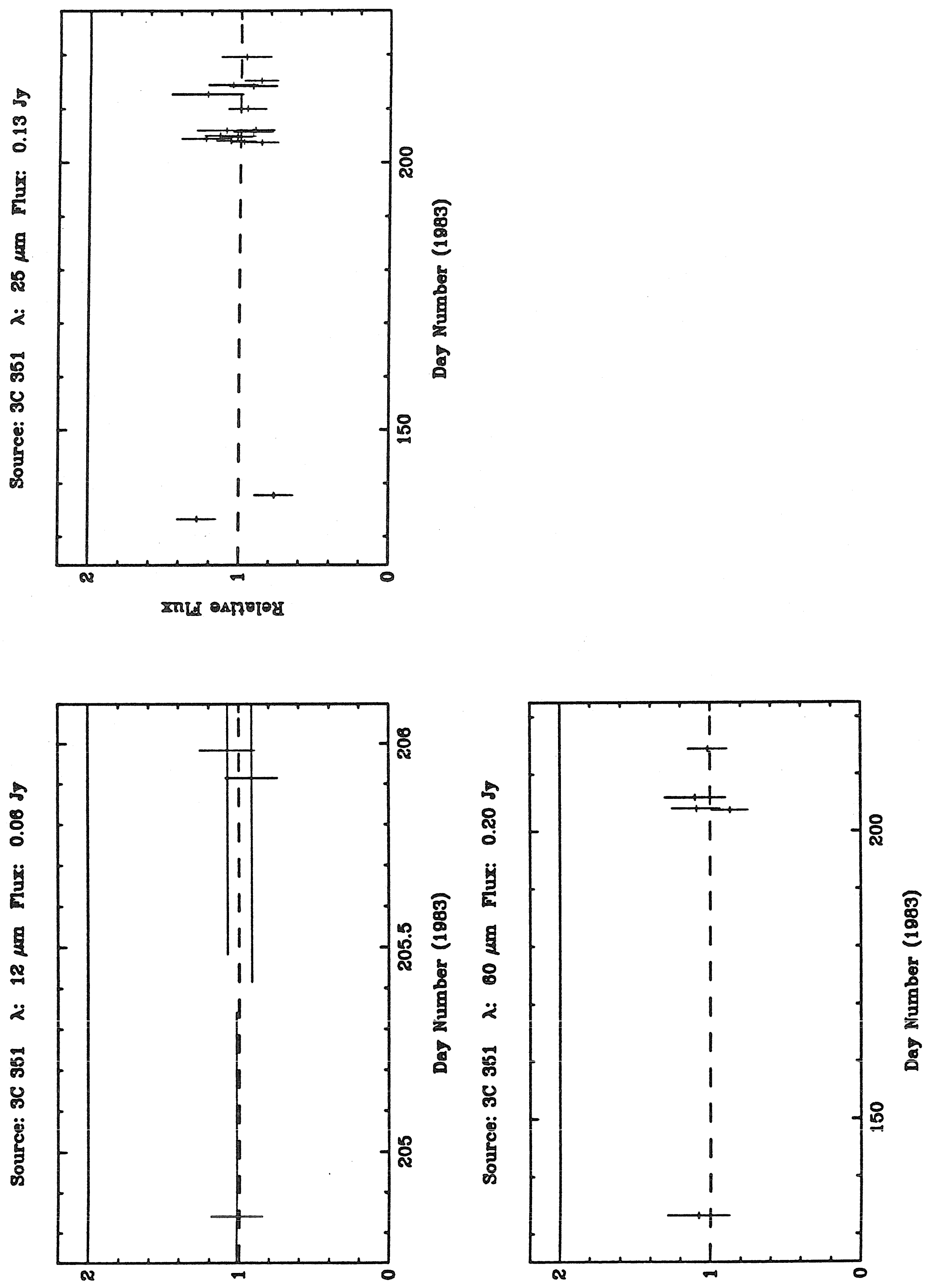
Source: 3C 351 λ: 25 μm Flux: 0.13 Jy
Relative Flux
2
1
0
Day Number (1983)
150
200
Source: 3C 351 λ: 12 μm Flux: 0.06 Jy
Relative Flux
2
1
0
Day Number (1983)
205
205.5
206
Source: 3C 351 λ: 60 μm Flux: 0.20 Jy
Relative Flux
2
1
0
Day Number (1983)
150
200

Figure 1 (q)

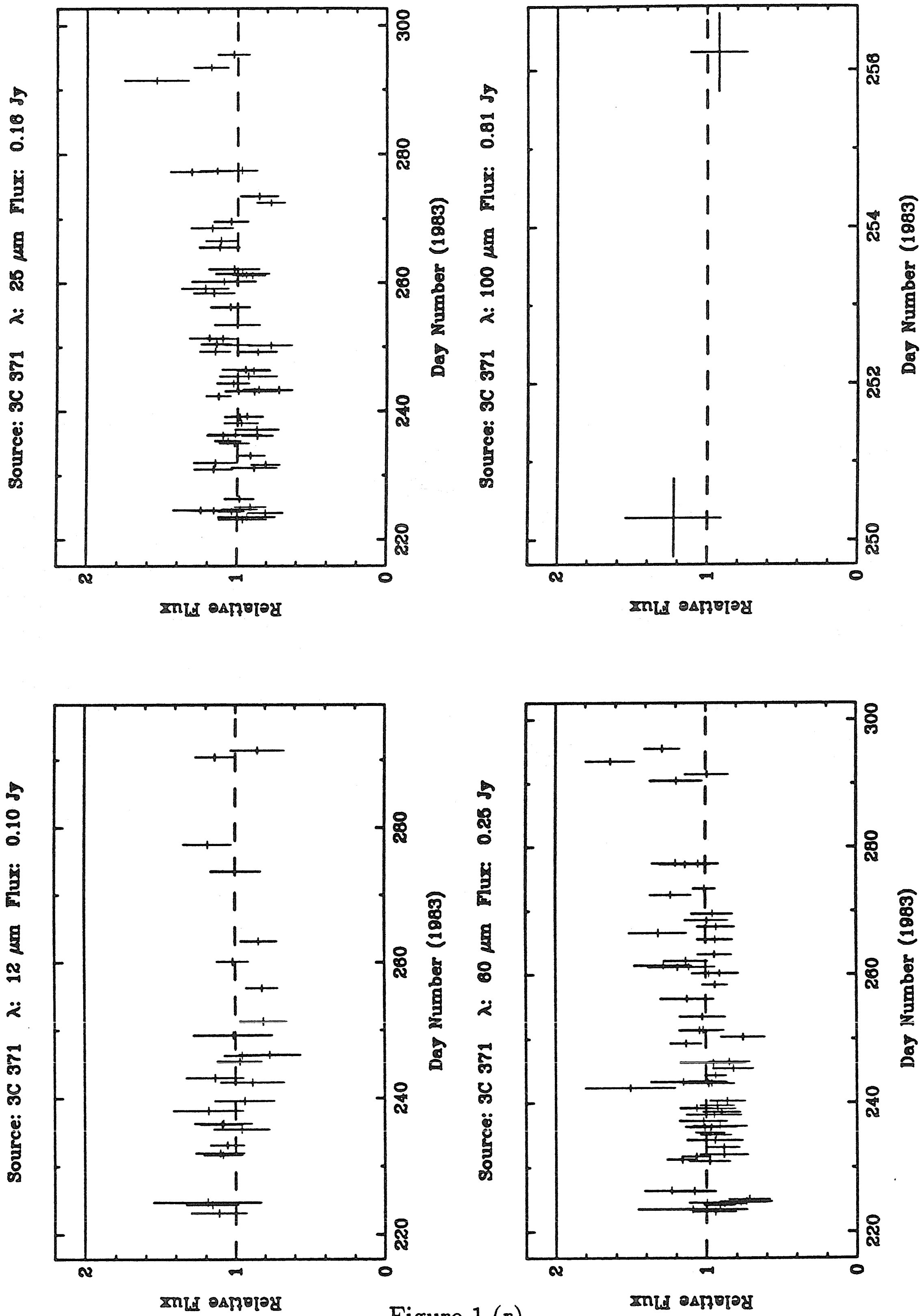
Source: 3C 371 λ: 12 μm Flux: 0.10 Jy
Source: 3C 371 λ: 25 μm Flux: 0.16 Jy
Source: 3C 371 λ: 60 μm Flux: 0.25 Jy
Source: 3C 371 λ: 100 μm Flux: 0.81 Jy
Relative Flux
0
1
2
Day Number (1983)
220
240
260
280
300
250
252
254
256

Figure 1 (r)

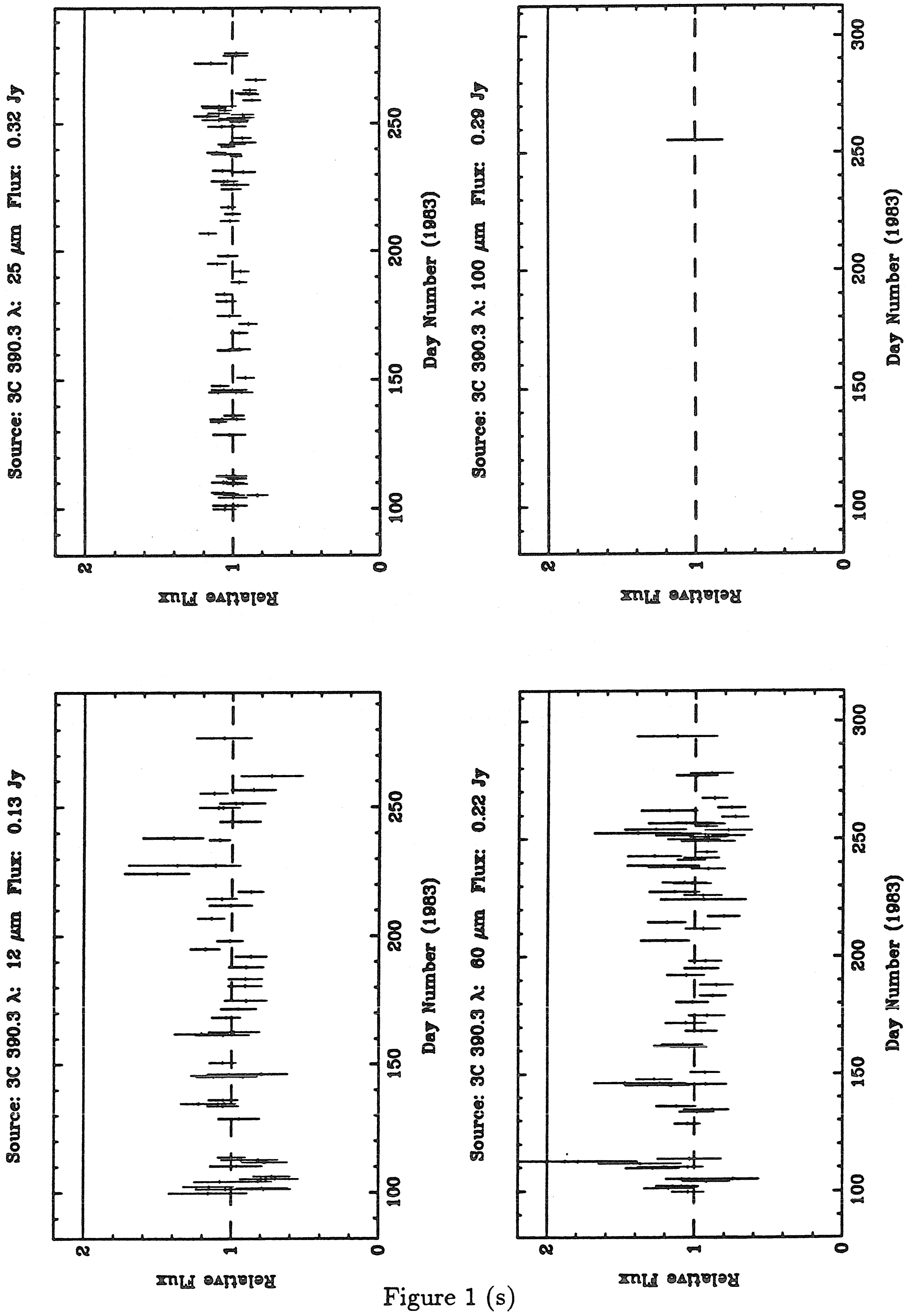
Source: 3C 390.3 λ: 25 μm Flux: 0.32 Jy
Source: 3C 390.3 λ: 100 μm Flux: 0.29 Jy
Source: 3C 390.3 λ: 12 μm Flux: 0.13 Jy
Source: 3C 390.3 λ: 60 μm Flux: 0.22 Jy
Relative Flux
Day Number (1983)
0
1
2
100
150
200
250
300

Figure 1 (s)

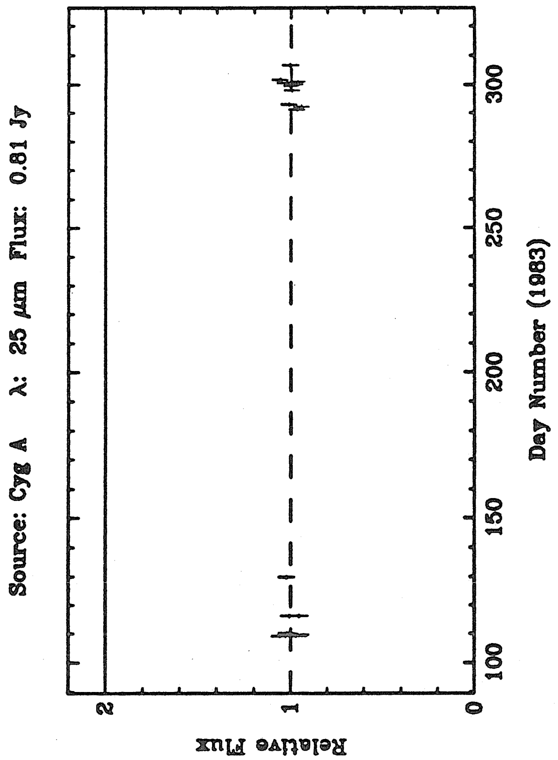
Source: Cyg A λ: 25 μm Flux: 0.81 Jy
Relative Flux
2
1
0
Day Number (1983)
100
150
200
250
300

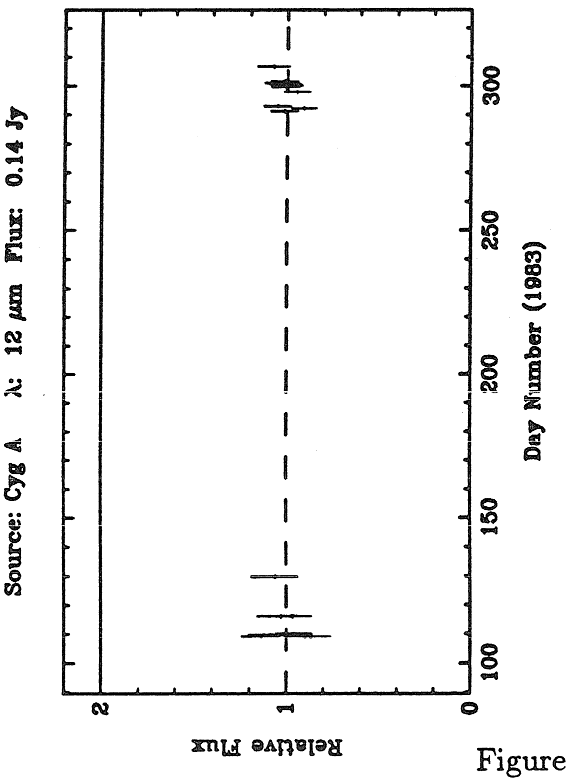
Source: Cyg A λ: 12 μm Flux: 0.14 Jy
Relative Flux
2
1
0
Day Number (1983)
100
150
200
250
300

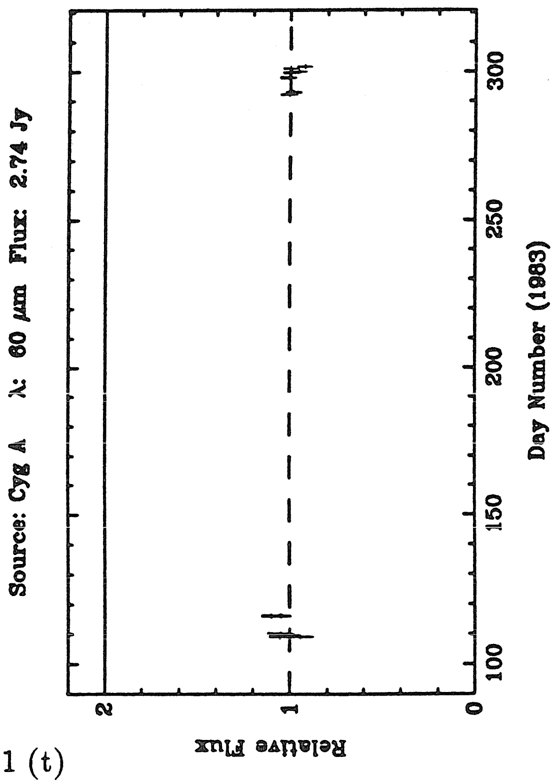
Source: Cyg A λ: 60 μm Flux: 2.74 Jy
Relative Flux
2
1
0
Day Number (1983)
100
150
200
250
300

Figure 1 (t)

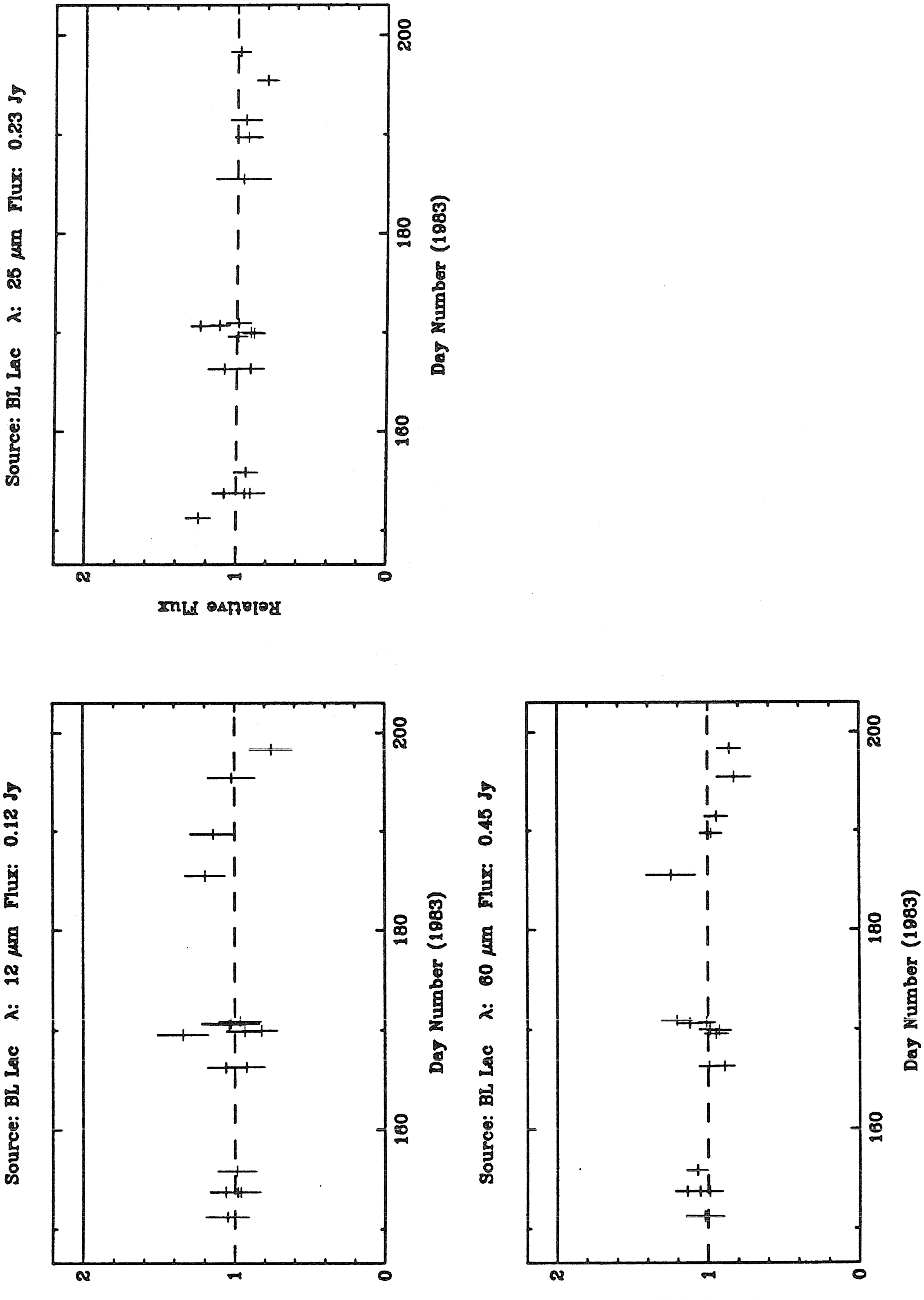
Source: BL Lac λ: 25 μm Flux: 0.23 Jy
Source: BL Lac λ: 12 μm Flux: 0.12 Jy
Source: BL Lac λ: 60 μm Flux: 0.45 Jy
Relative Flux
0
1
2
Day Number (1983)
160
180
200

Figure 1 (u)

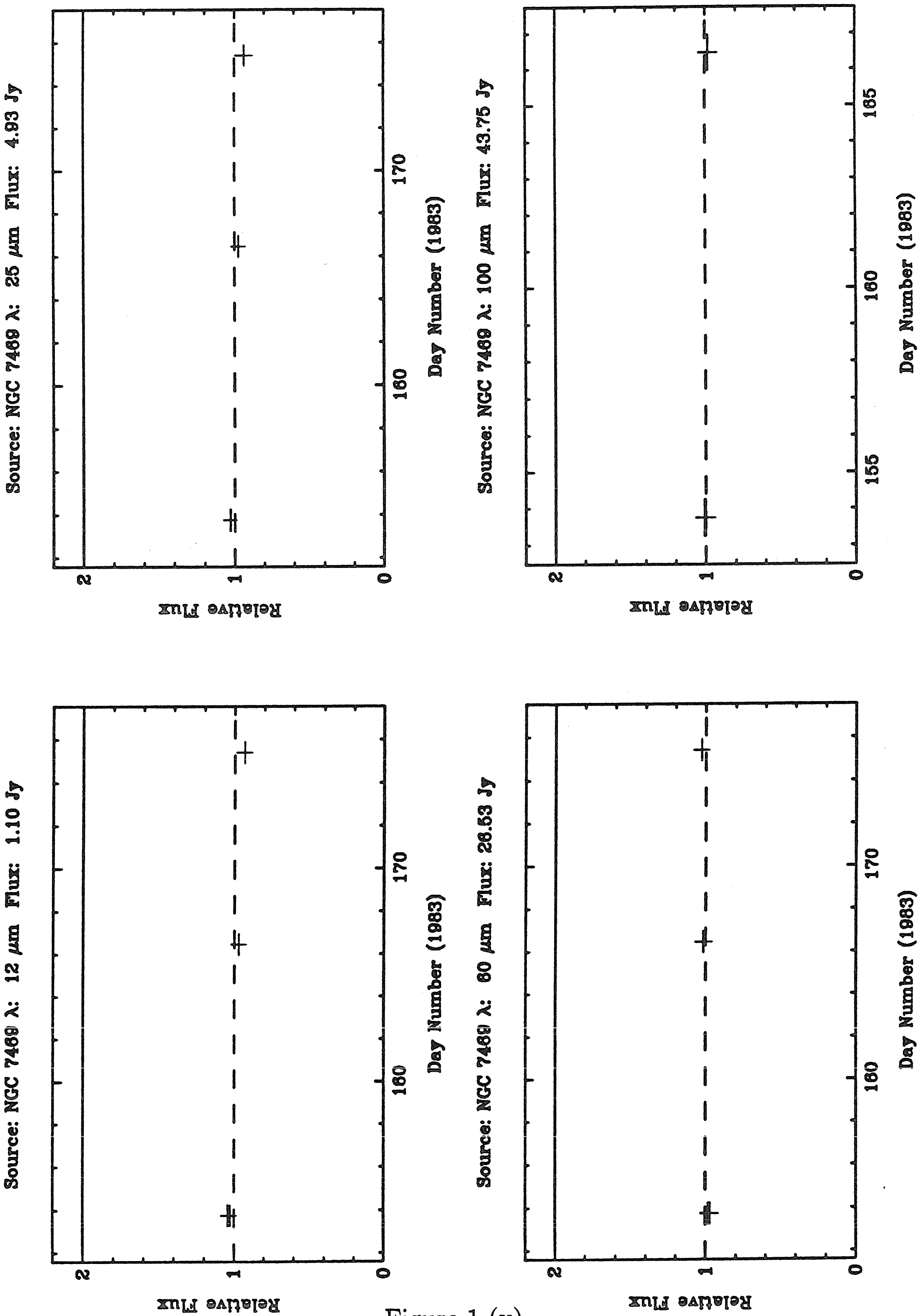
Source: NGC 7469 λ: 25 μm Flux: 4.93 Jy
Relative Flux
Day Number (1983)
160
170
0
1
2
Source: NGC 7469 λ: 100 μm Flux: 43.75 Jy
Relative Flux
Day Number (1983)
155
160
165
0
1
2
Source: NGC 7469 λ: 12 μm Flux: 1.10 Jy
Relative Flux
Day Number (1983)
160
170
0
1
2
Source: NGC 7469 λ: 60 μm Flux: 26.53 Jy
Relative Flux
Day Number (1983)
160
170
0
1
2

Figure 1 (v)

Chapter Seven

FUTURE WORK

The ultimate goal of my research is to determine physical conditions at the centers of active galactic nuclei (AGNs), and understand the mechanisms responsible for producing their enormous luminosities. As the highly energetic nonthermal processes believed to be operating produce energy over a very wide range of frequencies, the broad-band continuum must be measured to study unreprocessed radiation from deep within the nucleus. This work has begun the massive task of determining the broad-band properties of AGNs from radio through X-ray wavelengths. Spectral energy distributions of the CfA Seyfert galaxies–a complete, optically selected sample–will be determined and the correlation between spectral properties studied. Eventually, data on other well-defined samples of bright AGNs (e.g., the PG quasars, hard X-ray selected Seyfert 1 galaxies, etc.) will be included as well. It may be possible to create an improved classification system for AGNs, based on simple physical models of their broad-band properties.

The infrared and radio data for the CfA Seyfert galaxies have been fully analyzed, and the optical, ultraviolet, and X-ray data must now be incorporated. The optical spectra will be used to measure line and continuum fluxes and to test for selection effects. The CCD surface photometry will be used to separate the nonstellar continuum from starlight in the underlying galaxy. An initial examination of the CCD data suggests that the underlying galaxies may have a higher tendency to have bars, companions, and evidence for recent interactions than normal galaxies. Most of the Seyfert 1 galaxies in this sample were detected at X-ray wavelengths with the Einstein IPC and MPC and at ultraviolet wavelengths with IUE. It should be possible to produce complete X-ray-ultraviolet spectral energy distributions for most of these objects.

As usual, this research raises new questions as old ones are answered. A broad emission feature, centered near 5 μm, was found in the spectra of luminous AGNs. Its nature not been established, having been modeled as free-free emission from the broad-line region (Puetter and Hubbard 1985), emission from the outer regions of the accretion disk (Collin-Soufrin 1986), and thermal emission from hot dust (i.e., Barvainas 1986). Low-resolution spectra from 2.5 to 10 μm can be used to determine its exact shape, and variability studies may allow a limit to be placed on the size of the region in which it is produced.

Most quasars and luminous Seyfert 1 galaxies have spectra which rise from the optical into the infrared, and then cut off near ~80 μm. This suggests that the infrared emission from most radio-quiet quasars and Seyfert 1 galaxies is dominated by nonthermal radiation from a synchrotron self-absorbed region of order a light day across. It should soon be possible to detect bright, relatively dust-free quasars and Seyfert 1 galaxies at 1.3 mm with the IRAM 30-m telescope and at 800 and 350 μm with the Clerk Maxwell Telescope. Determination of the shape of the far-infrared turnover will allow an important test of this conclusion, as different mechanisms will yield different shapes.

It also appears that normal (low-polarization) quasars and Seyfert galaxies are not strongly variable in the far-infrared, although the IRAS data are not very well suited to monitor AGNs. It also seems that blazars vary much more slowly at far-infrared wavelengths than allowed by light-travel and beaming arguments. One possible explanation, which deserves theoretical study, is that a regulating mechanism may be operating in the central regions of AGNs. In any event, it is critical to make a more sensitive test of far-infrared variability in AGNs.

It appears that the radio spectra of some Seyfert 1 galaxies flatten out near 2 cm. If confirmed with a larger sample, millimeter measurements of the shape of this new component can be used to determine if it arises from a compact radio core or the low-frequency side of the optical-infrared continuum. Also, low-frequency WSRT data suggest that the radio spectra of some objects may be turning over between 20 cm and 90 cm. If this is the case, source parameters such as sizes, ages, and particle energies can be determined.

Finally, a more speculative but very interesting approach involves exploring the relationship between the physics of AGNs and compact galactic objects. It may be possible to determine masses, periods, and other orbital parameters for these relatively simple and nearby systems. Understanding these objects could yield clues to the physical conditions in and nature of the emission from the more distant and complex AGNs.

REFERENCES

Barvainas, R. 1986, preprint.

Collin-Soufrin, S. 1986, preprint.

Puetter, R. C. and Hubbard, E. N. 1985, *Ap. J.*, **295**, 394.